



**Silesian University
of Technology**

Faculty of Energy and Environmental Engineering

Department of Thermal Technology

Discipline of Environmental Engineering, Mining and Energy

**Experimental and numerical research of the
selective catalytic reduction system for diesel engine cars**

PhD thesis of

Damian Kurzydym, MSc, Eng.

Supervisor: Associate Professor Zbigniew Żmudka, PhD, DSc

Gliwice, 2022

Contents

Acknowledgments.....	6
Nomenclature.....	8
1 Introduction	15
1.1 Introduction to the exhaust emissions of internal combustion engines.....	16
2 Justification and motivation of topic selection	20
3 Research objectives	21
4 NO_x formation process and their aftertreatment systems	22
4.1 Exhaust Gas Recirculation (EGR).....	23
4.2 Lean-NO _x Traps (LNT)	25
4.3 Selective Catalytic Reduction (SCR).....	26
4.4 Ammonia Slip Catalyst (ASC).....	31
4.5 Combination of DPF and SCR.....	32
5 Historical background of emission standards in Europe	34
6 Emission test cycles according to EU regulations	40
7 Current status of the SCR catalyst and modeling.....	47
7.1 Basic information about structure of catalyst.....	47
7.1.1 Preparation of catalyst and coating.....	50
7.1.2 Vanadium-based catalyst	52
7.1.3 Cu-Zeolite catalyst	54
7.1.4 Fe-Zeolite catalyst.....	55
7.2 Ageing, poisoning and deposit problem in SCR.....	57
7.3 Design and development of SCR mixers	64
8 Methodology and research design	68
9 Experimental research.....	73
9.1 Flow tests in laboratory conditions	73
9.1.1 Results for flow tests.....	75
9.2 Flow rig tests of NO _x reduction in laboratory conditions.....	77
9.2.1 Principal factors that determine the flow through the catalyst.....	79
9.2.2 Boundary conditions for flow rig tests	80
9.2.3 Results for flow rig tests.....	82
9.3 Chemical analysis of SCR catalytic converter	101
9.4 Reverse engineering for CAD modelling.....	102

10 Numerical research	104
10.1 The governing equations in computational fluid dynamics (CFD).....	105
10.1.1 The mass, momentum and energy conservation equations	105
10.1.2 Species transport equations and finite-rate formulation for reactions.....	107
10.1.3 Turbulence k - ϵ model equations	108
10.1.4 Discrete Phase Model for spray.....	110
10.2 Data acquisition for CFD simulation	114
10.2.1 Porous model.....	115
10.2.2 Spray of Urea-Water-Solution (UWS) model and decomposition	115
10.2.3 Reaction kinetics and mechanism	119
10.3 Preparation of a CAD model and mesh for CFD simulation	128
10.3.1 2D CAD model with mesh for CFD simulation.....	128
10.3.2 3D CAD model with mesh for CFD simulation.....	130
10.4 2D axisymmetric flow simulation	132
10.4.1 Main settings with boundary conditions for 2D simulation.....	133
10.4.2 Simulation results for 2D axisymmetric model	134
10.5 3D model flow simulation.....	137
10.5.1 Main settings with boundary conditions for 3D simulation.....	137
10.5.2 Cold flow simulation results for 3D model	141
10.5.3 Hot flow simulation results for 3D model	145
10.5.4 Simulation results for improved mixer	152
11 Analysis and comparison of test results	158
11.1 Validation of results for a 2D axisymmetric model	158
11.2 Validation of results for a 3D model	159
11.3 Impact of other parameters on the research results	163
12 Emission tests in the certification laboratory	167
12.1 Regulations for a replacement exhaust gas aftertreatment system.....	169
12.2 Emission test results	171
13 Summary and conclusions	179
Bibliography	183
List of figures	194
List of tables.....	197
Appendices	199
I. Introduction to emissions of internal combustion engines	199
II. Systems limiting the emission of CO, HC and NO_x.....	207
A. Diesel Oxidation Catalyst (DOC)	210

B.	Three-Way Catalytic Converter (TWC).....	212
III.	Systems limiting the emission of PM	215
A.	Diesel Particulate Filter (DPF).....	218
B.	Gasoline Particulate Filter (GPF).....	223
IV.	Introduction to applied computational fluid dynamics (CFD)	226
A.	Modelling procedure	227
V.	User Defined Functions (UDFs)	231
A.	ETA index	231
B.	Eccentricity index.....	233
VI.	Research publications	235
	Abstract	236
	Streszczenie	237

Acknowledgments

This dissertation, after a six-year adventure with PhD studies while working full-time at Tenneco would not have been possible without the help, support and contribution of a number of individuals, whom I believe deserve special mention and acknowledgement. It is my pleasure to thank them.

First of all, I would like to express my sincerest gratitude to my supervisor, Professor Zbigniew Żmudka from the Department of Thermal Technology, Silesian University of Technology, who has been my supervisor since the beginning. I thank him for providing me with guidance and mentorship and the opportunity to do research in the area of harmful substance emissions and systems to reduce them in the automotive industry.

I am deeply grateful to Professor Adam Klimanek from the Department of Thermal Technology, Silesian University of Technology, who has been my auxiliary supervisor from the beginning, however, in the meantime he obtained his habilitation and legally could no longer be an auxiliary promoter in this dissertation. This, however, did not prevent us from working together in which I treated him as a valuable promoter. I appreciate it and thank him for his contribution, uncountable hours with me for discussion and giving me valuable suggestions in the area of numerical methods and implementation to the CFD simulation in ANSYS Fluent software.

Both promoters, I gratefully give thanks for their contributions regarding the preparation and reviews of our four scientific articles which were published at three international conferences, in which I participated.

I would like to thank my Engineering Manager Michał Bobula from EMEA, Emission Control Engineering at Tenneco (DRiV™) for initiating the idea for my PhD work, valuable comments and support. I would also like to thank my Product Management Director Julien Rousseau from the same unit for the financing of all costs related to carrying out the experimental research and participation in conferences. I also could not forget about Senior Training Manager Oscar Freddy Oskarsson from Tenneco (DRiV™) to whom I am also grateful for great technical training which introduced me to the world of exhaust systems.

I would like to give special thanks to Quality Manager Enrique Sales from Tenneco Automotive Valencia for building all my prototypes for testing together with the new mixer prototypes. Moreover, here also I can thank Managing Director Sergio Del Re and Technical

Sales Lorenzo Costa from ITACAT Srl for suggestions and technical support in the selection and delivery of vanadium catalysts for my prototypes.

I am also indebted to Engineering Supervisor Szymon Twaróg from Tenneco Clean Air Europe for valuable tips and assistance in selecting boundary conditions for my experimental tests. I would also like to give thanks to Dr. Daniel Trzebiński from the same unit for help and support during my first steps in preparing a numerical simulation for a catalyst converter in ANSYS Fluent software.

I also thank Technical Director Dr. Rafał Sala and Supervisor of the Catalyst Testing and Engine Calibration Laboratory Dr. Jakub Dzida from BOSMAL Automotive Research and Development Institute Ltd for valuable technical advice during test planning and selection of the boundary conditions for my tests.

I also wish to express my appreciation to Engineering Supervisor Grzegorz Zienkiewicz from Tenneco Clean Air Europe, Rybnik Engineering Center, for testing pressure drops for my test prototypes in the flow lab as well as to Quality Engineer Piotr Gąsiorek from Tenneco Silesia for the 3D laser scanning of SCR systems. Additionally, I would also like to express my appreciation for the technical assistance and performed flow rig tests for my test prototypes by Engineering Manager Dr. Günter Palmer from Tenneco Clean Air Europe, Edenkoben Engineering Center.

I would like to thank Dr Michał Kubecki, Dr. Marta Kubiczek and Piotr Knapik from Łukasiewicz Research Network - Institute for Ferrous Metallurgy for the analysis of the composition of elements contained in the sample of vanadium catalyst.

Last but not least, I also wish to express my cordial appreciation to Team Leader Components & Systems Automotive Michael Ebert and Senior Expert Exhaust System Peter Kallen from TÜV SÜD Auto Service GmbH for valuable comments, preparing prototypes for tests and testing them in the emission laboratory during the NEDC drive cycle.

Lastly, but most importantly I would like to thank my wife Judyta, daughters Melania and Marcelina as well as the whole family for their love, patience and support that allowed me to write this work. Without their help and encouragement, this study would not have been completed. They believed in me and my ability to finish my degree, even in times when I did not believe I could do so.

Nomenclature

Abbreviations

AM	aftermarket
ANR	ammonia NO _x ratio
AOC	ammonia oxidation catalyst
ASC	ammonia slip catalyst
BDC	bottom dead centre
BET	Brunauer-Emmett-Teller surface
BMD	bag mini diluter
CC	close-coupled
CCRT	catalyzed continuously regeneration trap
CF	conformity factor
CFCs	chlorofluorocarbons
CFD	computational fluid dynamics
cGPF	catalyzed gasoline particulate filter
CI	compression ignition
CLD	chemiluminescence detector
CO	carbon monoxide
CO ₂	carbon dioxide
COP	conformity of production
CoV	coefficient of variation
CPSI	cells per square inch
CRT	continuously regeneration trap
CSF	catalyzed soot filter
CVS	constant volume sample
CYA	isocyanic acid (HNCO)
DEF	diesel exhaust fluid (AdBlue)
DF	deterioration factor
DI	direct injection
DOC	diesel oxidation catalyst
DPF	diesel particulate filter
DPM	discrete phase model
EC	European commission
ECE	economic commission for Europe
ECU	electronic control unit
EEA	European environment agency
EEC	European economic community
EGR	exhaust gas recirculation
ETA	estimated total relative area of velocity distribution
EU28	group of 28 countries in European Union
EUDC	extra urban driving cycle
EV	exhaust valve
FAP	filtre à particules
FBC	fuel borne catalyst
FID	flame ionization detector
FTIR	fourier transform infrared spectroscopy

FVM	finite volume method
FWC	four-way conversion catalyst
GDI	gasoline direct injection
GSA	specific geometric surface area of a monolith
GPF	gasoline particulate filter
HC	hydrocarbons
Hex8	8 Node Linear Hexahedron
HPL	high pressure loop
ICE	internal combustion engines
ICP-AES	inductively coupled plasma-atomic emission spectrometry
IDI	indirect injection
IR	infrared
ISC	in service conformity
IV	intake valve
JRC	joint research center
LNT	lean NO _x traps
LPL	low pressure loop
MIL	malfunction indicator lamp
MVEG	motor vehicle emissions group
NEDC	new European driving cycle
NFPA	national fire protection association
NH ₃	ammonia
NDIR	non dispersive infrared
NMHC	non-methane hydrocarbons
N ₂ O	nitrous oxide
NO	nitrogen oxide
NO ₂	nitrogen dioxide
NO _x	nitrogen oxides
NSAI	National Standards Authority of Ireland
NSR	NO _x storage reduction catalyst
NTE	not-to-exceed
NURBUS	non-uniform rational b-spline
OBD	on-board diagnostics
OEM	original equipment manufacturer
OFA	relative open front area
OP	operating point
OSC	oxygen storage capacity
PAHs	polycyclic aromatic hydrocarbons
PEMS	portable emissions measurement systems
PFI	port fuel injection
PGM	platinum group metals
PM	particulate matter
PMP	particle measurement procedure
PMR	power to mass ratio
PN	particulate number
QCL	quantum cascade lasers
Quad4	4 Node Linear Quadrilateral
RANS	Reynolds averaged Navier-Stokes
RDE	real driving emissions

RE	reverse engineering
RNG	renormalization group
SAPO	silico-alumino-phosphate
SCR	selective catalytic reduction
SCRf	SCR coated on a DPF
SCRoF	SCR coated on a DPF
SDPF	SCR coated on a DPF
SEM	scanning electron micrograph
SI	spark ignition
SiC	silicon carbide
SOP	solid particle counter
SO _x	sulphur oxides
SSA	specific surface area
TDC	top dead centre
Tet4	4 Node Linear Tetrahedron
THC	total hydrocarbon
Tri3	3 Node Linear Triangle
TSP	total suspended particulates
TWC	three-way catalyst
UDC	urban driving cycle
UDF	user defined functions
UFP	ultrafine particles
UI	uniformity index
UNECE	United Nations Economic Commission for Europe
UUT	unit under test
UV	ultraviolet analyzer
UWS	urea-water solution
VANS	volume average Navier-Stokes
VOCs	volatile organic compounds
WLTC	worldwide harmonized light vehicle test cycles
WLTP	worldwide harmonized light vehicle test procedure
ZSM	zeolite Socony Mobil

Greek symbols

α_{ANR}	feed ratio
α_m	permeability of the medium, m ²
α_A	stoichiometric coefficient
α	exponent representing the order of reaction
α_k	inverse effective Prandtl number for kinetic energy
α_w	wall acceleration
α_ε	inverse effective Prandtl number for dissipation rate
β_B	stoichiometric coefficient
β	exponent representing the order of reaction
β_r	temperature exponent
γ_{UI}	uniformity index
γ_C	stoichiometric coefficient
γ	exponent representing the order of reaction

ΔL_j	thickness of the medium, m
Δp	pressure drop, Pa
δ_D	stoichiometric coefficient
δ_w	washcoat thickness, mm
ε	energy dissipation rate
ε_b	reactor bed porosity (porous medium)
η	catalyst effectiveness factor
$\eta_{j,r}'$	rate exponent in reaction r for reactant
$\eta_{j,r}''$	rate exponent in reaction r for product
λ	excess air ratio
μ	laminar fluid viscosity, Pa·s
μ_d	droplet dynamic viscosity, Pa·s
μ_{eff}	effective viscosity, Pa·s
μ_t	turbulent viscosity, Pa·s
$\nu_{i,r}'$	stoichiometric coefficients for reactant in reaction r
$\nu_{i,r}''$	stoichiometric coefficients for product in reaction r
ρ	density, kg/m ³
ρ_b	bulk (apparent) density, kg/m ³
ρ_s	solid density, kg/m ³
ρ_∞	density of the bulk gas, kg/m ³
σ_{SD}	standard deviation
σ	droplet surface tension, N/m
$\bar{\tau}$	stress tensor, Pa
$\bar{\tau}_{eff}$	effective stress tensor, Pa
τ_g	magnitude of the shear stress of the gas flow, Pa
τ_w	stress that the wall exerts on the film, Pa
\emptyset	specific field variable
$\bar{\emptyset}$	average value of the field variable

Roman symbols

A	chemical element (substrate)
A_a	surface area, m ²
A_{OFA}	open front area of the monolith, m ²
A_p	droplet surface area, m ²
A_R	cross section of the reactor, m ²
A_r	pre-exponential factor or frequency factor, units vary
B	chemical element (substrate)
$B_{m,i}$	Spalding mass number for species i
C	chemical element (product)
C_i	molar concentration of i species, mol/m ³
$C_{j,r}$	molar concentration of species j in reaction r , mol/m ³
C_{NOin}	mole fraction of NO at inlet SCR catalyst, ppm
C_{NOout}	mole fraction of NO at outlet SCR catalyst, ppm
$C_{1,2,3\varepsilon}$	model constants

C_2	inertial resistance, 1/m
c_p	specific heat at constant pressure, J/(kg·K)
D	chemical element (product)
D_m	monolith diameter, m
$D_{i,m}$	mass diffusion coefficient for species i in the mixture, m ² /s
$D_{T,i}$	thermal (Soret) diffusion coefficient
d	diameter, m
\bar{d}	size parameter (mean diameter), m
d_c	coated hydraulic diameter, m
d_h	uncoated hydraulic diameter, m
d_p	particle (droplet) diameter, m
E	sum of specific internal and kinetic energy, J
E_r	activation energy for the reaction, J/kmol
F	total volumetric feed flow rate, m ³ /s
F_f	force per unit area necessary to keep the film on the surface, N
F_{idr}	drag force, N
F_{ig}	force of gravity, N
F_{im}	virtual mass force, N
F_{io}	other forces e.g. from particle collisions, N
F_{ip}	pressure force, N
f	friction factor
G	limit value of the emissions of the pollutant
G_b	production of turbulence kinetic energy due to buoyancy
G_k	production of turbulence kinetic energy due to the mean velocity gradients
g	gravitational acceleration, m/s ²
h	current film height at the particle location, m
h_{fg}	latent heat of vaporization, J/kg
h_j	specific enthalpy, J/kg
h_j^0	enthalpy of formation of species j , J/kg
I	unit tensor
J_j	diffusion flux of species j , kg/(m ² ·s)
K	Kuhnke impingement model
k	turbulence kinetic energy, m ² /s ²
$k_{c,i}$	mass transfer coefficient of component i , m/s
k_{eff}	effective (molecular and turbulent) thermal conductivity, W/(m·K)
k_f	reaction rate constant, units vary
$k_{f,r}$	forward rate constant for reaction r , units vary
k_{film}	film mass transfer coefficient, m/s
k_{va}	apparent reaction rate constant, s ⁻¹ (mol/cm ³) ^x
k_v	intrinsic reaction rate constant, s ⁻¹ (mol/cm ³) ^x
L	cell pitch, m
L_m	monolith length, m
L_{real}	amount of air sucked into the cylinder, kg
$L_{stoichio.}$	amount of air desired for the combustion reaction, kg
M	mean value of the emissions of one pollutant from the replacement part
M_{exh}	molecular mass for exhaust gas, kg/mol

M_j	molar mass of species j , kg/mol
M_{urea}	molecular mass for urea, kg/mol
$M_{w,i}$	molecular weight of species i , kg/mol
m_d	droplet mass, kg
\dot{m}_{exh}	mass flow rate of the exhaust gas, kg/s
m_i	mass of component in droplet, kg
\dot{m}_p	film parcel vaporization rate, kg/s
N	number of chemical species in the system
N_c	cell density, cpsi
\dot{N}_i	vapour mass flux of species i , kg/m ² /s
N_R	sum of the reaction sources
$NH_{3,in}$	mole fraction of NH ₃ from the urea, ppm
$NO_{x,in}$	mole fraction of NO _x in exhaust gases, ppm
n	size distribution (spread parameter)
n_f	number of facets
n_p	number of data points
p	pressure, Pa
$Q_{p,cond}$	conduction from the wall, W
$Q_{p,conv}$	convective heat flux at the surface, W
R	universal gas constant, J/(kmol·K)
R_i	net rate of production of species i by chemical reaction, kmol/(m ³ ·s)
$\hat{R}_{i,r}$	molar rate of creation or deconstruction of species i in reaction r , kmol/(m ³ ·s)
R_j	volumetric rate of creation of species j , kmol/(m ³ ·s)
R_m	radius to the edge of monolith, m
R_v	intrinsic reaction rate, moles of NO/(s·cm ³ of catalyst)
R_{va}	apparent reaction rate, moles of NO/(s·cm ³ of reactor volume)
R_ε	additional term for rapidly strained flows
Re_d	Reynolds number
r_f	rate of a chemical reaction, units vary
r_{vmax}	radius to the point of maximum velocity, m
S	mean value of the emissions pollutant from the original part
Sc	Schmidt number
S_h	volumetric heat sources, W/m ³
S_i	body force (source term), N/m ³
S_j	source vector component in direction j , N/m ³
S_k	user-defined source term for kinetic energy, kg/(m·s ³)
S_m	any user-defined sources of mass, kg/(m ³ ·s)
S_ε	user-defined source term for dissipation rate, kg/(m·s ⁴)
T	temperature, °C or K
T_p	particle temperature, K
T_{sat}	droplet saturation temperature, K
T_w	wall temperature, K
t	time, s
t_w	wall thickness, m
UI_{NH_3}	uniformity index of NH ₃
UI_{NO}	uniformity index of NO
UI_v	uniformity index of velocity

V_O	entire body volume of porous medium, m ³
V_R	reactor volume, m ³
V_v	void volume of porous medium, m ³
v	fluid velocity, m/s
v_{ave}	average velocity, m/s
v_c	velocity of gases in monolith channel, m/s
v_i	velocity in direction i , m/s
v_{id}	droplet velocity, m/s
v_j	velocity in direction j , m/s
v_p	film particle velocity, m/s
v_{pn}	normal impingement velocity, m/s
X_{NO}	average NO conversion, %
X_{NO_x}	average NO _x conversion, %
x_i	each of the values of the data
\bar{x}	mean of the x_i
Y_d	mass fraction of droplets with diameter greater than d
Y_i	local mass fraction of species i
$Y_{i,s}$	vapour mass fraction at the surface
$Y_{i,\infty}$	vapour mass fraction in the bulk gas
Y_M	contribution of the fluctuating dilatation in compressible turbulence
z	height of the reactor, m

1 Introduction

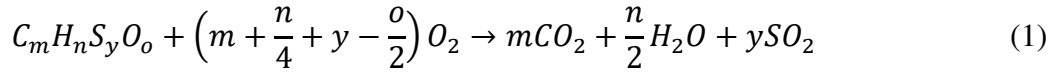
Diesel engines are widely used in off-road machineries, ships, heavy-duty trucks, light-duty vehicles and passenger cars. Compression ignition (CI) engines have shown great durability and operation in recent years. Mainly due to a better fuel economy, high energy output (torque), lower emissions of carbon dioxide CO₂ (greenhouse gas) in comparison to spark ignition (SI) engines. However, diesel engines produce noticeably higher emissions of nitrogen oxides (NO_x) and particulate matter (PM). The emission of these gases has adverse effects on human health and the environment. Vehicle population is projected to grow close to 1300 million by the year 2030 [21].

The emission levels can be reduced through development of engine-out emissions (primary methods), alternative fuels or the performance of the emission control system (secondary methods). To achieve the PM emission at the required level, Diesel Particulate Filters (DPF) are commonly used. On the one hand, NO_x emission is very effectively reduced in the traditional stoichiometric gasoline engine by using a Three-Way (oxidation-reduction) Catalyst (TWC). On the other hand, NO_x emission removal by TWC in diesel engines is ineffective due to lean operation and high content of oxygen in the exhaust gas. The trend of stringent emissions standards have led to the introduction of new aftertreatment technology for NO_x reduction. One of the most promising systems which is able to reduce more than 90% of diesel engine-out NO_x emissions is urea Selective Catalytic Reduction (Urea-SCR, abbreviated as SCR) which focuses attention in this work. Originally only applied in stationary power plants, now SCR systems are installed in millions of mobile diesel engines. An SCR system needs a chemical reagent which is an aqueous solution of urea, injected into the hot exhaust where it is decomposed to ammonia (NH₃). Using a special mixer design is possible to uniform mixing of the exhaust gases and in the correct type of catalyst, the NO_x reduction can be achieved.

The development of improved SCR design concepts require solutions of complex physical phenomena. Computational fluid dynamics (CFD) is an effective tool which is able to solve engineering problems, such as fluid flow, heat transfer and chemical reactions in complex systems. Numerical modelling can be applied where experiments are difficult, dangerous, expensive and time-consuming. Simulations also accelerate prototyping, process control, optimization and manufacturing of many products. The accuracy of predictions requires assessment and validation of the computational techniques with experimental data which has been done in this thesis based on the designed SCR system.

1.1 Introduction to the exhaust emissions of internal combustion engines

A negative phenomenon related to the combustion process is exhaust emissions. The process of burning hydrocarbon fuels in real engine conditions, does not proceed according to ideal stoichiometric relationships [5]:



The ideal combustion process assumes that the hydrocarbons in fuel are burned in the presence of oxygen resulting in water and carbon dioxide. This ideal process is not possible because the burning does not occur in the presence of pure oxygen, but in the presence of air, whose chemical composition is approximately 78% nitrogen, 21% oxygen and 1% other components [7]. In addition, the fuel contains various admixtures and pollution. Therefore, engine exhaust gas contains harmful substances and chemical compounds. Their formation during the operation of an internal combustion engine is among others as a consequence of inadequate fuel preparation and combustion conditions in the system [5]. In practice, it is generally accepted that 14.7 kg of air should be supplied to burn 1 kg of standard fuel. For such a composition of the air-fuel mixture, the combustion reaction should be complete and its products should not include oxygen. Such an ideal mixture composition is called a stoichiometric composition. In fact, the engine combustion never occurs under perfectly stoichiometric conditions.

More information can be read in the appendices at the end of this dissertation. In particular, basic information is described there on the operation of internal combustion engines as well as the influence of harmful gases (CO, HC, NO_x, SO_x, PM, CO₂ and NH₃) on the environment and people. What's more there is basic information described there about exhaust aftertreatment systems (Diesel Oxidation Catalyst, Three-Way Catalytic Converter, Diesel Particulate Filter and Gasoline Particulate filter) of these harmful gases.

Fig. 1 and Fig. 2 compare the composition of the exhaust gases (without a catalytic converter) for SI and CI engines. The amount of pollutants has a negligible effect on the engine process (from the point of view of energy) but has potential to endanger human health and the environment. The diesel engine emits less CO₂ than SI engines do, however the NO_x concentrations and particle emission represent a critical magnitude [3].

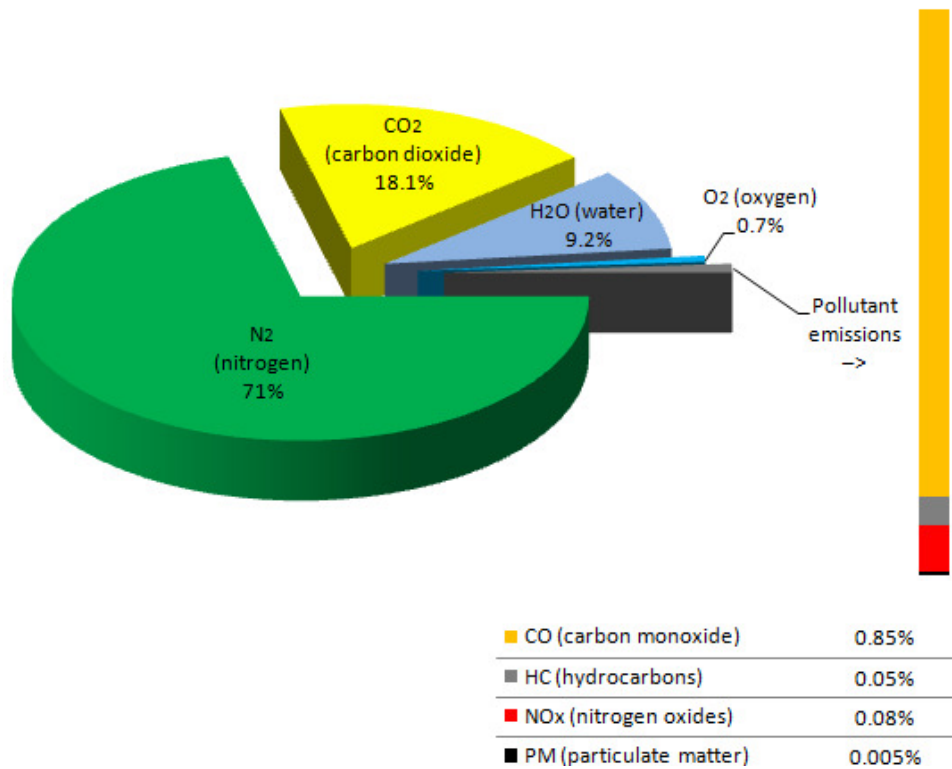


Fig. 1. The average composition of exhaust gases from a petrol vehicle [4]

Adapted from *Układy oczyszczania spalin i pokładowe systemy diagnostyczne samochodów*, Rokosch U., ISBN 978-83-206-1657-6; Copyright 2007 Wydawnictwo Komunikacji i Łączności.

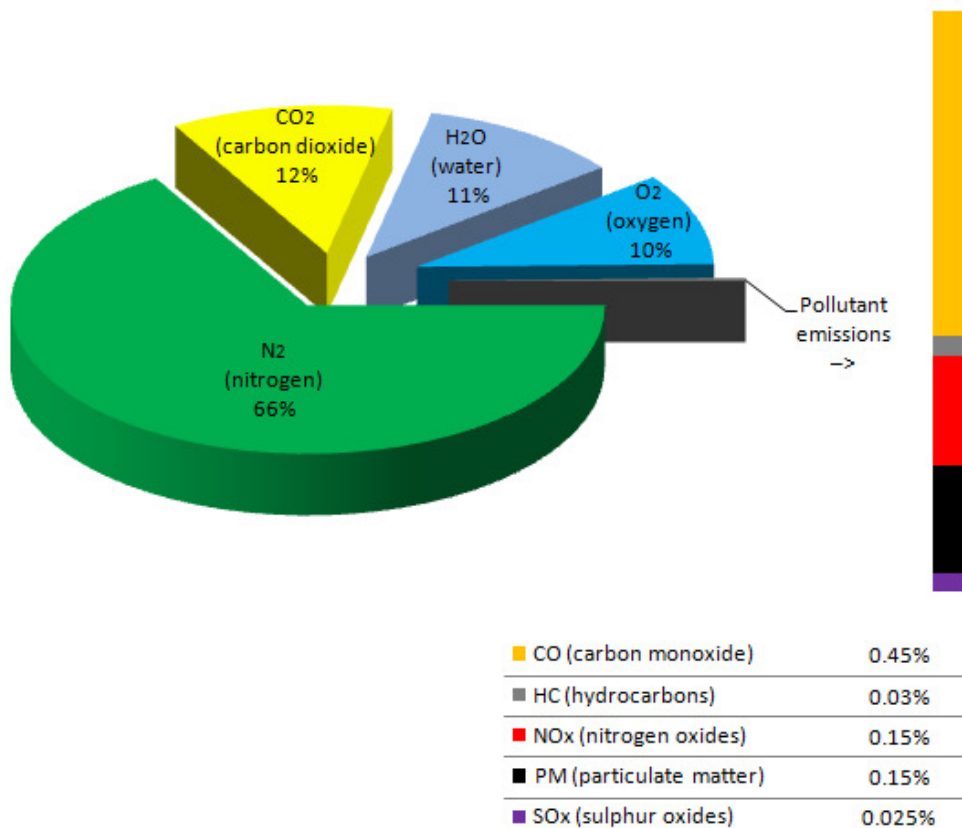


Fig. 2. The average composition of exhaust gases from a diesel vehicle [4]

Adapted from *Układy oczyszczania spalin i pokładowe systemy diagnostyczne samochodów*, Rokosch U., ISBN 978-83-206-1657-6; Copyright 2007 Wydawnictwo Komunikacji i Łączności.

According to the EEA (European Environment Agency), road transport continues to be the largest source of NO_x emissions (39% in the EU28 i.e. group of 28 countries in European Union) in 2016, followed by the energy production and distribution sector, and the commercial, institutional and households sector. For the 30 European cities (Fig. 3), the average contribution of the transport to overall nitrogen oxides emissions was 47% [8].

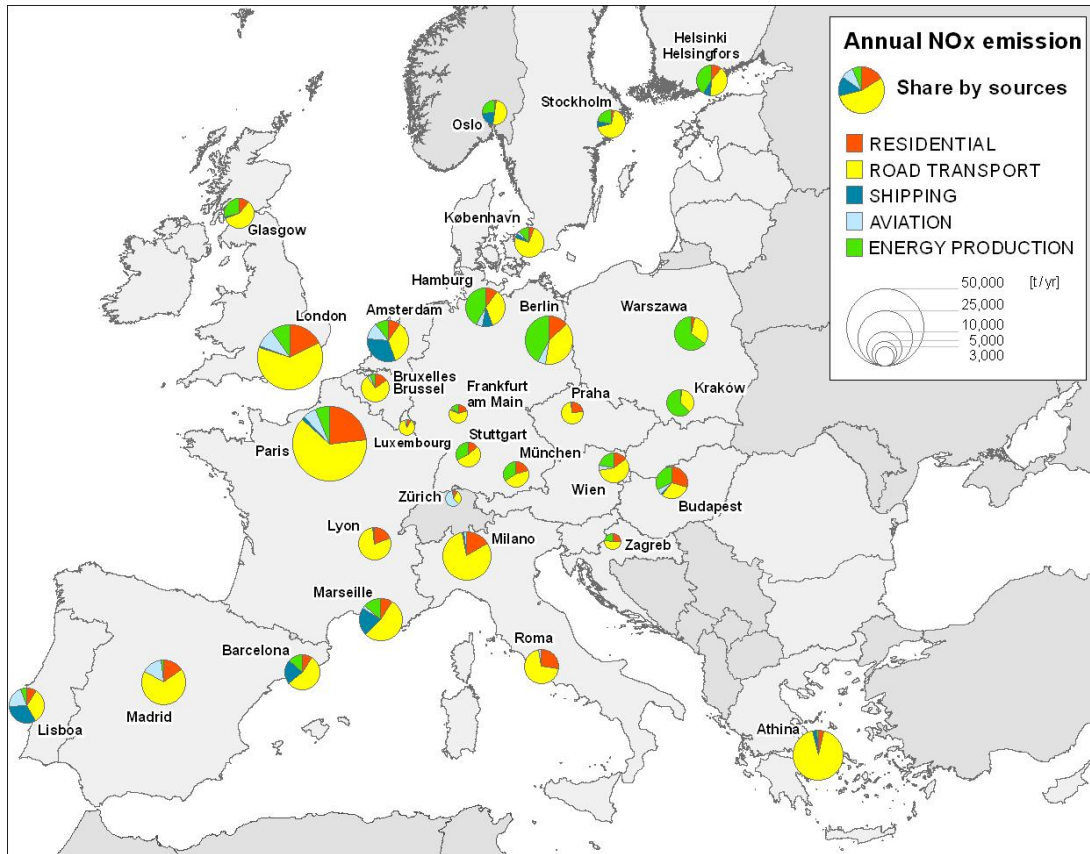


Fig. 3. Share of different sectors in NO_x emissions for 30 European cities [8]

Reproduced from *Urban NO₂ Atlas*, Degraeuwe B., Pisoni E., Peduzzi E., De Meij A., Monforti-Ferrario F., Bódis K., Mascherpa A., Astorga-Llorens C., Thunis P., Vignati E., ISBN 1831-9424; Copyright 2019 European Union (CC BY 4.0).

In the case of classic engines, it can be stated that the emission of particulate matters from spark ignition engines is three orders of magnitude lower than that of compression ignition engines. Particulate emissions have great ecological significance, they are classified as carcinogens [4]. In the European Union, air quality standards for protecting human health from PM are as follows: PM₁₀ with limit value of 50 µg/m³ per day and not to be exceeded on more than 35 days per year and PM_{2.5} with limit value of 25 µg/m³ per day. The map (Fig. 4) shows PM₁₀ daily mean concentrations in the European Union [11].

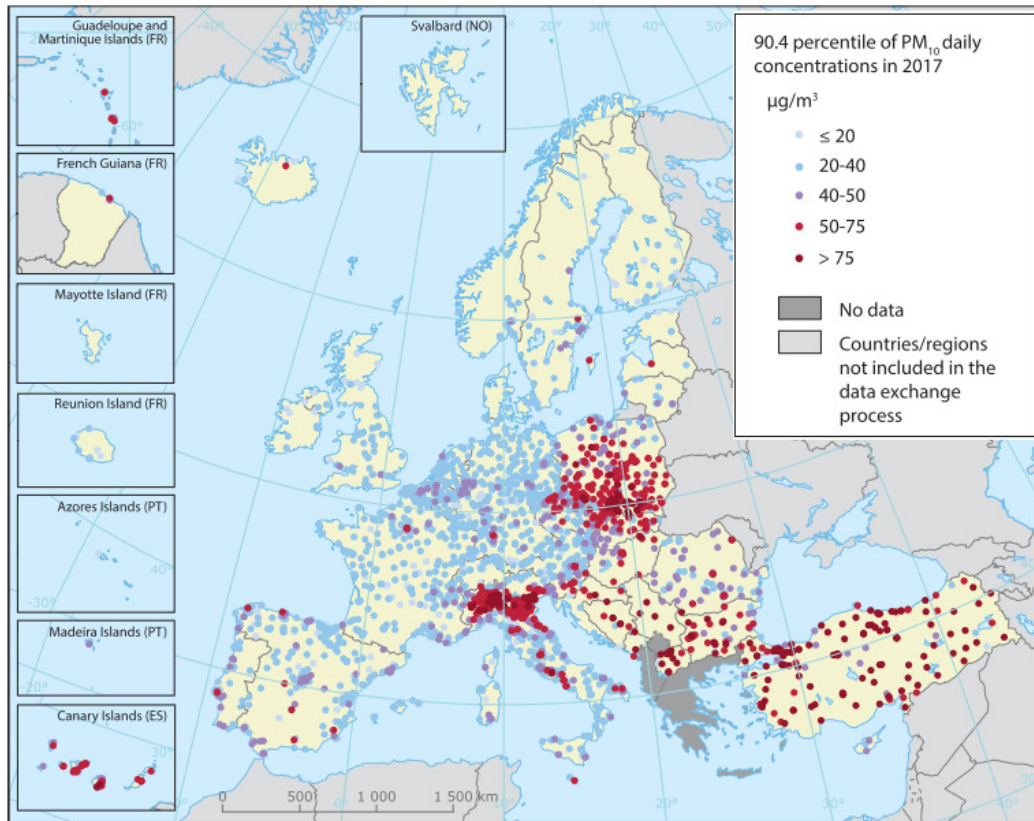


Fig. 4. Concentrations of PM_{10} , 2017- daily limit value [11]

Reproduced from *Air quality in Europe*, ISBN 978-92-9480-088-6; Copyright 2019 European Environment Agency (CC BY 4.0).

The main sectors of CO_2 emissions are presented in Fig. 5 and their producers as highly industrialized countries whose economies need large amounts of energy in Fig. 6.

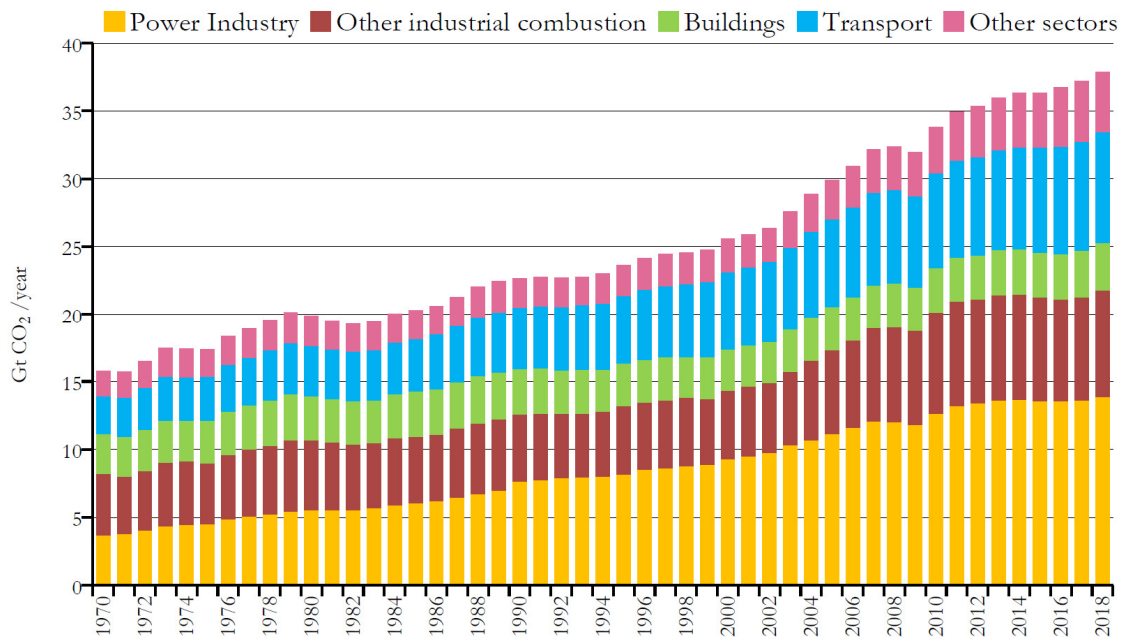


Fig. 5. Total global annual emissions of fossil CO_2 by sector [12]

Reproduced from *Fossil CO_2 and GHG emissions of all world countries*, Crippa M., Oreggioni G., Guizzardi D., Muntean M., Schaaf E., Lo Vullo E., Solazzo E., Monforti-Ferrario F., Olivier J. and Vignati E., ISBN 978-92-76-11100-9; Copyright 2019 European Union, JRC (CC BY 4.0).

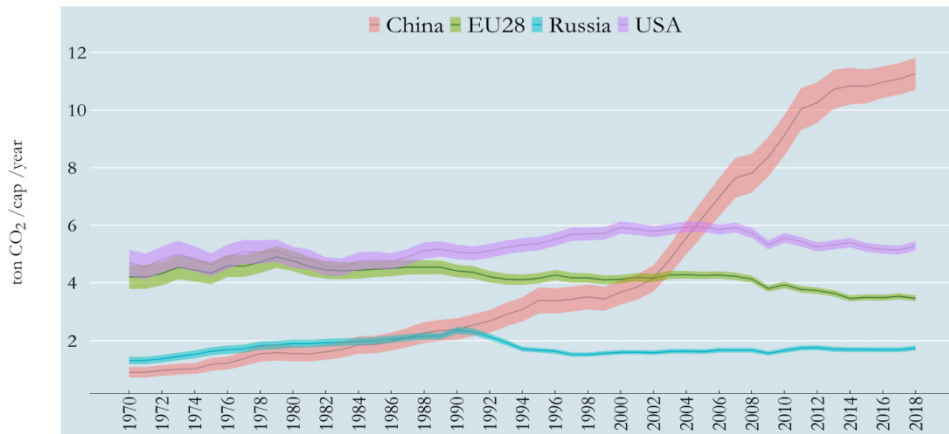


Fig. 6. Annual emissions of fossil CO₂ for the EU28 and large emitting countries [12]
 Reproduced from *Fossil CO₂ and GHG emissions of all world countries*, Crippa M., Oreggioni G., Guizzardi D., Muntean M., Schaaf E., Lo Vullo E., Solazzo E., Monforti-Ferrario F., Olivier J. and Vignati E., ISBN 978-92-76-11100-9; Copyright 2019 European Union, JRC (CC BY 4.0).

Reducing carbon dioxide emissions can be achieved by limiting the consumption of fuel and energy. Therefore, efforts to use alternative energy sources are justified, and this problem is also recognized by the car industry. Carbon dioxide emissions must be considered on a global scale. Although in recent years it has been possible to reduce emissions slightly in the countries of the European Union, it should be expected that the obtained ecological benefit will be compensated by the growing emissions in rapidly developing countries [4].

2 Justification and motivation of topic selection

Selective catalytic reduction (SCR) is not a new technology known in the world. Starting in the late 1970s, this technology started to be installed in thermal power plants, then in gas turbines and installations for NO_x control from coal-fired power plants. In 2005, the SCR system began to be used on a large scale in heavy-duty truck applications. However, this dissertation is focused on the SCR system installed for light-duty vehicles (i.e. passenger cars). The first passenger car equipped with OEM (Original Equipment Manufacturer) SCR system was the Mazda CX-7 2.2 MZR-CD 173KM which met the Euro 5 emission standard and was produced in 2009-2012.

The first decade after the first production and installation of original SCR systems in passenger cars with diesel engines, determines the first signal for the development of these systems by manufacturers of spare parts (aftermarket). The motivation for the choice of the topic is dedicated to the fact that the SCR system in a passenger car has not been introduced yet on the secondary market by WALKER in-house. Working in the Aftermarket Emission

Control Engineering at Tenneco (DRiV division), has contributed to the need to develop a new SCR system for the aftermarket under the WALKER brand. A preliminary research in the field indicated that there is room for improvement regarding the SCR system's effectiveness by a careful analysis of the subsequent processes occurring in the system, i.e. the evaporation and mixing of the reactants prior to the catalyst, proper distribution of flow through the catalyst and selection of appropriate thermal conditions for process. This indicates that a considerable improvement in operational efficiency and thus a reduction of NO_x and NH₃ emission can be achieved. To achieve this goal, a coupled approach needs to be applied incorporating both extensive experimental research and advanced numerical methods based on computational fluid dynamics (CFD).

3 Research objectives

The aim of the dissertation is to conduct experimental and numerical research for a selective catalytic reduction (SCR) system of passenger cars with a diesel engine to improve the efficiency and reduce the cost of the system. The research consists of comparing the results for two different SCR systems: existing and new developed. The developed SCR system is aimed at introducing it to the secondary market, which is also associated with the development of its own mixer design. Therefore, in the research work analyzes have been carried out for their various constructions and verification if a universal mixer can be constructed for various operating points of the SCR system design.

Numerical modelling by means of computational fluid dynamics (CFD) tools have been used to reduce the costs of experimental research and for modelling the reaction kinetics as well as the development of full models of the entire SCR system. Models of each part of the SCR system (injection, mixers, catalyst) have been developed and validated based on the available experimental data. The validated model has then been used in designing new and improving SCR systems.

In summary, the main objectives of the present study are to:

- acquire knowledge of NO_x aftertreatment systems and their Europe's emission standard, applicable tests as well as the current status of the SCR system and modelling,
- carry out experimental tests in laboratories for the various constructions of SCR systems and mixer designs,

- develop a complete CFD model capable of predicting the SCR system performance under various operating conditions,
- validate the model against experimental data to show that the applied models and solution techniques are appropriate,
- demonstrate the applicability of the developed new SCR system and mixer through passing emission tests at the certification unit authorizing to obtain approval and be ready to sell the new developed SCR system for aftermarket.

4 NO_x formation process and their aftertreatment systems

The NO_x are produced during engine combustion, especially at high temperatures. Most of this is nitrogen oxide (NO), with a small amount of nitrogen dioxide (NO₂). There are also some elements of other nitrogen-oxygen combinations. These are all grouped together as a NO_x, where x defines some suitable number. Regulations to reduce NO_x emission are very stringent due to the fact they are very undesirable [2]. There are few different ways, where NO can be formed. The thermal NO, which is formed among the combustion products at high temperatures according to Zeldovich mechanism, the prompt NO, which is initiated in the flame front via the Fenimore mechanism, NO formed from N₂O mechanism, and fuel NO, which is produced by nitrogen portions in the fuel [3], [7], [39].

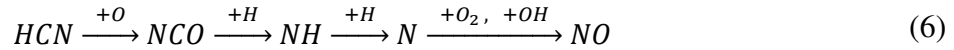
The thermal or Zeldovich mechanism appears “behind” the flame in the hot burned gases (above 1800 K). Y. B. Zeldovich first postulated the mechanism in 1946 and consists of three elementary reactions [3], [7], [39]:



In 1971, Fenimore suggested an additional NO formation mechanism, in which NO is formed near the burner surface, in the flame front, and called this “prompt NO” due to fast formation. The Fenimore mechanism takes place at temperatures as low as 1000 K and is initiated by reaction between N₂ and hydrocarbon radicals (CH) [39]:



The hydrogen cyanide (HCN) and molecular nitrogen (N), reacts afterwards to NO through a series of reactions. The main reaction sequence is [7]:



The formation of NO via fuel-nitrogen (HCN) is slightly dependent on temperature (NO is formed at low temperatures, below 1100 K) [7]. The conversion of nitrogen bound in the fuel to NO does not matter due to negligible amounts of nitrogen. On the other hand, it does matter with some low-quality heavy oils [3].

In the nitrous oxide or “laughing gas” (N₂O) mechanism, NO is formed through unstable gas (N₂O) and any gas component (M) according to the following reaction:



The N₂O may react subsequently through oxidation and form NO:



This reaction mainly appears under lean premixed combustion, at low temperatures and with high point pressures. This mechanism has only a minor contribution to the total formation of NO in comparison with the thermal and prompt mechanism [3], [39].

Reaction forming NO₂ is mainly formed by reaction Eq. (8) at low flame temperatures. Usually, the ratio of NO₂ to NO in the exhaust gas of internal combustion engines is relatively low. In combustion processes, more NO₂ is formed by reaction [3]:



The formation of NO_x depends on pressure, air-fuel ratio, combustion duration and temperature (at low temperatures very little NO_x is created). Compression ignition engines have higher compression ratios, higher temperatures and pressure which contributes to generating higher levels of NO_x [2]. There are several techniques available to NO_x reduction, such as lean NO_x traps (LNT), SCR and cooled exhaust gas recirculation (EGR) which are described subsequently [40].

4.1 Exhaust Gas Recirculation (EGR)

The methods aimed at minimizing the concentration of nitrogen oxides in the exhaust gases can be divided into two groups [41]:

- methods affecting the combustion process (i.e., for example EGR),
- method of treating exhaust gases in the exhaust systems (e.g. LNT or SCR).

Lowering the maximum combustion temperature reduces the emission of nitrogen oxides. Such an effect can be obtained by increasing the heat capacity of the sucked charge, by bringing with the fresh load a certain amount of substance having a greater heat capacity than the air-fuel mixture. In other words, recirculate a controlled portion of exhaust gases (reduced temperature by passage through intercooler) into the engine combustion chamber through a valve [13]. For this purpose, in practice, the exhaust gas recirculation (Fig. 7) system is used. This system uses a greater heat capacity in the exhaust gas to lower the maximum combustion temperature (peak cylinder temperature) and hinder the reaction of nitrogen and oxygen. The phenomenon of slowing down the course of the combustion reaction is used here, because the exhaust gas particles introduced into the fresh load do not directly participate in the combustion process (inert gases leading to a decrease of oxygen concentration), however they take some of the energy radicals (heat absorbing of CO_2 - thermal effect and dissociation of CO_2 - chemical effect), of which the number depends on the speed of flame propagation, pressure and process temperature [19], [41].

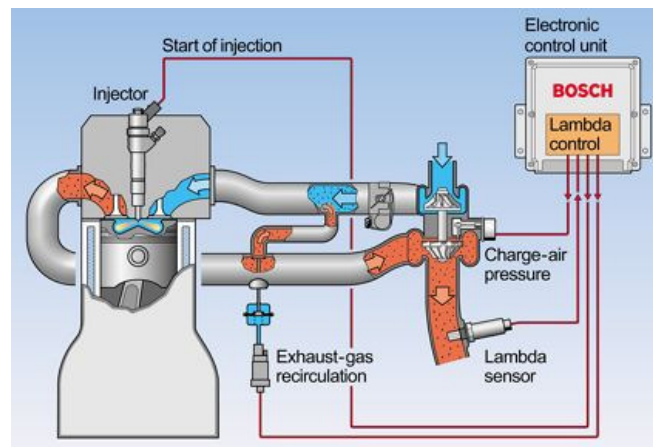


Fig. 7. Schematic representation of exhaust gas recirculation. Adapted from [41]
Adapted from Maszyny Górnicze, Koncepcja system redukcji tlenków azotu z ognioszczelnego napędu spalinowego, Kaczmarczyk K., 1/2015, 23-28; Copyright 2015 (CC-BY-NC).

Improper EGR distribution (rerouted exhaust gases not mix homogeneously) may result in a higher rate of particulate matter emissions. Precisely regulating the amount of recirculated exhaust gases by ECU, contributes to the balance between a reduction in nitrogen oxide emissions and engine efficiency.

There are two main types of EGR system in diesel engines i.e.: high pressure loop EGR and low-pressure loop EGR. For HPL EGR, exhaust gas is drawn from upstream of the turbine and for LPL EGR, exhaust gas is drawn from after the DPF [42]. Due to the different advantages (LPL: lower fuel consumption, higher heat absorbing capacity) and disadvantages (LPL: erosion, awkward plumbing), both are also used in combination [19].

4.2 Lean-NO_x Traps (LNT)

The use of engines burning lean mixtures (reduction of fuel consumption through direct fuel injection) resulted in the need to develop a new type of catalytic reactor to reduce the concentration of NO_x. A classic three-way catalytic converter (TWC) is not able to effectively reduce nitrogen oxides at the moment when the engine is powered by a lean mixture (high oxygen content in the exhaust gas) [43]. The Lean NO_x Traps (LNT) or NSR (NO_x Storage and Reduction catalyst) is currently the leading deNO_x concept for smaller lean-burn (diesel or direct injection gasoline) passenger cars with limited space or in which urea is difficult to dose. Conversion of nitrogen oxides in the LNT system is normally 70-80%, much lower than in the next generation SCR system (alternative) at above 95% [44].

The LNT reactors store nitrogen oxides when the engine is powered by a lean mixture (storage period), while when the engine is running on a rich mixture (short reduction period), the NO_x accumulated in the reactor is released and reduced. A LNT catalyst needs sites for NO_x adsorption (alkaline compound like Ba - barium) and also sites for NO_x oxidation and reduction (noble metal like Pt - platinum ~ 1-2 wt%). The storage compounds as well as the noble metals should be dispersed on porous materials with high surface area (e.g. Al₂O₃) washcoated over a monolithic structure (cordierite), which give a general formulation Pt-Ba/Al₂O₃. The LNT mechanism (Fig. 8) can be explained by the following steps [23]:

- oxidation of NO to NO₂ using platinum (lean conditions),
- adsorption of NO_x - barium carbonate converts to barium nitrate (lean conditions),
- injection and evolution of the used reductive species (H₂, CO or HC) in rich cond.,
- release of the stored NO_x from the catalyst surface to the gas stream (rich conditions),
- reduction of NO_x to N₂ by CO/HC/H₂ as there is a surplus of the species (rich conditions).

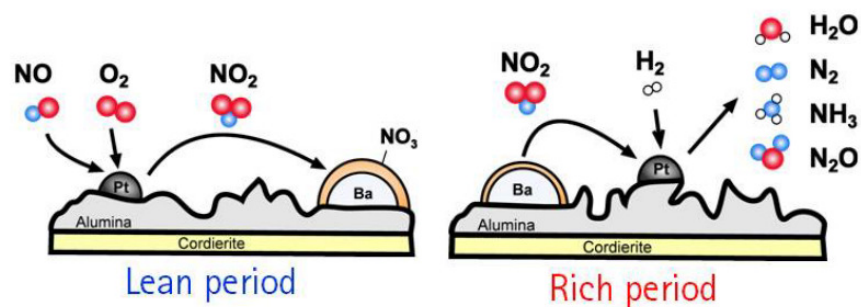
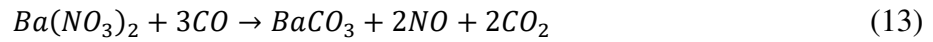
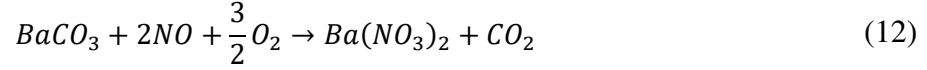
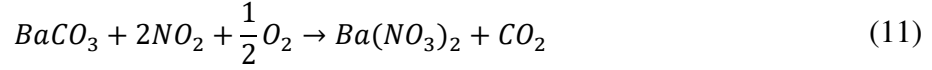


Fig. 8. Schematic representation of storage and reduction NO_x by LNT catalyst [23]
 Reproduced with permission from *NO_x Storage and Reduction for Diesel Engine Exhaust Aftertreatment*, Pereda-Ayo B., González-Velasco J. R.; The Authors copyright 2013, Licensee Intech (CC BY 3.0).

The overall reduction of NO_x is obtained by cyclic changes of air-to-fuel ratio and the main reactions are as follows [3]:



4.3 Selective Catalytic Reduction (SCR)

Selective catalytic reduction (SCR) is another technology to reduce NO_x emission to near zero levels. SCR technology was first applied in thermal power plants in the late 1970s, then in gas turbines in the 1990s and installations for NO_x control from coal-fired power plants [47]. The first wide-scale use of SCR for mobile diesel engines in Europe was in 2005 for heavy-duty truck applications [46]. The SCR system uses an injector to inject the urea-water solution (UWS) also known as AdBlue (in Europe) or diesel exhaust fluid (DEF in the US), which decomposes into ammonia (NH_3) in the hot exhaust gases and reduces the NO_x inside a catalyst to eco-friendly nitrogen (N_2) and water (H_2O) [13]. A typical structure, physical and chemical processes in a SCR system is shown in Fig. 9 on the basis of the researched system in this dissertation.

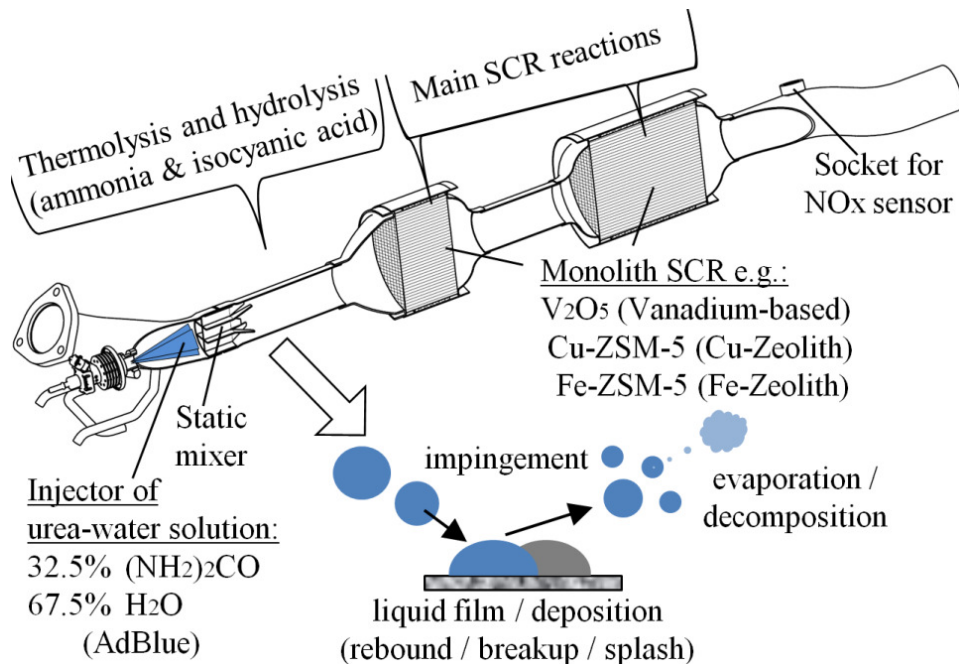


Fig. 9. Sketch showing the physical and chemical processes in SCR system

Some un-reacted ammonia may be released into the atmosphere, which is an undesired secondary toxic emission (known as an “ammonia slip”) by over-injection of AdBlue, low temperature condition, degraded catalyst or poorly mixed gases by the mixer. A good SCR system combines high NO_x conversions with low ammonia slip (maximum ammonia slip levels of 5-10ppm) [45], [47]. The control system works in an open-loop or closed-loop system. The first one uses NO_x estimation algorithm to evaluate the amount of NO_x in exhaust gas by engine speed, exhaust temperature and load to determine the amount of UWS to inject. The second one (closed-loop system) to calculate the amount of UWS to inject using data obtained through a NO_x sensor for on-board diagnostics (OBD) [13], [48].

Three general families of SCR catalysts are in commercial use today (Fig. 10), which differ in some properties. Vanadia-based SCR catalysts (one of the cheapest) contain V₂O₅ (1-3%) as the active component, typically impregnated on an anatase TiO₂ support together with WO₃ to stabilize the vanadia and increase thermal durability. V₂O₅-WO₃/TiO₂ characterizes high conversion in medium range temperatures and limited high thermal stability with risk of vanadium emission at temperatures > 650°C. Cu-zeolite SCR catalysts (Cu-ZSM-5), exhibit higher NO_x conversion at low temperatures, while Fe-zeolite SCR catalysts (Fe-ZSM-5), show higher NO_x reduction at high temperatures. Furthermore, Cu-ZSM-5 catalysts have the greatest possibility of ammonia storage but are susceptible to sulphur poisoning and require an occasional high-temperature cleaning step (>500°C) [45], [46]. The substrate of a catalyst is usually a monolith honey comb structure made of ceramic with high surface area. Increasing cell density from 300 to 400 cpsi is more effective on the DeNO_x performance than an increased active component in the SCR system [45].

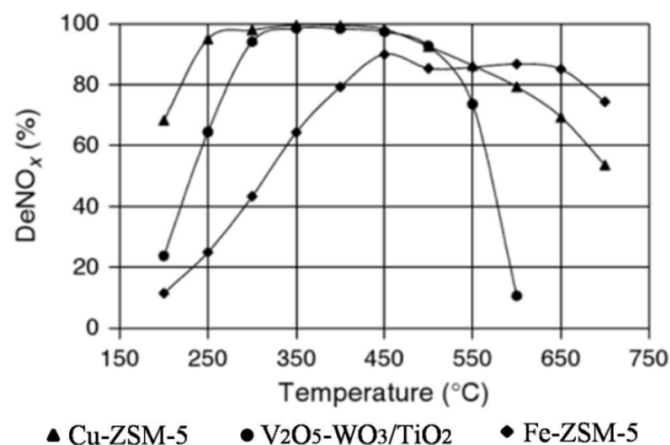
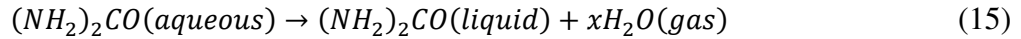


Fig. 10. Conversion performance over various types of SCR catalysts [45]

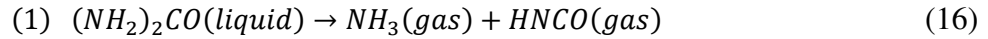
Feed gas: 10% O₂, 5% H₂O, 1000ppm of NO. NH₃ slip=10ppm, GSHV=52000h⁻¹.

Reprinted from *Studies in Surface Science and Catalysis, Vol. 171, Kröcher O., Chapter 9 Aspects of catalyst development for mobile urea-SCR systems — From Vanadia-Titania catalysts to metal-exchanged zeolites, 261-289, Copyright 2007, with permission from Elsevier.*

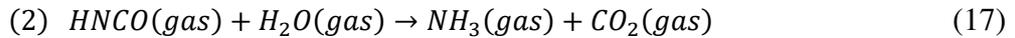
The 32.5% of urea and 67.5% pure water are injected into the exhaust gas as an urea-water solution, where the water evaporates from droplets by following reaction [47]:



Pure urea is then heated and thermally decomposed (thermolysis) into the ammonia and isocyanic acid in the gas phase ahead of the SCR catalyst according to [45]:



The isocyanic acid is converted with water in hydrolysis reaction also to NH₃ as well as to CO₂ [45]:

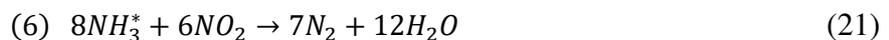
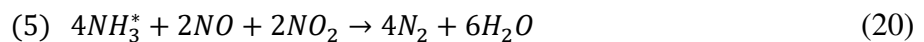
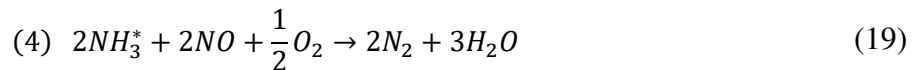


Then NH₃ takes part in the reactions of SCR catalysts. Thermolysis and hydrolysis reactions appear more rapidly than SCR reactions. The efficiency of reactions to produce ammonia from UWS depends largely on exhaust gas temperature and starts above 130°C [20]. When the gas temperature is less than 200°C, during decomposition of urea, reaction can generate byproducts (cyanuric acid, biuret, melamine, ammelide etc.) which can create deposits - highly undesired. Due to this, urea injection starts when exhaust temperature is higher than 180°C [46], [47]. However, full conversion of UWS to NH₃ is not completed by entrance to the catalyst. Nonetheless, an increase of the hydrolysis reaction in the gas phase before the entrance of the catalyst, can be achieved by higher temperature, appropriate injection design, good mixer design, system isolation or lengthening the gas path. Urea injection quality and mixing are complex but can affect conversion efficiency up to 10% [20].

The ammonia adsorption process (NH₃^{*} is adsorbed by the free substrate side of the SCR catalyst - what is related with ammonia storage capacity) is a two-way reaction which can be explained by the following equation [47], [48]:



Among these reactions, there are three key SCR reactions [47], [48]:



The first reaction (19) is known as “standard SCR” reaction and has a high potential of NO_x reduction at temperatures above 300°C. NO_x is composed mainly of NO (>90%) in exhaust

gases, which reacts with NH_3 according to the standard SCR reaction [47]. Although the “fast SCR” reaction according Eq. (20), is much faster than standard SCR reaction and NO_x conversion can be effectively increased by ratio 1:1 of $\text{NO}:\text{NO}_2$ [20]. In diesel exhaust gas, the NO_2/NO_x fraction is only 5-10% and this fraction can be increased by a diesel oxidation catalyst (DOC) with platinum as an active component [45]. This leads in turn to promote the oxidation NO to NO_2 and improving the NO_x reduction efficiency in SCR, particularly at low temperatures (Fig. 11). Furthermore, the reaction of (21) takes place, which is much slower than the fast SCR reaction and still slower than the standard SCR reaction, therefore it is called “slow SCR” or “ NO_2 -SCR” reaction [47], [48].

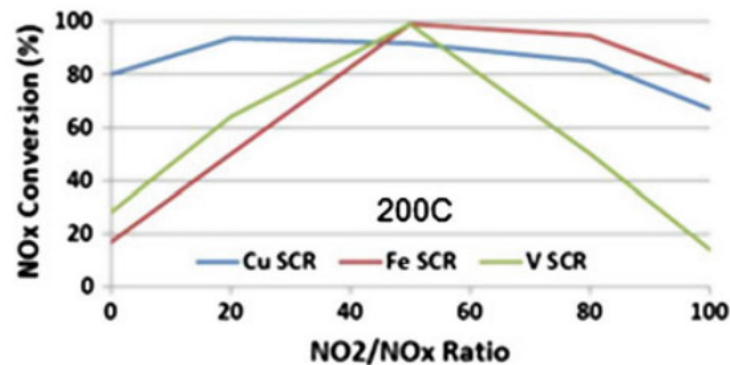


Fig. 11. De NO_x performance of SCR catalyst during different NO_2/NO_x ratio [46]
 Republished with permission of Springer, from *Review of Selective Catalytic Reduction (SCR) and Related Technologies for Mobile Applications*, Johnson T. V., in *Urea-SCR technology for de NO_x after treatment of diesel exhausts*, ed. Nova I., Tronconi E., ISBN 978-1-4899-8071-7, 2014; permission conveyed through Copyright Clearance Center, Inc.

The adsorbed NH_3^* can also be desorbed or oxidized to N_2 and H_2O by following reaction:



All the mentioned chemical reactions in the SCR system are perfectly illustrated in Fig. 12.

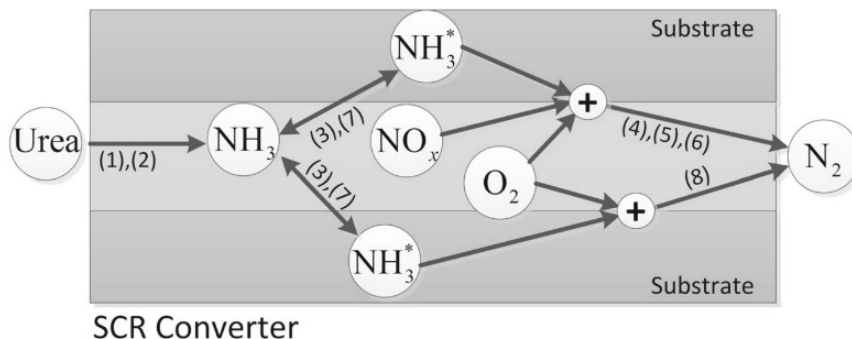
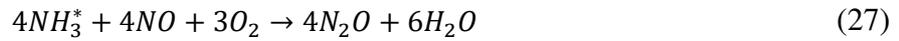
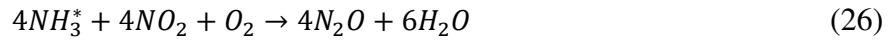
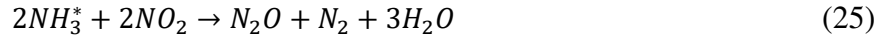


Fig. 12. Main chemical reactions in SCR system [48].

Republished with permission of Springer, from *Emission Control Science and Technology, Diesel Engine SCR Control: Current Development and Future Challenges*, Yuan X., Liu H., Gao Y., Vol. 1, 2015; permission conveyed through Copyright Clearance Center, Inc.

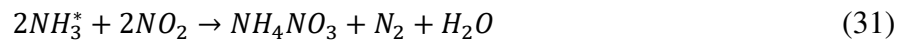
Several other reactions referred to in the SCR converter occur as undesired and they are normally neglected but may be considered depending on the catalyst formulation or temperature range. Eq. (24) and Eq. (25) appear if NO₂ levels are high in NO_x above 50% which leads to the emission of nitrous oxide (greenhouse activity - destroy ozone) as well as in Eq. (26), Eq. (27) and Eq. (28) at temperature about 450°C [47], [48], [49]:



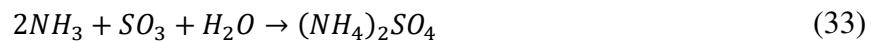
Oxygen is rich in diesel exhaust gas and also may oxidize NH₃ and NO to produce NO and NO₂ [47], [48]:



The reaction (31) results in the formation of ammonium nitrate, which is formed at temperatures below 200°C and NO₂>50% of NO_x, and can form deposits on the active material of the catalyst leading to its temporary deactivation [46], [47], [48], [49].



The SCR catalysts are also sensitive to the sulphur content in the fuel. Sulphur can accumulate in the active sides of the catalyst below 200°C, which decreases the catalytic activity by ammonium sulphates (deposits) i.e. Eq. (32) and Eq. (33). However, sulphates at high temperatures (above 500°C) can be thermally decomposed [20], [47].



4.4 Ammonia Slip Catalyst (ASC)

In a diesel exhaust gas aftertreatment system as the last element (downstream of the SCR catalyst), often appears the ammonia slip catalyst (ASC) or otherwise known as ammonia oxidation catalyst (AOC). Actually, the ASC oxidizes potentially unreacted NH_3 after the SCR system through e.g. platinum on washcoat [52]. It is the best if the catalyst oxidizes NH_3 to N_2 and H_2O as in Eq. (23) without forming at higher temperatures unwanted oxidation products such as N_2O (Eq. (28)) or NO_x like in Eq. (29) and Eq. (34).



As ammonia has a strong, pungent odour it is crucial to avoid its emission into the environment. An ammonia slip can be caused by overdosing of UWS or by an improper distribution (by an injector or mixer) of ammonia over the monolith's cross-section [51].

Recently, the ASC has been applied at the monolith outlet of SCR or as a catalyst with a dual-layer. This catalyst contains a conventional base (washcoat as a lower layer), platinum group metals (PGM) e.g. $\text{Pt}(1.5\text{g}/\text{ft}^3)/\text{Al}_2\text{O}_3$ and an additional top selective catalytic reduction active layer (Fig. 13). The NO_x formed in the lower layer reacts with NH_3 in the upper layer in such a way that the NO_x is reduced while maintaining high N_2 selectivity [51], [52].

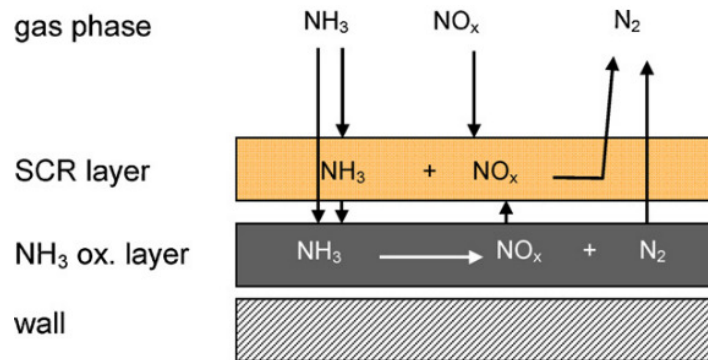


Fig. 13. Layout of the dual-layer catalyst [51]

Reprinted from Catalysis Today, Vol. 188, Scheuer A., Drochner A., Gieshoff J., Vogel H., Votsmeier M., Runtime efficient simulation of monolith catalysts with a dual-layer washcoat, 70-79, Copyright 2012, with permission from Elsevier.

In order to get desired NO_x conversion and avoid NH_3 slip at the outlet of the exhaust system, an appropriate urea injection rate is required. Fig. 14 shows the effect of ammonia NO_x ratio (ANR) on NO_x conversion and NH_3 slip at steady state engine operation. Theoretically, $\text{ANR}=1$ is required for converting 100% of NO_x , as in Eq. (35) [50]. When $\text{ANR}=1$ or higher, NO_x conversion reaches the highest level, however, the ammonia slip increases significantly, therefore ASC may be helpful [51].

$$ANR \approx \text{urea flow (g/s)} / (2 \times \text{NO}_x \text{ flow (g/s)}) \quad (35)$$

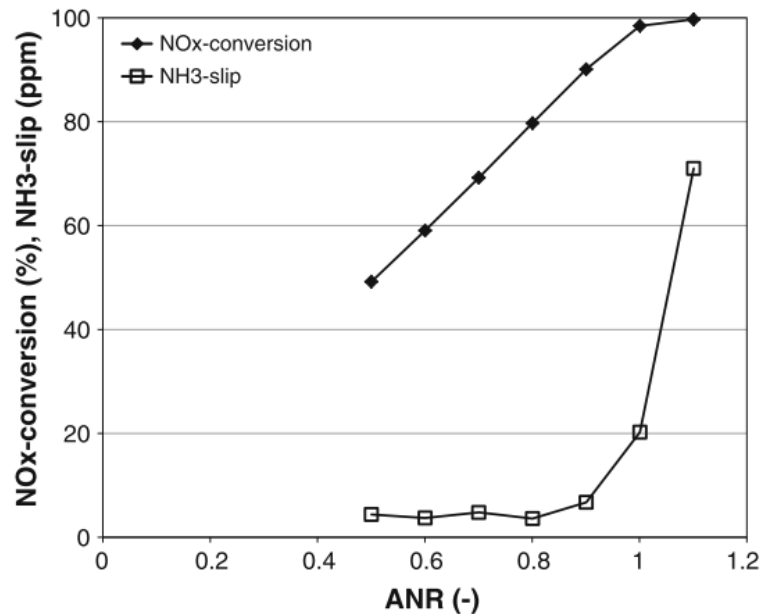


Fig. 14. NO_x conversion and NH₃ slip as a function of Ammonia NO_x Ratio (ANR) [50] *Reprinted with permission of Springer, from Vanadia-Based Catalysts for Mobile SCR, Jansson J., in Urea-SCR technology for deNO_x after treatment of diesel exhausts, ed. Nova I., Tronconi E., ISBN 978-1-4899-8071-7, 2014; permission conveyed through Copyright Clearance Center, Inc.*

4.5 Combination of DPF and SCR

The modern designs are based on close-coupled (CC) exhaust construction due to a lack of space and it is a very challenging process for the appropriate atomization of a urea-water solution which is always supported by numerical simulations. This architecture consists of a diesel oxidation catalyst (DOC) and SCR coated on a particulate filter (Fig. 15) at the outlet side, marked as SCRof, SCRF or SDPF [53], [54], [57], [58].

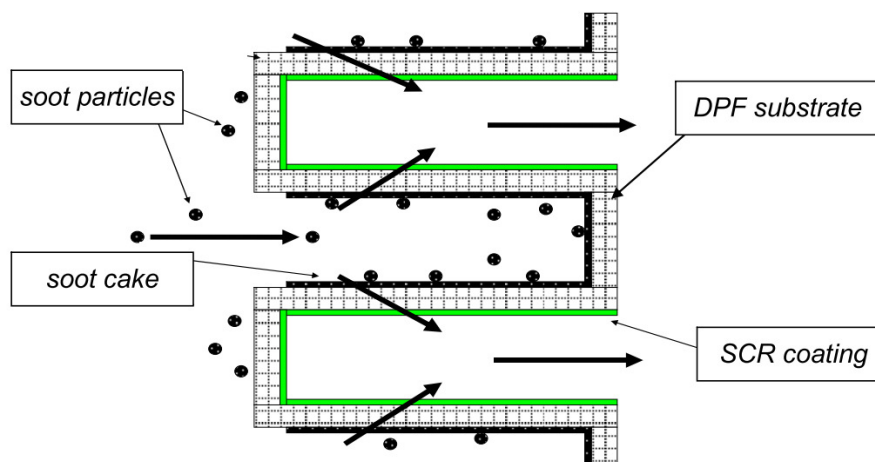


Fig. 15. SCR coated on a DPF [57]

Reprinted with permission from Downsizing of the EuroVI exhaust aftertreatment components to fit into the EuroIII silencer, Döring A., Emmerling G., Rothe D.; The Authors copyright 2012 (OA).

This solution makes the exhaust gas aftertreatment smaller (Fig. 16) and combines the reduction of NO_x and PM filtration in one substrate. SDPF can be installed closer to the engine, which has the effect of earlier NO_x conversion by a faster attainment of the operating temperature (light-off). Moreover, this combination reduces packaging volume and costs [53], [54], [57].

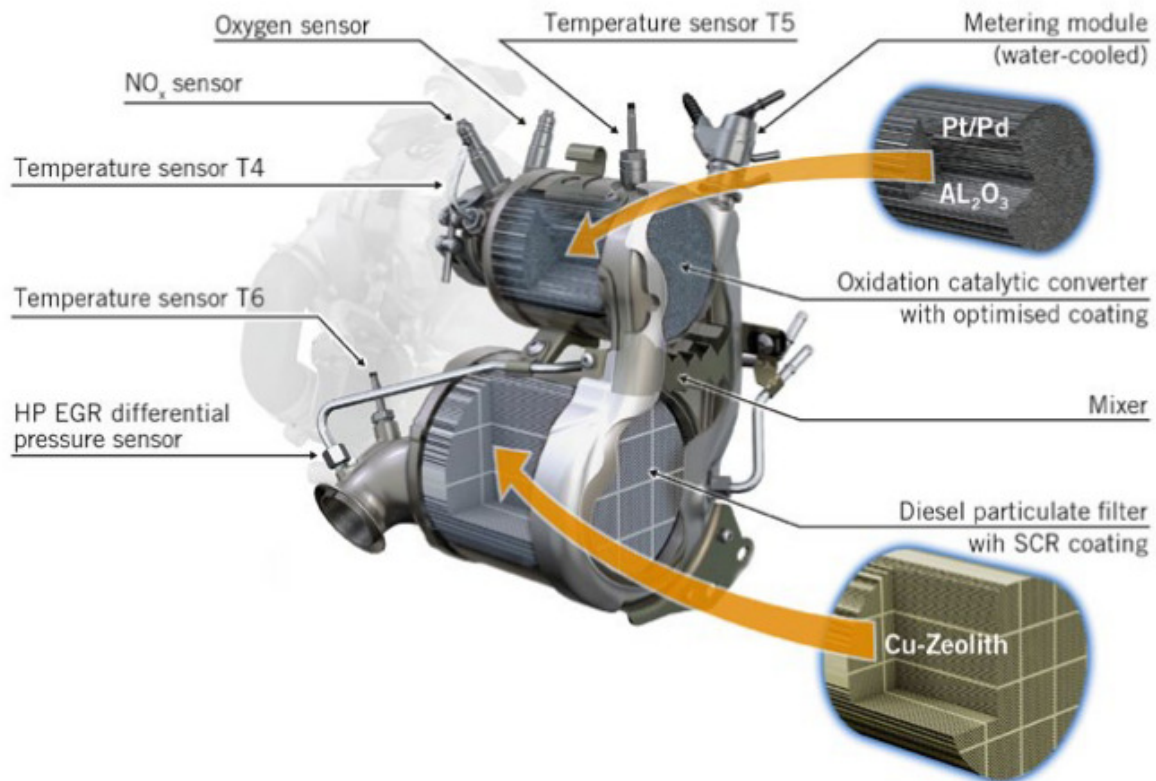


Fig. 16. Compact design of exhaust gas aftertreatment [55]

Republished with permission of Springer, from *MTZ worldwide, The euro 6 engines in the modular diesel engine system of Volkswagen*, Neusser H. J., Kahrstedt J., Dorenkamp R., Jelden H., Vol. 74, 2013; permission conveyed through Copyright Clearance Center, Inc.

On the contrary, the distance between the injector and the SCR catalyst is very reduced. The injected UWS has limited space and time for decomposition and mixing performance, which directly influences ammonia distribution and NO_x reduction. Spray-wall interaction (wall film formation) can be well eliminated by using a static mixer (with baffles and swirl function) downstream of an injector, which eliminates the ammonia slip with a satisfactory level of backpressure. This described process can be very well simulated by CFD (computational fluid dynamics) methods [53], [55], [56].

As a result of the increasing pressure to develop the exhaust gas aftertreatment smaller and low-cost meeting the tightening legislative requirements, it is desirable to combine multiple functionalities (Fig. 17) and use all possible connections between devices [58].

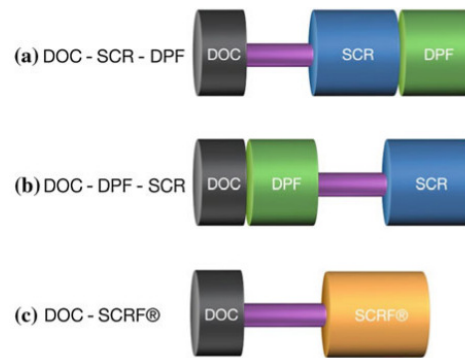


Fig. 17. Different design layouts for combination of DPF and SCR [58]

Republished with permission of Springer, from *SCR Reactor Models for Flow-Through and Wall-Flow Converters*, Karamitros D., Koltsakis G., in *Urea-SCR technology for deNO_x after treatment of diesel exhausts*, ed. Nova I., Tronconi E., ISBN 978-1-4899-8071-7, 2014; permission conveyed through Copyright Clearance Center, Inc.

Placing the SCR catalyst upstream of the DPF reduces warm-up temperature, however, permissive of the reduction of cold start NO_x emissions. On the other hand, a DPF placement in front of the SCR catalyst is ideal for its regeneration management but there is a problem with SCR cold-start efficiency as a result of the large mass of the DPF to be heated [58].

5 Historical background of emission standards in Europe

Starting from the 90s, the exhaust emission technology in Europe has been in the process of rapid and constant development for which an impulse are European environmental control directives known as the EURO directives. The task of all these directives is to regulate exhaust emissions for new vehicles sold within the territory of the European Union. These directives establish the maximum permitted levels of emissions during the mandatory tests to be applied to all vehicles travelling on European roads. The implementation of these directives in recent years has involved significant technological changes in vehicles among which mention should be made of the development of more efficient and cleaner engines through the use of more sophisticated emission control systems. In recent decades, the technical development related to the emissions control systems for vehicles was spectacular with diesel engines being those in which technological change is the most visible [60].

In 1992, the year when the Euro 1 (Fig. 18) directive (91/441/EC) came into force, the exhaust system of a standard diesel car (M₁ - for 8 passengers + driver) consisted of only two or three silencers. It was a very simple emission control system, which did not contain any active element to its processing. It was not necessary to stay below the maximum established exhaust emission limits referred to in the directive. Their only goal was to keep the

backpressure at an acceptable level to ensure proper operation of the engine, as far as reducing the noise generated by the engine to the level provided by directive [59], [60].

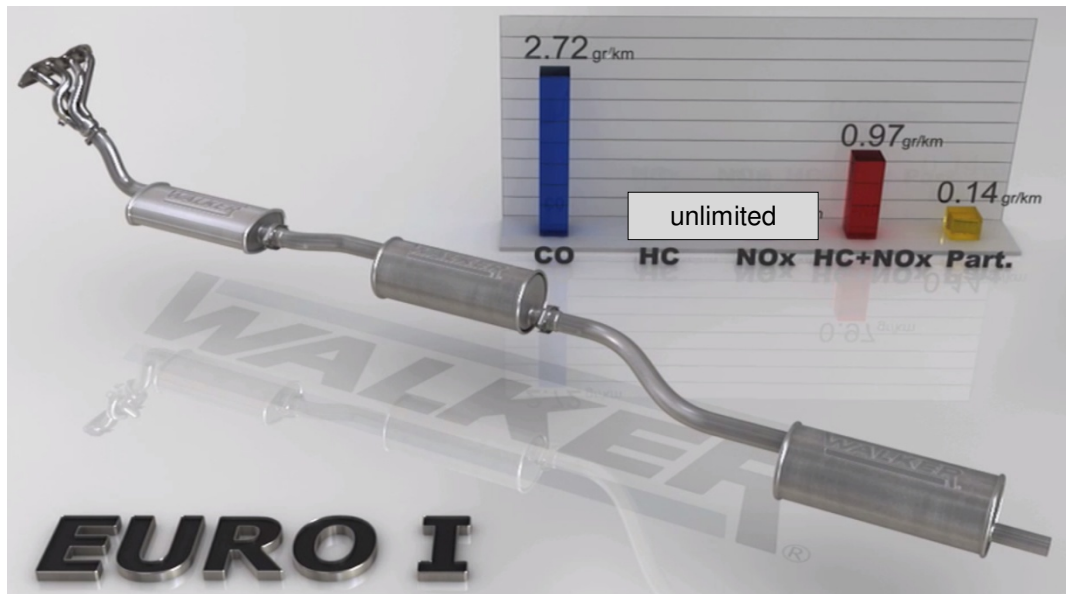


Fig. 18. Example of an exhaust system for Euro 1 (Category M₁, Diesel) [60]
Reproduced from Tenneco EMEA, Technical Advanced Digital Information System (TADIS): Emission control (<https://ta.garagegurus-eu.info/tadis/tadis-html-en/>), Copyright 2022, Tenneco Inc.

The years passed and in 1996 the Euro 2 (Fig. 19) directive (94/12/EC) came into force, which significantly reduced carbon monoxide (CO) emissions. Therefore, it has become necessary to include oxidation catalysts (DOC) in the exhaust systems. For the operation of these catalysts, it is necessary to achieve a minimum activation temperature of approx. 300°C thus they are located close to the exhaust manifold outlet [59], [60].



Fig. 19. Example of an exhaust system for Euro 2 (Category M₁, Diesel) [60]
Reproduced from Tenneco EMEA, Technical Advanced Digital Information System (TADIS): Emission control (<https://ta.garagegurus-eu.info/tadis/tadis-html-en/>), Copyright 2022, Tenneco Inc.

Four years later, in 2000, the Euro 3 (Fig. 20) directive (98/69/EC) came into force. This directive further restricts the permissible maximum limit for carbon monoxide and for the first time sets a separate limit for nitrogen oxides, and also reduces again permissible maximum limits of the sum of NO_x and unburned hydrocarbons as well as particulate emissions into the atmosphere [59], [60].



Fig. 20. Example of an exhaust system for Euro 3 (Category M₁, Diesel) [60]
Reproduced from Tenneco EMEA, Technical Advanced Digital Information System (TADIS): Emission control (<https://ta.garagegurus-eu.info/tadis/tadis-html-en/>), Copyright 2022, Tenneco Inc.

This standard also introduced the need to measure the amount of exhaust gas from the moment the engine is started and not 40s later as it was in previous standards, which forces manufacturers to create more perfect injection systems so that they can meet its requirements. The first lambda sensors were installed in diesel vehicles [60].

With the entry of the Euro 4 (Fig. 21) directive (2002/80/EC), the limits for CO, the sum of NO_x and HC as well as PM have again been significantly lowered, necessitating the introduction of more modern and efficient systems to manage these emissions. These changes gave rise to the mass implementation of OBD II (On-Board Diagnostic level 2) systems that include catalyst performance monitoring systems. For this purpose, broadband lambda sensors have appeared that manage the mixes of combustion air much more efficiently. At the same time, the use of a second lambda probe at the outlet of the catalyst is standardized, which is used to monitor the efficiency of the catalyst by consuming oxygen as a result of oxidation reactions taking place inside the catalyst [59], [60].



Fig. 21. Example of an exhaust system for Euro 4 (Category M₁, Diesel) [60]
Reproduced from Tenneco EMEA, Technical Advanced Digital Information System (TADIS): Emission control (<https://ta.garagegurus-eu.info/tadis/tadis-html-en/>), Copyright 2022, Tenneco Inc.

Four years later, in 2009, the Euro 5 (Fig. 22) directive (715/2007) came into force, which pays special attention to a significant reduction in the emission limits of particulate matter in exhaust gases. In order to achieve this ambitious goal, diesel particulate filters also known as DPF have appeared. Their task is to retain solid particles in the internal filter and then periodically burn them and transform them into carbon dioxide and H₂O. It should be noted that despite the official Euro 5 directive entered into force in 2009, most manufacturers had already equipped their vehicles with the DPF systems. The DPF system was first used as standard equipment on a passenger car in 2001 by the PSA group on the Peugeot 607 [59], [60].



Fig. 22. Example of an exhaust system for Euro 5 (Category M₁, Diesel) [60]
Reproduced from Tenneco EMEA, Technical Advanced Digital Information System (TADIS): Emission control (<https://ta.garagegurus-eu.info/tadis/tadis-html-en/>), Copyright 2022, Tenneco Inc.

In 2014, the Euro 6 (Fig. 23) directive (459/2012) entered into force, which draws attention to the drastic reduction of threats related to NO_x . For this purpose, modern emission control systems have been developed, such as SCR systems - systems for selective catalytic reduction of nitrogen oxides through urea-water solution (trade name - AdBlue). These systems convert nitrogen oxide molecules into molecular nitrogen N_2 which is harmless available in the atmosphere. AdBlue is injected into the exhaust pipe through the injector directly in front of the mixer located at the inlet of the SCR catalyst. This mixer has an important function, ensuring that the molecules of ammonia from AdBlue mixed uniformly before entering the reduction catalyst so that the reaction was carried out in the most effective way [59], [60].

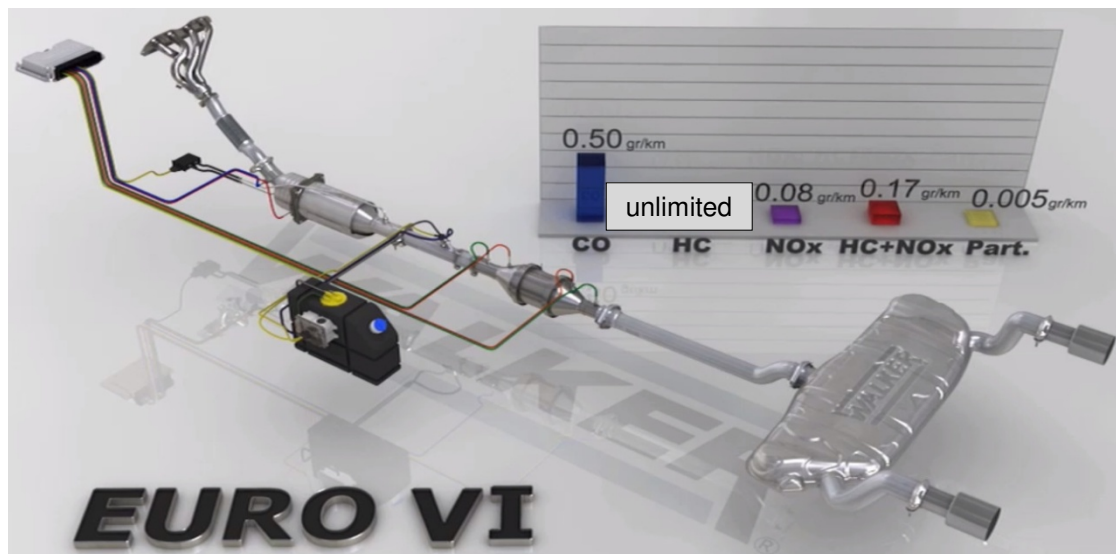


Fig. 23. Example of an exhaust system for Euro 6 (Category M₁, Diesel) [60]
Reproduced from Tenneco EMEA, Technical Advanced Digital Information System (TADIS): Emission control (<https://ta.garagegurus-eu.info/tadis/tadis-html-en/>), Copyright 2022, Tenneco Inc.

As can be seen, exhaust systems have evolved a lot in just two decades, from a not very technologically complex mechanical system to one of the most complex and technologically advanced systems that exist in modern vehicles. This evolution was also associated with a significant increase in prices in the case of introducing repairs of this type of systems, which means that today more than ever it is necessary to constantly improve technical knowledge that allows access to this technology [60].

European Union emission standards for new gasoline and diesel passenger cars (Category M₁ with a reference mass not exceeding 2610 kg) are summarized in the Tab. 1. All dates refer to new type approvals. The EC directives also specify a second date (one year later), unless indicated otherwise - which applies to first registration (entry into service) of existing, previously type-approved vehicle models [59].

Tab. 1. Emission standards for gasoline and diesel passenger car [59]

Reproduced from source: DieselNet.com

Stage	Date	CO	HC	HC+NO _x	NO _x	PM	PN
		[g/km]					
Positive Ignition (Gasoline)							
Euro 1†	1992.07	2.72(3.16)	-	0.97(1.13)	-	-	-
Euro 2	1996.01	2.2	-	0.5	-	-	-
Euro 3	2000.01	2.3	0.20	-	0.15	-	-
Euro 4	2005.01	1.0	0.10	-	0.08	-	-
Euro 5	2009.09 ^b	1.0	0.10 ^d	-	0.06	0.005 ^{e, f}	-
Euro 6	2014.09	1.0	0.10 ^d	-	0.06	0.005 ^{e, f}	6.0×10 ^{11 e, g}
Compression Ignition (Diesel)							
Euro 1†	1992.07	2.72(3.16)	-	0.97(1.13)	-	0.14(0.18)	-
Euro 2, IDI	1996.01	1.0	-	0.7	-	0.08	-
Euro 2, DI	1996.01 ^a	1.0	-	0.9	-	0.10	-
Euro 3	2000.01	0.64	-	0.56	0.50	0.05	-
Euro 4	2005.01	0.50	-	0.30	0.25	0.025	-
Euro 5a	2009.09 ^b	0.50	-	0.23	0.18	0.005 ^f	-
Euro 5b	2011.09 ^c	0.50	-	0.23	0.18	0.005 ^f	6.0×10 ¹¹
Euro 6	2014.09	0.50	-	0.17	0.08	0.005 ^f	6.0×10 ¹¹
At Euro 1-4, passenger cars > 2500 kg were type approved as Cat. N ₁ (light commercial vehicles) † values in brackets are conformity of production (COP) limits a. until 1999.09.30 (after that date DI (Direct Injection) engines must meet IDI (Indirect Injection) limits) b. 2011.01 for all models c. 2013.01 for all models d. and NMHC (non-methane hydrocarbons) = 0.068 g/km e. applicable only to vehicles using DI engines f. 0.0045 g/km using the PMP (Particle Measurement Programme) measurement procedure g. 6.0×10 ¹² 1/km within first three years from Euro 6 effective dates							

It should be noted that the last Euro 6 emission standard has also evolved since its introduction (Fig. 24). The main stages of the Euro 6 standards are related to changes in the conduct of emission tests. The New European Driving Cycle (NEDC) procedure used in previous standards has been superseded by new tests called the Worldwide harmonized Light vehicles Test Procedure (WLTP) and Real Driving Emissions (RDE) testing, which will be discussed in the next chapter. A conformity factor (CF) for NO_x and PN has also been introduced which determines the maximum ratio between the legislated emissions limit under laboratory testing (WLTP) and those measured in real driving conditions (RDE). The CO₂ emissions have also been lowered from 130 to 95 g/km [61], [62].

Test Cycle		2014	2015	2016	2017	2018	2019	2020	2021
Method	RDE	09	09	04	09	09	09		
		Regulation 692/2008				Regulation 2017/1151 with amendments			
NEDC	Voluntary	EU 6b							
WLTP	Voluntary					EU 6c			
WLTP	Mandatory					EU 6d-temp /CF:NO _x 2.1; PN 1.5			
WLTP	Mandatory					EU 6d /CF:NO _x 2.1; PN 1.5			
WLTP	Mandatory					EU 6d /CF:NO _x 1.43; PN 1.5			
Fuel consumption		130 g/km CO ₂				95 g/km CO ₂			
		New Type Approval				New Vehicles			

Fig. 24. Timing and stages of the Euro 6 emission standard (Category M₁) [61], [62]
 Adapted from Ricardo, *Expectations for Actual Euro 6 Vehicle Emissions*; © 2018, Ricardo plc.
 Adapted from Continental, *Worldwide Emission Standards and Related Regulations*; © 2019, CPT Group GmbH.

It is worth adding that several other countries in the world (Fig. 25) also comply with exhaust emission standards, but they are named differently and have their own exhaust emission limits. The most demanding pollutant emission regulations are in the US. From 2023 China will be more stringent than Europe [62].

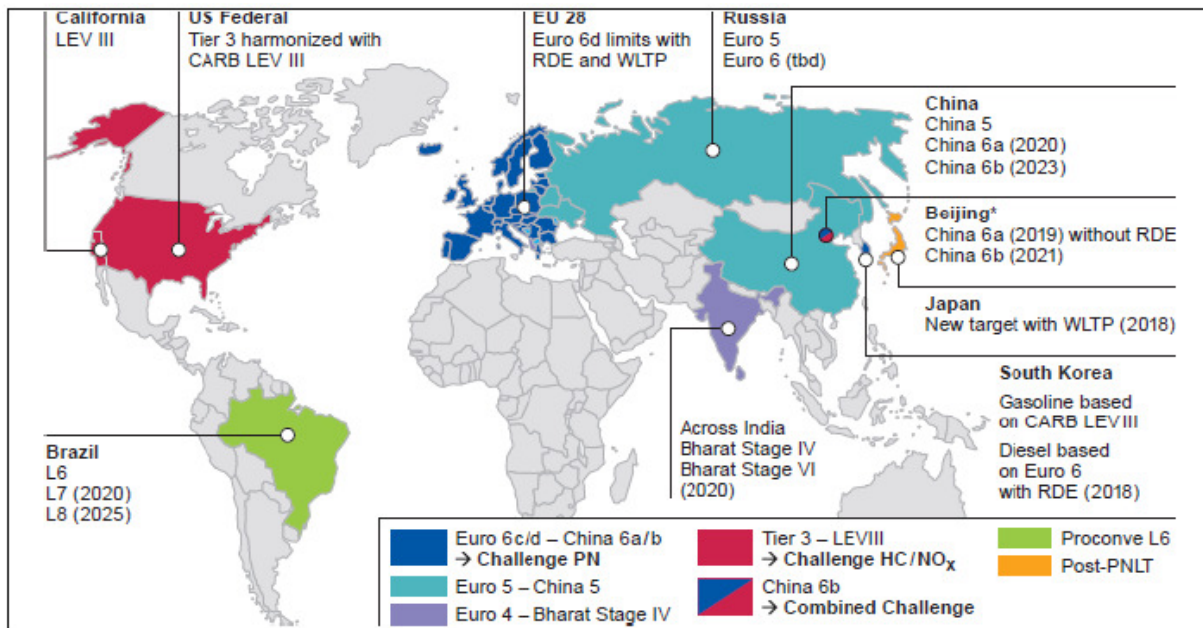


Fig. 25. Global emission standards [62]

Adapted from Continental, *Worldwide Emission Standards and Related Regulations*; © 2019, CPT Group GmbH.

6 Emission test cycles according to EU regulations

The purpose of the emission tests is to obtain a certificate (approval) allowing a new type of car to be driven on public roads. They are performed as part of the work undertaken before the start of serial production [5]. The most important organizations in the European

Union responsible for emission regulations and test cycles in the form of directives/regulations are [4], [63]:

- the European Parliament,
- the Council of the European Union,
- the European Commission (EC).

Over the years, the European Economic Community (EEC) and later the European Union have formed a series of directives and regulations, mostly based on the technical propositions of the UNECE (United Nations Economic Commission for Europe) [63]. In Western Europe, the first standard for toxic emissions from vehicles, based on the Urban Driving Cycle (UDC), appeared in 1972 and was called ECE 15/01 (Economic Commission for Europe) [4]. The Euro 1 standard began in 1992 and the ECE-15 test cycle (UDC) was equipped with the second part of the test cycle called EUDC (Extra Urban Driving Cycle) as shown in Fig. 26, they are also known as MVEG-A (The Motor Vehicle Emissions Group). The first part of the UDC test represents the driving conditions of a car in city traffic and consists of four, identical elementary urban cycles, repeated without breaks, marked ECE. This part of the cycle has a low car speed, low engine load and low exhaust gas temperature [4], [5].

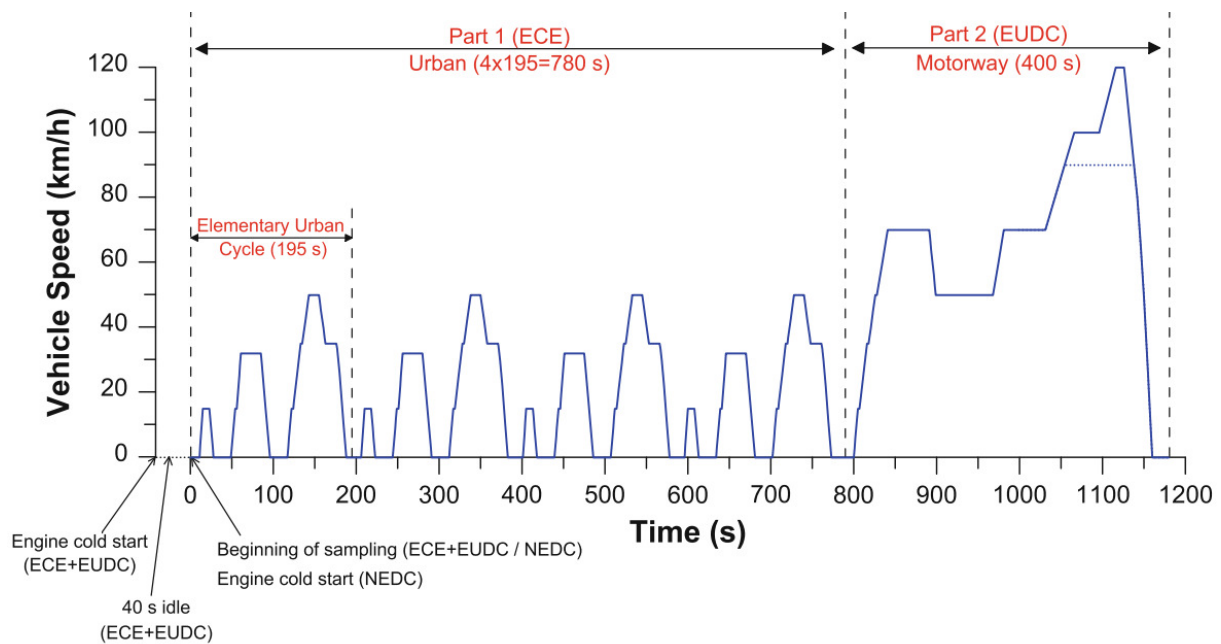


Fig. 26. Driving cycles (NEDC): urban (ECE) + extra urban (EUDC) cycle [63]
Republished with permission of Springer, from *Driving and Engine Cycles*, Giakoumis E. G., ISBN 978-3-319-49033-5, 2017; permission conveyed through Copyright Clearance Center, Inc.

In turn, the second part of the cycle (EUDC) is performed immediately after the first part and takes into account a more aggressive way of driving at higher vehicle velocities up to 120km/h. The test consists of several modes such as idle, accelerations, steady speed driving,

and decelerations. There is a dashed line at the end of the EUDC cycle (Fig. 26) that reflects a version of the cycle for cars powered by low-power engines ($\leq 30\text{kW}/1000\text{kg}$ and $\leq 130\text{km/h}$) [5], [63].

For conformity with the Euro 1 and 2 emission standards, the car (run-in and driven for at least 3000 km) was kept for conditioning at least 6h before the test in a room with temperature between 20 and 30°C. After the preconditioning, the appropriate test cycle began with a phase of operating the engine idle for 40 seconds (cold start) before the beginning of exhaust gas sampling for analysis, i.e. emissions from this phase were not included in the final result for the entire cycle. Since 2000, with the entry into force of the Euro 3 standard, exhaust gas collection for analysis begins when the engine is cold (without the 40s warm-up period). This modified cold-started procedure is known as New European Driving Cycle (NEDC) or MVEG-B. This change leads to a higher number of pollutants taken into account due to the first minutes after cold start the aftertreatment devices have not reached their operating temperature [5], [63].

Emission testing on a chassis dynamometer with a CVS (Constant Volume Sample) tunnel as a part of the approval tests is shown in Fig. 27. The idea behind the measurement is to determine the exhaust emissions of the car for which the test section is simulated according to the appropriate driving cycle. The vehicle is on rollers (chassis dynamometer), and the exhaust gases are led to the measuring tunnel, where they are diluted with previously purified air, so as to obtain a constant flow rate of the air-exhaust mixture.

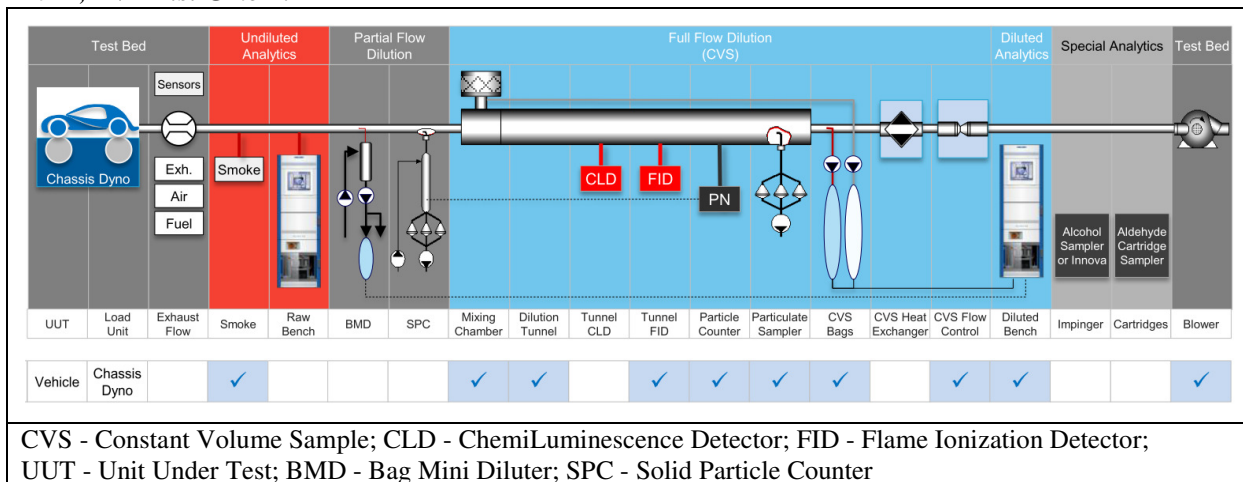


Fig. 27. Front (left) and back (right) of the roller test bench under climatic chamber [66]
Reprinted from Applied Thermal Engineering, Vol. 106, Fernández-Yáñez P., Armas O., Martínez-Martínez S., Impact of relative position vehicle-wind blower in a roller test bench under climatic chamber, 266-274, Copyright 2016, with permission from Elsevier.

The specified small portion of the resulting mixture is continuously drawn from a tunnel and stored for the duration of test in tanks - measuring bags. The concentration of the individual exhaust components in the test bags, which is obtained at the end of the test, is therefore equal to the average concentration for the entire duration of the test. During the test, the total amount of exhaust gas emitted from the tailpipe is also determined. The final result is the mass of the given compound contained in the exhaust gas, calculated from the determined concentration in the measuring bag, taking into account the total amount of exhaust gas. To ensure the accuracy of the method, purified exhaust dilution air is taken for analysis throughout the test. The final measurement result is corrected for the measured amount of exhaust gas components, which is received together with the air diluted [4].

The exhaust emission measurement stand and its main devices are better presented in the Tab. 2. Carbon monoxide and carbon dioxide are tested by the NDIR (Non Dispersive InfraRed) method. This method uses the absorption of infrared radiation by compounds contained in the exhaust gas. A chemiluminescent analyzer CLD is used to measure nitrogen oxides. On the other hand, the FID detectors are used to detect hydrocarbons. Particulate matter is measured by the gravimetric method. It consists of measuring the mass of filters on which solid particles are deposited [4].

Tab. 2. Test bed layout for EU certification of light duty vehicles according to AVL [70] Adapted with permission from Passenger car emission regulations, Engeljehring K.; Copyright 2014, AVL List GmbH.



In Europe, each country has a dedicated type approval authority, which in turn appoints specific services (laboratories) to carry out homologation tests. If the prescribed procedures have been followed (required limits are not exceeded), type approval will be granted by the national type approval authority. Within strictly specified conditions, type

approval for one vehicle model can also be extended to similar models of the same manufacturer [63].

The Worldwide harmonized Light vehicles Test Cycle (WLTC) was developed at the United Nations level and can be considered as a more realistic driving cycle like those representing actual on-road vehicle emissions [42]. The WLTC cycles are part of the Worldwide harmonized Light vehicles Test Procedures (WLTP). Sometimes the WLTC and WLTP abbreviations are used interchangeably, however, the WLTP procedures include several WLTC test cycles, divided into categories as in Tab. 3. Class 3 is representative of vehicles driven in Europe and Japan, Class 2 for vehicles driven in India and low power vehicles in Japan and Europe and Class 1 for vehicles driven only in India. The WLTP replaced the NEDC test cycle of light-duty vehicles in Europe from September 2017 [59].

Tab. 3. WLTC test cycles [59]
 Reproduced from source: DieselNet.com

Category	Power to mass ratio PMR [W/kg]	Max speed v_{max} [km/h]	Speed phase sequence
Class 3b	PMR > 34	$v_{max} \geq 120$	Low 3 + Medium 3-2 + High 3-2 + Extra High 3
Class 3a		$v_{max} < 120$	Low 3 + Medium 3-1 + High 3-1 + Extra High 3
Class 2	$34 \geq PMR > 22$	-	Low 2 + Medium 2 + High 2 + Extra High 2
Class 1	$PMR \leq 22$	-	Low 1 + Medium 1 + Low 1

The most popular test for category 3 (3a and 3b trace look very similar) includes four sub-cycles (Fig. 28): low-speed, medium-speed, high-speed and extra high-speed, which represent more dynamic driving conditions, such as a higher maximum velocity and a smaller share of idling time during a laboratory cycle [42].

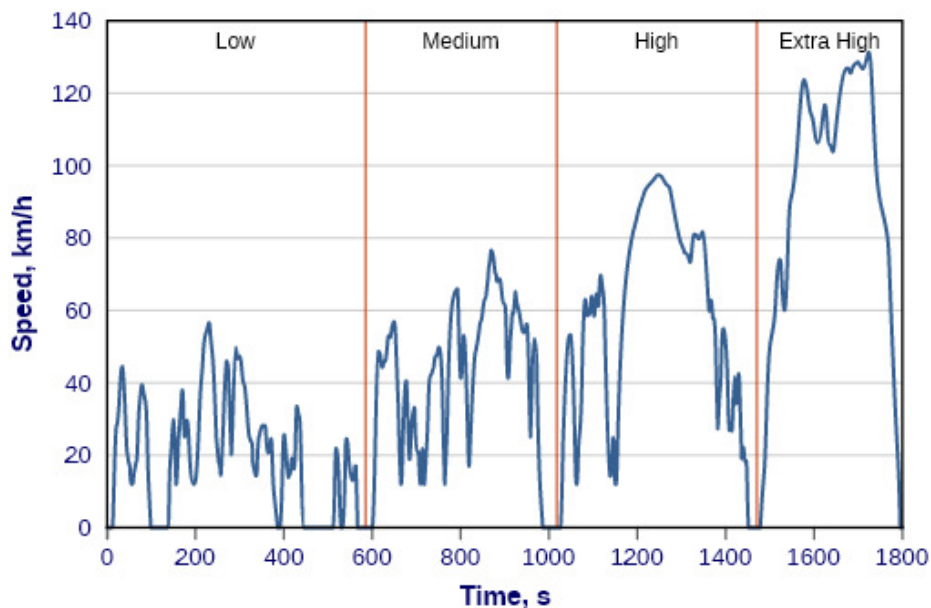


Fig. 28. WLTC cycle for Class 3b vehicles [59]
 Reproduced with permission from source: DieselNet.com

The EU's Joint Research Center (JRC) implemented an additional complementary WLTP test under real road conditions. In order to narrow the large discrepancy between real world emissions and laboratory tests, the real driving emissions (RDE) test procedures using (Fig. 29) Portable Emissions Measurement Systems (PEMS) have been introduced in the EU. This procedure allows analyzing emissions on different driving conditions with real on-road variables such as e.g. traffic, different altitudes and weather conditions [65].



Fig. 29. Portable Measurement Systems (PEMS) on a vehicle [70]

Adapted with permission from Passenger car emission regulations, Engeljehring K.; Copyright 2014, AVL List GmbH.

Measurement of the RDE become obligatory from September 2017, together with Euro 6d-temp because previously for Euro 6b and 6c it only served as a voluntary test for monitoring purposes. Contrary to previous vehicle emission tests and parameters just as engine load and vehicle speed are no longer determined by a fixed pattern, but are generally defined by the traffic situation, driver behavior and the course of the route during the RDE test [68]. The emissions of the NO_x measured in the RDE test shall not-to-exceed (NTE) the conformity factor $\text{CF}=2.1$ times the maximum limit (for Euro 6d-temp that is 80 mg/km), or 168 mg/km. However, for Euro 6d, this ratio of road emission and the emission specified by the legislation has been reduced to 1.43 as well as CO_2 reduction to 95 g/km. For both these Euro standards also there is $\text{CF}=1.5$ for PN [67], [69]. An example of the RDE test is shown in the Fig. 30.

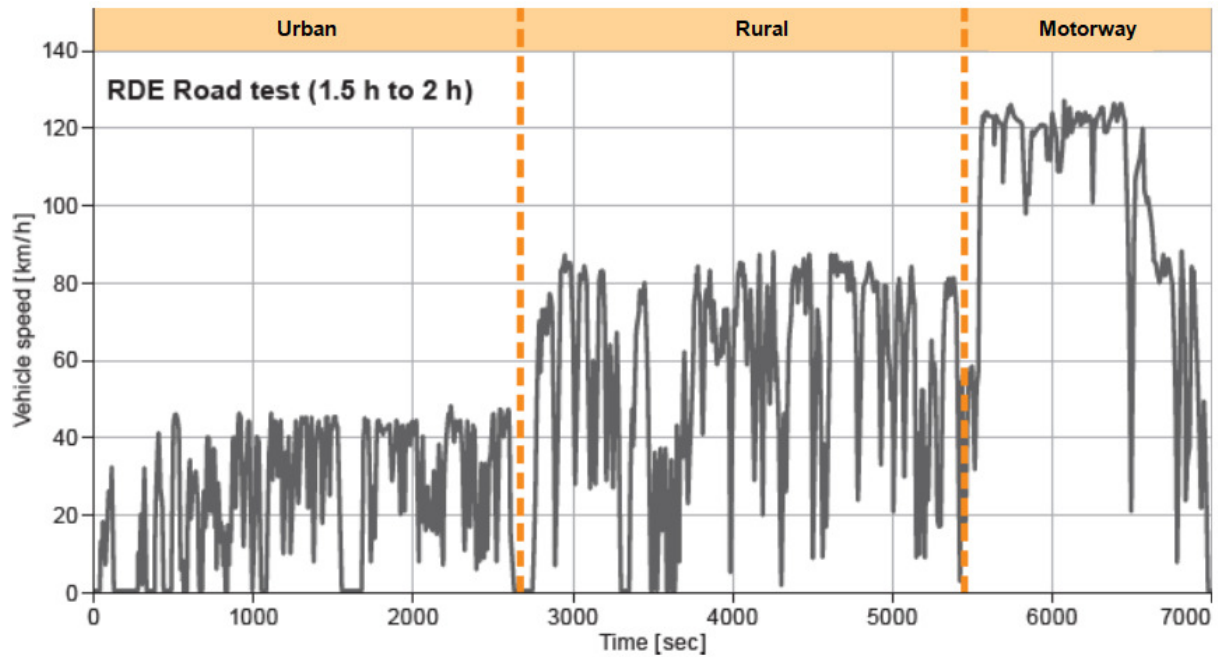


Fig. 30. Example of RDE test cycle recorded during road testing [62]

Adapted from Continental, *Worldwide Emission Standards and Related Regulations*; © 2019, CPT Group GmbH.

The Tab. 4 summarizes the main parameters for the emissions test cycles in Europe and compares their key differences.

Tab. 4. Comparison of parameters from key emission cycles

Parameters	NEDC	WLTP (Class 3b)	RDE
Duration	1180s (~20 min)	1800s (30 min)	90-120 min
Distance	11.03 km	23.27 km	urban 34%, rural 33%, motorway 33% with tolerance $\pm 10\%$, min. distance: 16 km in each area
Max. speed [km/h]	120	131.3	145
Avg. speed [km/h]	33.6	46.5	15-40 in urban area
Stop duration [%]	23.7	12.6	6-30% in urban area
Gear shift points	fixed	different	different
Temperature [°C]	20 ÷ 30	14 ÷ 23	-7 ÷ 35
Other	From Euro 3: deletion of the 40s idle period prior to bag sampling start	All equipment options are considered in terms of their influence on aerodynamics, weight and rolling resistance	Altitude: normal ≤ 700 m, extended ≤ 1300 m; Vehicle weight: up to 90% of GVM; Elevation: < 1200m/100km Weather and traffic: all conditions; Consumption: all turned on e.g.: AC/Radio

The new regulations retain the previously existing forms of vehicle type control (periodic) in terms of emissions, i.e.:

- Conformity of Production tests (CoP) - verification of production vehicles to comply with type approval requirements and an ISO norm;

- In Service Conformity tests (ISC) - verification of vehicles in accordance with type approval requirements over the useful life of 100,000 km or 5 years.

It should be mentioned that there are also durability requirements tests (an ageing test) of 80,000 km driven in accordance cycles (on the road or on a chassis dynamometer). A manufacturer may choose to have the deterioration factors (DFs) such as: CO: 1.5, THC and NMHC: 1.3, NO_x: 1.6, PM and PN: 1.0 used as an alternative to testing based on test track ageing [62], [64].

7 Current status of the SCR catalyst and modeling

The previous chapters review the main topics related to the emission of harmful substances from internal combustion engines, methods of reducing them and their legal issues as well as the possibilities of CFD simulation. The intention of this chapter is to present the knowledge in the area of catalysts used in the SCR system, which is the main topic of this dissertation. The structure of the catalyst and the process of their production will be presented, as well as its main parameters related to its structure and efficiency. Moreover, it is also important to present the main problems and challenges that can be encountered in SCR systems and the process of designing their mixers.

7.1 Basic information about structure of catalyst

The channel size and structure of the monolith play an important role in the overall performance. The channels of the most common substrates typically have square shaped cross-sections that extend in one dimension, similar to a honeycomb structure (Fig. 31). These channels provide space for the flow of gases that interact with the active catalyst dispersed on the channels walls via washcoating [93].

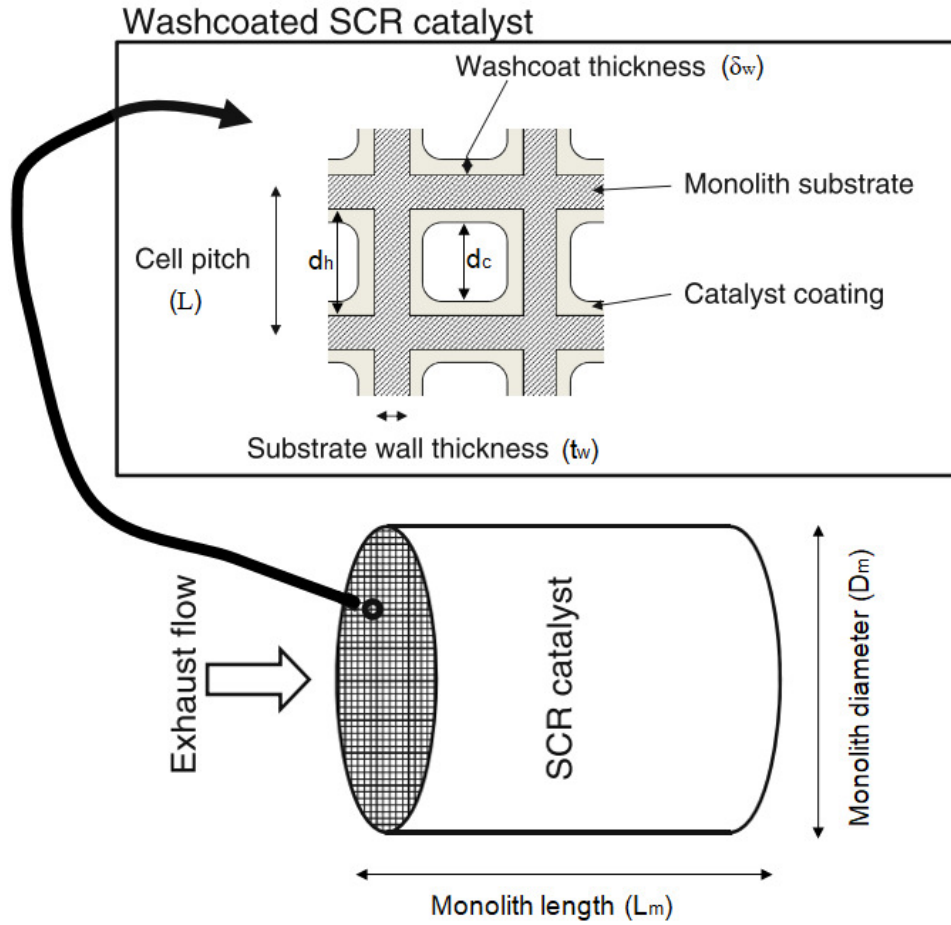


Fig. 31. SCR catalyst with catalytic material coated on a monolith substrate [50]
 Republished with permission of Springer, from *Vanadia-Based Catalysts for Mobile SCR*, Jansson J., in *Urea-SCR technology for deNO_x after treatment of diesel exhausts*, ed. Nova I., Tronconi E., ISBN 978-1-4899-8071-7, 2014; permission conveyed through Copyright Clearance Center, Inc.

Cell configurations and properties of monolith are described in terms of geometric and hydraulic parameters. Repeat distance of cell spacing (cell pitch L) is the distance measured from the centre of one cell wall of a square channel to the next wall. The cell density N_c is defined as the number of cells per unit of cross-section area and is expressed by the number of cells per square inch (CPSI) or per square centimeter [50], [93].

In this work, one of the SCR monolith has the following geometric dimensions: monolith length $L_m = 3''$, monolith diameter $D_m = 5.66''$, $N_c = 300 \text{ cpsi}$ ($1/\text{inch}^2$), wall thickness $t_w = 0.23\text{mm}$ (9mil) and washcoat thickness $\delta_w = 0.13\text{mm}$ ($130\mu\text{m}$).

The cell density N_c is defined by Eq. (36).

$$N_c = \frac{1}{L^2} \quad (36)$$

Thus the cell pitch L for the tested monolith is:

$$L = \sqrt{1/N_c} = \sqrt{1/300} = 0.578'' = 1.47\text{mm} \quad (37)$$

Sometimes, the cell density N_c is expressed in number of cells per square centimeter, therefore:

$$N_c = \frac{1}{(0.147\text{cm})^2} = 46 [1/\text{cm}^2] \quad (38)$$

The hydraulic diameter d_h decreases as the cell density increases for a monolith. The hydraulic diameter is different for uncoated (d_h) and washcoated (d_c) monolith since washcoating with catalyst materials changes the wall thickness t_w .

$$d_h = L - t_w = 1.47\text{mm} - 0.23\text{mm} = 1.24\text{mm} \quad (39)$$

$$d_c = d_h - 2\delta_w = 1.24\text{mm} - 2 \cdot 0.13\text{mm} = 0.98\text{mm} \quad (40)$$

The porosity ε_b of a porous medium is defined as [94]:

$$\varepsilon_b = \frac{V_v}{V_o} \quad (41)$$

where:

V_v - is the void volume, V_o - is the entire body volume of a porous medium.

This means that a solid material have a porosity of $\varepsilon_b = 0$ and a volume containing “only voids” would have a porosity of $\varepsilon_b = 1$. The relative open front area (OFA), also called void fraction, is the same as porosity. Govender et al. [96] presented relative OFA in a simple formula for previously calculated data:

$$\varepsilon_b = OFA = \frac{(L - t_w^*)^2}{L^2} = \frac{(1.47 - 0.49)^2}{1.47^2} = 0.44 \quad (42)$$

where:

t_w^* - is the wall thickness together with washcoat ($2\delta_w$) because it affects the relative OFA.

Another important parameter is the specific geometric surface area (GSA) or catalyst loading areas, which is the summation of all the channel wall areas defined by the combination of CPSI and wall thickness and is a key parameter for pressure drop and reactions controlled by mass transfer [95]. Govender et al. [96] presented GSA, as shown by Eq. (43):

$$GSA = \frac{4OFA}{d_c} = \frac{4 \cdot 0.44}{0.00098} = 1796 \frac{\text{m}^2}{\text{m}^3} \quad (43)$$

In designing monolithic catalysts, there is a balance between specific geometric surface area (GSA) and pressure drop. The frictional pressure drop of exhaust gases in substrate channels can be calculated using the Darcy equation [97]:

$$\Delta p = \frac{f L_m \rho v_c^2}{2 d_c} \quad (44)$$

$$v_c = \frac{\dot{m}_{exh}}{\rho A_{OFA}} \quad (45)$$

where:

f - is the friction factor (dimensionless), L_m - the monolith length, ρ - the gas density at operating conditions, v_c - the linear velocity of gas in channel at operating conditions, d_c - the coated hydraulic diameter, \dot{m}_{exh} - total mass flow rate, A_{OFA} - is the open front area of the monolith.

One of the goals of this work is to determine the pressure drop in SCR catalysts, which refers to the static pressure drop of gases moving through obstructions (monolith). The average pressure in the exhaust pipe during the exhaust stroke is meant as the exhaust pressure and the atmospheric pressure is the ambient pressure. The difference between these two pressures is commonly defined as exhaust backpressure. In other words, the exhaust backpressure can be defined as the resistance pressure imposed on the engine due to the resistance of the exhaust system in order to discharge the flow from engine to the outside ambient. In accordance with the terminology used in fluid dynamics, the use of the term as in experimental practice “monolith backpressure” in favor of “monolith pressure drop” should be avoided. An increase in exhaust backpressure decreases NO_x , due to the increased exhaust gas remaining in the cylinder. Excessive backpressure in the exhaust system creates overmuch heat (e.g. exhaust valves and turbine), lowers engine power output (0,3 kW of power per 10 mbar of pressure loss) and increases the fuel consumption, that may cause poor performance (e.g. reduced intake manifold boost pressure and cylinder scavenging) and damage of the engine parts (e.g. turbocharger problems – seals, increased pumping work etc.). Therefore backpressure in a certain level (specified by the engine manufacturer) contributes to the proper operation of the engine and reduces emissions [77].

7.1.1 Preparation of catalyst and coating

Extrusion is a process extensively used to shape ceramic monoliths with a honeycomb structure. A schematic diagram of the extrusion process is presented in Fig. 32. The crucial processing operations in extrusion are: paste preparation, extruding the paste through the die, drying and thermal treatment. To prepare a molding paste consisting of the porous powder,

inorganic and organic additives and solvent (e.g. water), a kneading machine is used. The molding paste must have a significant plasticity and have acceptable cohesion. To make the paste moldable with the necessary mechanical strength with the possibility of later cutting, some inorganic particulate binders are used such as aluminosilicates, alumina, silica, titania, zirconia or combinations of these components [98]. Typically, the main components of vanadium-based SCR catalysts are ammonium metavanadate (NH_4VO_3), colloidal silica with 10% WO_3/TiO_2 and optional pore building agent [45].

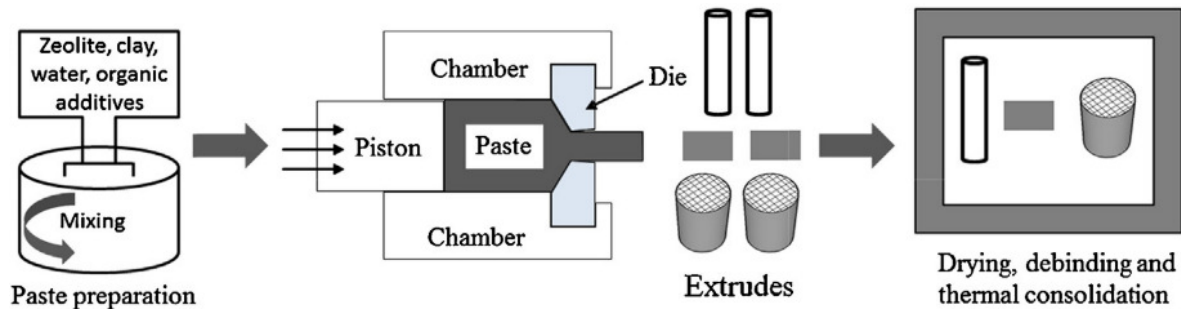


Fig. 32. Schematic diagram of the extrusion process [98]

Reprinted from *Journal of the European Ceramic Society*, Vol. 34, Akhtar F., Andersson L., Ogunwumi S., Hedin N., Bergström L., *Structuring adsorbents and catalysts by processing of porous powders*, 1643-1666, Copyright 2014, with permission from Elsevier.

The washcoating procedure, which is also called dip coating (Fig. 33) is impregnated from aqueous solutions. The method consists of dipping the substrate into a slurry of the catalyst (10-20 s) and subsequently withdrawing under controlled speed. This step is followed by blow-off excess suspension and gentle drying with hot air (90°C). The control of deposited catalyst (vanadia) must be carried out and the process is repeated as many times as necessary to achieve the desired loading on the substrate. Finally, the coated monolith is calcined (50h at 550°C) to achieve a thin catalyst layer adhered to the surface of the substrate [45], [59]. Other methods are also used such as impregnation, spray coating, precipitation, sol-gel, hydrothermal etc. [108].

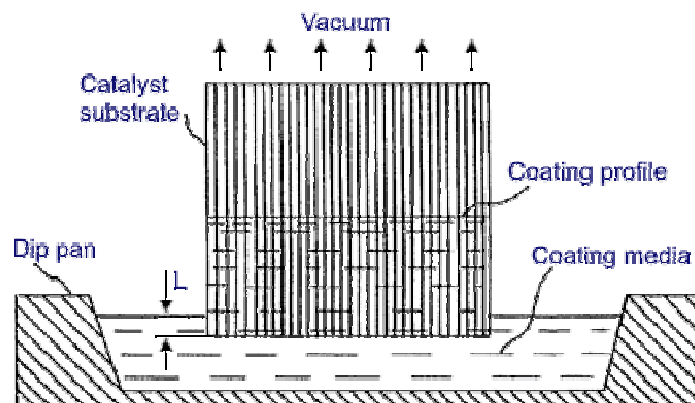


Fig. 33. Schematic representation of coating process [59]

Reproduced with permission from source: DieselNet.com

7.1.2 Vanadium-based catalyst

The Vanadia SCR catalyst consists of V_2O_5 (Vanadium pentoxide) as an active component and is usually impregnated on an anatase support TiO_2 (Titanium dioxide), which has large surface area and porous structure. It is often also used together with WO_3 (Tungsten trioxide) to stabilize V_2O_5/TiO_2 and increase thermal durability as well as to prohibit catalyst poisoning by SO_2 . V_2O_5 has high catalytic efficiency and economy at a given percentage [104]. Typical compositions are 1-3% V_2O_5 and about 10% WO_3 on the TiO_2 support. Kröcher et al. [45] advises to avoid more than 2% of V_2O_5 due to increased N_2O emission after ageing at $600^\circ C$. Most commercial SCR catalysts for mobile applications contain between 1.7 and 1.9 % V_2O_5 and it is better to increase cell density from 300 to 400 cpsi for De NO_x performance and enhance to capture the urea droplets in the catalyst than an increase of the vanadia concentration to 3% [45]. The active component is either washcoated onto an inert substrate or is extruded as well as produced in a way that the substrate walls contain active catalyst material throughout the entire wall. For mobile applications, common cell densities are 300 or 400 cpsi with the wall thickness from 4 mil (100 μm) to 8 mil (200 μm) and with the washcoat thickness from 20 to 100 μm [50].

The vanadia-based SCR catalysts typically have a temperature window of maximum NO_x conversion between ca. $250^\circ C$ and ca. $500^\circ C$. At low temperatures (before “light-off”), the reaction rate is low and hence there is low NO_x conversion. At higher temperatures above $500^\circ C$, the NO_x conversion is lowered due to oxidation of NH_3 by O_2 instead of reacting with NO and increased formation of N_2O [45], [50]. Increasing the V_2O_5 concentration increases the low-temperature activity of the SCR catalyst. However, this reduces the Specific Surface Area (SSA) of the catalyst washcoat material, for example 0.78 wt% of V_2O_5 has SSA 87 m^2/g while 3.56 wt% of V_2O_5 has SSA 64 m^2/g . Extension of the washcoat loading from 180 g/dm^3 to 540 g/dm^3 decreases the temperature for 70% NO_x conversion from 275 to $220^\circ C$ but this increases the washcoat thickness and leads to higher backpressure. Moreover at the same time, large pores lead to higher diffusion rate of reactants into the washcoat but reduce the specific surface area of the catalyst. A compromise is found for vanadia-based SCR catalysts and SSA should be about 75 m^2/g with pore sizes about 10 nm. It is also worth adding that the high content of vanadia promotes the phase transition of TiO_2 from anatase to rutile, which leads to lower thermal stability of the catalyst. Thus, addition of WO_3 or sometimes MoO_3 (Molybdenum trioxide) to V_2O_5/TiO_2 increases the activity of the catalyst

and enhances thermal durability of the catalyst by stabilizing the TiO₂ from phase transition (with WO₃, rutile formation is at 900°C instead at 700°C). The phase transformation leads to a loss of BET (Brunauer-Emmett-Teller) surface, which is related to describing specific surface area [45]. Thermal exposure of vanadia SCR catalysts lead to their thermal deactivation (loss in surface area of TiO₂ - sintering) with gradual loss in NO_x conversion and it can contribute to vanadia volatilization from catalysts [50].

To optimal sticking of the catalyst layer a colloidal silica is used as a binder, which results in a quaternary system V₂O₅/TiO₂-WO₃-SiO₂ [45]. Kobayashi et al. [105] found that the V₂O₅/TiO₂-SiO₂ catalyst with 10-20 mol% of SiO₂ shows higher activity than the pure TiO₂ catalyst and mentioned that the mixture of TiO₂ and SiO₂ oxides has a large BET surface area with good thermal stability as well as lower activity in oxidation of SO₂. Liu et al. [104] also describes that the introduction of Si into TiO₂ hindered phase transformation and enhanced both the number of acid sites (Brønsted acids) and oxidation properties, which improved deNO_x effectiveness. Numerous transition metals have been reported to be active in NO_x reduction, including TiO₂-supported V₂O₅, Fe₂O₃, CuO, MnO_x, and CeO_x catalysts. Among metal oxides, pure V₂O₅ or V₂O₅ supported by oxide carriers (Al₂O₃, SiO₂, ZrO₂, TiO₂ etc.) have been extensively investigated for improving the thermal stability of catalysts [10], [104].

The vanadia-based SCR catalysts are generally relatively resistant against sulphur poisoning [105]. However, at low-temperatures conditions they can be deactivated when running on high sulphur fuel due to blocking by sulphate species. Nonetheless, the formation of ammonium sulfate is a reversible process and above 350°C decomposition is noticeable. The hydrocarbon poisoning on vanadia-based SCR catalyst is less noticeable than zeolite-based SCR catalyst as well as oil poisonings [50].

The mechanism of the reaction over vanadia-based catalysts is most frequently represented by the Eley-Rideal or Langmuir-Hinshelwood mechanism. Li et al. [10] referred to the Topsøe mechanistic scheme shown in Fig. 34, that describes the reaction pathway of the adsorption of NH₃ on the Brønsted acidic sites (V⁵⁺ – OH) followed by activation of NH₃ via reaction at the redox sites (V⁵⁺ = O). The NH₃ is activated and can react with gaseous or weakly adsorbed NO, producing N₂ and H₂O [10].

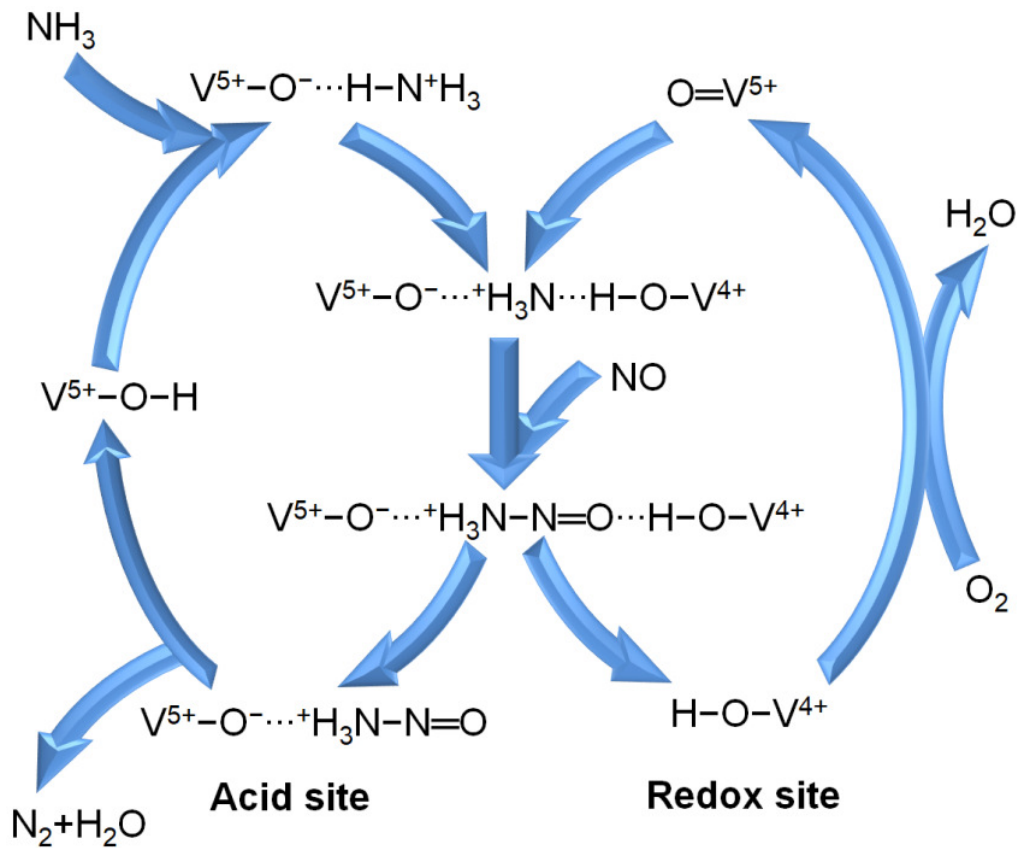


Fig. 34. Mechanistic cycle of the SCR reaction over the vanadium-based catalyst [10]

Adapted from *Front. Environ. Sci. Eng., The abatement of major pollutants in air and water by environmental catalysis*, Li J., He H., Hu C., Zhao J., Vol. 7, 2013; Copyright 2013, Higher Education Press and Springer-Verlag Berlin Heidelberg.

7.1.3 Cu-Zeolite catalyst

The zeolite-based catalyst with Cu (Cu-ZSM-5) shows better performance at lower (<300°C) and intermediate temperatures but its hydrothermal durability, high-temperatures activity and sulphur poisoning resistance are rather poor. Cu-ZSM-5 exhibits a strong oxidation potential that a considerable amount of N_2O are produced at higher temperatures but oxidizes much ammonia. Zeolite Socony Mobil-5 (ZSM-5) is an aluminosilicate zeolite and with Cu exhibit high NO decomposition rates and SCR activities but has poor hydrothermal stability because of dealumination and Cu migration [45]. Cu-ZSM-5 has medium-pores but recently, more and more are used with newer copper-exchanged small-pore zeolites with chabazite structure (Cu-SSZ-13/16 and silico-alumino-phosphate Cu-SAPO-34) [106], [108]. They showed higher NO_x conversion over a broad temperature range with higher hydrothermal stability. Qi et al. [106] shows that after hydrothermal treatment at 750°C the small-pore zeolites can still maintain the high SCR activity, while the Cu-ZSM-5 degrades significantly (Fig. 35).

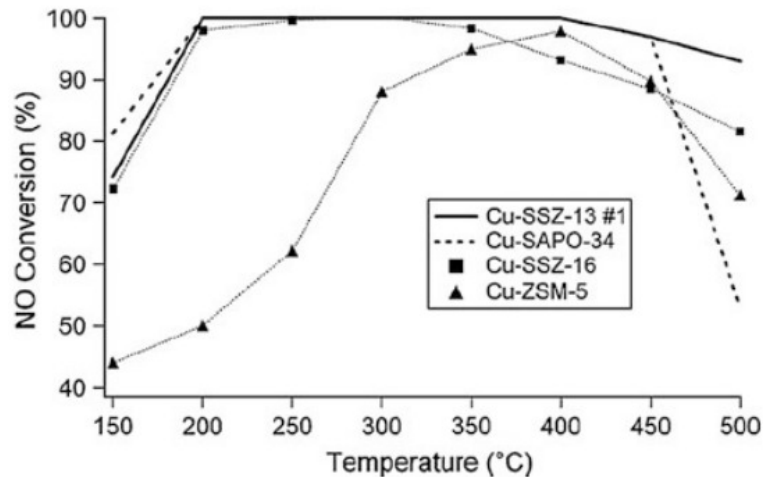


Fig. 35. SCR activity over the hydrothermally pretreated different copper zeolites [106]
 Republished with permission of Springer, from *Low-Temperature Selective Catalytic Reduction (SCR) of NO_x with NH₃ Over Zeolites and Metal Oxide-Based Catalysts and Recent Developments of H₂-SCR*, Qi G., Wang L., Yang R. T., in *Urea-SCR technology for deNO_x after treatment of diesel exhausts*, ed. Nova I., Tronconi E., ISBN 978-1-4899-8071-7, 2014; permission conveyed through Copyright Clearance Center, Inc.

In the mechanism of the reaction over copper zeolites (Fig. 36), the NH₃ is adsorbed on Cu²⁺, then this adsorbed NH₃ on the Cu²⁺ reacts with NO to form N₂ and H₂O, following this the Cu⁺ is re-oxidized to Cu²⁺ by O₂ [107].

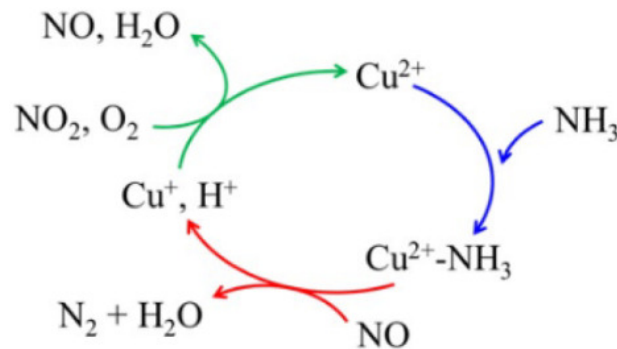


Fig. 36. Mechanism of the simplified copper redox cycle [107]
 Republished with permission of SAE International, from *Control Kinetic Modeling of Ammonia-SCR and Experimental Studies over Monolithic Cu-ZSM-5 Catalyst*, Eijima W., Shibata G., Kobashi Y., Koiwai R., Ogawa H., Shimizu K., Kusaka J., 2019-01-0024, 2019; permission conveyed through Copyright Clearance Center, Inc.

7.1.4 Fe-Zeolite catalyst

The zeolite-based catalyst with Fe (Fe-ZSM-5) shows better SCR performance at medium and higher temperatures (even over >550°C) and has better its hydrothermal durability and sulphur poisoning resistance than Cu-ZSM-5 [108]. Qi et al. [106] developed a new method for preparing the 2.5% Fe-ZSM-5 catalyst by the conventional incipient-wetness impregnation using NH₄-ZSM-5 and FeCl₂ (iron II chloride) as the iron precursor. The results of NO conversions show higher activities, especially in the lower temperature range

compared to other methods (aqueous ion-exchange) or precursors. It has also recently been proven that an Mn-Fe-ZSM-5 catalyst prepared by impregnation method demonstrated high deNO_x activity for SCR at low-temperature, however the manganese based catalysts have a willingness to be easily deactivated by SO₂ present in the exhaust gas, which is still a challenge [106].

If the ammonia is overdosed or at low and medium temperatures, the DeNO_x effectiveness is going down. It is caused by a competitive adsorption of ammonia on active Fe sites or due to the reduction Fe³⁺ to Fe²⁺. Fe-ZSM-5 has a low tendency for ammonia oxidation and N₂O formation at high temperatures and after ageing. However, Fe-ZSM-5 shows low activity at low temperature and tendency to produce N₂O at intermediate temperatures when only NO is in the feed [45]. Furthermore, in the middle temperature range, the dosed ammonia is consumed by the oxidation to nitrogen which requires a permanent overdosage of ammonia [109]. The Fe-zeolite is able to adsorb significant amount of ammonia (higher NH₃ storage capacity) compared to the vanadia-based catalyst (Fig. 37) and the storage capacity decreases on increasing the adsorption temperature [110].

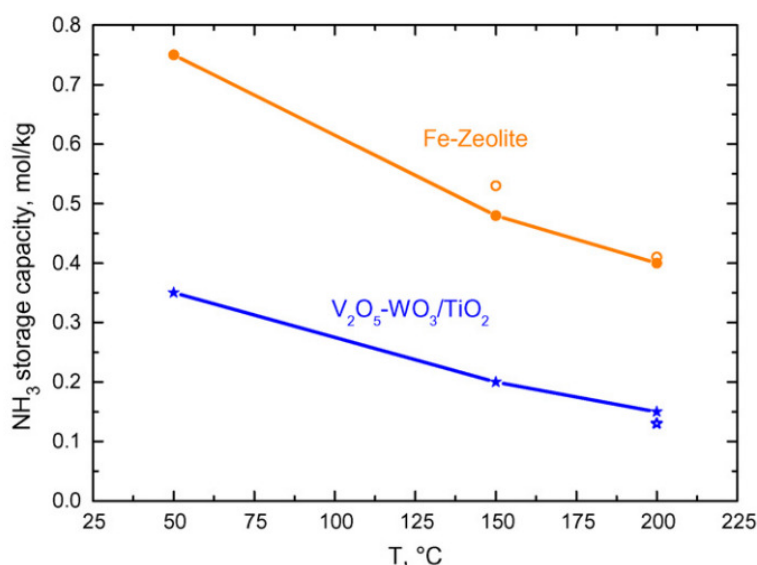


Fig. 37. Ammonia storage capacity of Fe-zeolite and vanadia-based catalyst [110]

Reprinted from Catalysis Today, Vol. 136, Grossale A., Nova I., Tronconi E., Study of a Fe-zeolite-based system as NH₃-SCR catalyst for diesel exhaust aftertreatment, 18-27, Copyright 2008, with permission from Elsevier.

Li et al. [10] mentioned that the Fe/HBEA (Zeolite beta, BEA) catalysts have been recently developed for SCR reaction and its possible mechanism is shown in Fig. 38. The NO and NH₃ adsorb and react on neighbouring Fe³⁺ sites and that NH₃ goes through several adsorption/desorption cycles on the substrate before adsorbing and reacting on the Fe³⁺ sites, which are lastly recycled by O₂.

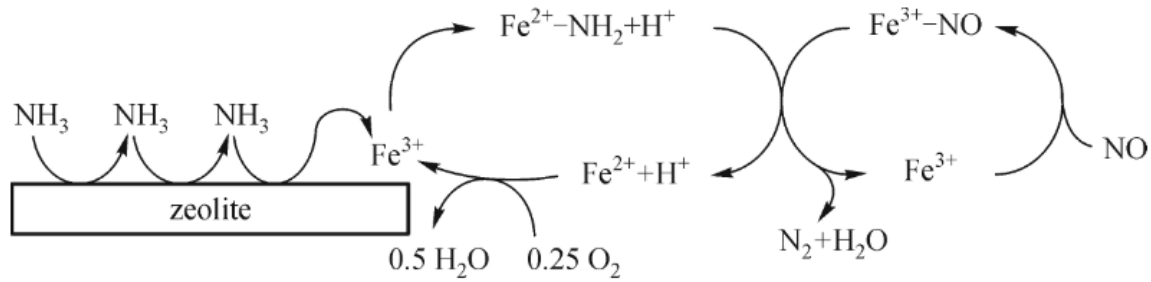


Fig. 38. Mechanism of the standard SCR reaction on Fe-zeolite [10]

Republished with permission of Springer, from *Front. Environ. Sci. Eng., The abatement of major pollutants in air and water by environmental catalysis*, Li J., He H., Hu C., Zhao J., Vol. 7, 2013; permission conveyed through Copyright Clearance Center, Inc.

7.2 Ageing, poisoning and deposit problem in SCR

The SCR catalysts in practical application must fulfil one of the main challenges which is their durability under hydrothermal conditions. Fe-ZSM-5 catalysts are very stable in the presence of H₂O, however above 500°C deactivation is always observed. At temperatures above 700°C, over 90% of Brønsted acidity is lost due to dealumination and the loss of surface area. Hydrothermal ageing has an effect on oxidation activity and the tendency of the metal species to cluster into metal oxide aggregates (metal ion migration), which promotes inactive metal-oxide particles [49]. Marberger et al. [112] conducted hydrothermal ageing at 600°C for 16 hours, for V₂O₅/WO₃-TiO₂ catalysts with different vanadia loading (Fig. 39).

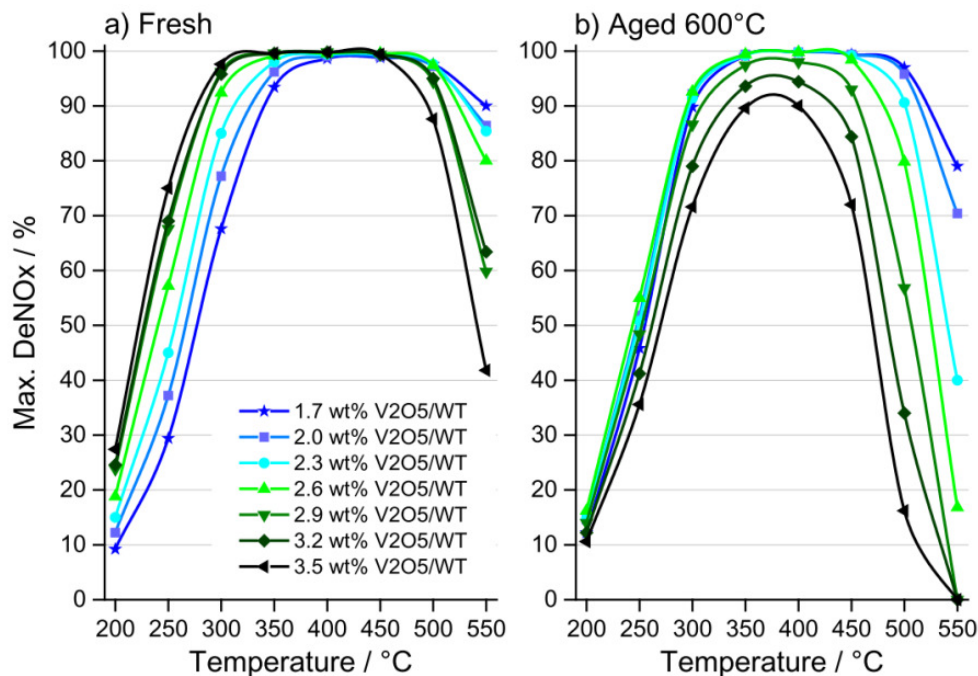


Fig. 39. NO_x reduction activity in the fresh (a) and aged state (b) [112]

Reprinted from *Catalysts*, Vol. 5, Marberger A., Elsener M., Ferri D., Kröcher O., An VO_x surface coverage optimization of V₂O₅/WO₃-TiO₂ SCR catalysts by variation of the v loading and by aging; The Authors copyright 2015, Licensee MDPI (CC BY 4.0).

For high V_2O_5 loading, the aged catalysts showed deactivation tendencies, however, below 300°C , the catalysts with loading up to 2.3% wt. of vanadium are more active than in the fresh state. Nonetheless, in the medium and high temperatures, the catalyst with high loading suffered from deactivation (low NO_x reduction) [112]. Xi et al. [111] carried out an ageing for 2 hour intervals with progressively increasing temperatures. Upon increasing the ageing temperatures, cracks are created within the washcoat and between the washcoat and substrate as shown in Fig. 40 by Scanning Electron Micrographs (SEM). The strength of adhesion between the washcoat and substrate decreased substantially and the TiO_2 phase changed from anatase to rutile. Moreover it was noticed that during increasing ageing temperature, the NH_3 storage capacity decreased due to the loss of acid sites of vanadia SCR catalyst as well as BET surface area (that leads to the formation of less active polymeric species and crystalline V_2O_5). Above 660°C , the vanadia SCR catalyst could be thermally damaged and above 630°C , the DeNO_x performance significantly decreases.

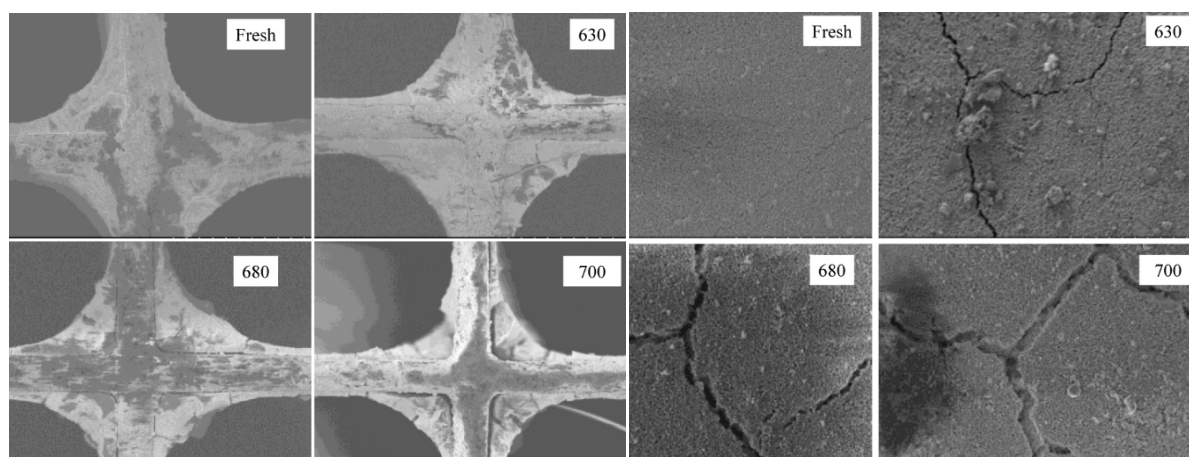


Fig. 40. SEM images along and perpendicular flow direction after ageing [111]

Republished with permission of SAE International, from *Effect of hydrothermal aging on the catalytic performance and morphology of a vanadia SCR catalyst*, Xi Y., Ottinger N. A., Liu Z. G., 2013-01-1079, 2013; permission conveyed through Copyright Clearance Center, Inc.

The next challenge for selective catalytic reduction catalysts is sulphur poisoning which is also a durability issue. Cu-SAPO-34 catalysts are sensitive to sulphur poisoning, even with ultra-low sulphur fuels, which can accumulate and decrease performance. Depending on temperature, a portion of SO_2 is oxidized to SO_3 and with water present a sulphuric acid (H_2SO_4) is formed [113]. Zhang et al. [113] showed that at low temperatures, the catalytic activity significantly decreased with addition of 50 ppm SO_2 . As shown in Fig. 41, the NO conversion dropped from 90% to 15% at 200°C . However, at temperatures above 300°C , there are no significant changes. It means that at higher temperatures Cu-SAPO-34 SCR catalyst is resistant to SO_2 and SO_3 poisoning. It should be added that the SO_2 poisoning

mechanism involves the formation of ammonium sulphate ($(\text{NH}_4)_2\text{SO}_4$) or ammonium bisulphate (NH_4HSO_4) according to Eq. (32) and Eq. (33), which may poison the active sites and block the pores.

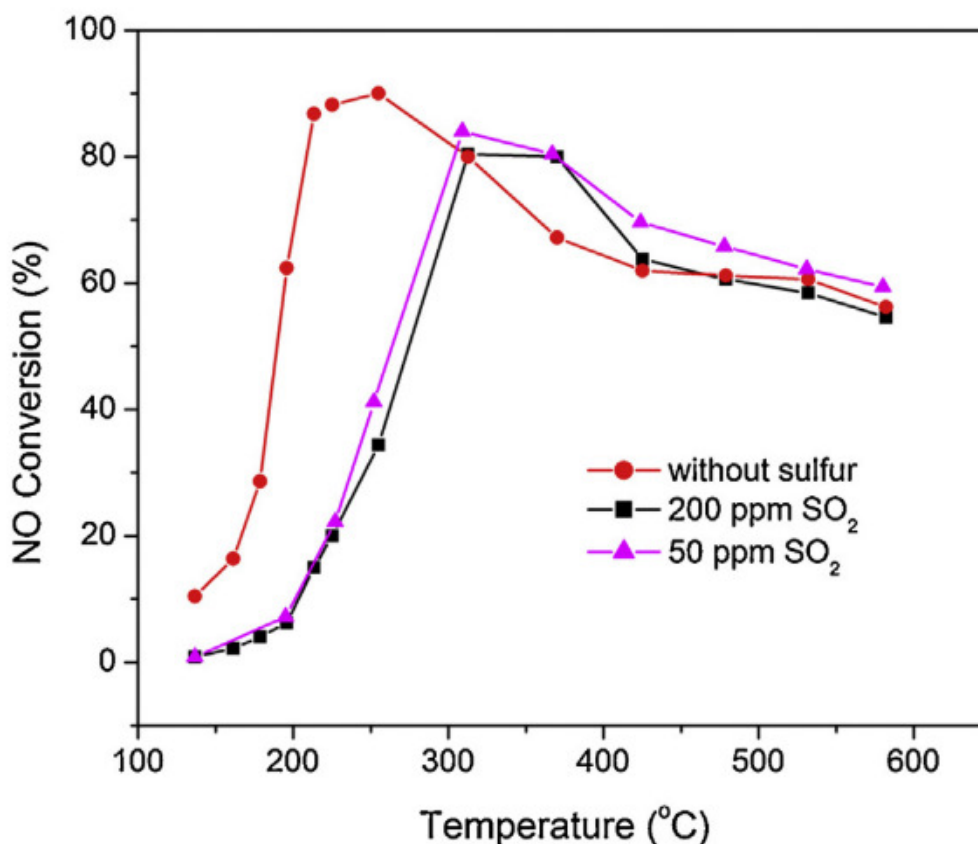


Fig. 41. SCR reaction activity with and without absence of SO_2 [113]

Reprinted from *Applied Catalysis B, Environmental*, Vol. 156-157, Zhang L., Wang D., Liu Y., Kamasamudram K., Li J., Epling W., *SO₂ poisoning impact on the NH₃-SCR reaction over a commercial Cu-SAPO-34 SCR catalyst*, 371-377, Copyright 2014, with permission from Elsevier.

The combination of metal sites with SO_x (SO_2/SO_3) can also result in simultaneously irreversible loss of active sites by forming metal sulphates [114]. Ma et al. [114] proved that for $\text{V}_2\text{O}_5\text{-WO}_3/\text{TiO}_2$ SCR catalyst, the NO conversion decreased slightly after introduction of SO_2 and was maintained at level of 85% at 250°C. However, with increased loading from of V_2O_5 from 1% to 3%, the resistance to SO_2 was improved. After the removal of SO_2 , the NO conversion could not recover to their initial levels, which indicates that SO_2 leads to an irreversible deactivation of the catalyst. In the $\text{V}_2\text{O}_5\text{-WO}_3/\text{TiO}_2$ SCR catalyst, the polymeric WO_x species result in less formation and deposition of $(\text{NH}_4)_2\text{SO}_4$, which can be quickly consumed via reaction with NO on more reactive V^{n+} sites. The formation process of metal sulphates from the reaction of SO_4^{2-} groups and gaseous SO_3 with Ti^{n+} sites is significantly blocked by WO_3 loading, leading to the superior resistance to SO_2 poisoning (Fig. 42).

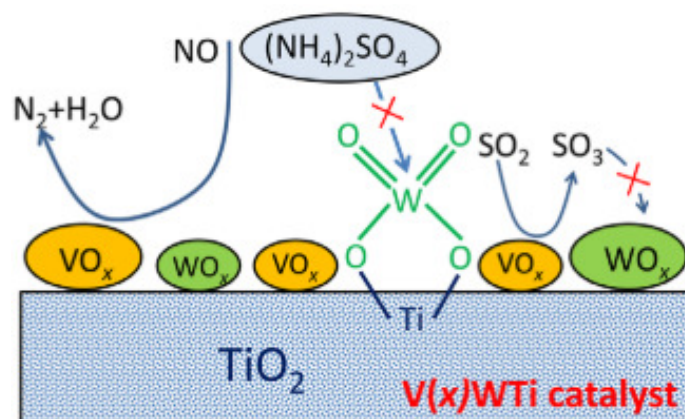


Fig. 42. The SO₂ deactivation mechanism over V₂O₅-WO₃/TiO₂ SCR catalysts [114]
 Reprinted from *Progress in Natural Science: Materials International*, Vol. 25, Ma Z., Wu X., Feng Y., Si Z., Weng D., Shi L., *Low-temperature SCR activity and SO₂ deactivation mechanism of Ce-modified V₂O₅-WO₃/TiO₂ catalyst*, Copyright 2015, with permission from Elsevier (CC BY NC ND).

Catalyst deactivation by SO₂ poisoning can be divided into three steps: (1) the adsorption of SO₂, (2) SO₂ oxidization to SO₃, and (3) the deposition of (NH₄)₂SO₄ / NH₄HSO₄ or the sulphation of active components. Han et al. [108] summarized (Fig. 43) the deactivation processes and the corresponding strategies for improving the poisoning resistance and the hydrothermal stability.

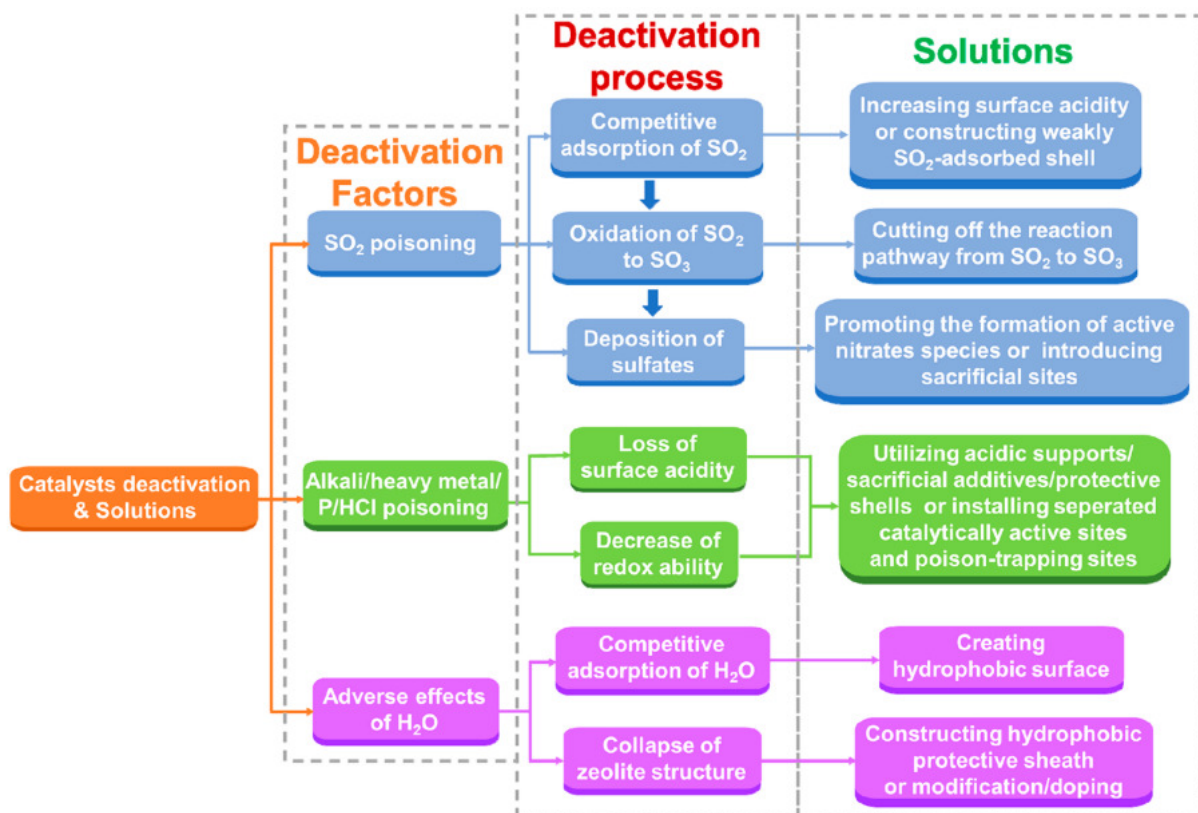


Fig. 43. Deactivation processes and the strategies for control them [108]
 Reprinted (adapted) with permission from *Selective Catalytic Reduction of NO_x with NH₃ by Using Novel Catalysts: State of the Art and Future Prospects*, Han L., Cai S., Gao M., Hasegawa J., Wang P., Zhang J., Shi L., Zhang D. Copyright 2019 American Chemical Society.

On the basis of above expected requirement, it is of significance to develop an eco-friendly SCR catalyst with a broad temperature window, good low temperature SO₂ and H₂O tolerance, strong high temperature hydrothermal stability and superior alkali, heavy metal, Phosphorus (P) and hydrochloric acid (HCl) [108].

Finally, deposit formation (Fig. 44) is one of the more serious problems in a selective catalytic reduction. Dosed in a short distance in front of the SCR reducing agent (AdBlue) should be a possibly short time to mix with exhaust gas and evaporate. Only an agent so prepared then undergoes the processes of thermolysis and hydrolysis, where as much volatile ammonia as possible should be released and its distribution on the SCR face should be as homogenous as possible. For this purpose, a mixer made of stainless steel is used in the space between the injection module and the SCR reactor, which does not increase the exhaust back pressure in the system too much [115].

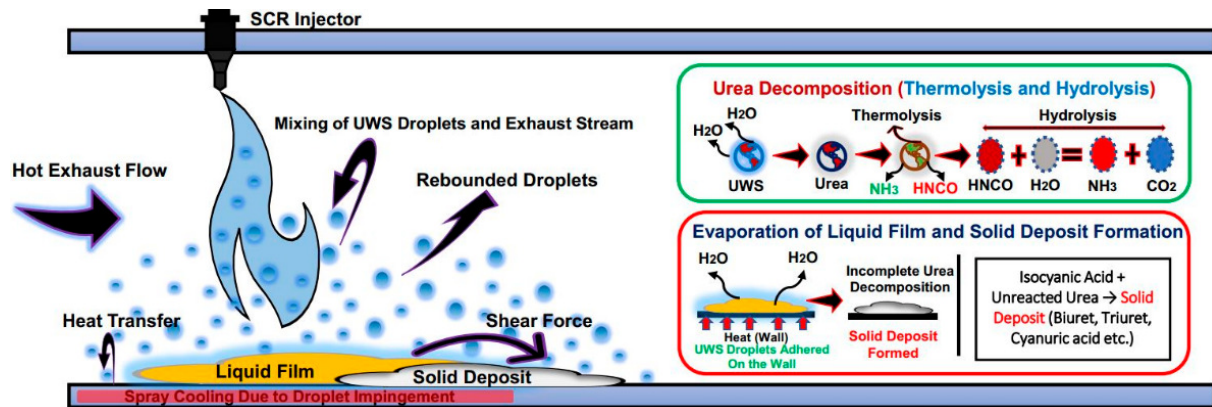


Fig. 44. Overall process from spray to deposit creation [117]

Reprinted from *Energies*, Vol. 12, Shahariar G. M. H., Lim O. T., *A study on urea-water solution spray-wall impingement process and solid deposit formation in urea-SCR de-NO_x system*; The Authors copyright 2018, Licensee MDPI (CC BY 4.0).

The function of the mixer is to break up the droplets of the urea solution spray, which on the one hand improves evaporation and mixing, and on the other hand contributes to reducing the formation of solid deposits causing blockage of the channels and deactivation of the monolith [115].

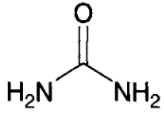
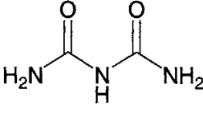
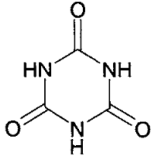
The commonly used reducing agent AdBlue is 32.5% eutectic urea in water. It is a non-flammable liquid that quickly decomposes in the environment, but reacts with some construction materials. The problem is to ensure the fluidity of the solution at low temperature, because below -11.5°C the solution crystallizes and the need to refill AdBlue (~0.1 L/100 km - for a 17 L tank, it is possible to travel 17 000 km, where 1 L costs approx. 0.45 €). A special heating system for the AdBlue tank should be provided, as well as a system for returning to the tank each time the engine is switched off, with both the supply lines and

the injection valve being empty. Another problem is the loss of AdBlue properties when exposed to temperatures above 40°C, as it begins to slowly decompose into ammonia and carbon dioxide. For this reason, the AdBlue tank is thermally insulated and additionally equipped with a relief valve, while the control system constantly monitors the temperature and pressure in the tank [115].

At low exhaust temperatures, a liquid layer of the medium forms on the supercooled surfaces, which then crystallizes after the water evaporates, forming a solid deposit. According to Zhentg et al. [119], the worst case scenario for deposit formation is when the exhaust gas temperature is low while NO_x level is high (low heat to decompose the large flow rate of urea). Sugimoto et al. [116] also mentions that deposits can form when urea fails to vaporize and instead remains as a liquid film (a precursor of deposit) on the mixing pipe, or when circulation of the exhaust gas flow results in high concentration of isocyanic acid (HNCO or CYA) created by the thermolysis of urea. The main components of deposits and conditions under which they form are shown in Tab. 5.

Tab. 5. Deposit composition and conditions for creation [116]

Adapted from Prediction for SCR systems performance using 3D CFD simulation: aiming at SCR development for various layouts, Sugimoto K.; Copyright 2017, YANMAR (OA).

Major component	Chemical formula	Reaction formula	Formation temperature
Solid urea		Urea water solution → solid urea + water	130°C or less
Biuret		HCO + urea → biuret	170 ÷ 190°C
Cyanuric acid		3HNCO → cyanuric acid	190°C or more

Other compounds also can form when these components (Tab. 5) react together (Fig. 45), such as triuret, ammelide, ammeline and melamine, which do not break down at high temperatures and there is a risk that these deposits will remain permanently [116], [117]. However, Lauer et al. [118] described that a complete elimination of solid products has been observed for temperatures above approximately 653 K for CYA, 873 K for ammelide and 973 K for ammeline. Deposit can be converted into ashes, be transported off the mixing section and be released into the environment, as mentioned also by Smith et al. [120].

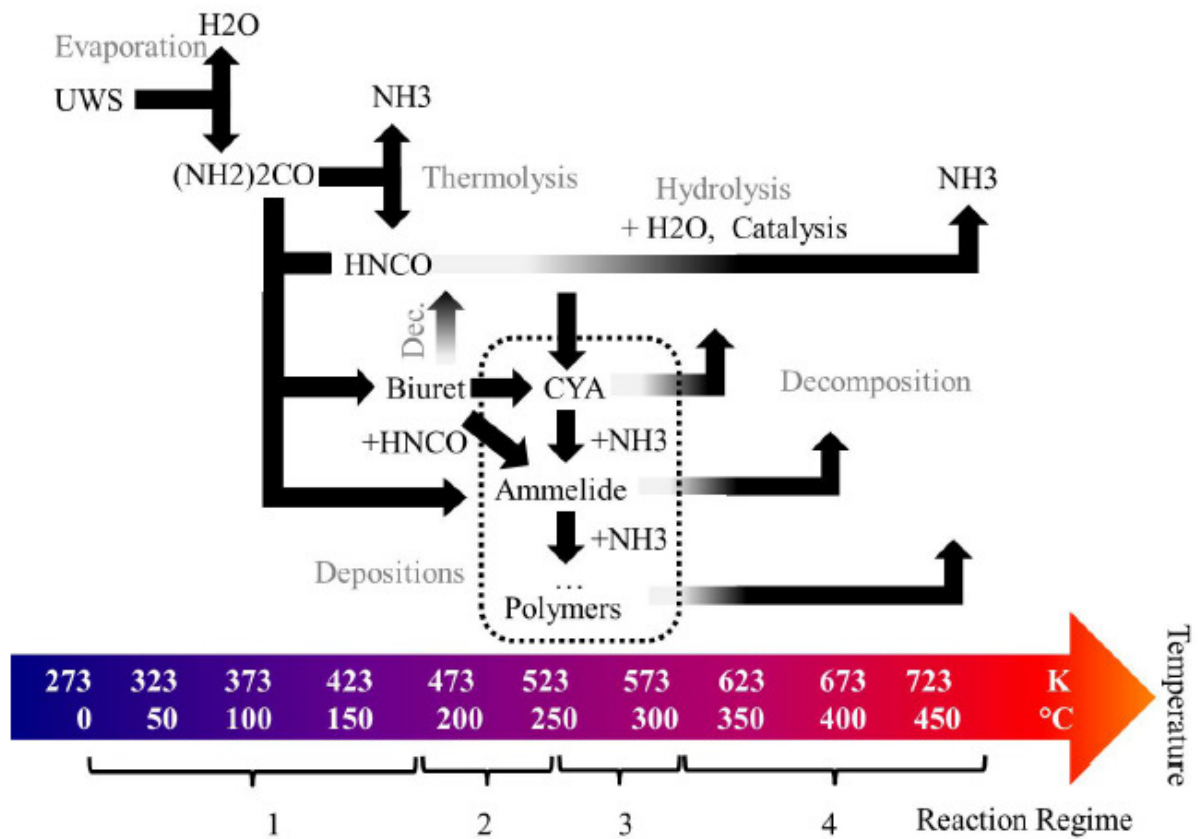


Fig. 45. UWS decomposition scheme including undesired deposit formation [129]
 Reprinted from *Simulation of the urea-water-solution preparation and ammonia-homogenization with a validated CFD-model for the optimization of automotive SCR-systems*, Fisher S.; The Author copyright 2012, (OA).

Deposits also form on the tip of the injector, the mixer surface, exhaust gas flow path (pipe) and the face of the SCR catalyst (Fig. 46).



Fig. 46. Deposit formation on the pipe, catalyst, injector and mixer [116], [120]
 Republished from *Prediction for SCR systems performance using 3D CFD simulation: aiming at SCR development for various layouts*, Sugimoto K.; Copyright 2017, YANMAR (OA).
 Republished with permission of SAE International, from *Optical and numerical investigations on the mechanisms of deposit formation in SCR systems*, Smith H., Lauer T., Mayer M., Pierson S., 2014-01-1563, 2014; permission conveyed through Copyright Clearance Center, Inc.

This phenomenon is, however, reversible and the solid urea decomposes under the influence of prolonged exposure to high temperature. The aim is to minimize the phenomena of deposit formation to such an extent that it does not have a negative impact on the assumed final

emission level and system functionality under various vehicle operating conditions. The factors having a direct impact on the formation of deposits are: the shape and geometry of the exhaust system, the degree of AdBlue mixing and evaporation in the exhaust gas, the dosing strategy - especially in transient states, and possible injector leaks [115]. Zheng et al. [119] also pointed out some important factors, which contribute to urea deposit formation (Tab. 6).

Tab. 6. Contributing factors to urea deposit formation [119]

Adapted from *Investigation of urea deposits in urea SCR systems for medium and heavy duty trucks*, Zheng G., Fila A., Kotrba A., Floyd R., 2010-01-1941; Copyright 2010, SEA International.

Type	Factor
Geometry	Pre-injector exhaust pipe design
	Injector mount geometry and type of injector
	Post-injector pipe design
	Mixer type, orientation and location
	SCR inlet exhaust pipe design
Engine	Engine conditions
Injector	Injector dosing strategy
	Injector spray characteristics (velocity, diameter, angle)
Insulation	Thermal retention and insulation (heat shield or air gap)
Control	Injector pulse width and frequency

It should be assumed that the most favorable conditions for this phenomenon are the phases of engine heating, long-term operation at low exhaust temperatures and continuous driving in an intensive urban cycle. In the systems used, the reducing agent AdBlue is fed to the exhaust system via an electronically controlled dosing injector, with an average dosing pressure of 5 bar. The amount of the injected dose of the agent is calculated in the ECU control unit as a function of such variables as: mass emission of nitrogen oxides, exhaust gas temperature, ratio of the mass flow of exhaust gases to the reactor volume (space velocity), NO_2/NO_x ratio and the mass of ammonia remaining in the catalyst. A complex problem is to determine the current mass of ammonia accumulated in the catalyst and to maintain such current saturation that ensures the maximum reduction of nitrogen oxides with the minimum possible ammonia emission after the catalyst (ammonia slip) [115].

7.3 Design and development of SCR mixers

A diagram of the best way to achieve the optimal NO_x aftertreatment system is presented in Fig. 47. The most important part of the development process flow is the initial engineering. It consists of the definition of goals (emission regulation, type of UWS, level of NO_x reduction and backpressure), quantifying inputs (engine emission data, allowable

packaging space and work cycle) and development of the initial design. The next step is simulation that allows the quick evaluation of designs without the additional costs associated with building hardware and running tests. After this step, hardware testing should be performed to evaluate NO_x reduction and deposit formation. Following a defined process will help to complete the NO_x aftertreatment system, meeting the emission certification and saving time, effort and money [78], [127].

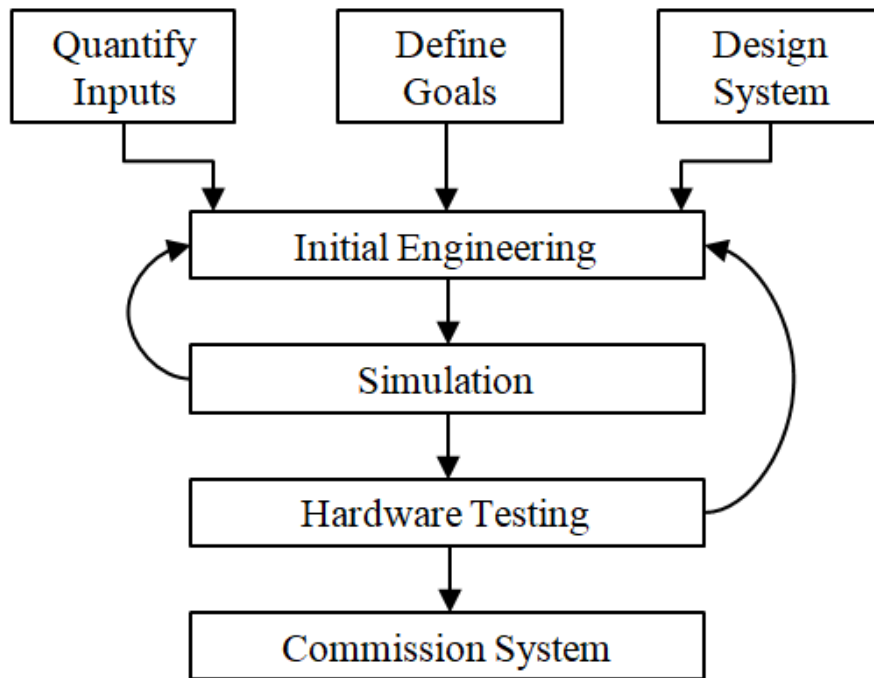


Fig. 47. SCR development process flow [127]

Adapted from DEF systems and aftertreatment architecture considerations, Floyd R., Michael L., Shaikh Z., in Urea-SCR technology for deNO_x after treatment of diesel exhausts, ed. Nova I., Tronconi E., ISBN 978-1-4899-8071-7, 2014; Copyright 2014, Springer.

Focusing attention on the process of designing a mixer (Fig. 48), many parameters affect the performance of a mixer such as tube diameter, injector types, injector mounting angle, exhaust flow direction, mass flow rate, temperature, mixing length etc. As mentioned in the study of Zheng et al. [100], it is unrealistic to expect a mixer to perform well in all applications without carefully tuning it to a given exhaust environment. Therefore, the development cycle starts with a new 3D concept through CFD (pressure drop and uniformity of flow) then prototypes and laboratory tests are initiated to confirm analytical results. Finally, deposit and durability are studied and eventually final changes are introduced [78], [100].

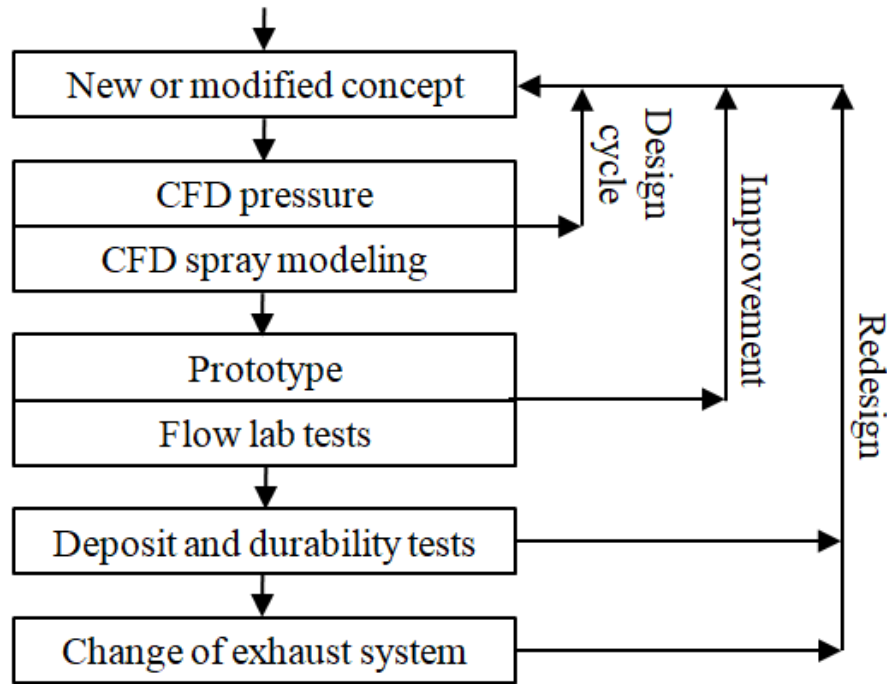
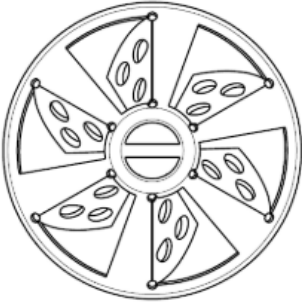
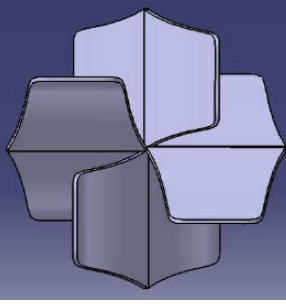
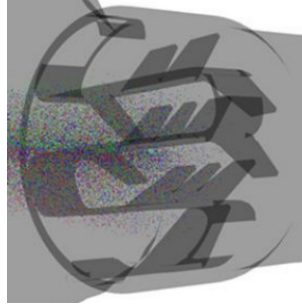
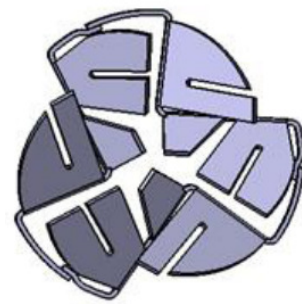
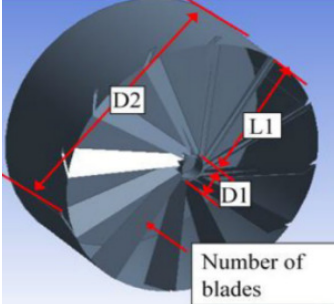
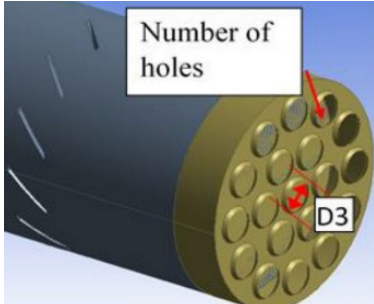
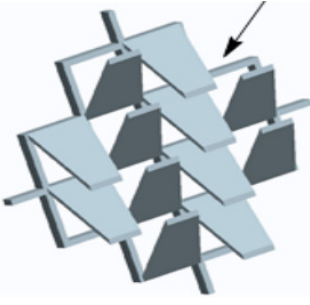
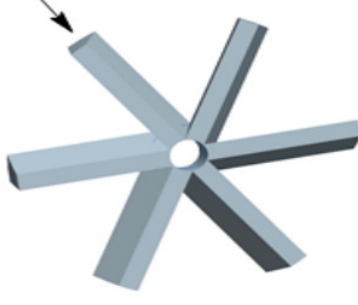
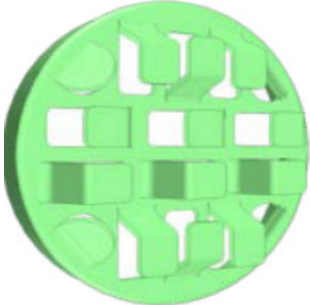
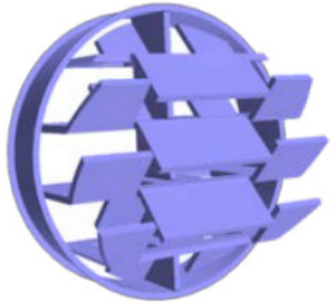


Fig. 48. Mixer development process flow [100]

Adapted from *Mixer development for urea SCR applications*, Zheng G., Palmer G., Salanta G., Kotrba A., 2009-01-2879; Copyright 2009, SEA International.

The proper mixer selection and location (by optimizations) can lead to improving the velocity and uniformity flow of gases on the inlet of SCR catalyst, so that the usable surface of the catalyst is as large as possible. Without accurate distribution, the SCR system increases urea-water solution consumption, decreases NO_x reduction as well as increases NH₃ slip. The trade-off between mixing efficiency and backpressure is also a key factor in designing because higher mixing efficiency generates higher backpressure (some moderate backpressure penalty is tolerated to deliver mixer performance [89]). The mixer needs to be placed in a location where the performance will be as good as possible under all of the operating conditions [127]. Zheng et al. [119] proved experimentally that “good” SCR systems with optimized urea mixing and low back pressure can be for a straight pipe with 45 degree injector mounting or S-bent pipe with 90 degree injector mounting (coaxial). The mixer improves droplet evaporation, breakup and distribution of the spray. As already mentioned in the earlier section, mixers are quite effective in reducing deposits. In summary, mixers must have the possibility of strong turbulence to force cold and hot streams and mix them. Moreover, mixers need to mix liquid droplets as well as have the functionality of evaporating liquid droplets and mix them with gaseous streams [100]. Tab. 7 shows the most common designs of static mixers which are installed in SCR systems.

Tab. 7. Examples of static mixers

		
2-Stage mixer [100]	Cone mixer [100]	Cone mixer [100]
		
Butterfly mixer [100]	Mixer [125]	Mixer [123]
		
Double mixer (fan + perforation) [121]	Flapper-style mixer [122]	
		
Line type mixer [80]	Swirl type mixer [80]	Mixer VW (Eberspächer) [126]
		
Different mixers designs [124]		

- [80] Reprinted from *Processes*, Vol. 7, Mehdi G., Zhou S., Zhu Y., Shah A. H., Chand K., *Numerical Investigation of SCR Mixer Design Optimization for Improved Performance*; The Authors copyright 2019, Licensee MDPI (CC BY 4.0).
- [100] Republished with permission of SAE International, from *Mixer development for urea SCR applications*, Zheng G., Palmer G., Salanta G., Kotrba A., 2009-01-2879, 2009; permission conveyed through Copyright Clearance Center, Inc.
- [121] Republished with permission of SAE International, from *Design optimization of urea injectors and mixers in a compact SCR system*, Praveena V., Jesu M. L., 2018-28-0025, 2018; permission conveyed through Copyright Clearance Center, Inc.
- [122] Republished with permission of SAE International, from *3D-semi 1D coupling for a complete simulation of an SCR system*, Abidin Z., Das K., Roberts C., 2013-01-1575, 2013; permission conveyed through Copyright Clearance Center, Inc.
- [123] Reprinted from *Indian Journal of Science and Technology*, Vol. 9, Choe M., Choi D., *Study of the optimization of the SCR catalyst position in by exhaust system of using mixer*; The Authors copyright 2016 (CC BY 4.0).
- [124] Reprinted from *IJISET*, Vol. 4, Rajadurai S., Sukumaran S., *NO_x aftertreatment using urea SCR for Tier 4 final application*; The Authors copyright 2017 (CC BY 4.0).
- [125] Reprinted from *Journal of Materials Science & Nanotechnology*, Vol. 6, Habchi C., Nicolle A., Gillet N., *Numerical study of deposits formation in SCR systems using urea-water solution injection*; The Authors copyright 2018 (CC BY 4.0).
- [126] Reprinted from *Journal of KONES*, Vol. 18, Brzeżański M., *Diesel engines with respect to Euro 6 and Bin5/Lev II emission limits*; The Authors copyright 2018 (CC BY 4.0).

8 Methodology and research design

In order to validate the physic-chemical phenomena in the SCR system for CFD simulation, it was necessary to perform experimental tests. The subject of the research was the SCR system with the reference number for the original 3AA254400AX. This part is dedicated to the VW Passat (B7, facelift) 2.0 BlueTDI 103kW (140 PS or 138 hp at 4200 rpm and 320 Nm at 1750-2500 rpm), which was produced between 2010-2014, however already compliant with the Euro 6b emission standard for diesel engine code CFFB (Fig. 49).



Fig. 49. Car with the tested SCR system [130]
Reproduced from source: <https://de.motor1.com>

The Fig. 50 shows in a simplified way the engine of this car with the exhaust gas aftertreatment system and their accessories while Fig. 51 is a real representation. It should be noted here that the diesel oxidation catalyst (DOC) and diesel particulate filter (DPF) are in one unit and were not taken into account in the validation process - only the SCR catalyst.

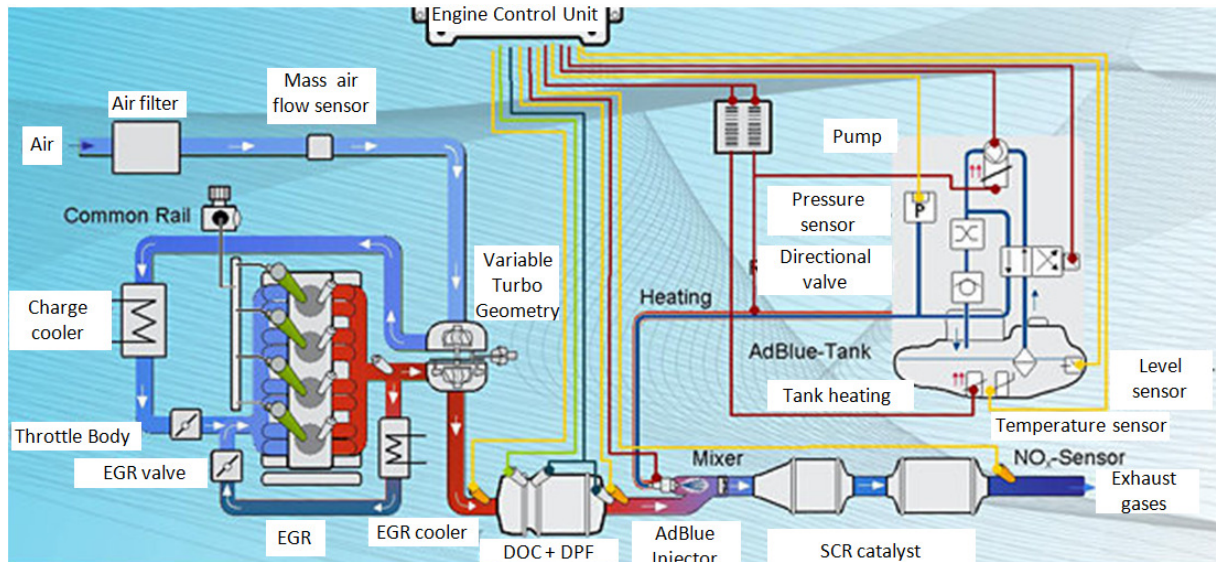


Fig. 50. Scheme of the exhaust gas aftertreatment system for a dedicated car [130]
Adapted from source: <https://de.motor1.com>

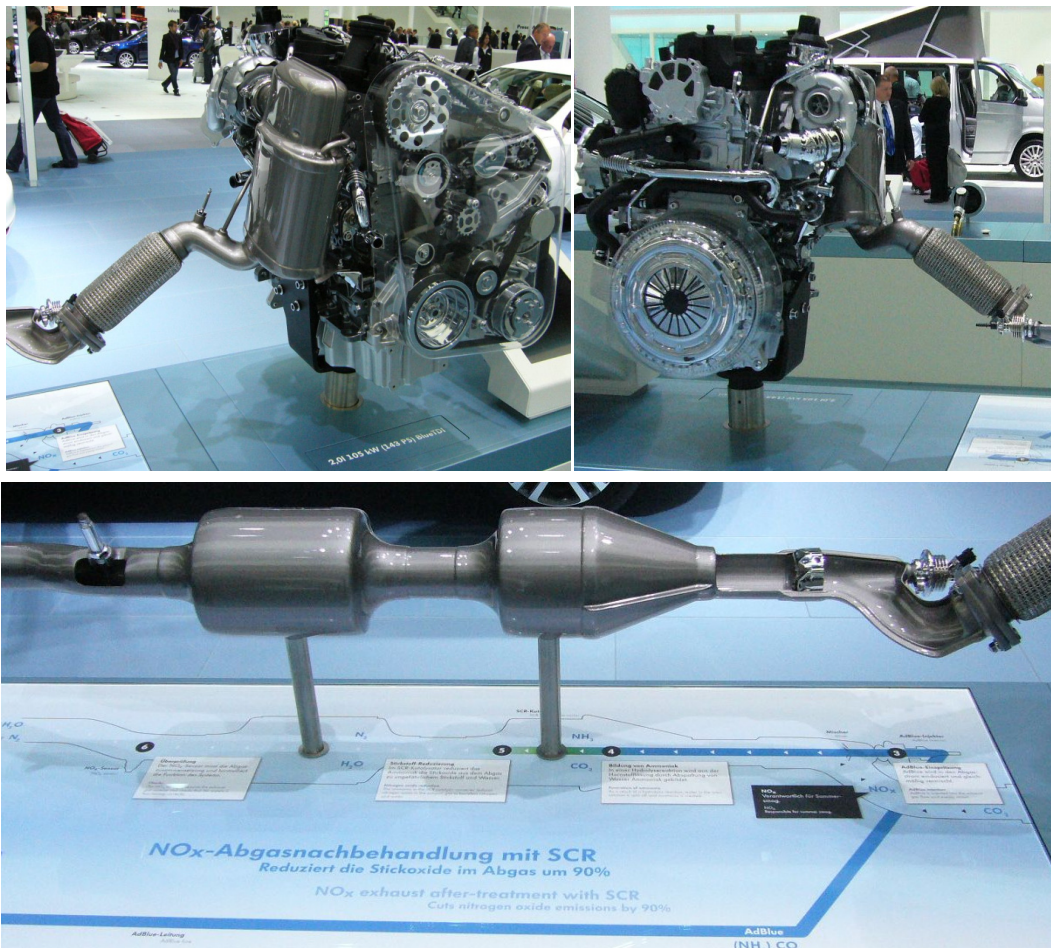
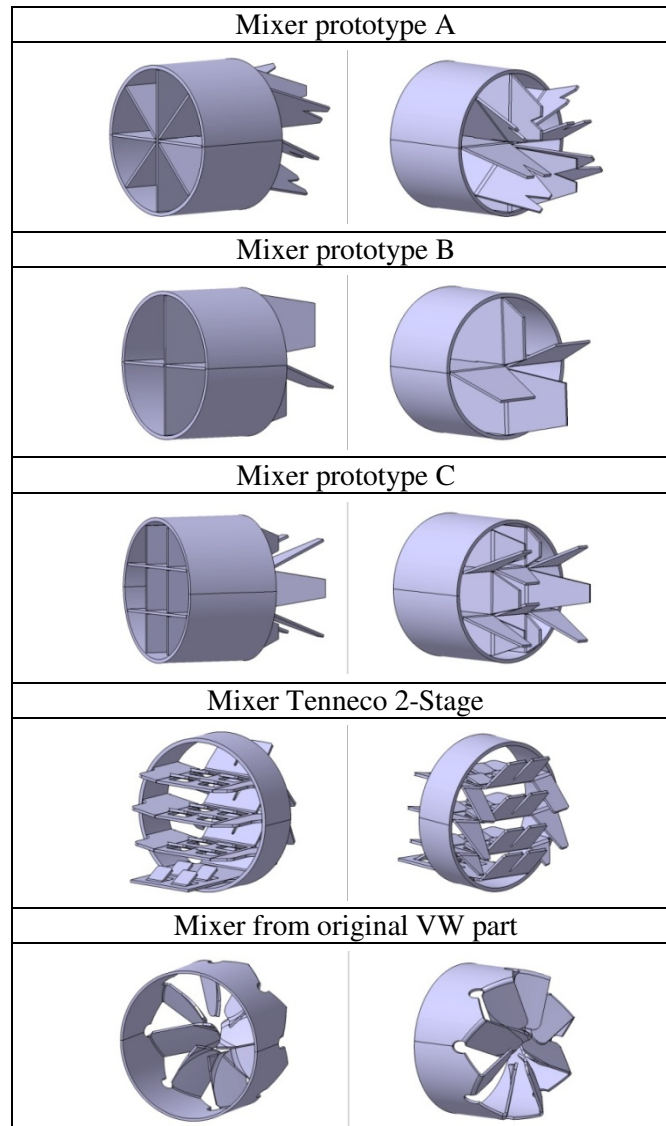


Fig. 51. Engine and aftertreatment system unveiled at the motor show
Private images used courtesy of Prof. Marek Brzeźański

The SCR system was examined with three proposed (prototype A/B/C) mixers. Concepts of mixers were planned for easy assembly (without the use of expensive tools) and

universal operation. For comparative purposes (e.g. the flow parameters and various degrees of UWS mixing), the Tenneco “2-Stage” mixer with 45° wings was also tested, which is an approved solution (patented) and adapted in a wide range of Tenneco products. Moreover, the mentioned mixers have also been compared with the original mixer from the VW SCR system, which is a product of Eberspächer. All described mixers are shown in the Tab. 8.

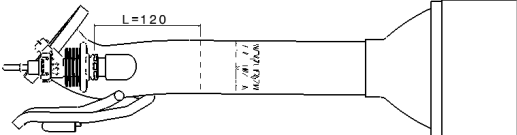
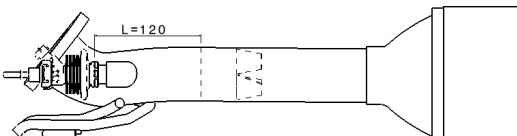
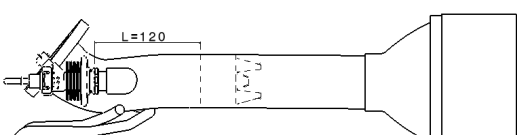
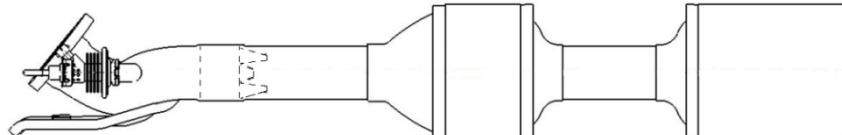
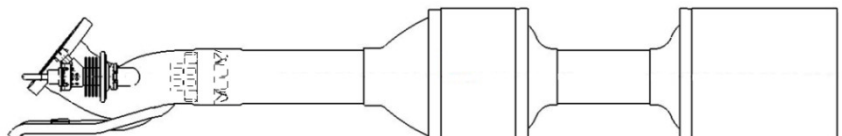
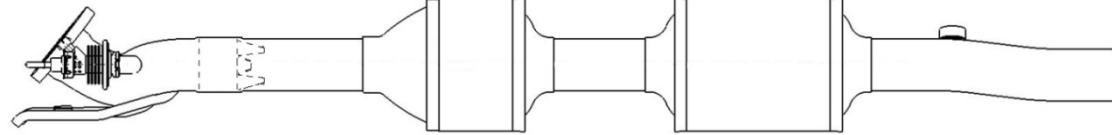
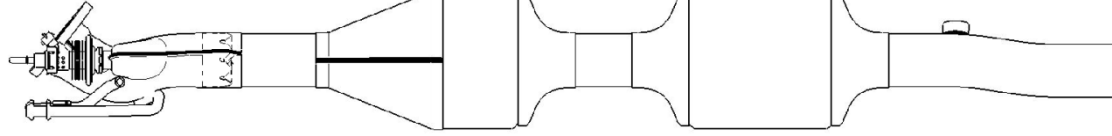
Tab. 8. Tested static mixers



The pressure drops (flow tests), flow distribution and conversion of NO_x (rig tests) within the SCR catalysts were tested in Tenneco research laboratories. Descriptions of the laboratory test equipment, setting conditions and results are presented in separate chapters. The measurements were divided into several stages, as presented in the Tab. 9. First, tests were performed for the front box (catalyst) only to check the impact of the prototype mixers’ design on the quality of mixing exhaust gases with urea solution. In two of the studied cases,

the mixing effect of the distance from the injector to the mixer, and the angle of the mixer were checked. Then the rear part (catalyst) was added and the best mixer prototype was compared with the Tenneco 2-Stage mixer. In the final stage the operation of the complete SCR prototype was compared with the operation of the original SCR part. Prototypes have been physically prepared by the Tenneco prototype shop.

Tab. 9. Investigated cases

Case 1: Prototype with mixer A; injector-mixer distance $L=120\text{mm}$ & moved to $L=155\text{mm}$

Case 2: Prototype with mixer B; injector-mixer distance $L=120\text{mm}$

Case 3: Prototype with mixer C; injector-mixer distance $L=120\text{mm}$ & rotated by 90°

Case 4: Prototype with mixer C (1 st and 2 nd box)

Case 5: Prototype with mixer Tenneco 2-Stage (1 st and 2 nd box)

Case 6: Prototype with mixer C (complete part) / with low & high loading

Case 7: Original VW part and mixer (complete part)


The tested prototypes have a vanadium catalyst as the active component impregnated and supported on an anatase and silica (V_2O_5/TiO_2-SiO_2). In turn, the original SCR system had Cu-zeolite [126]. Detailed information about the geometrical and chemical properties of SCR monoliths for all cases are in Tab. 10 in which the designation of the main geometric parameters of the monolith have already been presented in Fig. 31.

In addition, two complete WALKER prototypes were prepared for emission tests in the certification unit (TÜV SÜD Product Service GmbH) with different loadings. One with a low loading of the active (Vanadium) site and the second with higher. For example, in Tab. 10 if the low loading (row 1 and 2) had a weight of washcoat and active site (Vanadium) 215 g/dm^3 , then the 3 wt% V_2O_5 weighted 6.5 g/dm^3 (183.6 g/ft^3) and for high loading (260 g/dm^3) it was 7.8 g/dm^3 (220.3 g/ft^3) for rows 3 and 4 respectively. The impact of these loadings have been investigated during emission tests (NEDC cycle) on the chassis dynamometer with a real dedicated car for this SCR system.

Tab. 10. Geometrical and chemical properties of SCR monoliths

Part	Box	$D_m \times L_m$ [inch]	CPSI $\left[\frac{1}{inch^2}\right]$	t_w [mm]	δ_w [μm]	Type of catalyst	Weight of washcoat & active site	% of active side in monolith
Proto with low loading	Front	5.66 x 3	300	0.23	110	V_2O_5/SiO_2-TiO_2	215 g/dm^3 (3 wt% V_2O_5)	1.36
	Rear	5.66 x 6	300	0.23	110	V_2O_5/SiO_2-TiO_2	215 g/dm^3 (3 wt% V_2O_5)	1.36
Proto with high loading	Front	5.66 x 3	300	0.23	130	V_2O_5/SiO_2-TiO_2	260 g/dm^3 (3 wt% V_2O_5)	1.60
	Rear	5.66 x 6	300	0.23	130	V_2O_5/SiO_2-TiO_2	260 g/dm^3 (3 wt% V_2O_5)	1.60
Original VW part	Front	5.66 x 3	N/A	N/A	N/A	Cu-ZSM-5	N/A	N/A
	Rear	5.66 x 6	N/A	N/A	N/A	Cu-ZSM-5	N/A	N/A

The 3D models of SCR systems for CFD simulations have been prepared on the basis of a reverse engineering (subsection 9.4). The CFD numerical model was developed by means of commercial ANSYS Fluent CFD software. Models of each part of the SCR system (injection, mixers, catalysts) were developed and validated based on the available experimental data. The validated model was then used to find an improved design of the system elements. Tab. 11 summarizes the cases and studies performed.

Tab. 11. The scope of research for individual cases

Case (Tab. 9)	Experimental flow tests in laboratory	Experimental rig tests in laboratory	CFD simulations	Emission tests in the certification unit
1-5	YES	YES	YES	NO
6-7	YES	YES	YES	YES

9 Experimental research

This chapter presents the experimental tests that were carried out for the validation of the model for CFD numerical simulations. First, prototypes of the SCR system were built at the prototype shop in Tenneco Automotive Iberica located in Valencia. On the basis of the prototype drawings (simplified in Tab. 9) and the purchased original part, a fixture (Fig. 52) was built. The fixture allows the geometry of the original part to be reproduced with the help of various bases that are important in terms of the correct installation of parts under the car.



Fig. 52. Fixture in the phase of construction of a prototype of the SCR

The prepared prototypes were then sent to the laboratory for flow tests at Tenneco Automotive Polska in Rybnik. At this stage, the pressure drops were checked for all parts. Meanwhile, at Tenneco Silesia in Stanowice, all parts were scanned with a 3D laser arm in order to recreate their geometry for the purposes of reverse engineering and then CFD numerical simulations.

Subsequently, the parts were sent to Tenneco Automotive Germany in Edenkoben for flow rig tests in the laboratory. The flow distribution and conversion of NO_x within the SCR catalysts were investigated. After these tests, the SCR monolith from one prototype was checked for chemical composition at Łukasiewicz Research Network - Institute for Ferrous Metallurgy in Gliwice.

9.1 Flow tests in laboratory conditions

Experimental measurements for pressure drops were made in the laboratory (flow lab) test facility at Tenneco Automotive Polska in Rybnik. As mentioned in chapter 7.1, the tested pressure drop in SCR catalysts refers to the static pressure drop of gases moving through obstructions (e.g. monolith). In experimental practice, there is also talk about backpressure of an exhaust system which is the result of gas flow (from combustion in an engine) and flow resistance (in the exhaust pipes, catalytic converter, DPF, SCR, muffler etc.) as shown in the Fig. 53.

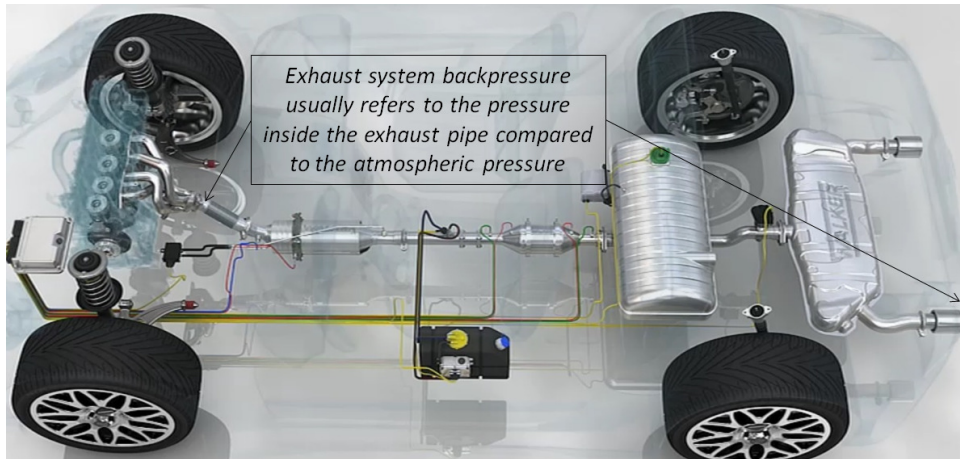


Fig. 53. Exhaust system backpressure [60]

Reproduced from Tenneco EMEA, Technical Advanced Digital Information System (TADIS): Emission control (<https://ta.garagegurus-eu.info/tadis/tadis-html-en/>), Copyright 2022, Tenneco Inc.

The test stand, presented in Fig. 54, consisted of a feed tube with thermal mass flowmeter (ABB Sensyflow FMT700-P) of air inflow (in 8 growing values (60-580 kg/h) at 23°C) and micro manometer (for static pressure) installed on the inlet side. In addition, the stand also allows measuring the temperature of air at the inlet of the feed tube and ambient temperature and pressure. The results were collected on a computer in Excel files through the LabVIEW software and input module (NI PXIe-1062Q).

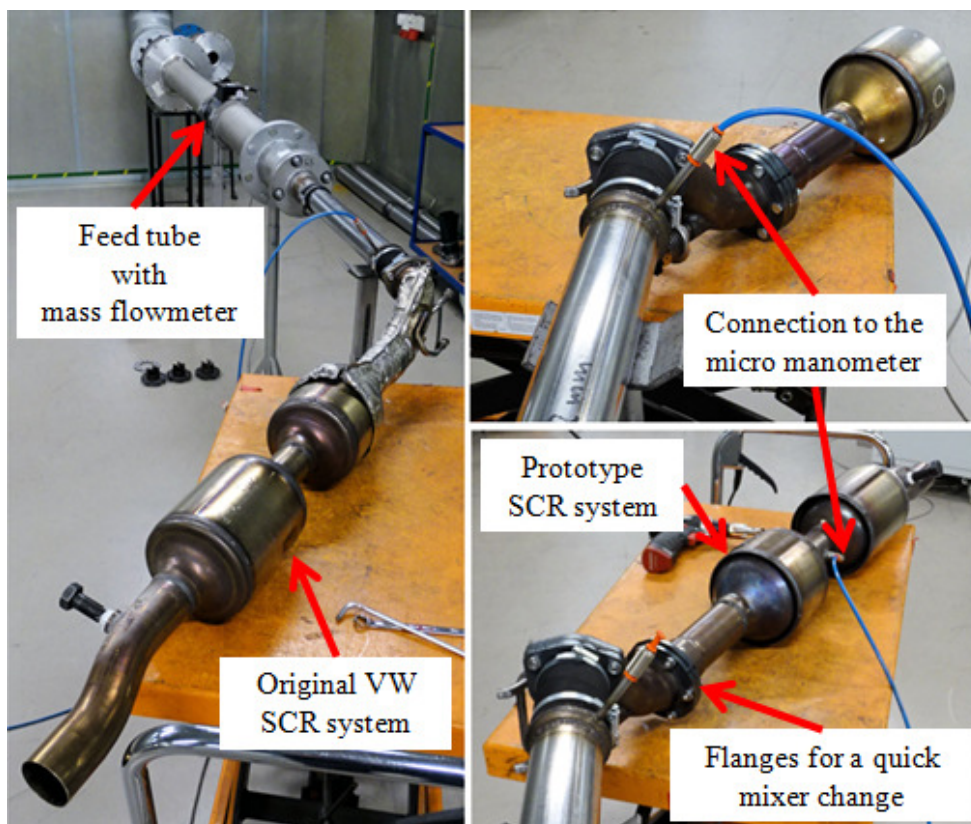


Fig. 54. Measurement of pressure drops: original part (left), prototypes (right)

9.1.1 Results for flow tests

The tested prototype was equipped with flanges that connected the mixer to the pipes. It was therefore possible to quickly adapt the prototype to another mixer. The pressure drops for the investigated cases (at the inlet and between the boxes) as well as for prototype mixers were collected and used for calculating the coefficients (viscous and inertial resistance) for the CFD porous model. In the plot (Fig. 55) there are differences in pressure drops for tested prototype mixers for Case 1-3 and a reference case without mixer. The quoted quadratic polynomial equation has been used for mentioned coefficients of the CFD porous model, only for the first monolith and Cases 1-3.

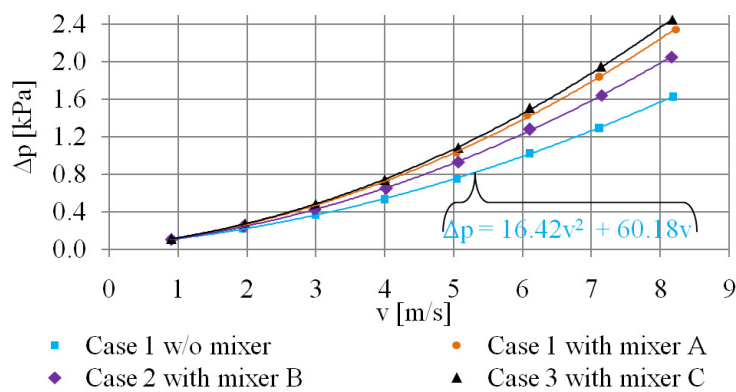


Fig. 55. Results of pressure drops for Case 1-3

Afterwards the pressure drops for Case 6 were tested on the inlet and between boxes without mixer and with mixer C for a comparison of the complete prototype with the original part. For the original part (Case 7), the pressure drop was tested only at the inlet side in order not to mechanically interfere (welding the connecting stub) into the pipe between the boxes. The construction of the original mixer (Fig. 56) was also checked with an endoscope (IPLEX NX).



Fig. 56. Endoscopic photo of the original mixer

In the plot (Fig. 57) a comparison of results of pressure drops for Case 6 and Case 7 can be seen. The red dotted line means that the value of backpressure for replacement part shall not

exceed the value of the original part by more than 25 % according to directive 70/157/EEC which has been met.

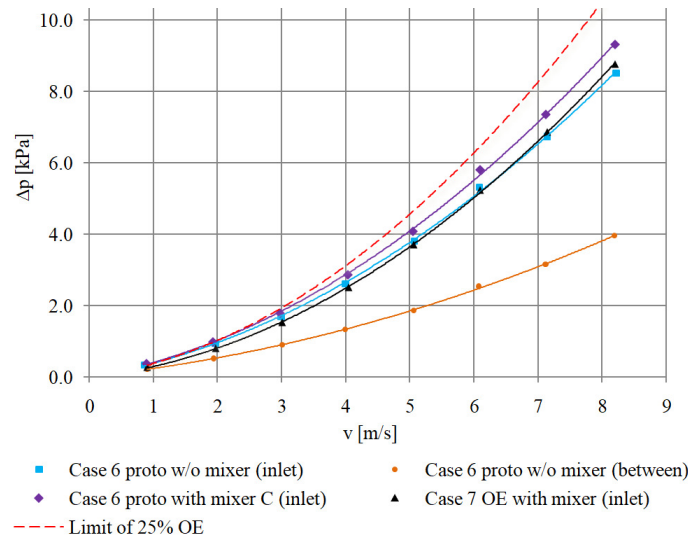


Fig. 57. Results of pressure drops for Case 6-7

On the basis of results from Fig. 57, the pressure drops on individual monoliths were determined. Measurement between boxes for part without a mixer (Case 6) allowed to determine the pressure drop for the second monolith (Fig. 58). The difference between the inlet measurements and that between boxes established the pressure drop for the first monolith. For the original part, a similar pressure drop for the second monolith was assumed as for the prototype part due to the lack of measurement between boxes. The results prepared in this way allowed to determine the quadratic polynomial equation for each monolith separately for the CFD porous model. For Case 4 and 5, the same calculated data was also assumed.

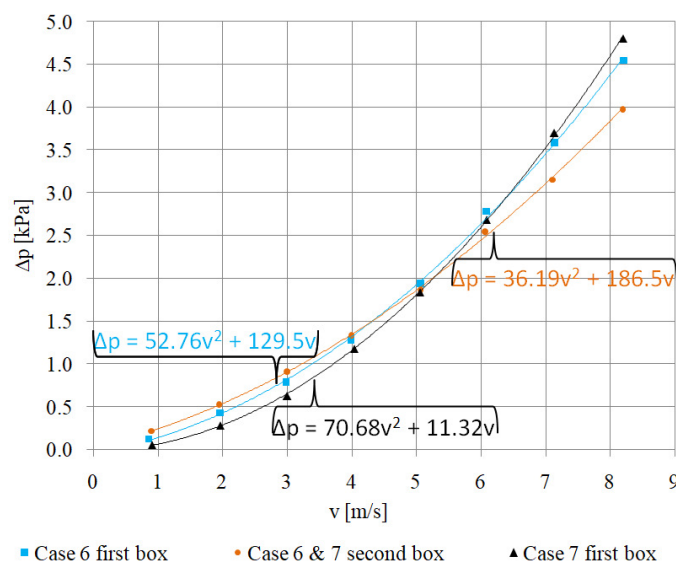


Fig. 58. Results of pressure drops for individual boxes

9.2 Flow rig tests of NO_x reduction in laboratory conditions

Another test stand (Fig. 59), was used to study the velocity distribution at the monolith's outlet surface (Fig. 60). The construction of the X-Y platform allows for automatic scanning of the entire cross-section area with a resolution of 137 sampling points (with 10 mm grid size, 5 Hz sample frequency, 15 s leadoff time and 3 s sample time). The locally measured value by anemometer was recorded and the velocity profile was generated on this basis. In order to mimic as much as possible the given operating parameter of the engine in real time, the stand also has gas burners, a NO_x dispenser, and AdBlue dosing system, a sampling probe for CLD (chemiluminescence detector) and FTIR (fourier transform infrared spectroscopy) gas analysis. In addition, it was equipped with mass flow, temperature and pressure sensors. Under steady state conditions, the collected data allows to determine the NO_x reduction efficiency and ammonia slip (Fig. 60) for several engine operation conditions.

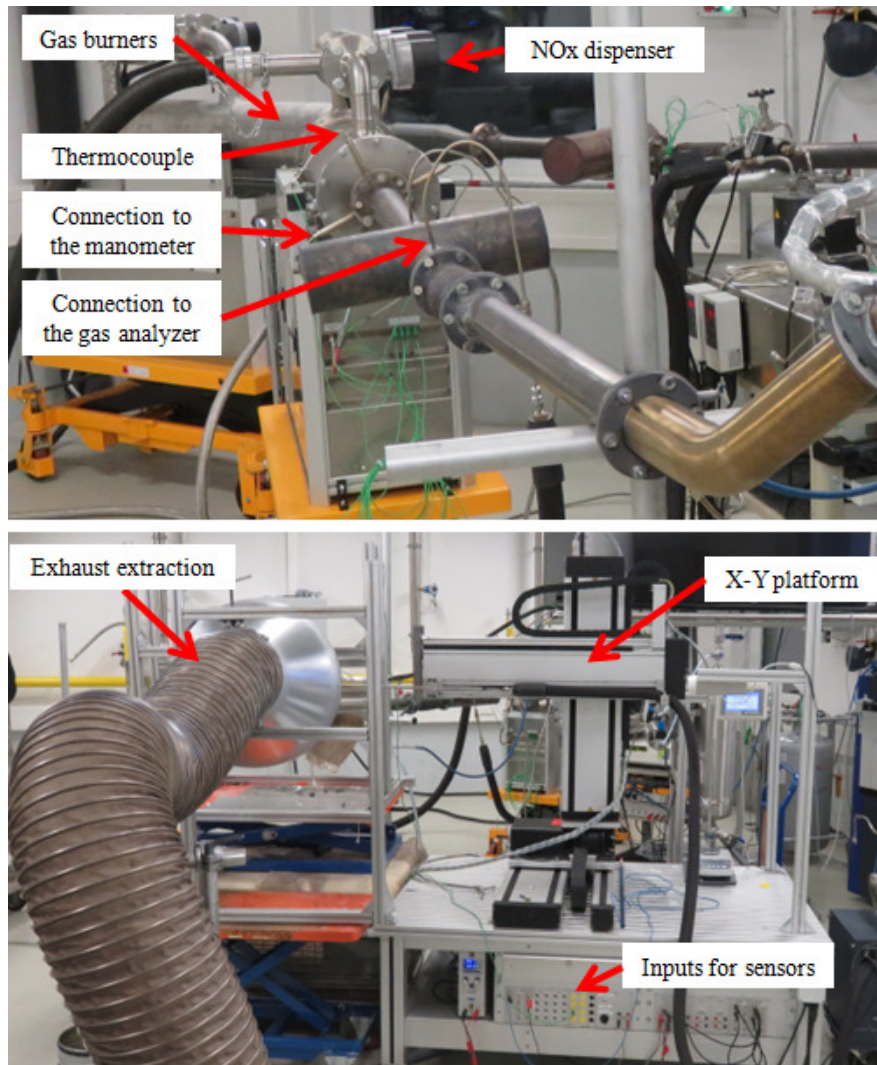


Fig. 59. Flow rig

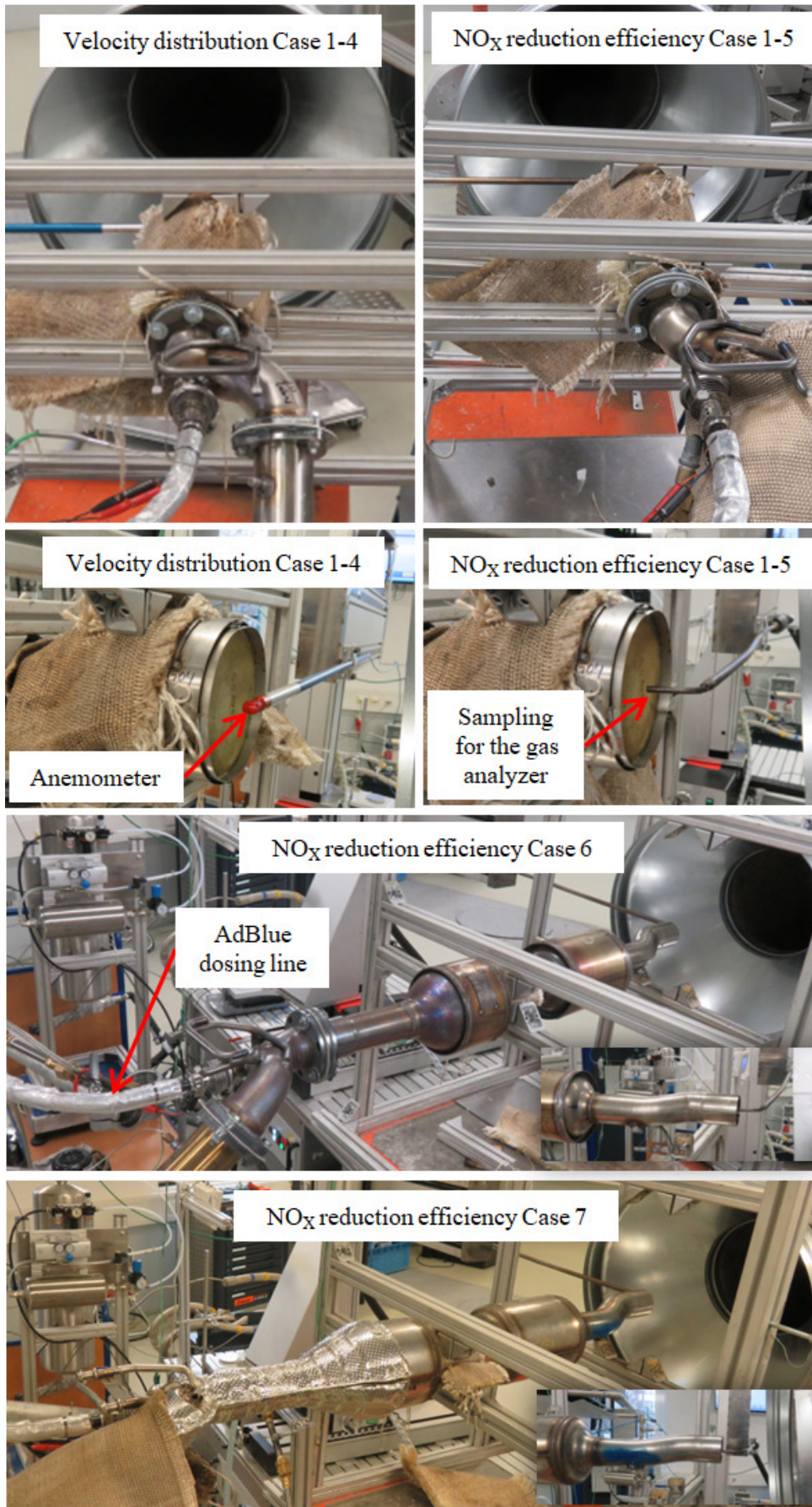


Fig. 60. Cases during flow rig tests

9.2.1 Principal factors that determine the flow through the catalyst

In this work, several very important factors and parameters are used, thanks to which it has been possible to determine the effectiveness and efficiency of the tested SCR system. In SCR system the required amount of UWS dosing for complete conversion of NO_x can be determined by means of the feed ratio α_{ANR} which is related to ammonia to NO_x ratio (ANR) according to Eq. (35) and defines as [78], [99], [100]:

$$\alpha_{ANR} = \frac{NH_{3,in}}{NO_{x,in}} \quad (46)$$

where:

$NH_{3,in}$ - number of NH₃ molecules from the urea, $NO_{x,in}$ - number of NO_x molecules in exhaust gases.

Sala et al. [99] and Zheng et al. [100] determined that the stoichiometric feed ratio of $\alpha = 1$ is theoretically required for complete conversion of NO_x. Thus knowing the mole fraction of NO at inlet SCR catalyst (C_{NOin}) and outlet SCR catalyst (C_{NOout}), the average NO conversion for standard SCR reaction according to Murkute et al. [101] is given by:

$$X_{NO}[\%] = \frac{C_{NOin} - C_{NOout}}{C_{NOin}} \cdot 100\% \quad (47)$$

To evaluate the flow velocity distribution or e.g. the ammonia distribution, the uniformity index (UI) is commonly used. The uniformity represents how a specified variable varies over a surface, where a value of 1 indicates the highest uniformity [78], [102]. The area-weighted (captures the variation of the quantity) UI is calculated as:

$$\gamma_{UI} = 1 - \frac{\sum_{i=1}^{n_f} [(|\varnothing_i - \bar{\varnothing}|) A_{ai}]}{2|\bar{\varnothing}| \sum_{i=1}^{n_f} A_{ai}} \quad (48)$$

where:

\varnothing - specific field variable, $\bar{\varnothing}$ - average value of the field variable, n_f - number of facets, i - facet index of a surface, A_a - surface area.

Uniformity index $\gamma_{UI} \geq 0.94$ can be treated as a very good result and the value at this level is considered satisfactory.

Mixture homogeneity is one of the most important parameters used in SCR systems. To evaluate the quality of mixing degree of ammonia with exhaust gases, the coefficient of variation (CoV) is used and defined as [78], [103]:

$$CoV = \frac{\sigma_{SD}}{\bar{x}} = \frac{1}{\bar{x}} \sqrt{\frac{\sum_{i=1}^{n_p} (x_i - \bar{x})^2}{n_p}} \quad (49)$$

where:

σ_{SD} - standard deviation, x_i - each of the values of the data, \bar{x} - the mean of the x_i , n_p - the number of data points.

CoV is defined as the standard deviation of concentration (e.g. NH_3), over the mean concentration. If the value of CoV is equal to 0, it means that the system is mixed completely and the efficiency of the mixing operation is 100%. A large CoV means an uneven distribution of ammonia [78].

The eccentricity index determines the place on the monolith surface with the highest flow rate. It is desirable that such sites do not occur at the edge of the monolith, therefore this parameter should be ≤ 0.5 . Eccentricity is specified by the following equation [78]:

$$Eccentricity = \frac{r_{v_{max}}}{R_m} \quad (50)$$

where:

$r_{v_{max}}$ - radius to the point of maximum velocity, R_m - radius to the edge of the monolith.

The last parameter for checking the flow in the SCR system is ETA (estimated total relative area of velocity distribution) index. ETA index for 10% is area range with velocity $\pm 10\%$ of mean velocity, i.e. narrow range of areas ought to be avoided where there is large higher velocity compared to the mean velocity. ETA index for 10% should be > 0.7 (70% of the area range with velocity $\pm 10\%$ of mean velocity should be reached) whereas ETA index for 20% should be 1 [78].

For numerical simulations, ETA index and Eccentricity were checked by implementing them into ANSYS Fluent using User Defined Functions (UDFs) through Microsoft Visual Studio 2017 and C++ language (presented in Appendices V).

9.2.2 Boundary conditions for flow rig tests

Experimental flow rig tests were carried out in two ways. First, tests were carried out only for air flow and ambient temperature (“cold flow”) with the operating inlet conditions as in Tab. 12. This allowed for comparison of the mixer prototypes in terms of the best distribution of velocity fields for cases 1-4 (Tab. 9).

Tab. 12. Operating inlet conditions for cold flow without UWS

\dot{m} [kg/h]	T [°C]	Working fluid
115	22	Only air

In the second type of tests (“hot flow”), the UWS (AdBlue) with three injections (5 bar with a frequency of 4Hz) as well as other components of the inlet gases have been taken into account. Such settings allowed for checking the degree of mixing and distribution of NH₃ as well as the NO_x reduction efficiency in monoliths. The operating parameters and the composition of the inlet exhaust gases used are shown in Tab. 13.

Tab. 13. Operating inlet conditions for hot flow with UWS

Load	\dot{m}_{exh} [kg/h]	T [°C]	NO _x [ppm]	AdBlue dosing [g/h]	NO/NO _x ratio	O ₂ [%]	CO ₂ [%]	H ₂ O [%]	N ₂ [%]	NH ₃ /NO _x ratio
OP1:High	541	501	500	650.5	0.97	15.3	2.1	4.8	balanced	0.75
OP2:Med.	206	404	128	63.6		16.0	1.8	3.7		
OP3:Low	98	268	165	38.9		17.0	1.3	2.9		

The amount of NH₃ that needs to be injected under a given steady-state condition relates to the targeted ammonia to NO_x ratio (ANR) also called feed ratio. Through a dosing system metering of diesel exhaust fluid (DEF), the ammonia (NH₃ in ppm) can be determined in the exhaust stream as [127]:

$$NH_3 = \frac{\frac{DEF \cdot 0.325}{M_{urea}} \cdot 2}{\frac{\dot{m}_{exh} \cdot 10^3}{M_{exh}}} \cdot 10^6 \quad (51)$$

where:

DEF, g/h is the diesel exhaust fluid, other term for urea (AdBlue) mass flow dosing rate, M, g/mol is the molecular mass for urea 60.06 g/mol and for exhaust gas 28.84 g/mol, \dot{m}_{exh} , kg/h is the mass flow rate of the exhaust gas.

Not all cases from Tab. 9 have been tested in terms of all operational parameters (OP: Tab. 13) because of the cost and time consumption. Despite the fact that the measurement time for one case and one operation parameter was about one hour, then other actions were required, such as change system, setup system, burn out system and removal of system. Finally, the tests have been reduced (Tab. 14) to about two weeks and cost about 14 000 €.

Tab. 14. Tested operational parameters for individual cases

Case	Cold flow	OP1	OP2	OP3
1. Prototype with mixer A (1 st box)	X		X	
2. Prototype with mixer B (1 st box)	X		X	
3. Prototype with mixer C (1 st box)	X		X	
4. Prototype with mixer C (1 st and 2 nd box)	X	X	X	X
5. Prototype with 2-Stage mixer (1 st and 2 nd box)			X	
6. Prototype with mixer C (complete part)		X	X	X
7. Original VW part and mixer (complete part)		X	X	X

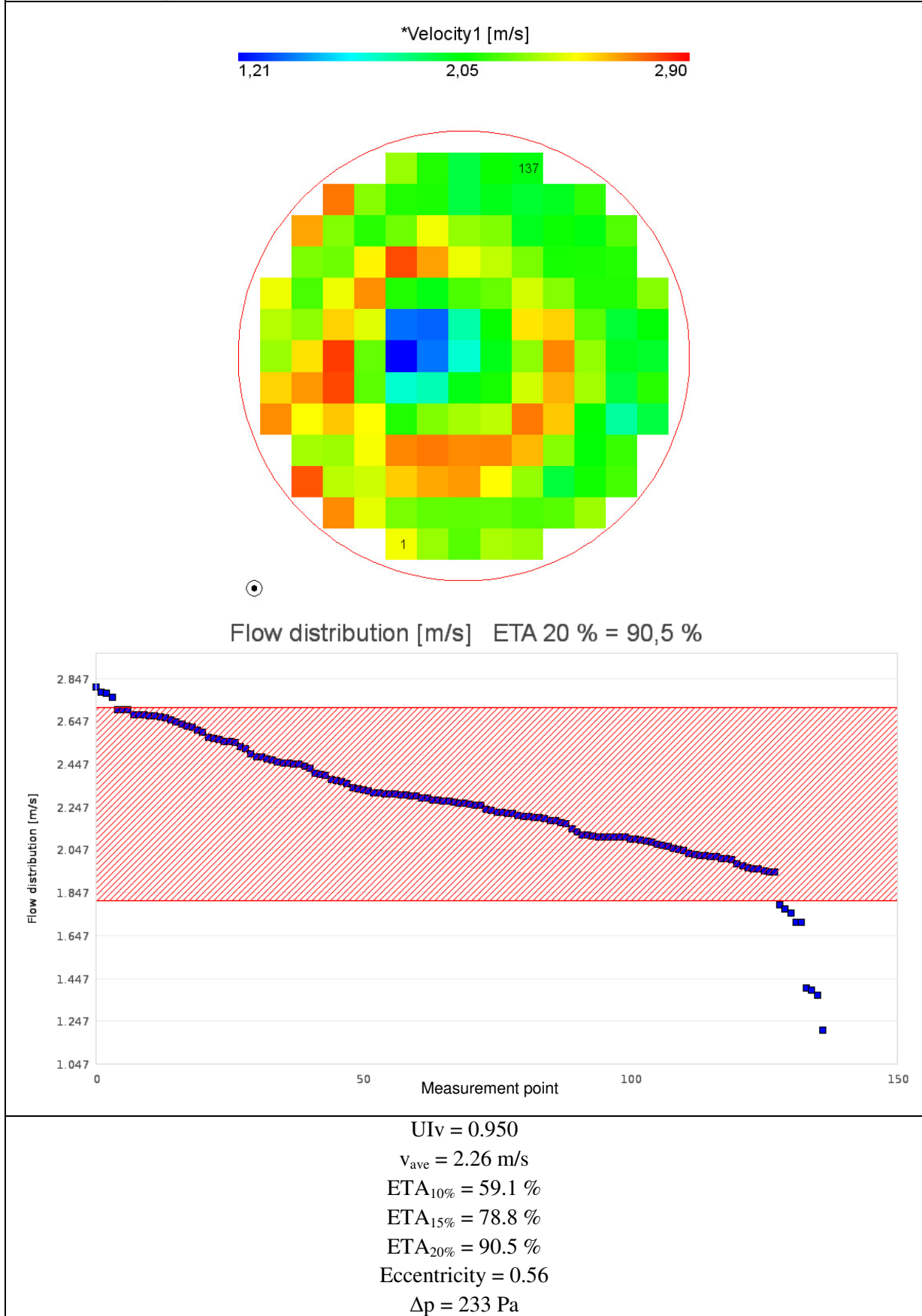
9.2.3 Results for flow rig tests

First, the results for the cold flow are presented in Tab. 15 for cases 1-4 in order to determine the best flow distribution at the outlet side of the monolith. In the graphs, the horizontal axis represents the measurement of 137 sampling points (zigzag movement from bottom to top). The red hatched field indicates the percentage coverage of the $ETA_{20\%}$ index.

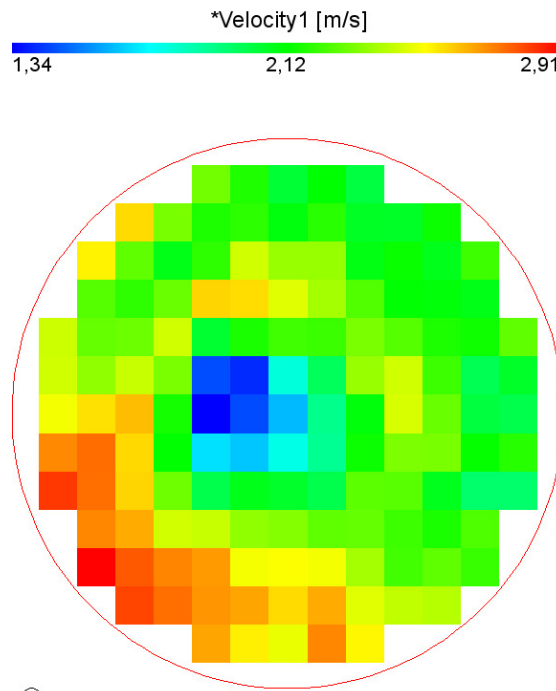
Based on factors such as uniformity index of velocity (UI_v), $ETA_{10/15/20\%}$, eccentricity index and pressure drop, the best mixer was selected for further experimental studies (case 4 and 6). Considering cases 1-3, the best $UI_v=0.953$ had the case 3 where the mixer C was rotated by 90° which mattered because without the rotation of the mixer, the uniformity index decreased to 0.950. For Case 1, the distance of the mixer from the injector also affected gas flow distribution. It was better for the distance 155mm ($UI_v=0.952$), however, the $ETA_{20\%}=90.5$ and $Eccen.=0.56$ already were more on the benefit for the distance 120mm with $UI_v=0.950$. Comparing the $ETA_{20\%}$, mixer C achieved the best value which was 92.7% of areas within tolerance $\pm 20\%$ of mean velocity. The eccentricity index obtained the best value 0.1 for case 3 where the mixer C was rotated by 90° which means that the best gas distribution was in the middle of the monolith. In the position of mixer $L=120$ mm, the case with mixer C had the greatest pressure drop (254Pa), which is related to the complexity of the mixer geometry but this also contributes to a better uniform distribution of gas. In case 4, adding a second box only confirmed the increase of $UI_v=0.956$ and thus selecting the mixer C for further experimental studies (Case 6).

Tab. 15. Velocity distribution for cold flow rig tests at outlet (Case 1-4)

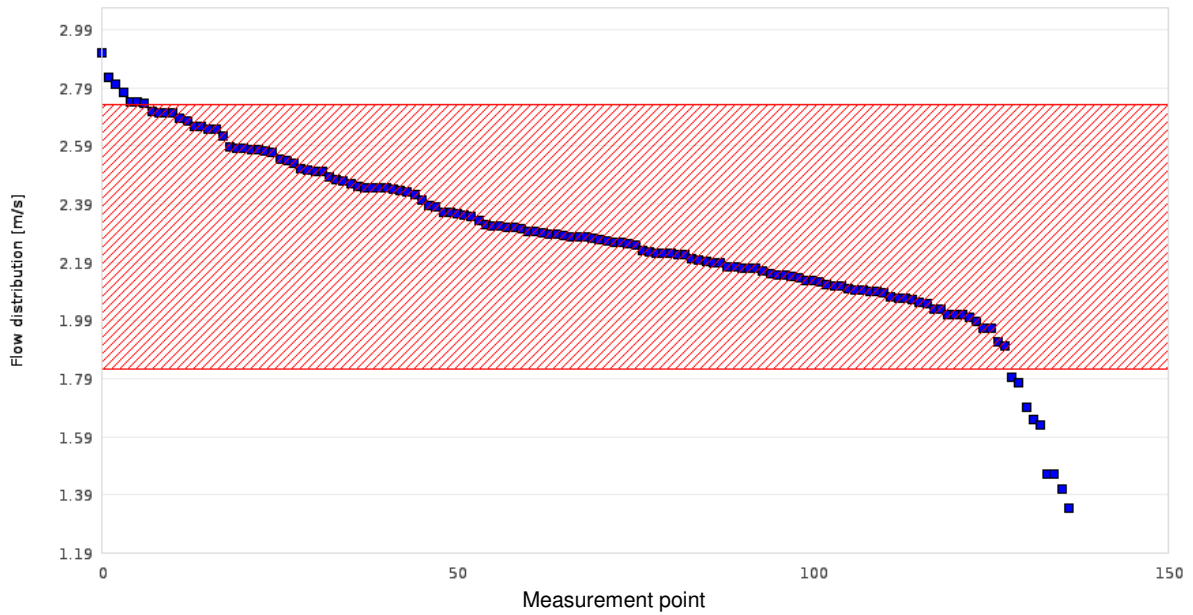
Case 1: Prototype with mixer A; injector-mixer distance L=120mm



Case 1: Prototype with mixer A; injector-mixer distance L=155mm



Flow distribution [m/s] ETA 20 % = 88,3 %



$UI_v = 0.952$

$v_{ave} = 2.27 \text{ m/s}$

$ETA_{10\%} = 62.8 \%$

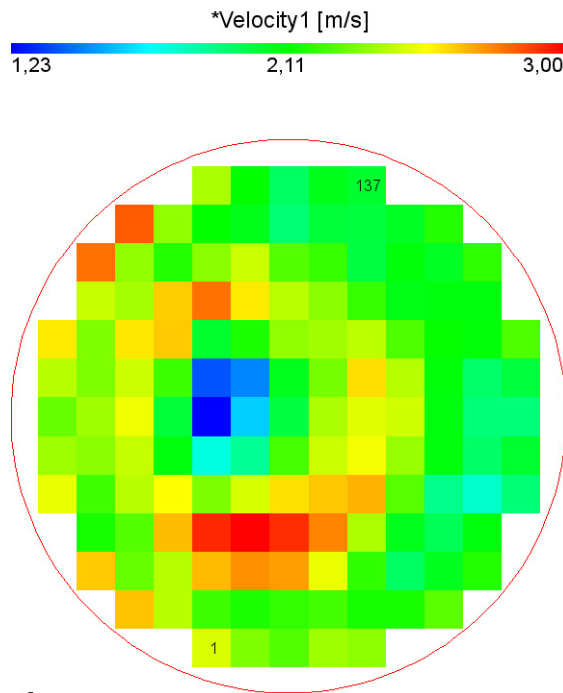
$ETA_{15\%} = 78.8 \%$

$ETA_{20\%} = 88.3 \%$

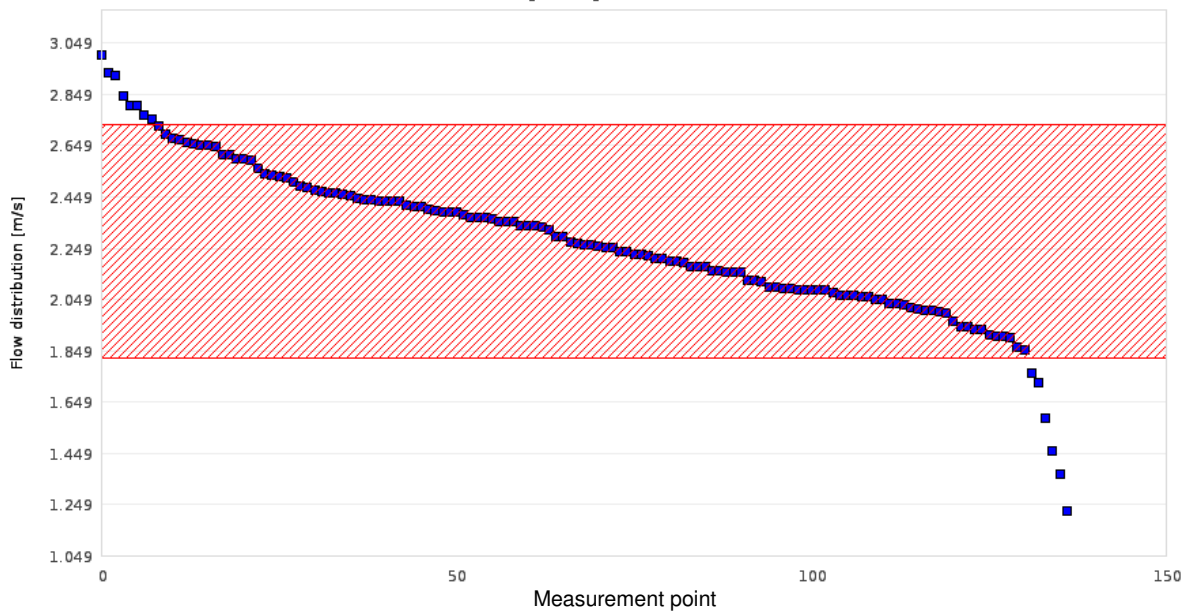
Eccentricity = 0.89

$\Delta p = 264 \text{ Pa}$

Case 2: Prototype with mixer B; injector-mixer distance L=120mm



Flow distribution [m/s] ETA 20 % = 89,8 %



$UI_v = 0.948$

$v_{ave} = 2.27 \text{ m/s}$

$ETA_{10\%} = 60.6 \%$

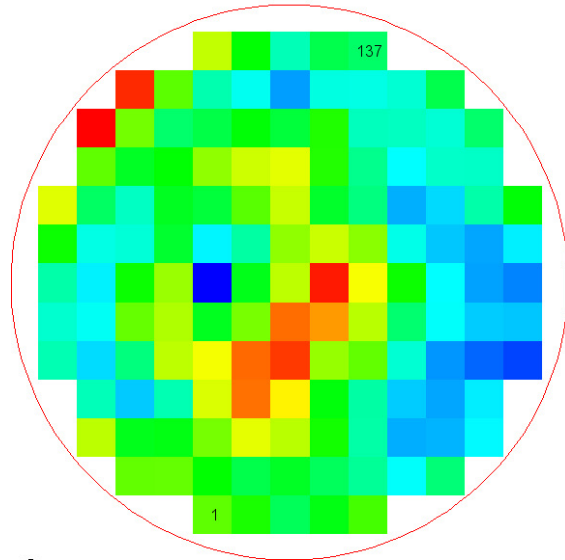
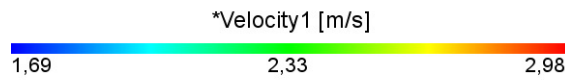
$ETA_{15\%} = 78.1 \%$

$ETA_{20\%} = 89.8 \%$

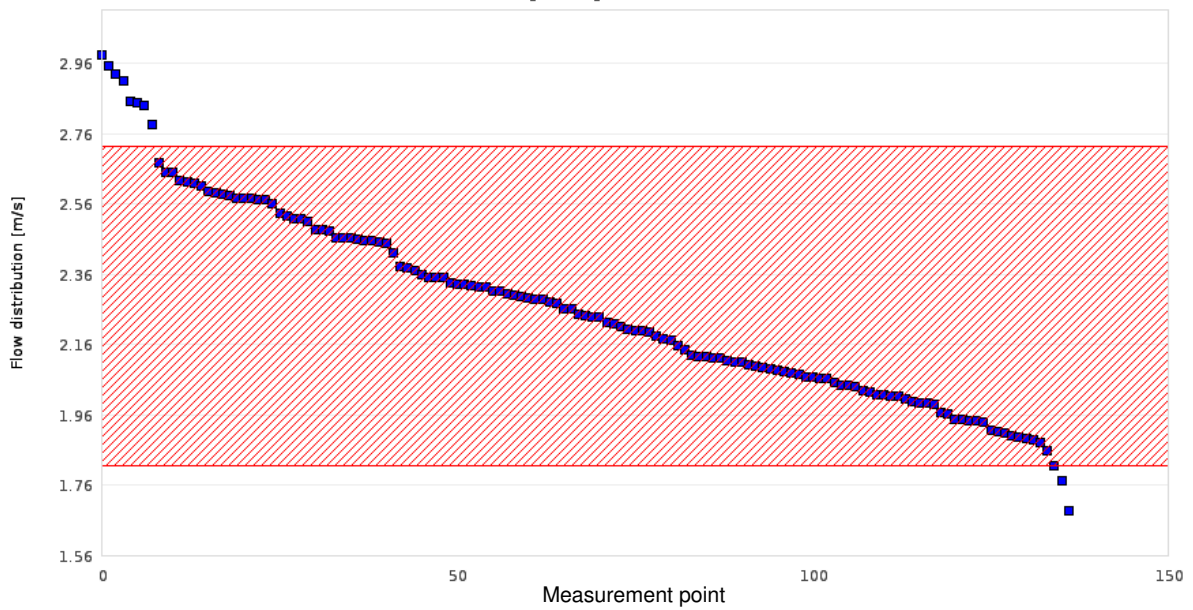
Eccentricity = 0.44

$\Delta p = 244 \text{ Pa}$

Case 3: Prototype with mixer C; injector-mixer distance L=120mm



Flow distribution [m/s] ETA 20 % = 92,7 %



$UI_v = 0.950$

$v_{ave} = 2.27 \text{ m/s}$

$ETA_{10\%} = 55.5 \%$

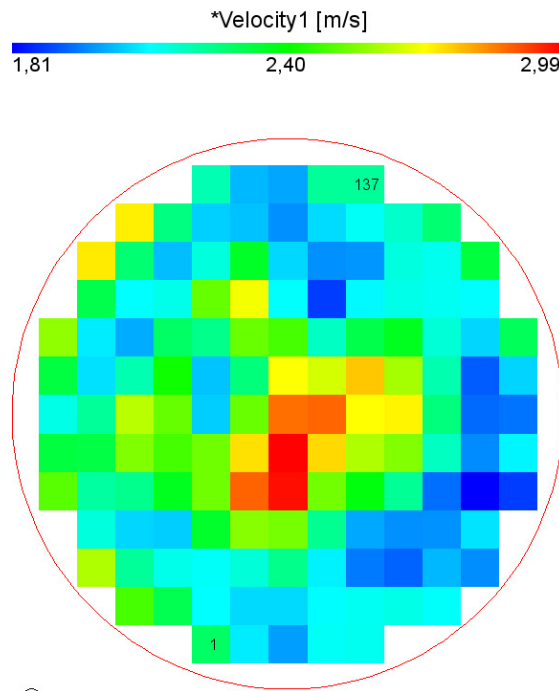
$ETA_{15\%} = 80.3 \%$

$ETA_{20\%} = 92.7 \%$

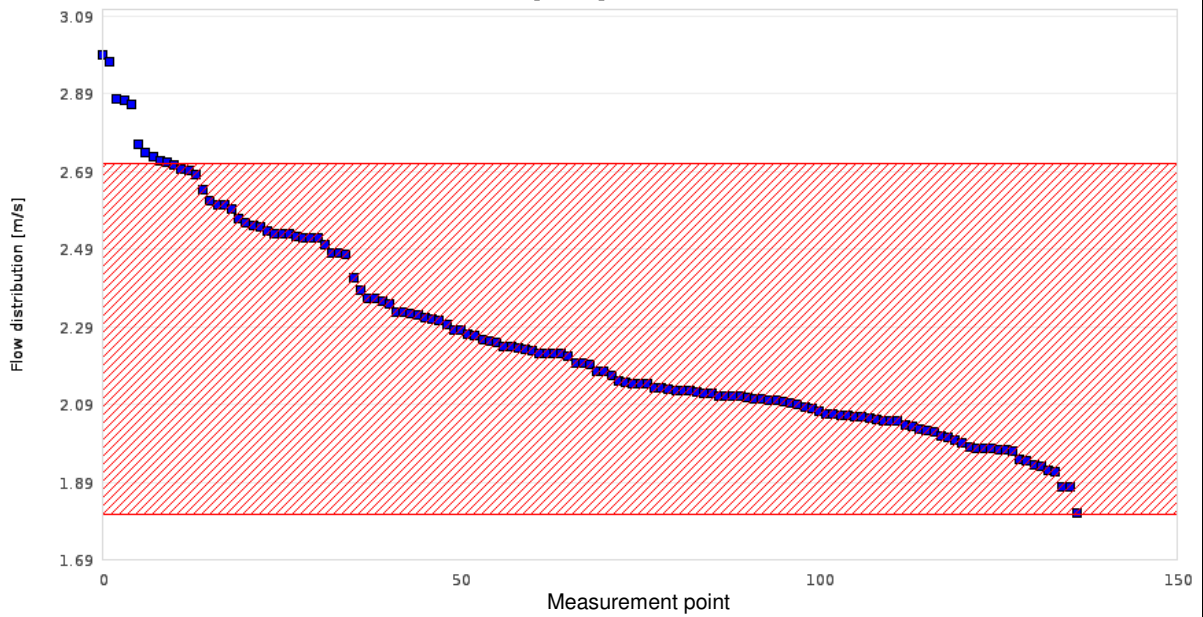
$Eccentricity = 0.89$

$\Delta p = 251 \text{ Pa}$

Case 3: Prototype with mixer C; injector-mixer distance $L=120\text{mm}$ & rotated by 90°



Flow distribution [m/s] ETA 20 % = 92,7 %



$$UI_v = 0.953$$

$$v_{ave} = 2.26 \text{ m/s}$$

$$ETA_{10\%} = 59.1 \%$$

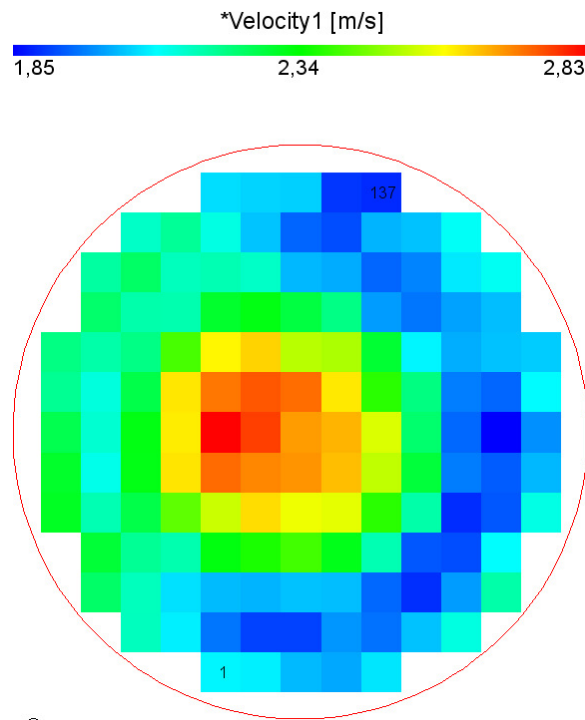
$$ETA_{15\%} = 83.9 \%$$

$$ETA_{20\%} = 92.7 \%$$

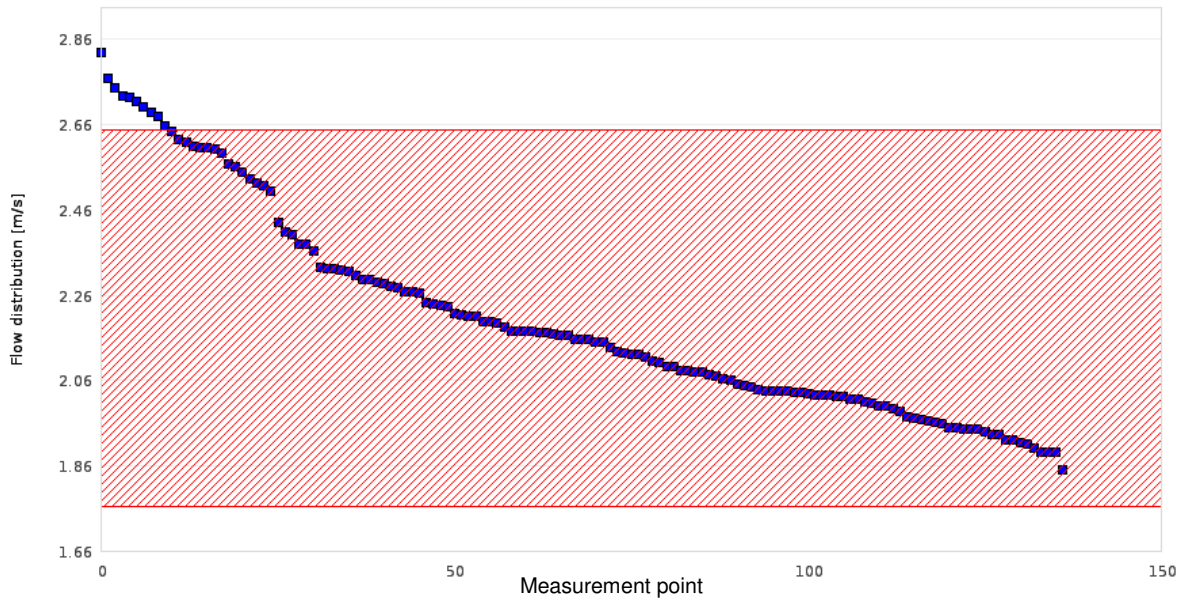
$$Eccentricity = 0.10$$

$$\Delta p = 254 \text{ Pa}$$

Case 4: Prototype with mixer C (1st and 2nd box)



Flow distribution [m/s] ETA 20 % = 92,7 %



UIv = 0.956

$v_{ave} = 2.21$ m/s

ETA_{10%} = 64.2

ETA_{15%} = 83.9

ETA_{20%} = 92.7

Eccentricity = 0.28

$\Delta p = 690$ Pa

Subsequently for hot flow with UWS, the overall conversion of nitrogen oxides (X_{NOx}) for cases 1-3 with OP2 (medium) was investigated. Tab. 16 shows the outlet surfaces of the SCR monoliths with NO and NH₃ mole fractions in ppm, moreover, the additional graph also shows the ammonia (NH₃) and isocyanic acid (HNCO) slip at individual points of the monolith. For comparison purposes, the uniformity indexes of NO (UI_{NO}) and NH₃ (UI_{NH_3}) have been determined as well as their average values on the outlet surfaces of monoliths.

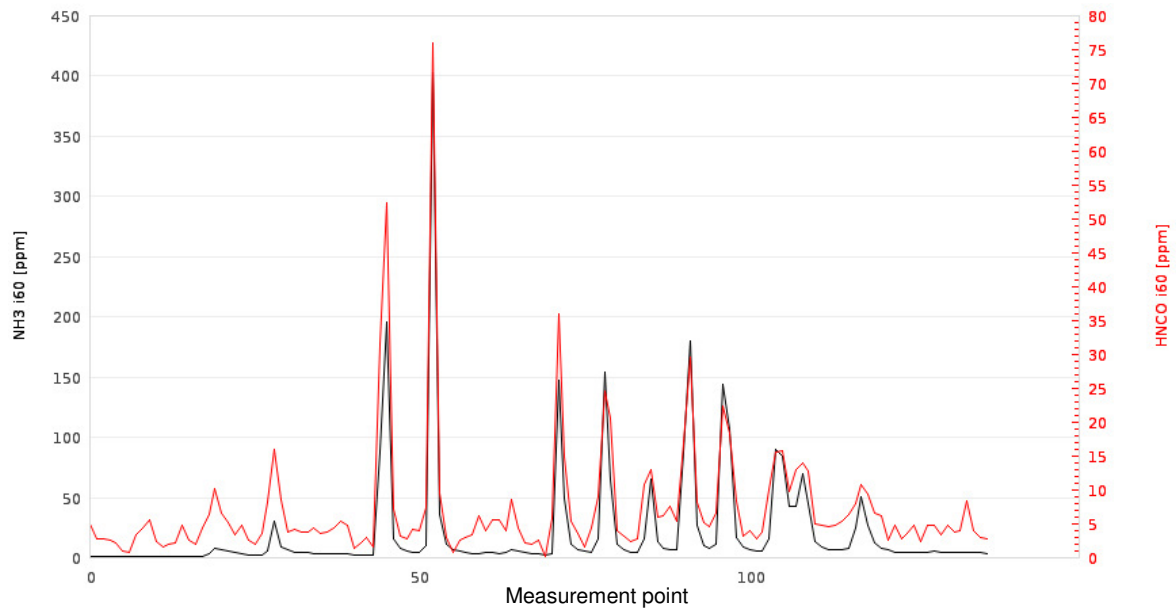
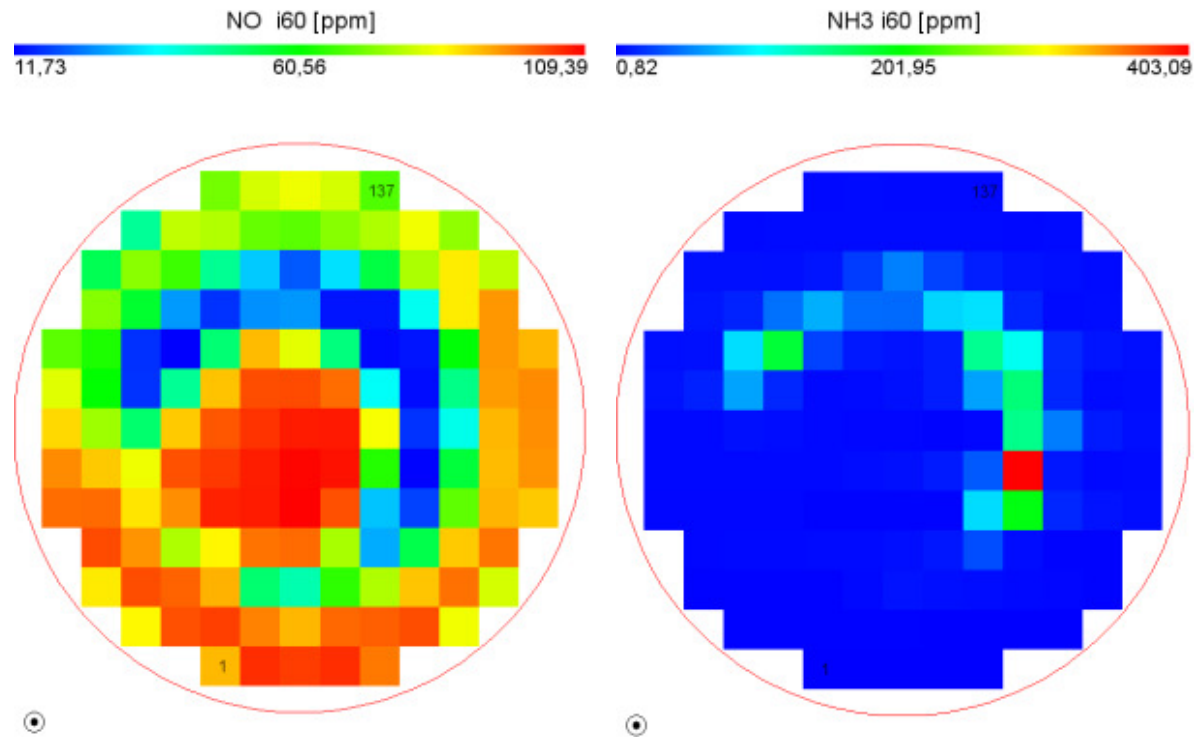
The best overall conversion of nitrogen oxides was obtained for mixer A (37.48%) for the distance of the mixer from the injector 155mm despite not being of the best uniformity index $UI_{NO}=0.845$ which was the best for mixer B ($UI_{NO}=0.860$). The weakest uniformity index $UI_{NH_3}=0.342$ was obtained by case 3 with rotated mixer C by 90° and thus had the greatest ammonia slip at one point about 640ppm, hence it is possible in this place the formation of a deposit due to high isocyanic acid at 140ppm. The optimal results were achieved for case 3 with not rotated mixer C, where the total conversion was $X_{NOx}=35.37\%$ and the uniformity index was $UI_{NO}=0.836$.

Afterwards, cases 4 and 5 were compared (Tab. 17) where a second box of SCR was added. For case 4, all operational parameters (high, medium and low) were tested. For case 5, only OP2 (medium) has been investigated with the patented Tenneco 2-Stage mixer.

Comparing the results for case 4, the best uniformity indexes UI_{NO} and UI_{NH_3} were obtained for the operating parameter OP3 (high) which was due to the greatest turbulence in the system. However, with a decrease in the mass flow of gases, the total conversion grew and for OP3 was $X_{NOx}=63.61\%$ which was caused by the slower flow of NO_x through the SCR catalysts and therefore had more time for their conversion. The SCR system did not achieve full conversion (100%) because the operating parameters (mainly NO_x) have been overestimated for the reason that the real engine emission for the dedicated SCR part was not known. Nonetheless, comparing cases 4 and 5 for OP2, the total conversion of NO_x increased by 8.57 percentage points in favor of case 5 and the ammonia slip decreased almost to zero ppm. This demonstrates the very good design of Tenneco 2-Stage mixer. The complicated design raises the degree of mixing (UI_{NH_3}) and pressure drop.

Tab. 16. NO_x reduction efficiency for hot flow rig tests at outlet (Case 1-3, OP2)

Case 1: Prototype with mixer A; injector-mixer distance L=120mm / OP2



$$UI_{NO} = 0.840$$

$$NO_{ave} = 74.16 \text{ ppm}$$

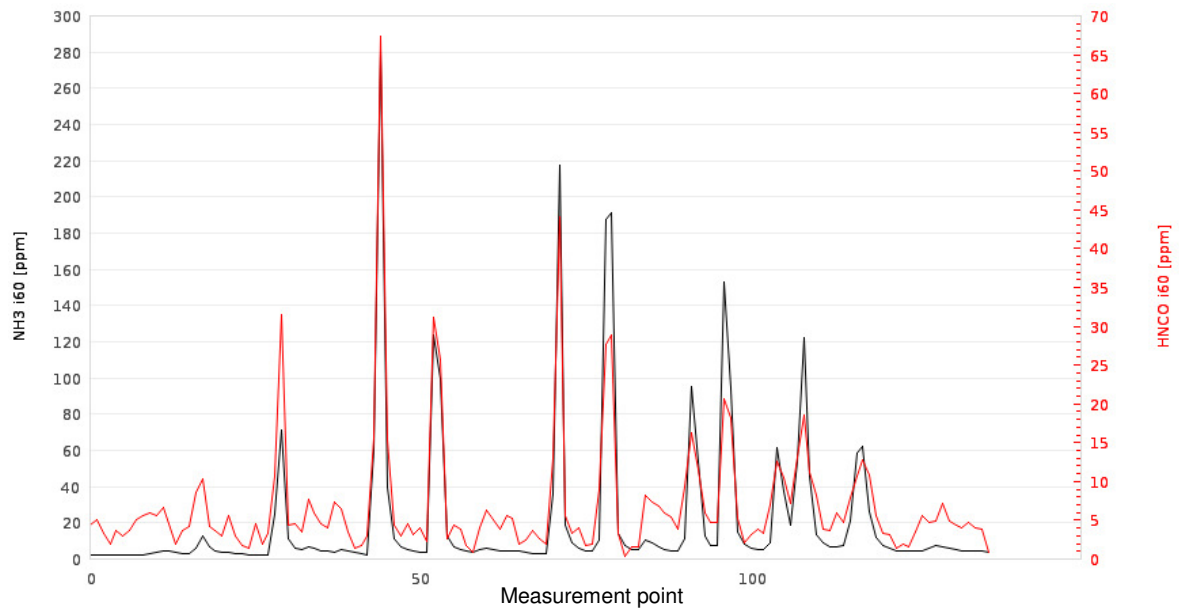
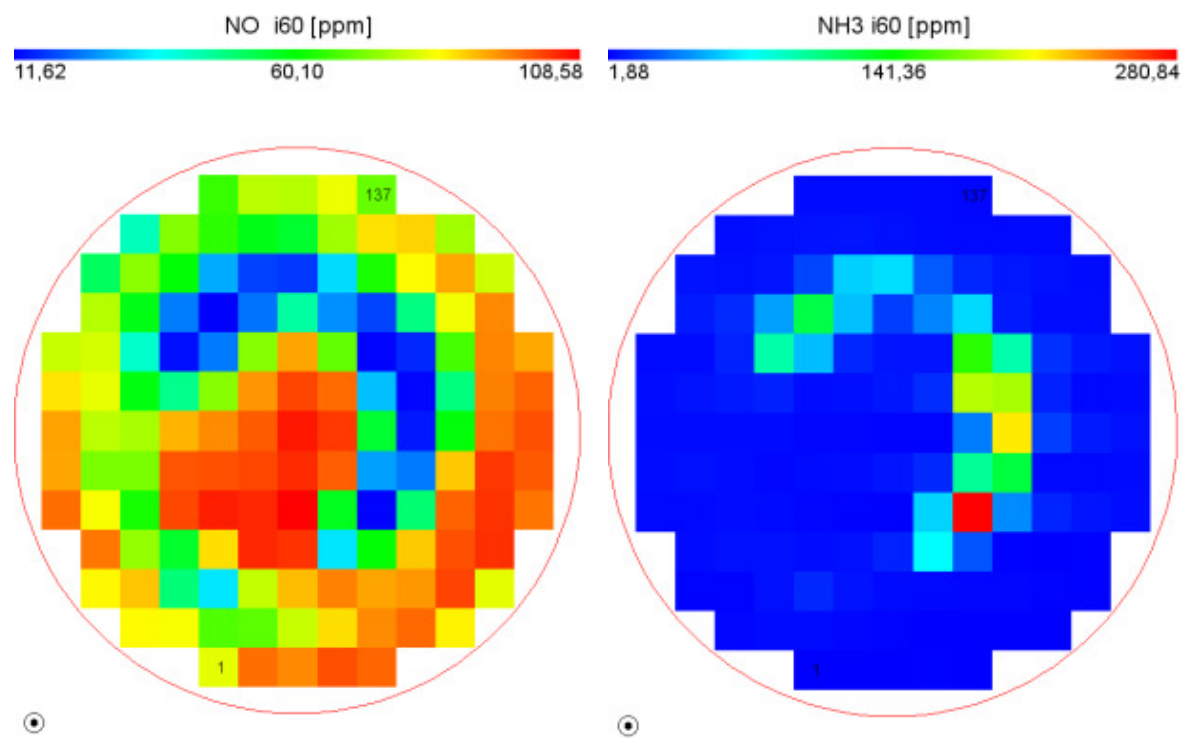
$$UI_{NH_3} = 0.386$$

$$NH_{3,ave} = 20.87 \text{ ppm}$$

$$\Delta p = 1571 \text{ Pa}$$

$$X_{NO_x} = 37.29 \%$$

Case 1: Prototype with mixer A; injector-mixer distance L=155mm / OP2



$$UI_{NO} = 0.845$$

$$NO_{ave} = 73.44 \text{ ppm}$$

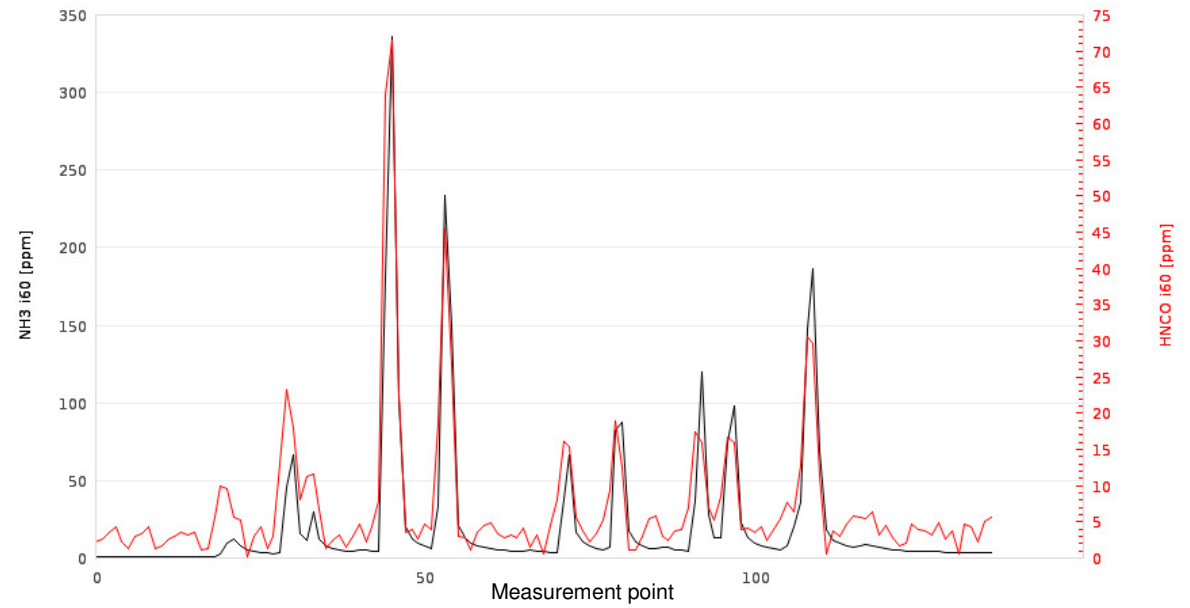
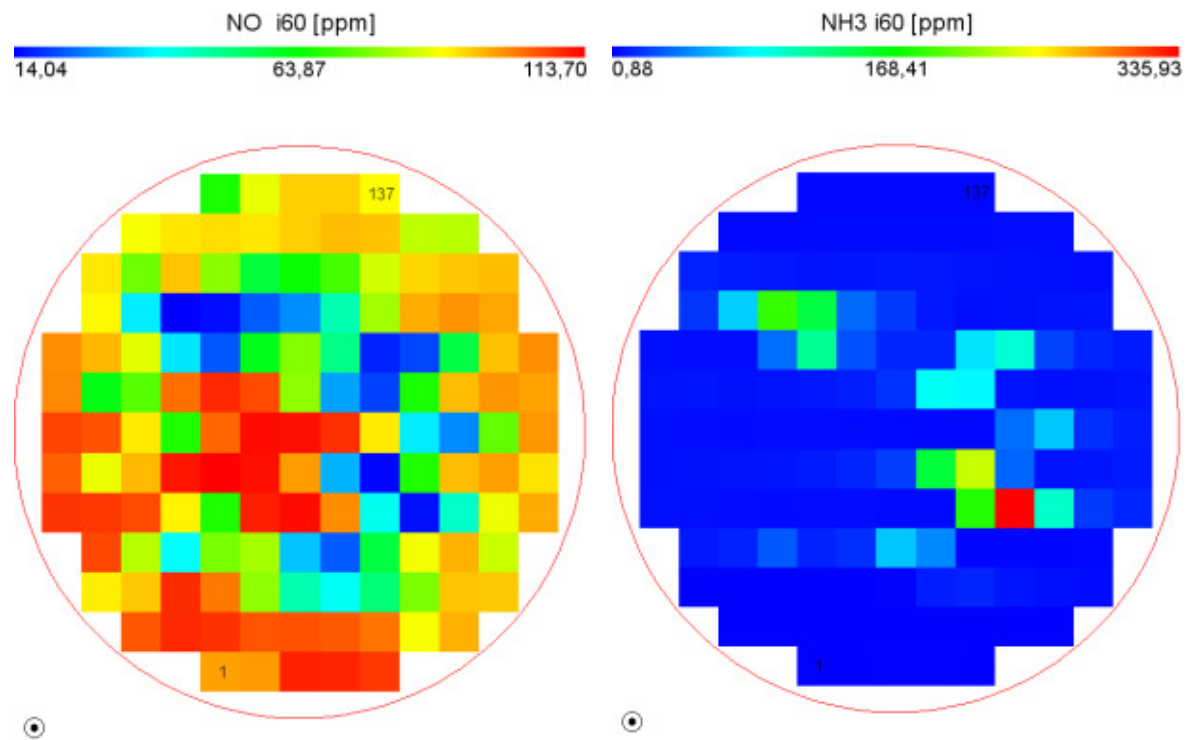
$$UI_{NH_3} = 0.404$$

$$NH_{3,ave} = 20.99 \text{ ppm}$$

$$\Delta p = 1639 \text{ Pa}$$

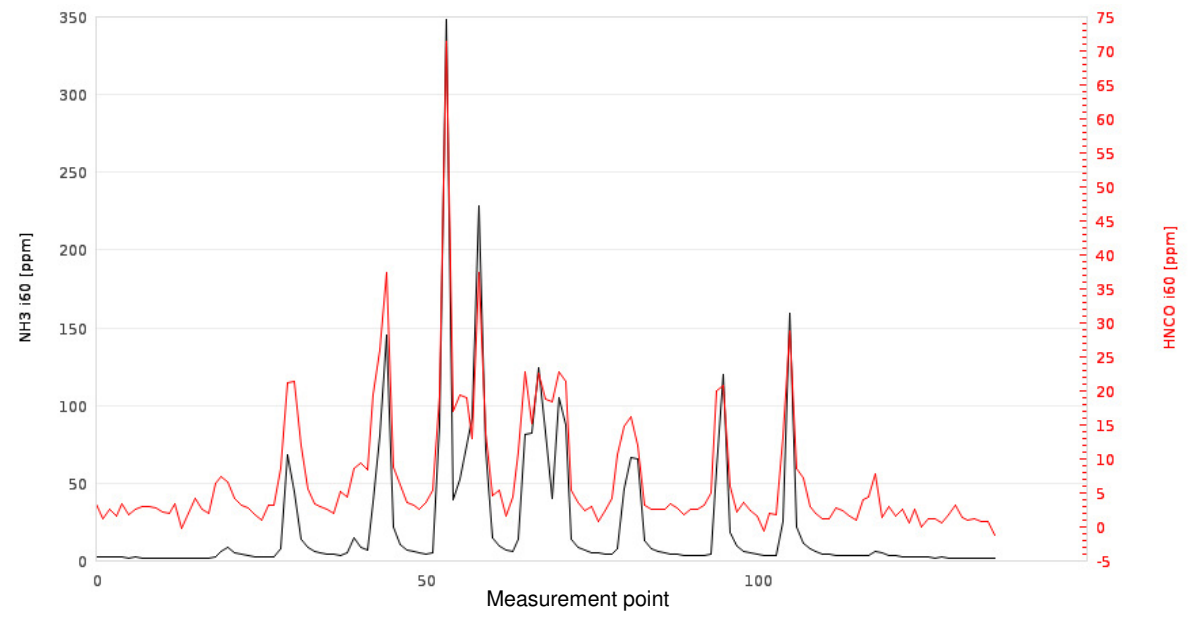
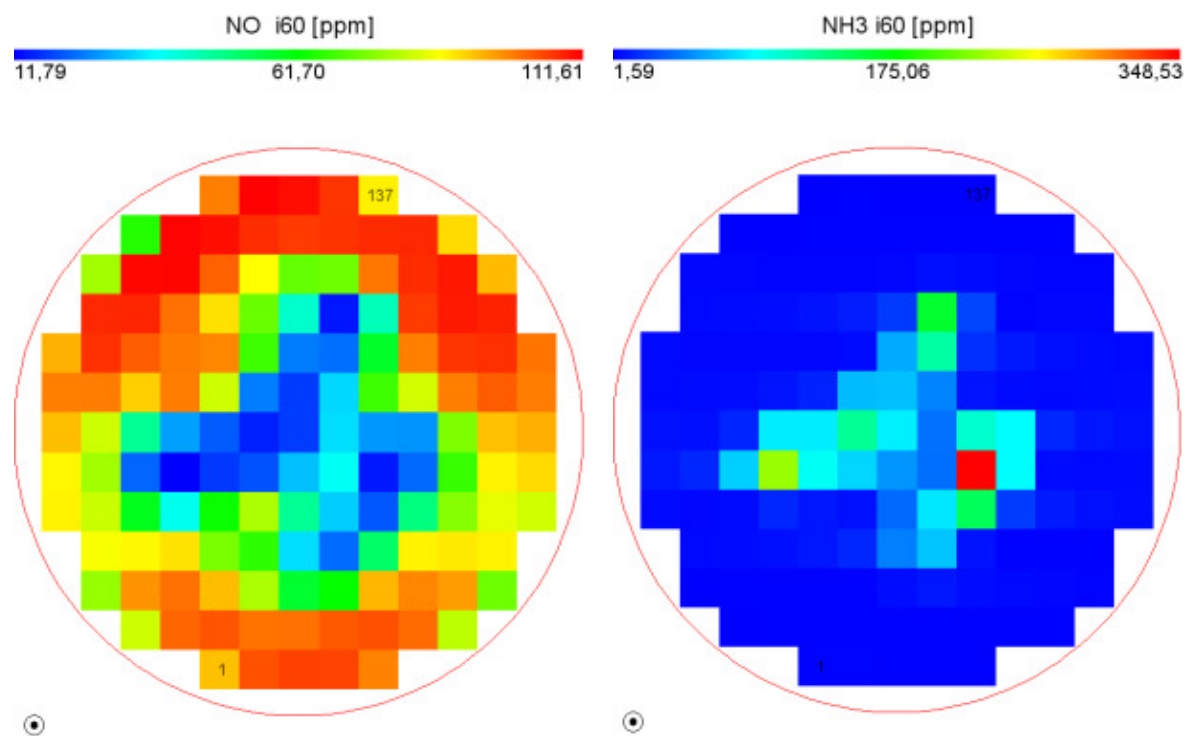
$$X_{NOx} = 37.48 \%$$

Case 2: Prototype with mixer B; injector-mixer distance L=120mm / OP2



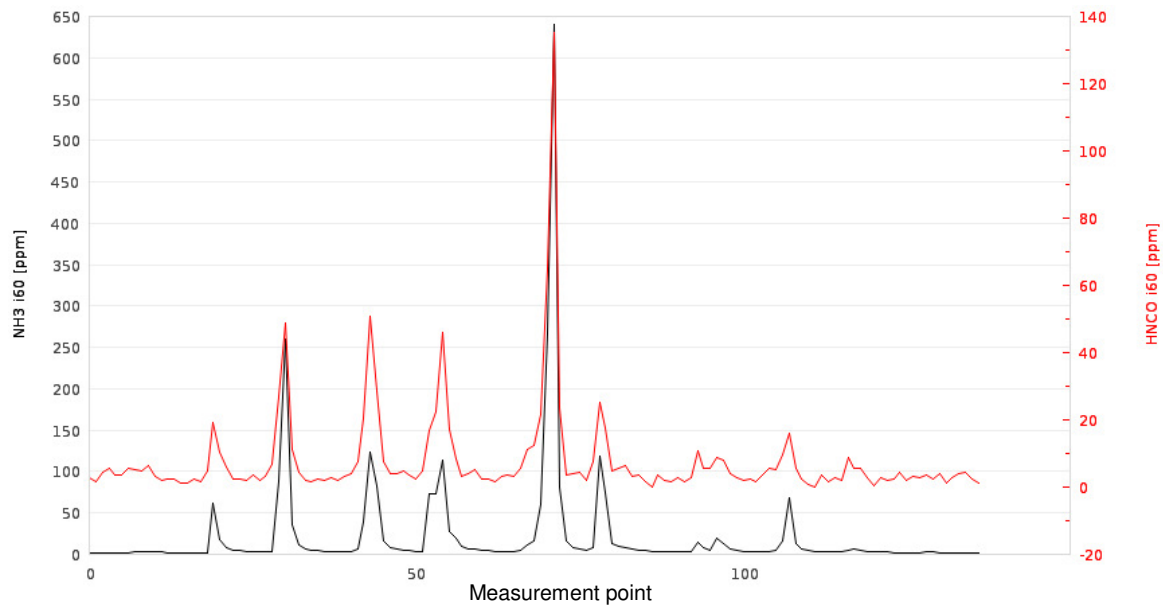
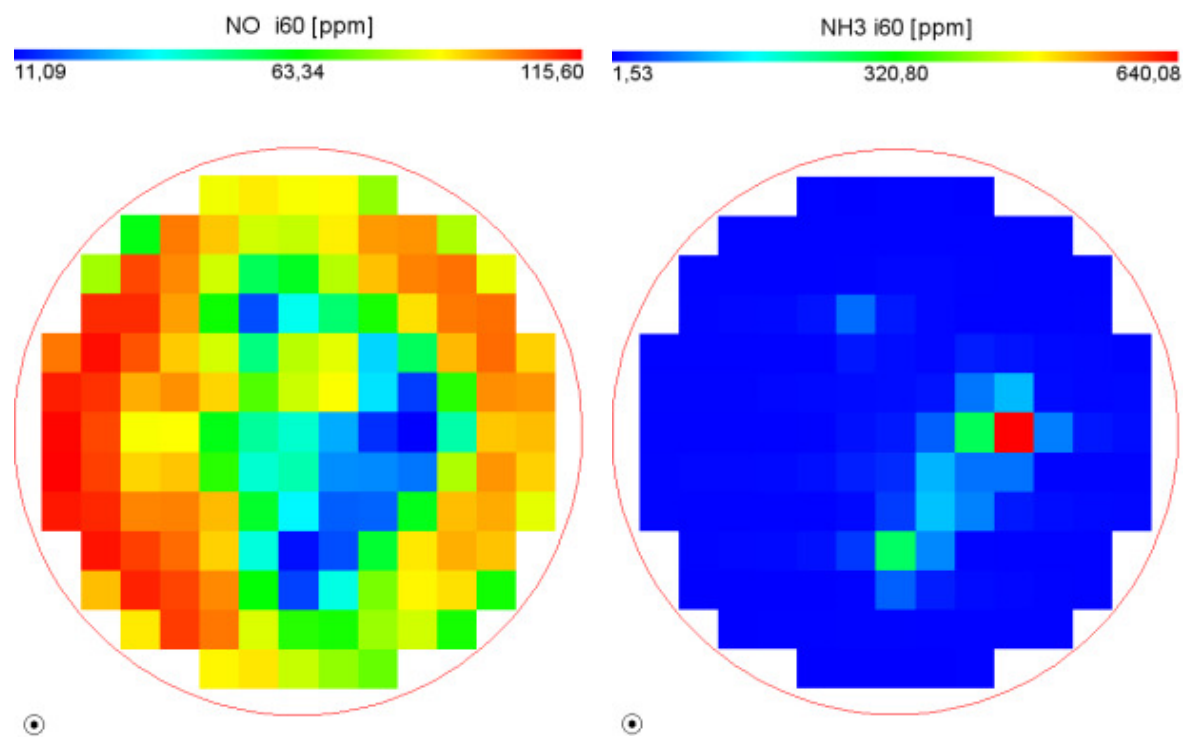
$U_{NO} = 0.860$
 $NO_{ave} = 80.82 \text{ ppm}$
 $U_{NH_3} = 0.408$
 $NH_{3,ave} = 21.78 \text{ ppm}$
 $\Delta p = 1452 \text{ Pa}$
 $X_{NOx} = 32.72 \%$

Case 3: Prototype with mixer C; injector-mixer distance L=120mm / OP2



$U_{NO} = 0.836$
 $NO_{ave} = 77.20 \text{ ppm}$
 $U_{NH_3} = 0.384$
 $NH_{3,ave} = 22.57 \text{ ppm}$
 $\Delta p = 1638 \text{ Pa}$
 $X_{NO_x} = 35.37 \%$

Case 3: Prototype with mixer C; injector-mixer distance L=120mm & rotated by 90° / OP2



$$UI_{NO} = 0.856$$

$$NO_{ave} = 79.53 \text{ ppm}$$

$$UI_{NH_3} = 0.342$$

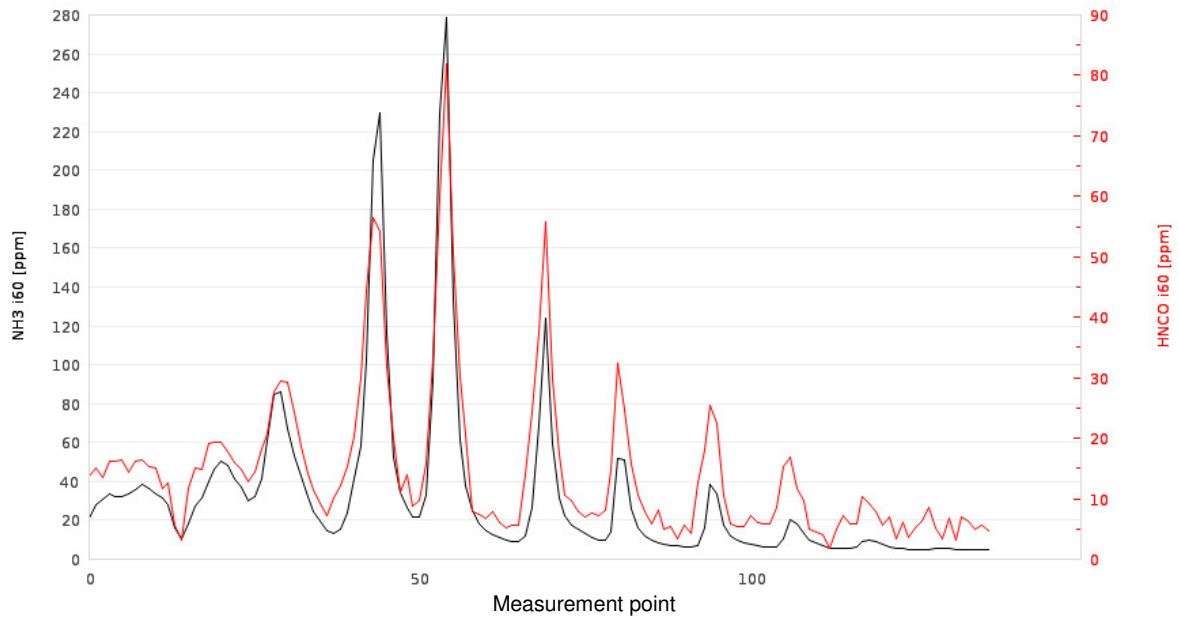
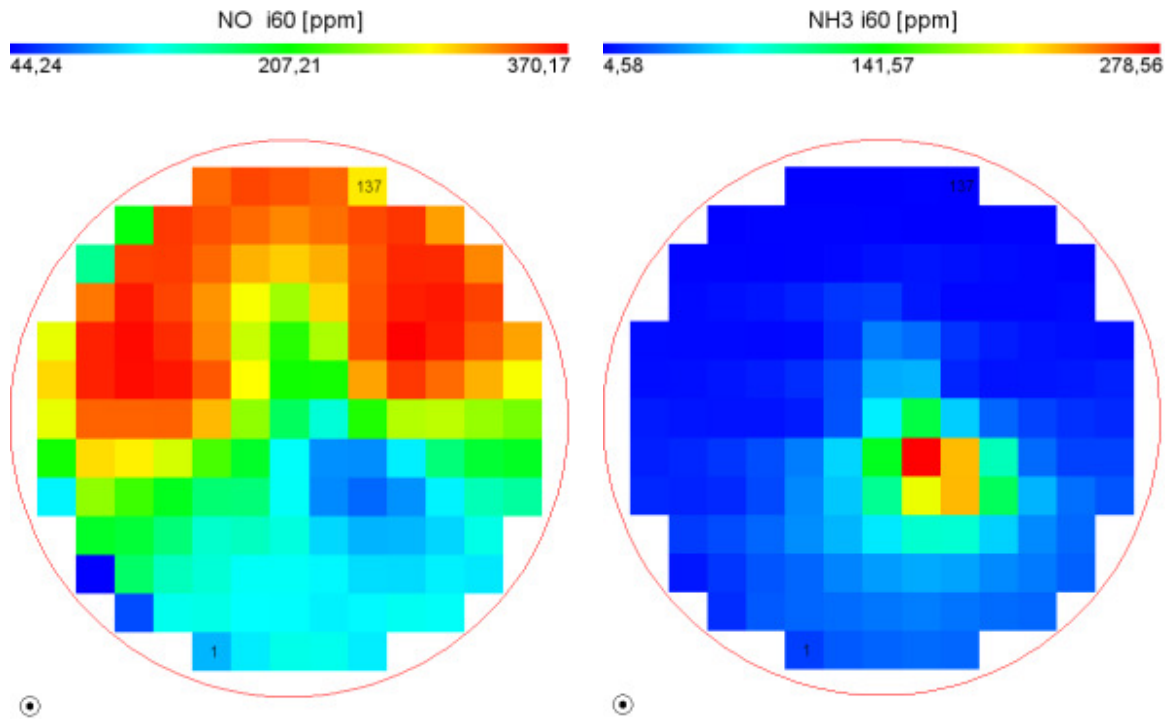
$$NH_{3,ave} = 21.16 \text{ ppm}$$

$$\Delta p = 1601 \text{ Pa}$$

$$X_{NOx} = 32.69 \%$$

Tab. 17. NO_x reduction efficiency for hot flow rig tests at outlet (Case 4-5, OP1-3)

Case 4: Prototype with mixer C (1st and 2nd box) / OP1 (High)



$$U_{\text{NO}} = 0.809$$

$$\text{NO}_{\text{ave}} = 236.78 \text{ ppm}$$

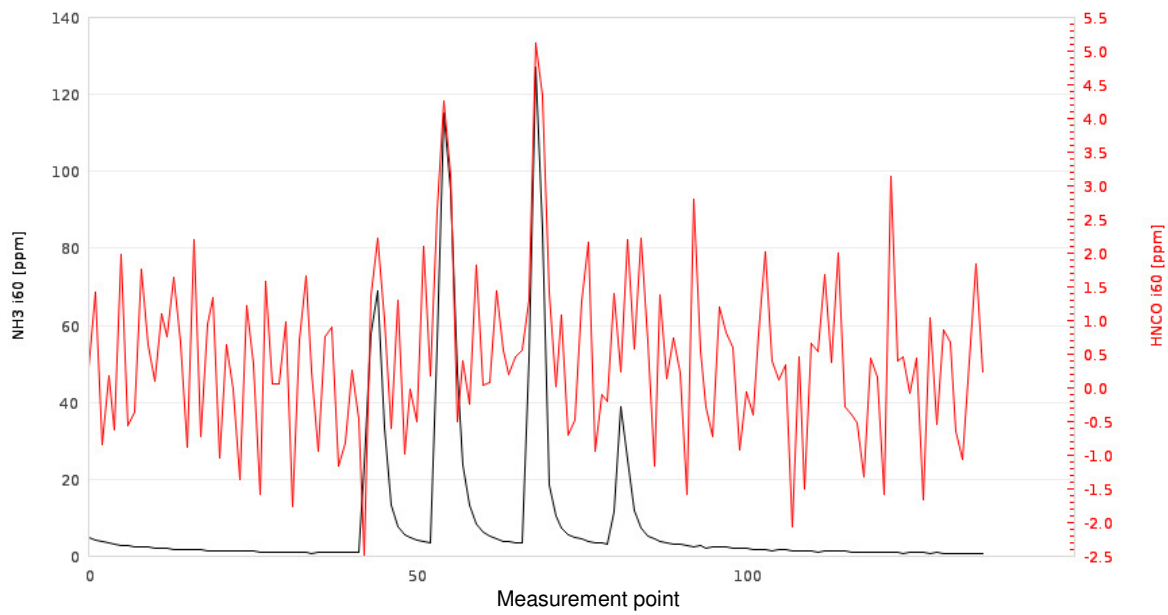
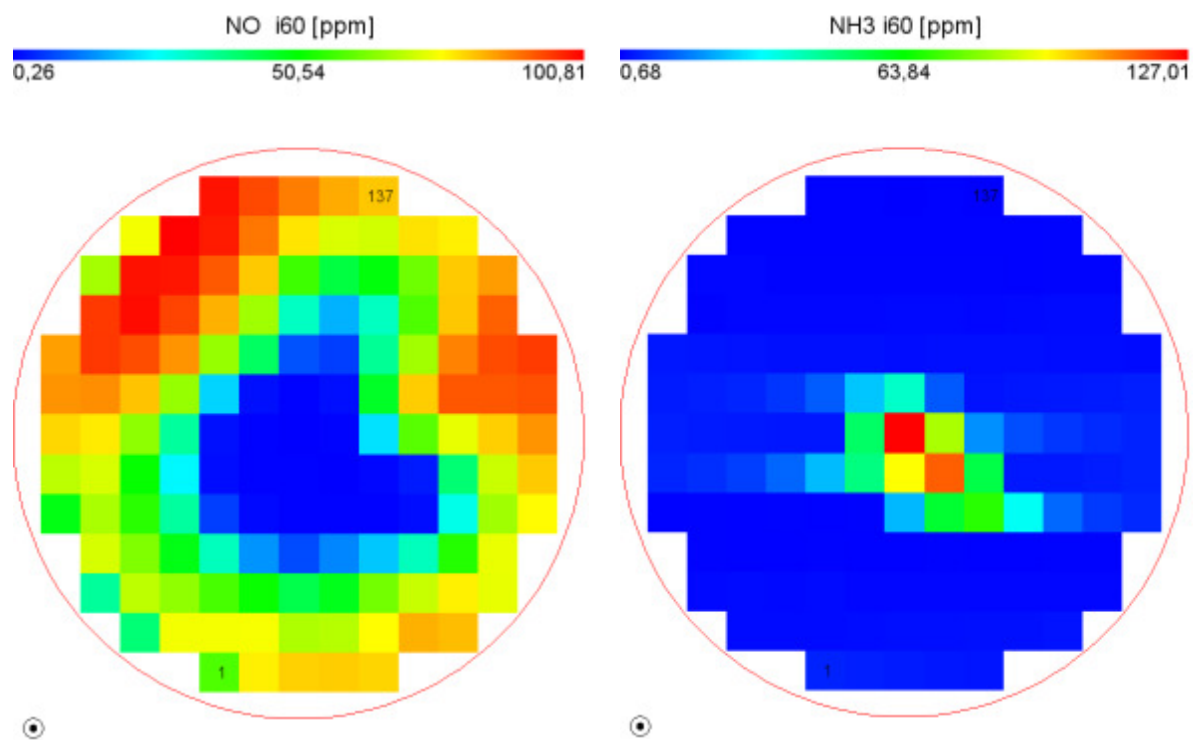
$$U_{\text{NH}_3} = 0.602$$

$$\text{NH}_{3\text{ave}} = 31.86 \text{ ppm}$$

$$\Delta p = 19736 \text{ Pa}$$

$$X_{\text{NO}_x} = 47.50 \%$$

Case 4: Prototype with mixer C (1st and 2nd box) / OP2 (Medium)



$$UI_{NO} = 0.765$$

$$NO_{ave} = 57.31 \text{ ppm}$$

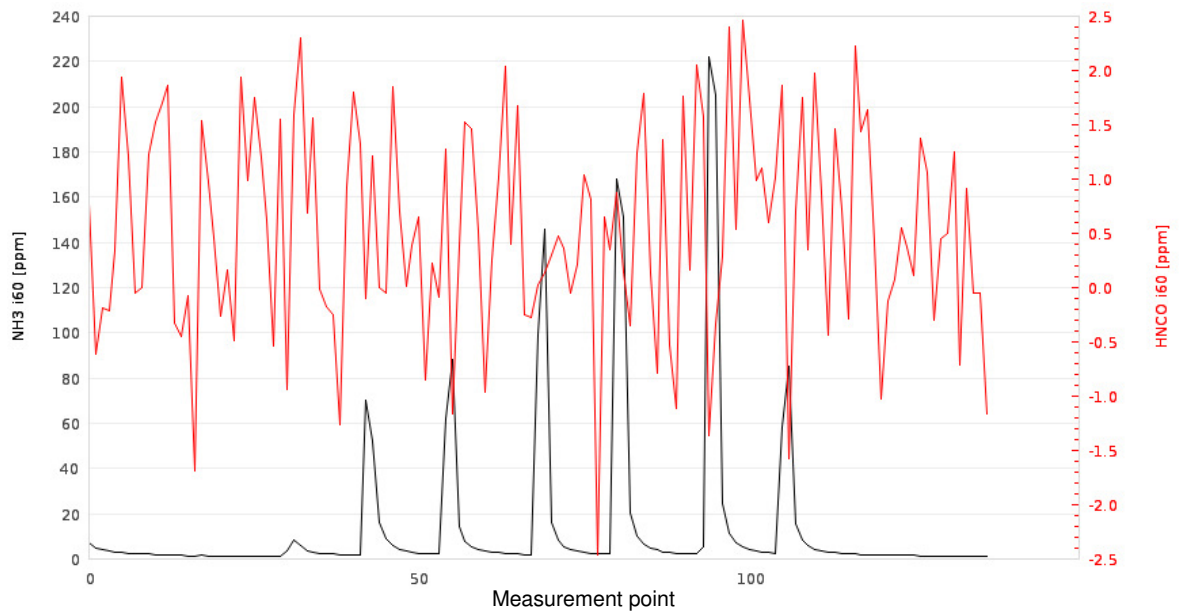
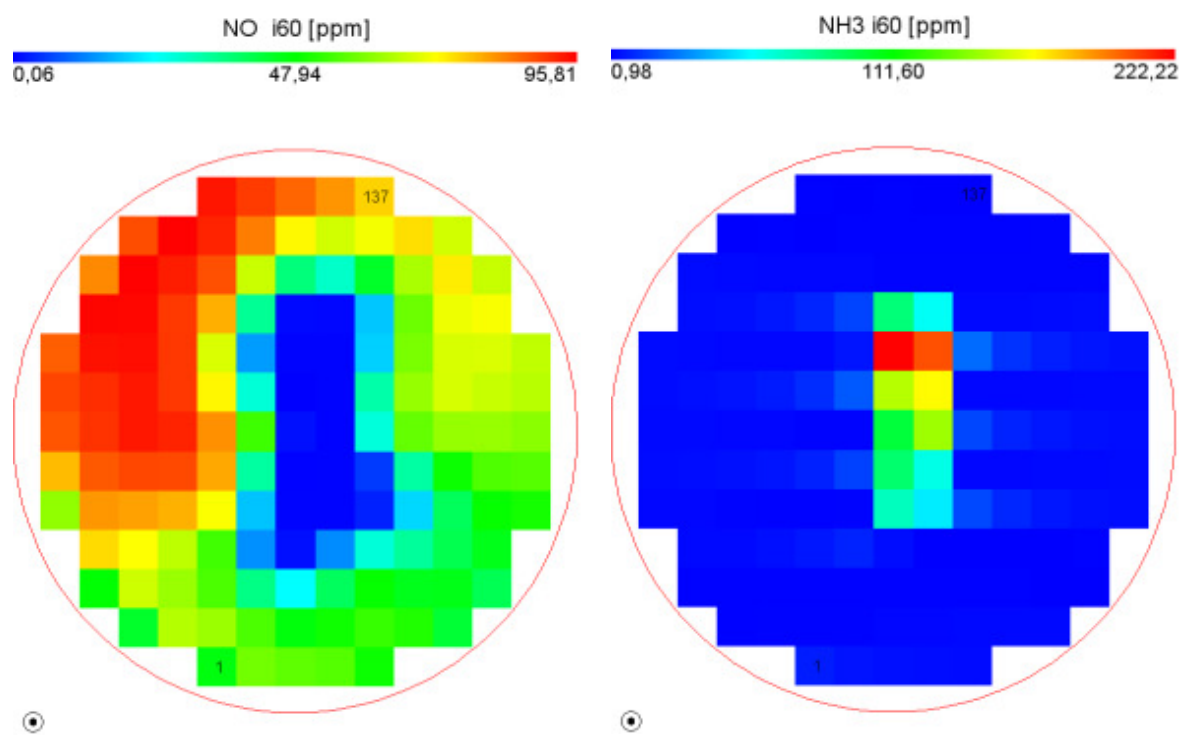
$$UI_{NH_3} = 0.375$$

$$NH_3_{ave} = 8.78 \text{ ppm}$$

$$\Delta p = 4852 \text{ Pa}$$

$$X_{NO_x} = 52.20 \%$$

Case 4: Prototype with mixer C (1st and 2nd box) / OP3 (Low)



$$U_{I_{NO}} = 0.790$$

$$NO_{ave} = 55.99 \text{ ppm}$$

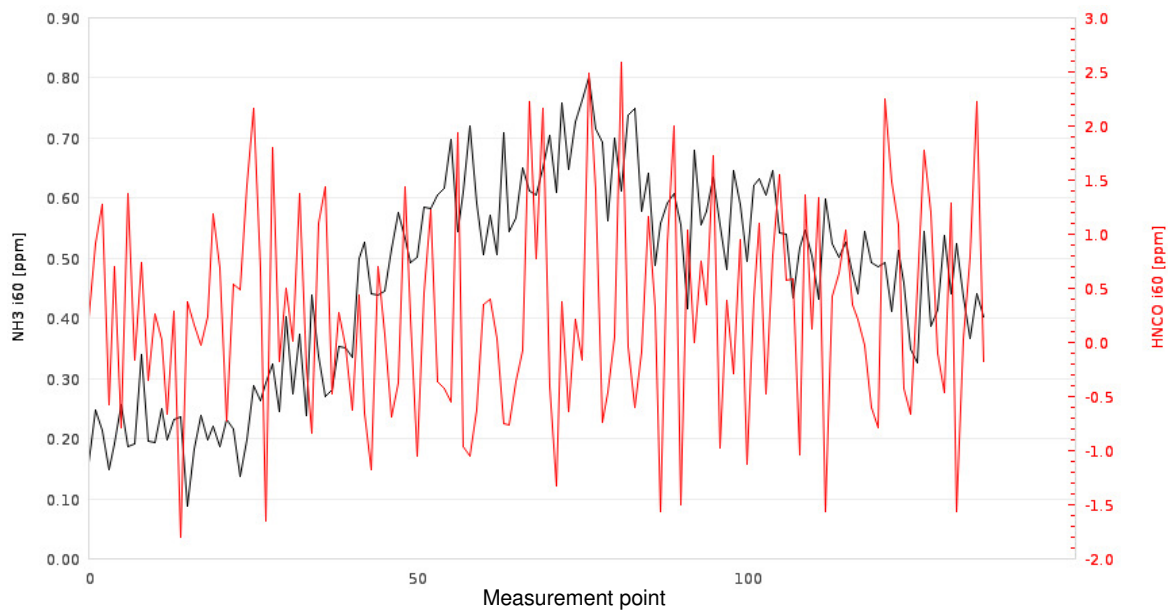
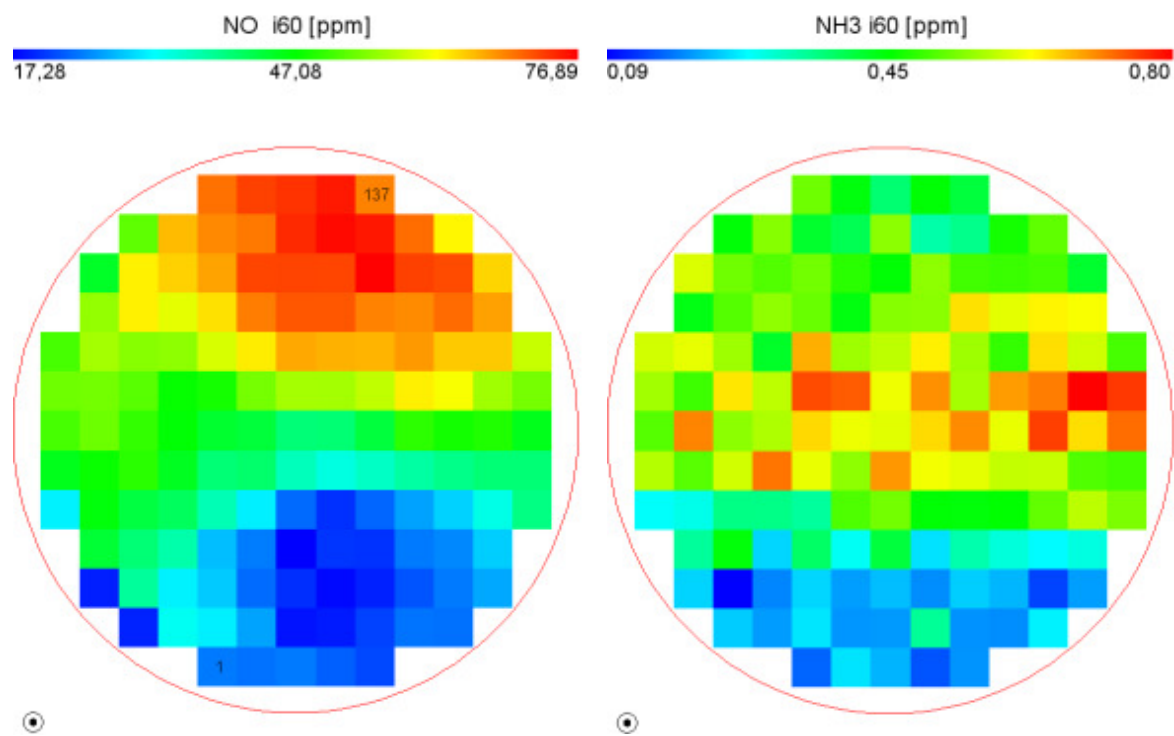
$$U_{I_{NH_3}} = 0.323$$

$$NH_{3,ave} = 13.68 \text{ ppm}$$

$$\Delta p = 1388 \text{ Pa}$$

$$X_{NOx} = 63.61 \%$$

Case 5: Prototype with mixer Tenneco 2-Stage (1st and 2nd box) / OP2 (Medium)



$UI_{NO} = 0.833$
 $NO_{ave} = 47.11 \text{ ppm}$
 $UI_{NH_3} = 0.847$
 $NH_{3,ave} = 0.47 \text{ ppm}$
 $\Delta p = 6276 \text{ Pa}$
 $X_{NOx} = 60.77 \%$

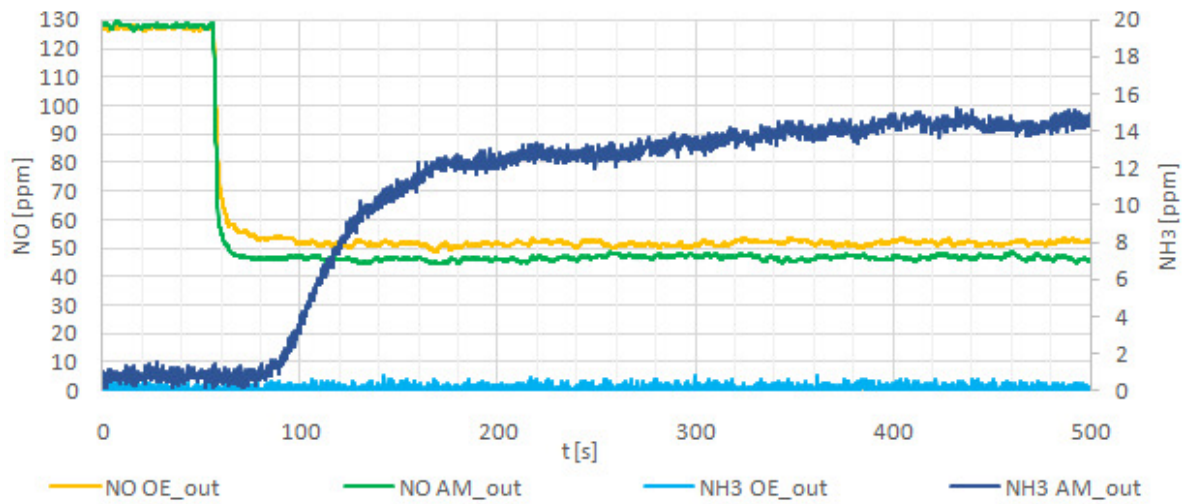
The last comparison presented in Tab. 18 shows the results of experimental tests for all three operating conditions that compare the complete WALKER aftermarket part (AM - case 6) with the original part (OE - case 7) at the outlet pipe (tailpipe) of SCR system.

For the high operating parameters (OP1), the conversion of nitrogen oxide (X_{NO}) was better for the original part $X_{NO}=63.44\%$ which gave a 5.77 percentage point better result than for the aftermarket part. On the other hand, the conversion of nitrogen oxide for OP2 in the spare part was better by 4.33 percentage points and for OP3 by 10.42 percentage points than in the original SCR part. Despite the fact that the ammonia slip for OP3 was at a similar level in both parts, the worrying situation with ammonia slip appears in aftermarket part for OP2 ($NH_{3_{ave_out_AM}}=14.32\text{ppm}$) and even more for OP1 ($NH_{3_{ave_out_AM}}=81.36\text{ppm}$). This can contribute to the formation of solid deposits, which increase the backpressure and deactivation of the catalyst. Therefore, an additional ammonia oxidation catalyst (AOC) as the last element of the system can be used or applied as a dual-layer (together with platinum of AOC) for instance on the last inch of the SCR monolith. However, in this case further research will be conducted to improve the design of the WALKER mixer. As the results of the Tenneco 2-Stage mixer tests show, ammonia slip can be well eliminated by developing a more complex mixer design.

Tab. 18. NO_x reduction efficiency for hot flow rig tests at tailpipe (Case 6-7, OP1-3)

Case 6: Prototype with mixer C vs. Case 7: Original VW part and mixer /complete part/ OP1	
$NO_{ave_out_OE} = 185.32 \text{ ppm}$ $NH_{3_{ave_out_OE}} = 2.37 \text{ ppm}$ $\Delta p_{OE} = 22668 \text{ Pa}$ $X_{NO_OE} = 63.44 \%$	$NO_{ave_out_AM} = 203.34 \text{ ppm}$ $NH_{3_{ave_out_AM}} = 81.36 \text{ ppm}$ $\Delta p_{AM} = 24744 \text{ Pa}$ $X_{NO_AM} = 57.70 \%$

Case 6: Prototype with mixer C vs. Case 7: Original VW part and mixer /complete part/ OP2



$$NO_{ave_out_OE} = 51.77 \text{ ppm}$$

$$NH_{3ave_out_OE} = 0.16 \text{ ppm}$$

$$\Delta p_{OE} = 4689 \text{ Pa}$$

$$X_{NO_OE} = 59.29 \%$$

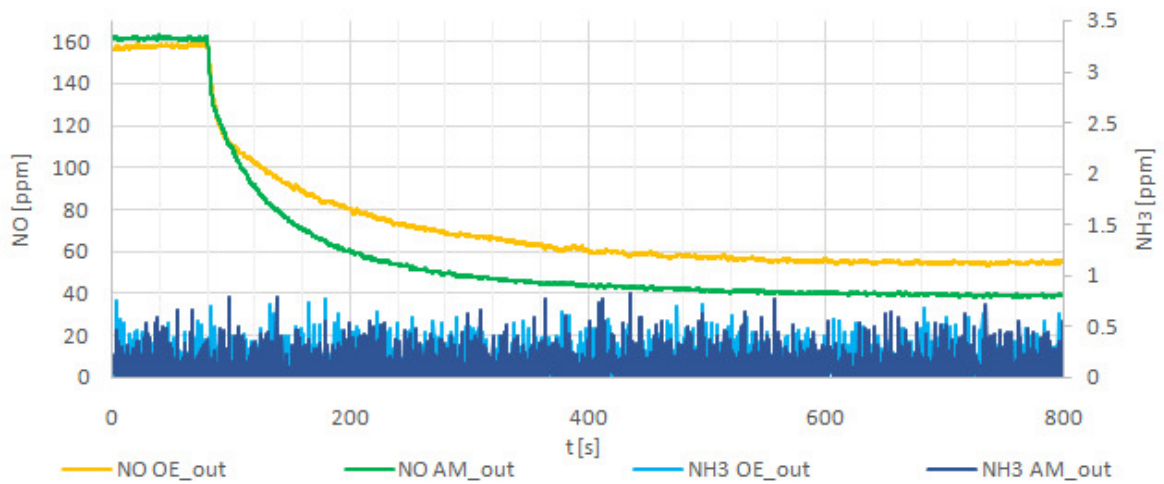
$$NO_{ave_out_AM} = 46.51 \text{ ppm}$$

$$NH_{3ave_out_AM} = 14.32 \text{ ppm}$$

$$\Delta p_{AM} = 5637 \text{ Pa}$$

$$X_{NO_AM} = 63.62 \%$$

Case 6: Prototype with mixer C vs. Case 7: Original VW part and mixer /complete part/ OP3



$$NO_{ave_out_OE} = 56.01 \text{ ppm}$$

$$NH_{3ave_out_OE} = 0.12 \text{ ppm}$$

$$\Delta p_{OE} = 1189 \text{ Pa}$$

$$X_{NO_OE} = 64.48 \%$$

$$NO_{ave_out_AM} = 40.52 \text{ ppm}$$

$$NH_{3ave_out_AM} = 0.09 \text{ ppm}$$

$$\Delta p_{AM} = 1518 \text{ Pa}$$

$$X_{NO_AM} = 74.90 \%$$

9.3 Chemical analysis of SCR catalytic converter

One of the stages of the experimental research was to check the chemical composition of the selected SCR catalyst. The active loading and other chemical elements were determined via inductively coupled plasma-optical emission spectrometry (ICP-OES). This method is also known as inductively coupled plasma-atomic emission spectrometry (ICP-AES) [132]. Fig. 61 shows a typical ICP-AES instrument. The main element of the ICP emission spectrometer is the plasma with a temperature around 8 000 - 10 000 K. Hot plasma breaks down compounds into atoms and ions. In the plasma, atoms and ions are excited to emit electromagnetic radiation as light. The light is separated by diffraction optics and a detector measures the light intensity. An element can be identified by the specific wavelength solved by the diffractive optics, and the emitted quantity of light (intensity) can be directly associated with the element's concentration [132], [133].

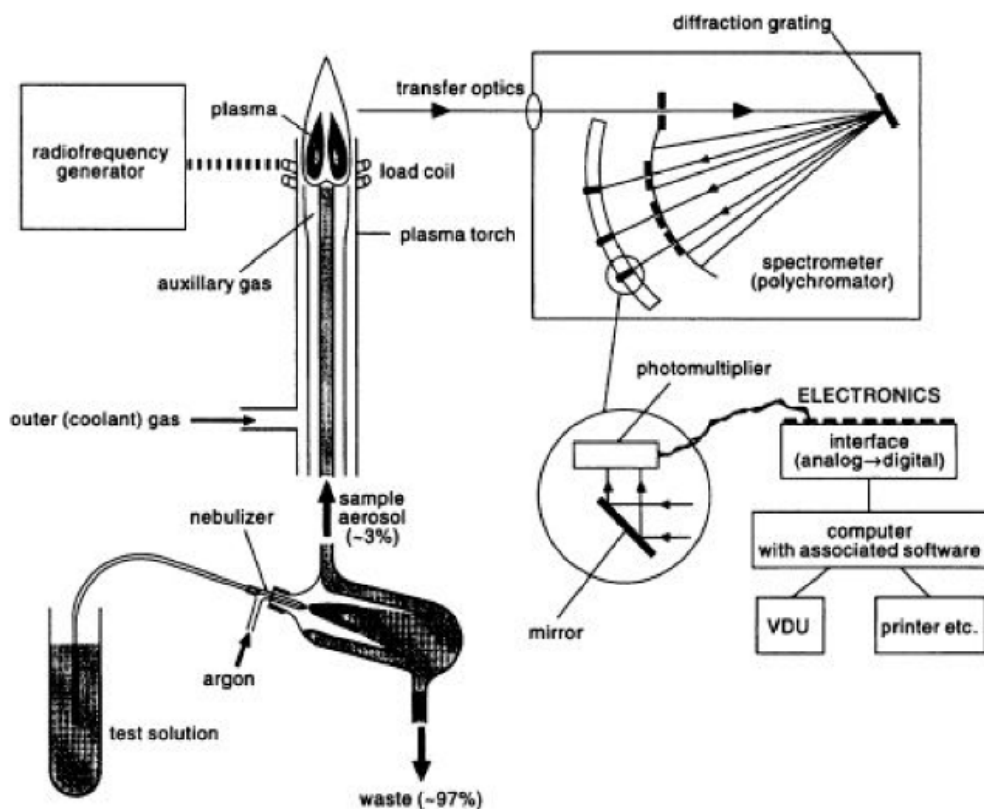


Fig. 61. Conventional simultaneous ICP atomic emission spectrometer [131]

Republished with permission of Lewis Publishers, from *Manual of physic-chemical analysis of aquatic sediments*, Mudroch E., Azcue J., M., Mudroch P., ISBN 9781566701556, 1996; permission conveyed through Copyright Clearance Center, Inc.

This one sample of vanadium catalyst has been analyzed in the laboratory of Łukasiewicz Research Network - Institute for Ferrous Metallurgy. The results of analysis i.e. the composition of elements contained in the SCR monolith are shown in Tab. 19.

Tab. 19. The results of the chemical composition analysis of the SCR catalyst

Research sample	Chemical compound	Result - mass fraction, [%]	Method and measuring device
SCR monolith with low loading	V ₂ O ₅	1.36	ICP-OES, Agilent 5100 SVDV
	TiO ₂	28.38	
	SiO ₂	35.32	
	Al ₂ O ₃	23.12	
	MgO	11.14	

9.4 Reverse engineering for CAD modelling

To start CFD simulation, first the 3D geometric models had to be prepared. For this purpose, reverse engineering was used. The process of duplicating an existing part without drawings, documentation or a computer model is known as reverse engineering (RE). In other words, RE is also defined as the process of obtaining a geometric CAD model from 3D points from scanning or digitizing the existing part. The generic process of RE is composed of three-phases: scanning, point processing and 3D model development [77].

In the beginning part geometries were scanned (Fig. 62) by noncontact scanning technology to obtain clouds of points from parts, which define the surface geometry. A laser scanner (ROMER Absolute Arm RA-7530) was used which has a measuring range of 3 m and point repeatability 0.03 mm. The output of the scanning were points clouds data from the Metrolog X4 software as raw data of points (X, Y, Z) in TXT format file.

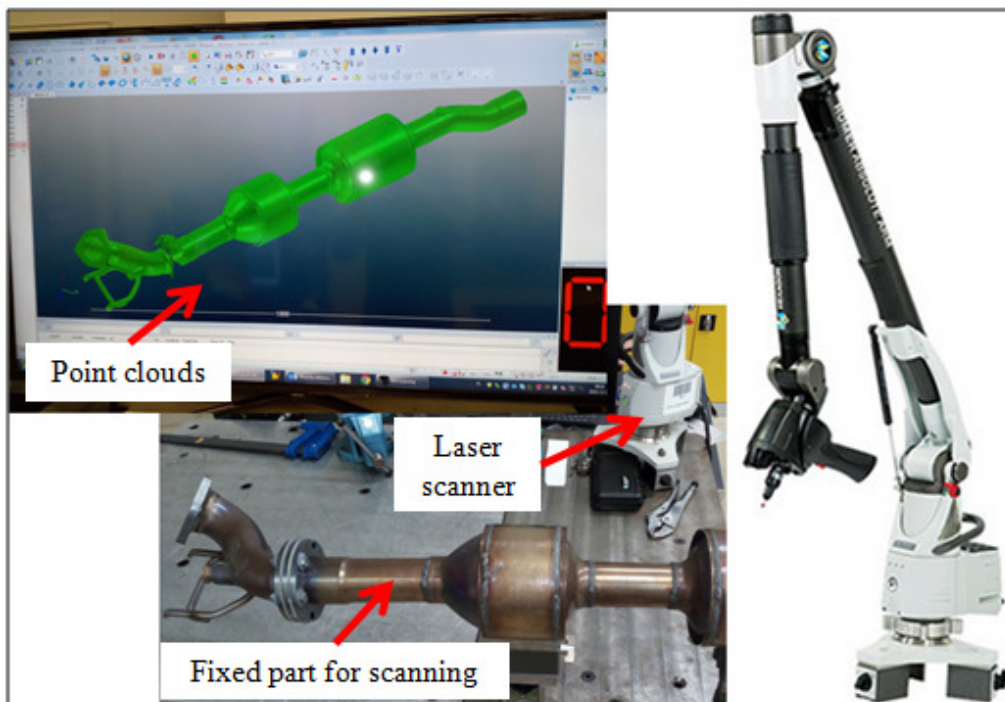


Fig. 62. Scanning a part with the ROMER Absolute Arm and obtaining a point cloud

The next step was loading the point cloud data to the Leios 2 software. Cleaning of noise and reduction of the number of points were applied. Using built-in tools, triangle meshes and cross-sections as NURBS (Non-uniform rational B-spline) were generated.

Finally, based on the base data (cross-sections, points, planes) from Leios 2, the 3D models of all SCR components in Catia v5 were reconstructed. The 3D models were made in the Generative Shape Design module and then Part Design module. The generated 3D models are presented in Fig. 63.

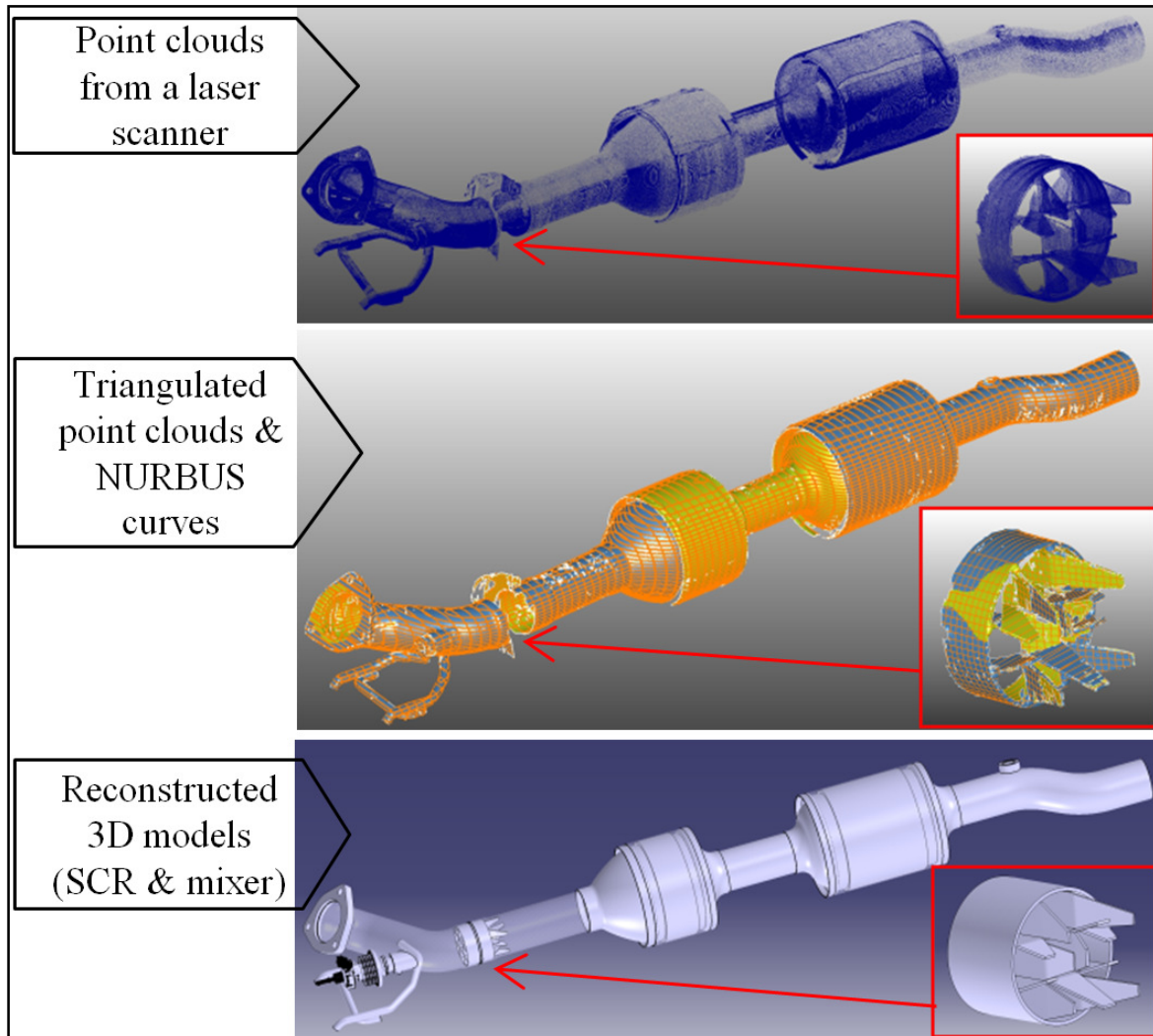


Fig. 63. Process of reverse engineering for the prototype of SCR system

The reverse engineering for the original part (Fig. 64) was similar as in the WALKER prototype. The exception was the VW mixer, in which the process ran differently due to not destroying parts (mixer cutout). Therefore, using the endoscope (IPLEX NX), the original mixer was reviewed, and thanks to this, the 3D model of the mixer in the Catia v5 program was reproduced as closely as possible.

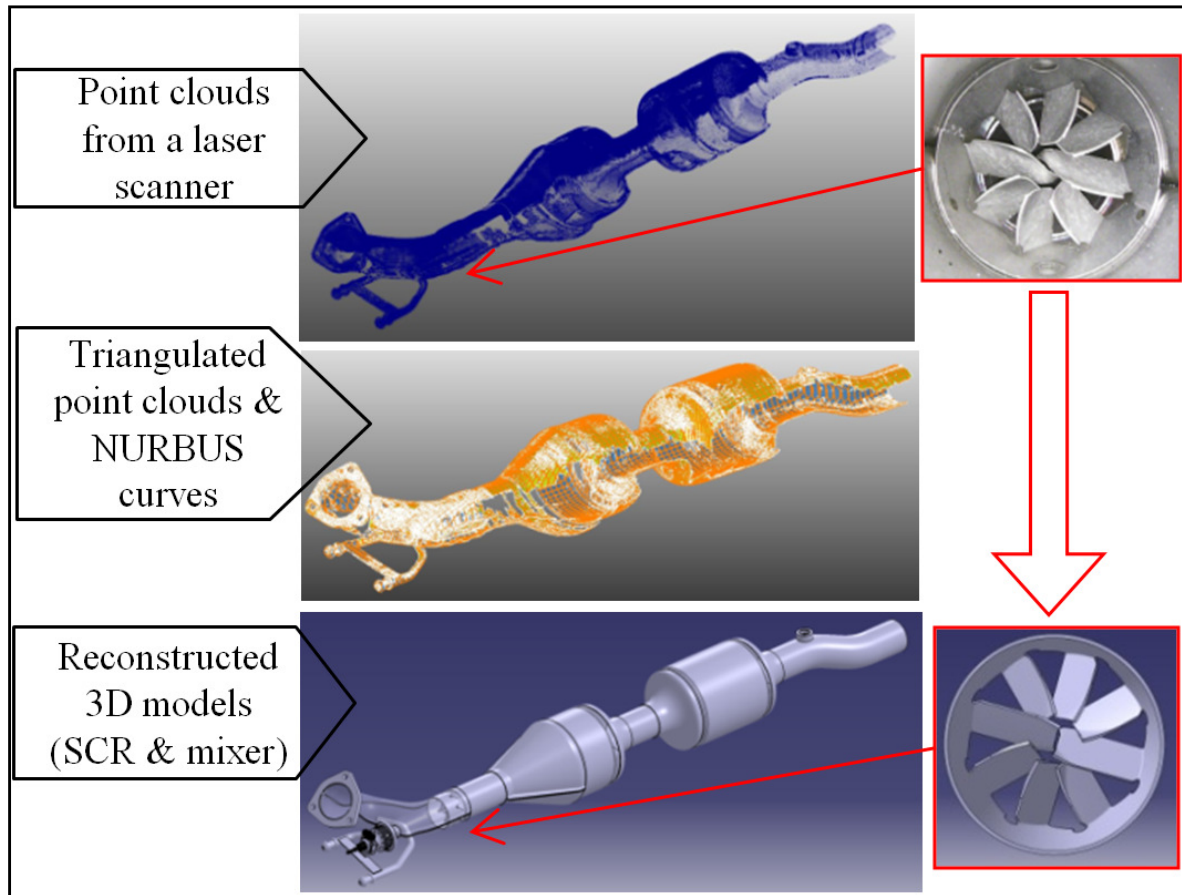


Fig. 64. Process of reverse engineering for the original SCR system

10 Numerical research

In this section, the main focus is on the basic governing equations in computational fluid dynamics (CFD), as well as on the equations describing the physicochemical phenomena occurring in the SCR system. In the appendices, basic information about CFD and modelling procedure can be found. In the following subsections, the necessary calculations that are required to be introduced in software as boundary conditions and input data for the numerical simulation will be performed. Preparation of a discrete model 2D/3D for simulation as well as necessary and relevant settings in the simulation program will be presented. The steps outlined in brief are intended to validate the numerical model of the SCR system with the previously presented experimental results.

10.1 The governing equations in computational fluid dynamics (CFD)

10.1.1 The mass, momentum and energy conservation equations

The governing equations for CFD simulations in this dissertation will be based on the ANSYS Fluent software and will be briefly described for complete and comprehensive understanding of them. The governing equations for the flow within the domain are the Reynolds Averaged Navier-Stokes (RANS) equations. The equation for *conservation of mass* (continuity equation), can be written as in Eq. (52) [73], [77], [81], [83]. The first term on the left hand side is the rate of change in time density and the second term describes the net flow of mass of the element and its boundaries (called the convective term) [72].

$$\frac{\partial \rho}{\partial t} + \nabla \cdot (\rho \vec{v}) = S_m \quad (52)$$

where:

ρ - density, t - time, \vec{v} - fluid vector velocity, S_m - any user-defined sources of mass added to the continuous phase from dispersed 2nd phase (e.g. vaporization of droplets).

The velocity fields is governed by the *momentum conservation equation* called volume averaged Navier-Stokes (VANS) [72], [73], [77]:

$$\frac{\partial}{\partial t}(\rho \vec{v}) + \nabla \cdot (\rho \vec{v} \vec{v}) = -\nabla p + \nabla \cdot (\bar{\tau}) + \rho \vec{g} + \vec{S}_i \quad (53)$$

where:

p - static pressure, $\bar{\tau}$ - stress tensor, \vec{g} - gravitational acceleration, \vec{S}_i - is the i -th body force (source term, force per unit volume). In this study, the momentum source arose, from interaction with dispersed phase and the presence of porous-media.

The stress tensor $\bar{\tau}$ is given by [73], [88]:

$$\bar{\tau} = \mu \left[(\nabla \vec{v} + \nabla \vec{v}^T) - \frac{2}{3} \nabla \cdot \vec{v} I \right] \quad (54)$$

where:

μ - molecular viscosity, I - unit tensor which is related to the effect of volume dilation.

For the porous zone (e.g. monolith of SCR), the velocity is replaced with the superficial velocity, which is equal to the fluid physical velocity inside the porous zone multiplied by the medium porosity. The source term vector \vec{S}_i of the external body force was non-zero in the porous zone and its components were modelled using the Darcy-Forchheimer formula for simple homogeneous porous zone [74], [76], [77]:

$$S_j = \frac{\Delta p}{\Delta L_j} = - \left(\frac{\mu}{\alpha_m} v_j + C_2 \frac{1}{2} \rho v_j^2 \right) \quad (55)$$

where:

S_j - source vector component in direction j , Δp - pressure drop, μ - laminar fluid viscosity, α_m - permeability of the medium, C_2 - inertial resistance, v_j - velocity in direction j , ρ - density, ΔL_j - thickness of the medium direction j .

As seen in Eq. (55), the first part account for viscous resistance (viscous loss), with a proportionally coefficient $1/\alpha_m$ and the second term accounts for inertial resistance (inertial loss) with inertial resistance coefficient C_2 . To find the viscous and inertial resistance coefficients for a porous material, a pressure drop correlation $\Delta p = f(v)$ modelled with a quadratic polynomial function will be determined from the experiments and used in the CFD simulations. From Eq. (55), it may be noticed that a source term will also take the form of parabolic function, which in general can be written in the form:

$$\Delta p = av^2 + bv \quad (56)$$

Comparing Eq. (55) with Eq. (56), the viscous and inertial resistance coefficients can be calculated from the following relations [76], [77]:

$$\frac{1}{\alpha_m} = - \frac{b}{\mu \Delta L_i} \quad (57)$$

$$C_2 = - \frac{2a}{\rho \Delta L_i} \quad (58)$$

The flow of thermal energy from material occupying one region in space to material occupying a different region in space is called heat transfer and can appear by conduction, convection and radiation. The *energy equation* solved in ANSYS Fluent includes all above mentioned heat transfer modes and has the following form [73]:

$$\frac{\partial}{\partial t} (\rho E) + \nabla \cdot [\vec{v}(\rho E + p)] = \nabla \cdot \left[k_{eff} \nabla T - \sum_j h_j \vec{J}_j + (\bar{\tau}_{eff} \cdot \vec{v}) \right] + S_h \quad (59)$$

where:

E - is the sum of specific inertial and kinetic energy, k_{eff} - effective (molecular and turbulent) thermal conductivity, \vec{J}_j - species j diffusion flux, T - temperature, h_j - specific enthalpy, $\bar{\tau}_{eff}$ - effective stress tensor.

The volumetric heat source S_h represents any energy source in the system, which can also include the heat generation rate due to radiation and from chemical reactions. In the latter case energy sources due to chemical reactions can be written as [73]:

$$S_{h,rxn} = - \sum_j \frac{h_j^0}{M_j} R_j \quad (60)$$

where:

h_j^0 - enthalpy of formation of species j , R_j - volumetric rate of creation of species j , M_j - molar mass of species j .

Other sources are due to the exchange of heat between discrete particles and the fluid, and due to radiation, which was not included in the numerical model because of its simplification.

10.1.2 Species transport equations and finite-rate formulation for reactions

ANSYS Fluent can be used to model the mixing and transport of chemical species by solving the conservation equations describing convection, diffusion, and reaction sources for each component species. Multiple simultaneous chemical reactions can be modelled, with reactions occurring in the bulk phase (volumetric reactions). Since the transport of multiple species has to be taken into account, the mass conservation of the subsequent species is also included in the set of equations. The convection-diffusion equation for the i^{th} species reads [73], [80], [84], [90]:

$$\frac{\partial}{\partial t} (\rho Y_i) + \nabla \cdot (\rho \vec{v} Y_i) = -\nabla \cdot \vec{J}_i + R_i + S_i \quad (61)$$

where:

Y_i - local mass fraction of species i , R_i - net rate of production of species i by chemical reaction, S_i - represent other sources of species i , e.g. from discrete phase.

The diffusion flux vector \vec{J}_i of species i can be calculated from Eq. (62) or (63), respectively, for laminar and turbulent flow regimes [73], [80], [90]:

$$\vec{J}_i = -\rho D_{i,m} \nabla Y_i - D_{T,i} \frac{\nabla T}{T} \quad (62)$$

$$\vec{J}_i = -\left(\rho D_{i,m} + \frac{\mu_t}{S_c}\right) \nabla Y_i - D_{T,i} \frac{\nabla T}{T} \quad (63)$$

where:

$D_{i,m}$ - mass diffusion coefficient for species i in the mixture, $D_{T,i}$ - thermal (Soret) diffusion coefficient, μ_t - turbulent viscosity, S_c - turbulent Schmidt number.

The finite-rate kinetics are incorporated by computing the chemical source terms using general reaction-rate expressions. The net source of chemical species i due to reaction is computed as the sum of the reaction sources over N_R reactions that the species participate in [73], [79], [90]:

$$R_i = M_{w,i} \sum_{r=1}^{N_R} \hat{R}_{i,r} \quad (64)$$

where:

$M_{w,i}$ - molecular weight of species i , $\hat{R}_{i,r}$ - molar rate of creation or deconstruction of species i in reaction r .

In this dissertation, non-reversible reactions will be used, thus the molar rate of creation or deconstruction of species i in a reaction r is given by [73], [79], [90]:

$$\hat{R}_{i,r} = (v''_{i,r} - v'_{i,r}) \left(k_{f,r} \prod_{j=1}^N [C_{j,r}]^{(\eta'_{j,r} + \eta''_{j,r})} \right) \quad (65)$$

where:

N - number of chemical species in the system, $v'_{i,r}$, $v''_{i,r}$ - stoichiometric coefficients for reactant and product respectively in reaction r , $k_{f,r}$ - forward rate constant for reaction r , $C_{j,r}$, $kmol/m^3$ - molar concentration of species j in reaction r , $\eta'_{j,r}$, $\eta''_{j,r}$ - rate exponent in reaction r reactant and product, respectively.

The forward rate constant for reaction is computed using the Arrhenius expression [73], [79], [90]:

$$k_{f,r} = A_r T^{\beta_r} e^{\left(\frac{-E_r}{RT}\right)} \quad (66)$$

where:

A_r - pre-exponential factor or frequency factor, β_r - temperature exponent (equal to 0 for this dissertation), E_r - activation energy for the reaction, R - universal gas constant.

10.1.3 Turbulence $k-\varepsilon$ model equations

In ANSYS Fluent software there are three $k - \varepsilon$ models for turbulent flows such as Standard, RNG and Realizable. The differences in the models are mainly for turbulent

viscosity, turbulent Prandtl numbers, generation and destruction terms in the dissipation of the turbulent kinetic energy equation [73]. The Standard $k - \varepsilon$ model is built on equations describing the turbulent kinetic energy (k), and its dissipation rate (ε). The model has two separate transport equations that allow for estimating independently the turbulent viscosity and the length scales. What is more, it is a semi-empirical model based on the assumption that the whole flow is turbulent and the molecular viscosity effects are insignificant [71].

In this study the RNG $k - \varepsilon$ model will be used as a first of two improved $k - \varepsilon$ models available in ANSYS Fluent. This model is derived from Navier-Stokes instantaneous equations using a technique called RNG (renormalization group). The improved model leads to following differences to the original one [71], [73]:

- additional term in the dissipation rate improving the accuracy for rapid strained flows;
- improved accuracy for swirling flows due to new effects of swirls on the turbulence;
- analytical equation for turbulent Prandtl number instead constant values;
- analytically-derived differential formula for effective viscosity of low-Reynolds no.

All of these features make the RNG model reliable and more accurate for a wider class of flows than the standard $k - \varepsilon$ model. Thus the RNG model allows for better handling of low-Reynolds numbers and near-wall flows. Moreover, it is good for moderately complex behavior like jet impingement, separating flows, swirling flows and secondary flows [73].

The transport equations for the RNG $k - \varepsilon$ model (a similar form to the to the standard $k - \varepsilon$ model) are [71], [82]:

$$\frac{\partial}{\partial t}(\rho k) + \frac{\partial}{\partial x_i}(\rho k v_i) = \frac{\partial}{\partial x_j} \left(\alpha_k \mu_{eff} \frac{\partial k}{\partial x_j} \right) + G_k + G_b - \rho \varepsilon - Y_M + S_k \quad (67)$$

$$\frac{\partial}{\partial t}(\rho \varepsilon) + \frac{\partial}{\partial x_i}(\rho \varepsilon v_i) = \frac{\partial}{\partial x_j} \left(\alpha_\varepsilon \mu_{eff} \frac{\partial \varepsilon}{\partial x_j} \right) + C_{1\varepsilon} \frac{\varepsilon}{k} (G_k + C_{3\varepsilon} G_b) - C_{2\varepsilon} \rho \frac{\varepsilon^2}{k} - R_\varepsilon + S_\varepsilon \quad (68)$$

where:

G_k - the production of turbulence kinetic energy due to the mean velocity gradients, G_b - the production of turbulence kinetic energy due to buoyancy, Y_M - the contribution of the fluctuating dilatation in compressible turbulence to the overall dissipation rate, $\alpha_k, \alpha_\varepsilon$ - the inverse effective Prandtl numbers, S_k, S_ε - user-defined source terms, R_ε - the additional term for rapidly strained flows which leads to a lower turbulent viscosity, v_i - fluid velocity, μ_{eff} - effective viscosity, $C_{1\varepsilon}, C_{2\varepsilon}, C_{3\varepsilon}$ - model constants.

10.1.4 Discrete Phase Model for spray

ANSYS Fluent allows for simulation of a discrete second phase in the Lagrangian frame of reference. This second phase consists of particles dispersed in the continuous phase. The trajectories of these discrete phase entities can be computed along with heat and mass transfer to and/or from them. The coupling between the continuous phase and the discrete second phase and its impact on discrete phase trajectories and the flow of continuous phase can be included. There are the following main options of discrete phase for: trajectory, turbulence, heating/cooling, vaporization/boiling, combusting particles, breakup/coalescence and collisions [74].

The CFD techniques together with the discrete phase model (DPM) allow to solve differential equations for trajectory, momentum, heat and mass transfer of every single spray droplet or their group. The particles are introduced in the flow domain with initial conditions of position, size, velocity, temperature and number of particles. The Lagrangian description of motion is then used for tracking the particles through the computational grid [92]. Using Newton's second law (the net force on an object is equal to the rate of change of its linear momentum in an inertial reference force), the particle motion is represented by the ordinary differential equation [73], [86], [89], [92]:

$$m_d \frac{d\vec{v}_{id}}{dt} = \vec{F}_{idr} + \vec{F}_{ip} + \vec{F}_{im} + \vec{F}_{ig} + \vec{F}_{io} \quad (69)$$

where:

m_d - droplet mass, \vec{v}_{id} - droplet velocity, \vec{F}_{idr} - drag force, \vec{F}_{ip} - pressure force, \vec{F}_{im} - virtual mass force, \vec{F}_{ig} - force of gravity, \vec{F}_{io} - other forces (e.g. from particle collisions).

The multicomponent particles are described as droplet particles containing a mixture of several components or species (e.g. UWS i.e. urea-water solution in SCR). The effect of the convective flow of the evaporating material from the droplet surface to the bulk gas phase (Stefan Flow) and the rate of evaporating mass (convection/diffusion controlled model) is given by [73], [78], [87]:

$$\frac{dm_i}{dt} = A_p k_{c,i} \rho \ln(1 + B_{m,i}) \quad (70)$$

where:

m_i - mass of component in droplet, A_p - droplet surface area, ρ - gas density.

The Spalding mass number $B_{m,i}$ for species i is given by:

$$B_{m,i} = \frac{Y_{i,s} - Y_{i,\infty}}{1 - Y_{i,s}} \quad (71)$$

where:

$Y_{i,s}$ - vapor mass fraction at the surface, $Y_{i,\infty}$ - vapor mass fraction in the bulk gas.

The mass transfer coefficient $k_{c,i}$ of component i is calculated from the Sherwood number correlation:

$$Sh = \frac{k_{c,i}d_p}{D_{i,m}} = 2.0 + 0.6Re_d^{1/2}Sc^{1/3} \quad (72)$$

where:

d_p - particle (droplet) diameter, $D_{i,m}$ - diffusion coefficient of vapor in the bulk, Sc - the Schmidt number, Re_d - the Reynolds number.

The single-rate model is used for thermolysis of UWS by the Arrhenius expression to calculate the mass transfer rate from the droplet to the bulk phase [53], [73], [87], [92] :

$$\frac{dm_d}{dt} = \pi d_p A_r e^{(-E_r/RT_p)} \quad (73)$$

where:

m_d - droplet mass, d_p - droplet diameter, A_r - pre-exponential factor, E_r - activation energy, T_p - particle temperature, R - universal gas constant.

The discrete phase model is also used to simulate the wall film, as shown in Fig. 65. ANSYS Fluent has a specific boundary condition for simulation of liquid droplets colliding with walls and creating thin films. Therefore, for fast transient effects, the transient Lagrangian particles to discrete physical effects is used as an Eulerian model for steady wall films [73].

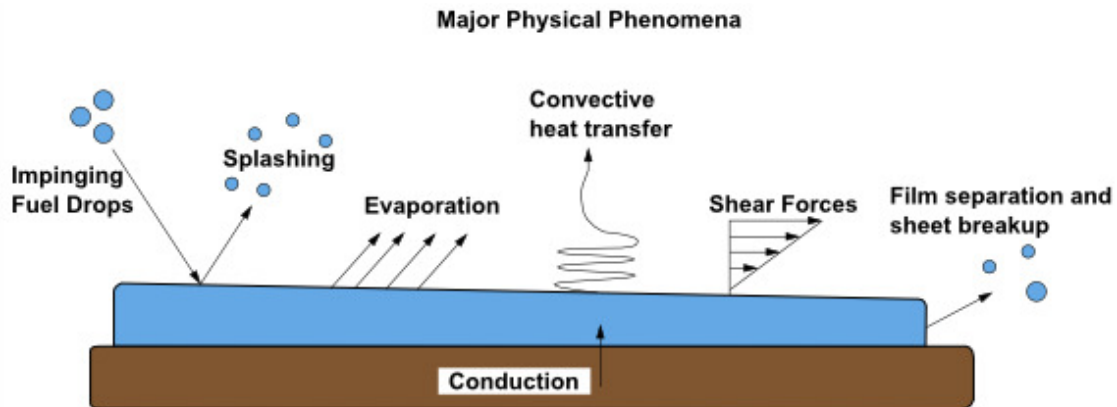


Fig. 65. Wall film model [73]
Copyright 2016, Images used courtesy of ANSYS, Inc.

Wall film creation (of a thickness $\sim 500\mu\text{m}$) is an important factor for the SCR due to urea crystallization at low temperature and forming deposits. Hence, not including the wall film formation in the SCR model can lead to an incorrect estimate of NO_x conversion. The temperature in the film changes relatively slowly (it never exceeds the boiling) but the heat transfer from the wall to the film takes place by conduction. A thin liquid film is created as liquid drops impinge on a solid surface in the domain. From this impingement there are several outcomes [73]:

- stick - the droplet impacts the wall with little energy and remains nearly spherical;
- rebound - the drop leaves the surface relatively undisturbed but with changed velocity;
- deposition (or spread) - the drop hits the wall with moderate energy and spreads out into the film (creating wall film);
- splash (or dry splash - thermal breakup) - part of the impinging drop joins the film (creating wall film) and other part leaves the wall in several other smaller drops.

The Kuhnke model (Fig. 66) considers all relevant impingement phenomena by classifying them into four regimes based on the dimensionless variables K and T^* .

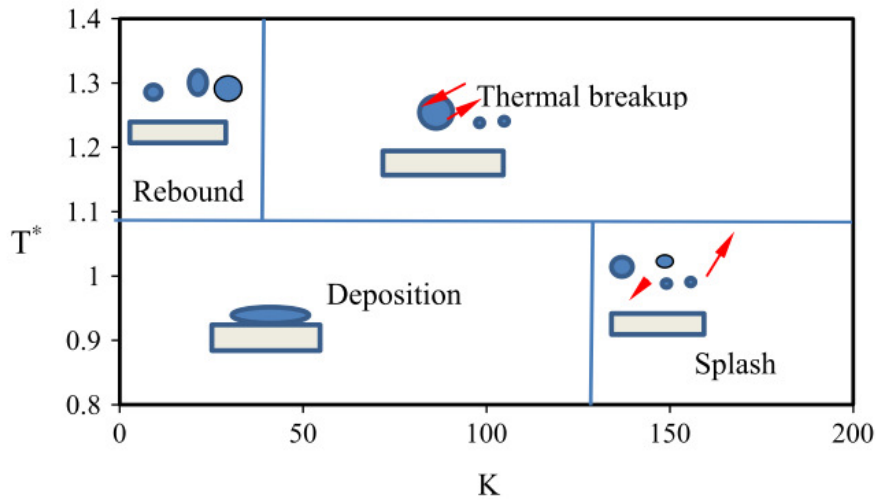


Fig. 66. Splashing regime map according to Kuhnke [85]

Reprinted from *Applied Thermal Engineering*, Vol. 111, Scheuer Prabhu S. S., Nayak N. S., Kapilan N., Hindasageri V., *An experimental and numerical study on effects of exhaust gas temperature and flow rate on deposit formation in Urea-Selective Catalytic Reduction (SCR) system of modern automobiles*, 1211-1231, Copyright 2017, with permission from Elsevier.

The Kuhnke impingement model is one of the most comprehensive models that takes into account the effect of several important parameters such as wall temperature, droplet impingement conditions, droplet material properties, surface roughness and wall film height [87]. To calculate the interaction between the droplets and the walls, the dimensionless parameters after substitution with Weber and Laplace Nos. are given by [53], [73], [85], [87]:

$$K = \frac{(\rho d_p)^{3/4} (v_{pn})^{5/4}}{\sigma^{1/2} \mu_d^{1/4}} \quad (74)$$

$$T^* = T_w/T_{sat} \quad (75)$$

where:

ρ - droplet density, d_p - droplet diameter, v_{pn} - normal impingement velocity, σ - droplet surface tension, μ_d - droplet dynamic viscosity, T_w - wall temperature, T_{sat} - droplet saturation temperature.

The four regimes are used to predict droplet behavior [53], [85]:

- for $T^* < 1.1$ and low droplet velocity, all the impacting droplets are deposited on the wall and create a film;
- for $T^* < 1.1$ and high velocity of the impacting droplet, splashing occurs, the droplet breaks into smaller droplets and part of the droplet mass forms a wall film;
- for $T^* > 1.1$ and low impact velocity, the droplets reflect and no film is formed due to the generated vapour sheet between the particles and the wall;
- for $T^* > 1.1$ and high impact velocity, the droplets are atomized into smaller droplets without transferring mass to the wall film.

ANSYS Fluent uses parcel based conservation equations of momentum, mass and energy for film tracking, after the film formation on a surface. For the momentum of a film parcel it solves Eq. (76) [73], [87]:

$$\rho h \frac{d\vec{v}_p}{dt} = \tau_g \vec{t} + \vec{\tau}_w + \vec{F}_f + \rho h (\vec{g} - \vec{\alpha}_w) \quad (76)$$

where:

\vec{v}_p - is the film particle velocity, τ_g - is the magnitude of the shear stress of the gas flow on the surface of the film, \vec{t} - is the unit vector in the direction of the film surface velocity, $\vec{\tau}_w$ - is the stress that the wall exerts on the film, \vec{F}_f - is the force per unit area necessary to keep the film on the surface, h - is the current film height at the particle location, ρ - density of liquid film, \vec{g} - acceleration due to gravity, $\vec{\alpha}_w$ - wall acceleration.

For the mass conservation, the vaporization rate is governed by convection/diffusion controlled model [73], [87]:

$$\dot{N}_l = k_{film} \rho_\infty \ln(1 + B_m) \quad (77)$$

$$B_m = \frac{Y_{i,s} - Y_{i,\infty}}{1 - Y_{i,s}} \quad (78)$$

where:

\dot{N}_i - vapor mass flux of species i , k_{film} - film mass transfer coefficient, ρ_∞ - density of the bulk gas, B_m - Spalding mass number, $Y_{i,s}, Y_{i,\infty}$ - mass fraction of species i on the film surface and in the bulk respectively.

For energy conservation, the energy flux from the gas side as well as energy flux from the wall side must be considered to obtain an equation for the temperature in the film. Therefore, the energy transfer from/to the film particle is then given by [73], [87]:

$$\frac{d}{dt}(m_p c_p T_p) = Q_{p,cond} + Q_{p,conv} - \dot{m}_p h_{fg} \quad (79)$$

where:

m_p, c_p, T_p - the mass, specific heat and temperature of the film parcel respectively, $Q_{p,cond}$ - the conduction from the wall, $Q_{p,conv}$ - the convective heat flux at the surface, \dot{m}_p - the film parcel vaporization rate, h_{fg} - the latent heat of vaporization.

One of the possible representations of the droplet diameter distribution (one of the basic parameters of an injection) in ANSYS Fluent is the Rosin-Rammler method. The distribution function of Rosin-Rammler is used to initialize droplet size distribution into the gas phase. An exponential relationship between the droplet diameter d and the mass fraction Y_d of droplets with diameter greater than d is defined in Eq. (80) [74], [78], [91]:

$$Y_d = e^{-(d/\bar{d})^n} \quad (80)$$

$$n = \frac{\ln(-\ln Y_d)}{\ln(d/\bar{d})} \quad (81)$$

where:

d - diameter, \bar{d} - size parameter (mean diameter), n - size distribution (spread parameter).

The larger the value of the spread parameter n , the narrower the droplet size distribution is.

10.2 Data acquisition for CFD simulation

This subsection will describe the necessary data that have been obtained from the literature as well as from experimental research with mandatory calculations which are needed for CFD simulations. First, a description of the data for the porous model will be provided based on previous pressure drop studies. Then, data for spray model and reaction

kinetics, which were acquired from literature will be described. Finally the necessary calculations and applied methodology will be presented.

10.2.1 Porous model

Input data of pressure drops for the porous model have already been presented in Fig. 55 and Fig. 58 in chapter 9.1.1 for all investigated cases from Tab. 9. The quoted quadratic polynomial equation has been used for calculating the coefficients (viscous and inertial resistance) for the CFD porous model. The formulas for the calculation of these coefficients have also already been derived (Eq. (57) and Eq. (58)) and described in chapter 10.1.1. For these formulas a density $\rho = 1.204 \text{ kg/m}^3$, dynamic viscosity $\mu = 1.82E - 05 \text{ Pa} \cdot \text{s}$ at temperature $T = 295 \text{ K}$ were used, as well as thickness for the front SCR monolith ($\Delta L = 0.0762 \text{ m}$) and rear SCR monolith ($\Delta L = 0.1524 \text{ m}$). By substituting these data into the formulas, it was possible to calculate the needed coefficients presented in the Tab. 20.

Tab. 20. Viscous and inertial resistance for porous model

Investigated case	Viscous resistance $1/\alpha_m, 1/m^2$	Inertial resistance $C_2, 1/m$
Case 1, 2, 3 Front Monolith	4.34E+07	357.94
Case 4, 5, 6 Front Monolith	9.34E+07	1150.12
Case 7 Front Monolith	8.16E+06	1540.76
Case 4, 5, 6, 7 Rear Monolith	6.72E+07	394.45

10.2.2 Spray of Urea-Water-Solution (UWS) model and decomposition

In this dissertation for 3D simulations, the particle stream for the injector of SCR will be defined as a type of solid-cone injection (Fig. 67). They key parameters to set the spray cone are the position coordinates of the origin, the diameters of the particles in the stream, the temperature of streams, the cone's axis and angle, the velocity magnitude of the streams, the radius of injection and the mass flow rate.

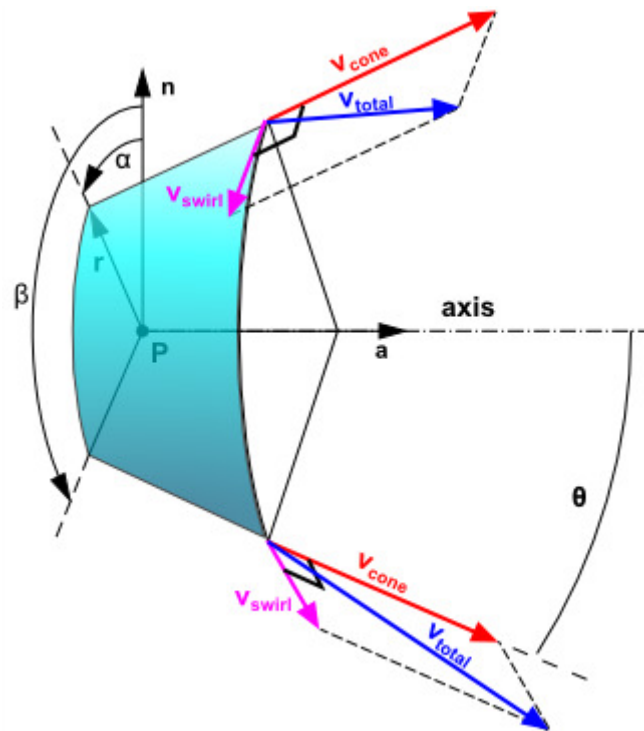


Fig. 67. Cone injector geometry [74]
Copyright 2013, Images used courtesy of ANSYS, Inc.

A BOSCH AdBlue injector (original reference number 3C0131113C) was used in this study. This injector (Fig. 68) has three nozzle holes, therefore in the CFD simulation, three separate solid-cone injections will be initiated.

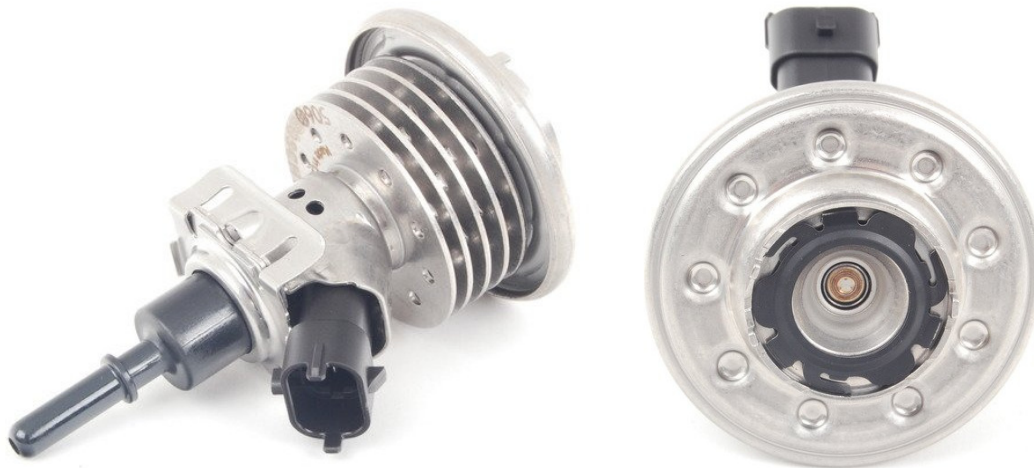


Fig. 68. Applied AdBlue injector in the SCR system

In order to correctly set up each injection in the ANSYS Fluent for CFD simulation, it was necessary to acquire the essential properties that describe the injector as well as its final spray. The vital parameters are presented in Tab. 21 and the visualization of the spray is shown in Fig. 69.

Tab. 21. The main parameters describing the injector

Parameter	Value
Number of nozzle holes	3
Hole diameter	0,12 mm
The diameter the holes are placed on	1,9 mm
AdBlue injection pressure	5 bar
Initial droplet velocity	24 m/s
Hole spacing angle	120°
Visual spray cone angle	16°
Single cone angle	8°
Injection angle	6°
Mass flow rate for all three injections (OP1)	0,6505 kg/h
Mass flow rate for all three injections (OP2)	0,0636 kg/h
Mass flow rate for all three injections (OP3)	0,0389 kg/h
AdBlue temperature	293,15 K

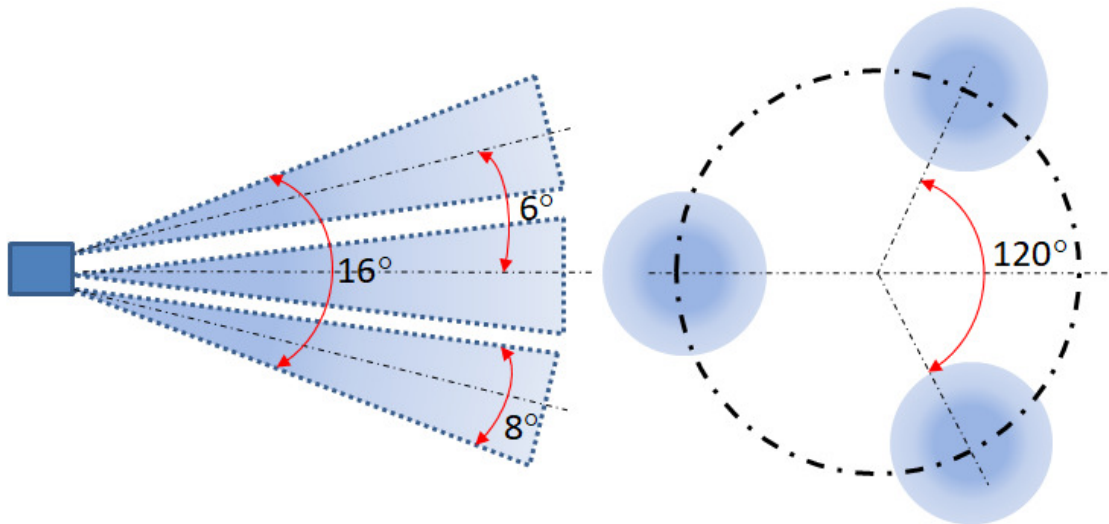


Fig. 69. Spray of injector with its main angles

The data presented in Tab. 21, however, are not sufficient to correctly define the injection simulation. It was required to obtain droplet distribution of urea-water-solution (UWS) for this type of injector. The same type of injector has been investigated by Shahariar et al. [86], therefore, UWS droplet distribution (Fig. 70) of this work will be used. UWS droplets are mainly ranged from 5 μm to 85 μm and such data was used for ANSYS Fluent as minimum and maximum droplet diameter. Moreover, it is required to enter data for the mean diameter (\bar{d}) and spread parameter (n) from Eq. (80) and Eq. (81). For this purpose, the Rosin-Rammler diameter distribution method was used [146]. Particle size distribution can be defined easily by fitting the size distribution data to the Rosin-Rammler Eq. (80). In this method, the complete range of particle sizes is divided into a set of discrete ranges, each to be defined by a single stream that is part of the group.

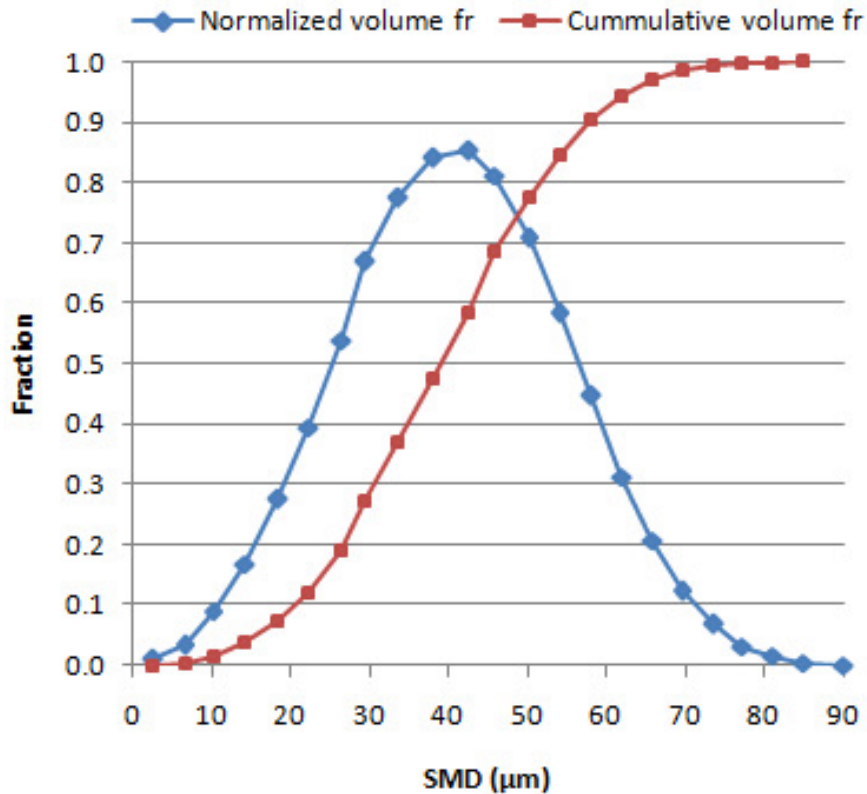


Fig. 70. UWS droplet distribution at 5 bar injection [86]

The particle size data from Fig. 70 show the following distribution as in Tab. 22.

Tab. 22. Particle size distribution

Diameter range [μm]	Mass fraction in range
0-10	0,017
10-20	0,056
20-30	0,201
30-40	0,203
40-50	0,298
50-60	0,129
60-70	0,081
70-80	0,013
80-90	0,003

To find the mean diameter (\bar{d}) and spread parameter (n) from Eq. (81), it is necessary to fit particle size data in terms of Rosin-Rammler format. The values of Y_d and n can be calculated and shown in Tab. 23. The value for \bar{d} is obtained by noting that this is the value of d at which $Y_d = e^{-1} \approx 0.368$. From Fig. 71, the value of d can be obtained where the value of Y_d is 0.368 what gives $\bar{d} = 45 \mu m$. Numerical value for n can be given as Eq. (81) by substituting data from Tab. 23 into this equation and calculate an average value ($n = 3.191$).

Tab. 23. The values of Y_d and n , determined from the given data in Tab. 24

Diameter, d [μm]	Mass fraction with diameter greater than d , Y_d	Spread parameter, n
10	0,983	2,70
20	0,927	3,17
30	0,726	2,78
40	0,524	3,55
50	0,226	3,96
60	0,096	3,01
70	0,015	3,27
80	0,003	3,11
90	0,000	
An average value of $n =$		3.191

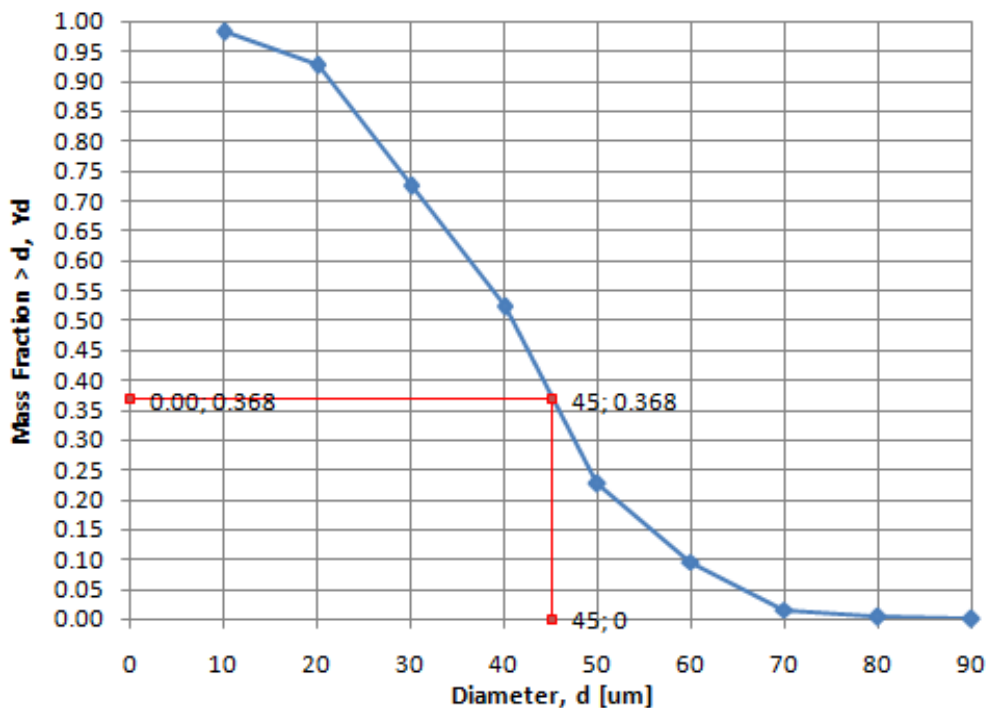


Fig. 71. Cumulative size distribution of particles

10.2.3 Reaction kinetics and mechanism

Another important element in the preparation and acquisition of data for CFD simulations was the implementation of reaction kinetics for the reduction of nitric oxide by a SCR catalyst. The ANSYS Fluent program is equipped with many ready models representing reactions and their kinetics, as well as a database with the necessary model constants. However, the software does not have a ready model for the SCR system. Due to the fact that more than 95% of NO flows into the tested SCR system during the experimental tests, therefore, the “standard SCR” reaction for stoichiometry from Eq. (19) and mechanistic cycle

(Fig. 34) was the main reaction considered. In this study a global mechanism, presented by Marangozis [139], is used. In this work, the catalytic processes are presented by the reaction taking place in the volume of the catalyst (volumetric reactions).

Chemical reaction kinetics, also known as reaction kinetics is the measurement or description of how quickly reactions occur (rate of reaction). The rate of a chemical reaction against a substrate or product is measured by the decrease in the number of moles of the selected substrate or the increase in the number of moles of the product per unit of time (t). The general chemical reaction can be written as an equation [141]:



where:

A, B, C, D - symbols of chemical elements/compounds, $\alpha_A, \beta_B, \gamma_C, \delta_D$ - stoichiometric coefficients.

In this example, the moles α_A of the reactant A reacts with the moles β_B of the reactant B , creating respectively γ_C and δ_D moles of a new product C and D . The rate of a chemical reaction can express both the rate of loss of reactants and the rate of formation of products. The reaction rate (r_f) is related to the stoichiometric coefficients and thus can be written as [141]:

$$r_f = -\frac{d[A]}{dt} = -\frac{\beta_B}{\alpha_A} \frac{d[B]}{dt} = \frac{\gamma_C}{\alpha_A} \frac{d[C]}{dt} = \frac{\delta_D}{\alpha_A} \frac{d[D]}{dt} \quad (83)$$

Chemical reaction rate according to the law of the mass action and the kinetic theory of gases can be represented as a function of the concentration of the reactants [141]:

$$r_f = k_f [A]^\alpha [B]^\beta \quad (84)$$

where:

k_f - reaction rate constant, α, β - exponents representing the order of reactions with respect to the concentration of substrates A and B , respectively.

The constant k_f strongly depends on the temperature. According to the kinetic theory of matter, the particles are constantly in motion and each of these particles has kinetic energy resulting from this motion. The higher the temperature, the greater the value of this energy. The particles must collide for the reaction to take place. The increase in temperature causes the intensification of the particle movement, as a result of which the probability of their collision is higher. During chemical reactions, bonds are broken and new ones are formed in

their place. This process requires energy, so particles with higher kinetic energy (fast moving) are transformed more easily than slow moving particles. Here another barrier can be defined, which is called activation energy. It specifies the minimum amount of energy that particles must have in order for their collision to initiate a reaction [141].

The dependence of the reaction rate on temperature was first determined by Arrhenius. He noticed an exponential relationship between temperature and the rate at which a given reaction occurs. The extended Arrhenius equation has already been described in Eq. (66). By combining Eq. (66) with Eq. (84), a general formula for the rate of a chemical reaction can be derived:

$$r_f = A_r T^{\beta_r} e^{(-E_r/RT)} [A]^a [B]^b \quad (85)$$

It should be noted that Eq. (85) is mainly used for elementary reactions, but it is also used to represent apparent global reaction rates. However, the global reaction consists of many elementary reactions, and in many cases they are also assisted by physical processes [141].

The solver in ANSYS Fluent uses Eq. (65) to calculate the reaction rate (for non-reversible reactions), which is then calculated according to the general reaction-rate expressions Eq. (64) from species transport Eq. (61). Modelling the reaction kinetics in the simplest case consists of specifying stoichiometric coefficients and parameters of the Arrhenius equation. For this purpose, the literature data was analyzed in terms of the kinetics of the reactions taking place during the selective catalytic reduction of nitrogen oxides. The simple kinetic model and data presented in the study of Marangozis et al. [139] have been used in this work. It corresponds to the model implemented in Fluent. A catalyst with a similar structure and active layer (0.8% V₂O₅-TiO₂ monolith) was chosen from among the available catalyst variants, which was most similar to the tested catalyst in this work. Marangozis [139] presents the reaction rate in two ways, calling them intrinsic and apparent. The first determines the internal reactivity of the active layer and is given by:

$$R_v = k_v C_{NO}^\alpha C_{O_2}^\beta C_{NH_3}^\gamma \quad (86)$$

where:

R_v , moles of NO/(s · cm³ of catalyst) - the intrinsic reaction rate, C_i , mol/cm³ - molar concentration of NO, O₂ and NH₃ respectively, α, β, γ - the reaction orders w.r.t. NO, O₂ and NH₃, which in this case are equal to 1, 0.25 and 0 respectively, $k_v, s^{-1}(mol/cm^3)^x$ - the intrinsic reaction rate constant, where $x = 1 - (\alpha + \beta + \gamma)$.

Eq. (86) does not take into account the influence of catalyst structure on the reaction process. An apparent reaction rate, takes into account the diffusion effects (reactants to active pores). Moreover, to express the apparent rate of reaction in terms of the volume of the reactor (catalyst + flowing exhaust gases), the Eq. (86) should be multiplied by $(1 - \varepsilon_b)$:

$$R_{va} = k_v \eta (1 - \varepsilon_b) C_{NO}^\alpha C_{O_2}^\beta \quad (87)$$

where:

R_{va} , moles of NO/(s · cm³ of reactor volume) - the apparent reaction rate, η (dimensionless) - the catalyst effectiveness factor, ε_b (dimensionless) - the reactor bed porosity ($\varepsilon_b = 0.44$ for this work).

Comparing Eq. (86) and (87), the relationship between the reaction rate constants can be determined:

$$k_{va} = k_v \eta (1 - \varepsilon_b) \quad (88)$$

Thus, the apparent reaction rate is:

$$R_{va} = k_{va} C_{NO}^\alpha C_{O_2}^\beta \quad (89)$$

Thereby, the apparent reaction rate constant can now be expressed by the Arrhenius equation:

$$k_{va} = A_r \exp\left(-\frac{E_r}{RT}\right) \quad (90)$$

where k_{va} and A_r are expressed in $[s^{-1}(mol/cm^3)^x]$.

Eq. (89) was used to determine the parameters of the Arrhenius equation in the simulations. To determine the value of the pre-exponential factor and activation energy, it was necessary to obtain kinetic data from Marangozis et al. [139] i.e.: exponents determining the order of reactions for all substances participating in the reaction (Tab. 25), the reaction rate constants and catalyst effectiveness factors (Tab. 44).

Tab. 25. Reaction orders for the Selective Catalytic Reduction of NO [139]
(stoichiometric NH₃/NO ratio with oxygen less than 3 vol %)

NH ₃	NO	O ₂	N ₂	H ₂ O
0	1	0.25	0	0

Tab. 26. Summary of catalyst reaction rate parameters [139]

Temperature T, K	Intrinsic reaction rate constant $k_v, s^{-1}(\text{mol}/\text{cm}^3)^x$	Catalyst effectiveness factor η	Pseudo-first-order apparent reaction rate constant $k_v\eta C_{O_2}^\beta, s^{-1}$
553	7.0E+03	0.07	15.0
554	6.7E+03	0.06	12.3
571	9.9E+03	0.05	15.0
573	1.1E+04	0.05	17.4
598	2.3E+04	0.03	20.4
611	2.4E+04	0.03	21.5
614	2.6E+04	0.03	23.2
623	3.8E+04	0.02	22.6
648	4.4E+04	0.02	25.9
651	4.8E+04	0.02	28.0
653	4.6E+04	0.02	27.1
668	9.2E+04	0.01	27.0

In Fig. 72 the plot of $\ln(k_{va}) = \ln(k_v\eta(1 - \varepsilon_b))$ versus $1/T$ is presented.

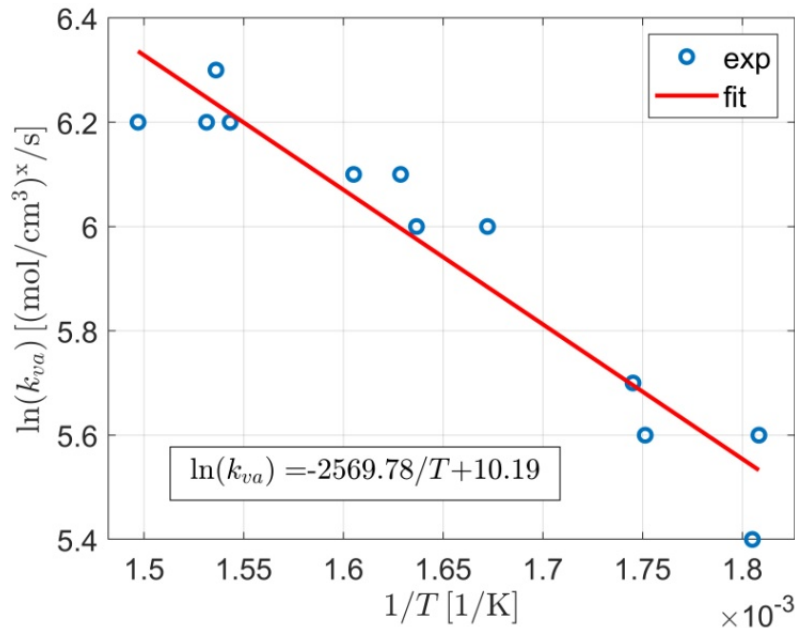


Fig. 72. Arrhenius plot of apparent reaction rate constant [139]

Based on the known values of the reaction rate constants and their link with the Arrhenius equation, it was possible to determine the activation energy and the pre-exponential factor. The use of the Arrhenius equation, however, has the advantage that it can be easily reduced from exponential to linear form (linear fit to the data from Tab. 44) by using a logarithmic scale for Eq. (91), since:

$$\ln(k_{va}) = \ln(A_r) + \ln\left(\exp\left(-\frac{E_r}{RT}\right)\right) \quad (91)$$

$$\ln(k_{va}) = \ln(A_r) - \frac{E_r}{R} \frac{1}{T} \quad (92)$$

The quotient $\frac{1}{T}$ can be treated as a variable of the equation, hence there is the form of Eq. (93). Replacing the quotient $\frac{1}{T}$ with the variable x , the classic form of a linear equation can be obtained (Eq. (122)).

$$f\left(\frac{1}{T}\right) = b - a \frac{1}{T} \quad (93)$$

$$f(x) = b - ax \quad (94)$$

Knowing the mechanism of linearization of the Arrhenius equation, it is possible to proceed to the determination of the values of E_r and A_r based on the Fig. 72. A straight line was fitted to the points by the method of linear regression. Through it, the values of the coefficients a and b of the linear equation were obtained, therefore:

$$b = \ln(A_r) \quad (95)$$

$$A_r = \exp(b) = \exp(10.19) = 2.65 \cdot 10^4 \text{ s}^{-1} \left(\frac{\text{mol}}{\text{cm}^3}\right)^{-0.25} \quad (96)$$

$$a = \frac{E_r}{R} \quad (97)$$

$$E_r = aR = 2569.78 \cdot 1.987 = 5106.15 \frac{\text{cal}}{\text{mol}} \quad (98)$$

The unit system used, however, is not compatible with that used by ANSYS Fluent, hence the need to adjust the units:

$$\begin{aligned} A_r &= 2.65 \cdot 10^4 \left[\text{s}^{-1} \left(\frac{\text{mol}}{\text{cm}^3}\right)^{-0.25} \right] \cdot \left(\frac{1}{1000} \left[\frac{\text{kmol}}{\text{mol}}\right]\right)^{-0.25} \cdot \left(100^3 \left[\frac{\text{cm}^3}{\text{m}^3}\right]\right)^{-0.25} \\ &= 4.72 \cdot 10^3 \left[\text{s}^{-1} \left(\frac{\text{kmol}}{\text{m}^3}\right)^{-0.25} \right] \end{aligned} \quad (99)$$

$$E_r = 5106.15 \left[\frac{\text{cal}}{\text{mol}}\right] \cdot 4.19 \left[\frac{\text{J}}{\text{cal}}\right] \cdot 1000 \left[\frac{\text{mol}}{\text{kmol}}\right] = 2.14 \cdot 10^7 \left[\frac{\text{J}}{\text{kmol}}\right] \quad (100)$$

To validate the appropriate conversion of kinetic data and implementation of reaction scheme into CFD model, a 1D analytical model presented in [139] has been used and compared with CFD simulation by 2D axisymmetric model, which will be presented in the next section. Molar flow rate of NO can be written as:

$$-FdC_{NO} = R_v\eta(1 - \varepsilon_b) dV_R = k_v\eta(1 - \varepsilon_b)C_{NO}^\alpha C_{O_2}^\beta dV_R \quad (101)$$

where: V_R - the reactor volume, F - the total volumetric feed flow rate.

Assuming a known flow rate, constant temperature and in the presence of oxygen, Eq. (101) can also be represented as:

$$\frac{dC_{NO}}{C_{NO}} = -\frac{k_v\eta(1 - \varepsilon_b)C_{O_2}^\beta}{F}dV_R \quad (102)$$

For a constant cross section of the reactor A_R and its height z , the reactor volume is described by Eq. (103). What's more, knowing that the total volumetric feed flow rate is the volume of reactor ($A_R z$) per unit of time t , thus the total volumetric feed flow rate is also A_R multiplied by its velocity v , which is represented in the Eq. (104).

$$dV_R = A_R dz \quad (103)$$

$$F = \frac{A_R z}{t} = A_R v \quad (104)$$

Therefore, after insertion and reduction can be written:

$$\ln \frac{C_{NO}}{C_{NO}^0} = -\frac{k_v\eta(1 - \varepsilon_b)C_{O_2}^\beta}{v} \cdot z \quad (105)$$

The initial (at the reactor inlet) molar concentration of nitric oxides C_{NO}^0 , can be introduced from the reactant conversion X_{NO} as in Eq. (47) and rearranged to:

$$X_{NO}(z) = 1 - \exp\left(-\frac{k_v\eta(1 - \varepsilon_b)C_{O_2}^\beta}{v} \cdot z\right) \quad (106)$$

The above presented kinetic data and a 1D analytical model will be used for validation in CFD simulation by the 2D axisymmetric model. However, for the 3D CFD model, another approach was used. Considering the effect of NH_3 concentration on the reaction rate in which a non-zero reaction order applied with respect to NH_3 . Marangozis et al. [139] described the reaction rate with zero order with respect to NH_3 for vanadia catalysts and it is correct when ANR (ammonia NO_x ratio) is high enough (close to 1). A non-zero reaction order was used for the 3D CFD simulation due to $ANR < 1$ in the experiments. What is more, Odebrand et al. [142] and Lintz et al. [143] found that apparent reaction order for NH_3 (from -0.15 to 0.29) increases with temperature and even negative value appears at low temperatures due to strong adsorption of NH_3 . Therefore, another kinetic data set presented in Tab. 27 from Iwasaki

[140] for the V_2O_5 -W/TiO₂ catalyst was used for 3D model simulation. In Fig. 120 the Arrhenius plot of apparent reaction rate $\ln(R_{va}^*)$ versus $1/T$ is presented.

Tab. 27. Kinetic data for V_2O_5 -W/TiO₂ catalyst [140]

Temperature T, K	Apparent reaction rate $R_{va}^*, \mu m/g/s$
473.5	0.5391
463.4	0.4219
453.5	0.3255
442.3	0.2240
432.2	0.1693
422.0	0.1198
411.9	0.0755
401.9	0.0625
391.8	0.0391

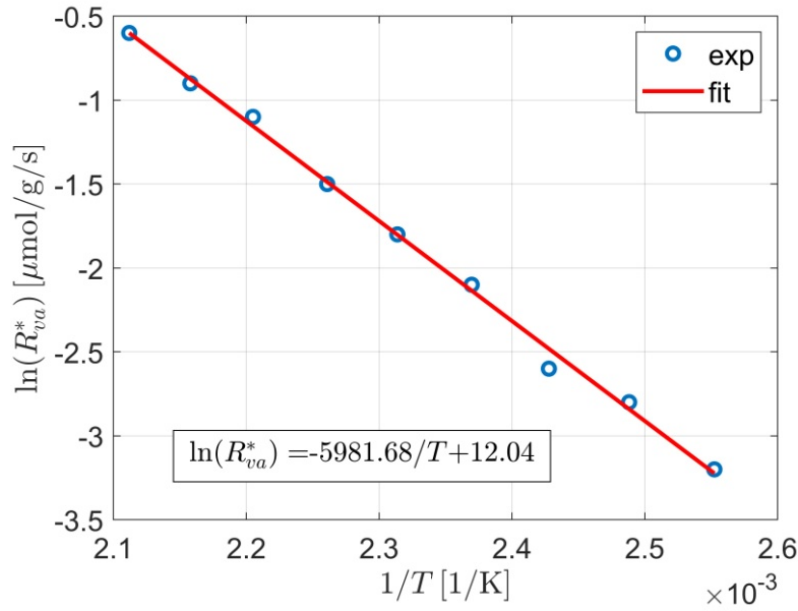


Fig. 73. Arrhenius plot of apparent reaction rate [140]

To determine the Arrhenius parameters from Eq. (89), mass units of $R_{va}^* [\mu m/g/s]$ should be adapted to the CFD code volume units of $R_{va} [kmol/m^3/s]$, by known bulk density $\rho_b [kg/m^3]$, hence [144]:

$$R_{va} = 10^{-6} R_{va}^* \rho_b \quad (107)$$

where the 10^{-6} factor is used for unit conversion. The bulk (apparent) density ρ_b is defined through known porosity according to Eq. (42) i.e. $\varepsilon_b = 0.44$ and the solid density $\rho_s = 3825 kg/m^3$, as stated in [145] for vanadium-based catalyst:

$$\rho_s = (1 - \varepsilon_b) \rho_b \quad (108)$$

The data presented in Fig. 120 was used to determine the activation energy $E_r = 4.97 \cdot 10^7 \text{ J/kmol}$ in required units as it was presented in Eq. (92). According to Iwasaki [140], the apparent activation energy on the Arrhenius plot for the $\text{V}_2\text{O}_5\text{-W/TiO}_2$ catalyst is the same. In order to calculate the pre-exponential factor A_r , an apparent reaction rate constant k_{va} was calculated as [138]:

$$k_{va} = \frac{R_{va}}{C_{NO}^\alpha C_{O_2}^\beta C_{NH_3}^\gamma} \quad (109)$$

Iwasaki [140] provides composition of the gas ($\text{NO}=0.05\%$, $\text{O}_2=8\%$, $\text{NH}_3=0.05\%$) and thus the Arrhenius plot could be prepared to calculate a pre-exponential factor. Reaction orders for O_2 and NO were assumed as previously ($\alpha = 1, \beta = 0.25$) according to Marangozis [139]. However, the effect of NH_3 concentration on the reaction rate was selected based on an analysis of literature data. Many authors for simplicity accept the value $\gamma = 0$. Nevertheless, as mentioned previously, in most cases for vanadia-titania catalyst, this value may range from -0.15 to 0.29 , depending on the temperature [142], [143]. The best representation of experimental results in 3D CFD simulations could have been obtained (which will be shown in the next section) for the rate exponents of NH_3 in the range from 0.096 to 0.130 depending on the operational parameters, as presented in Tab. 28. Assuming the individual data and applying Eq. (109), the Arrhenius plots allowed the evaluation of the pre-exponential factors. The obtained results are presented in Tab. 28. The remaining kinetic data in Tab. 28 are for the thermolysis and hydrolysis reactions of the injected urea-water-solution, which were taken from the ANSYS Fluent software.

Tab. 28. Kinetic data for 3D CFD simulations

Operating Point	Reaction rate exponent			Pre-exponential factor	Activation energy
Standard SCR reaction					
	NO	O ₂	NH ₃	$A_r, s^{-1}(\text{kmol}/\text{m}^3)^x$	$E_r, \text{J}/\text{kmol}$
OP1 (High):	1	0.25	0.130	1.99E+09	4.97E+07
OP2 (Med.):			0.127	1.92E+09	
OP3 (Low):			0.096	1.32E+09	
Thermolysis reaction					
	CO(NH ₂) ₂			A_r, s^{-1}	$E_r, \text{J}/\text{kmol}$
All	1			1.00E+15	1.00E+02
Hydrolysis reaction					
	HNCO	H ₂ O		A_r, s^{-1}	$E_r, \text{J}/\text{kmol}$
All	1	-0.001		2.50E+05	6.22E+07

10.3 Preparation of a CAD model and mesh for CFD simulation

In this subsection, the stages that must be fulfilled in order to prepare a model for numerical simulation will be briefly presented. First, an internal model of the SCR system will be created with simplified geometry. Then, a numerical grid will be adapted to the prepared model in the process of model discretization (meshing). A quick 2D axisymmetric model of the SCR system will be prepared first to confirm and validate the reaction kinetics. Finally, 3D models for all 7 cases from Tab. 9 will be created with appropriate mesh quality for the rest numerical simulations and subsequent validation with the experimental results.

10.3.1 2D CAD model with mesh for CFD simulation

The 2D axisymmetric model was created using Catia v5 software. A simplified axisymmetric model was created (Fig. 74) which consisted of two surfaces: inlet (pipe + cone) and porous medium (monolith). It is good to set the coordinate system in an axially symmetrical place of the model. In such a simplified model, the mesh can be easily adapted and numerical calculations can be performed quickly. The model has been saved and exported to the .igs file extension, which allows it to be easily imported into the ANSYS environment.

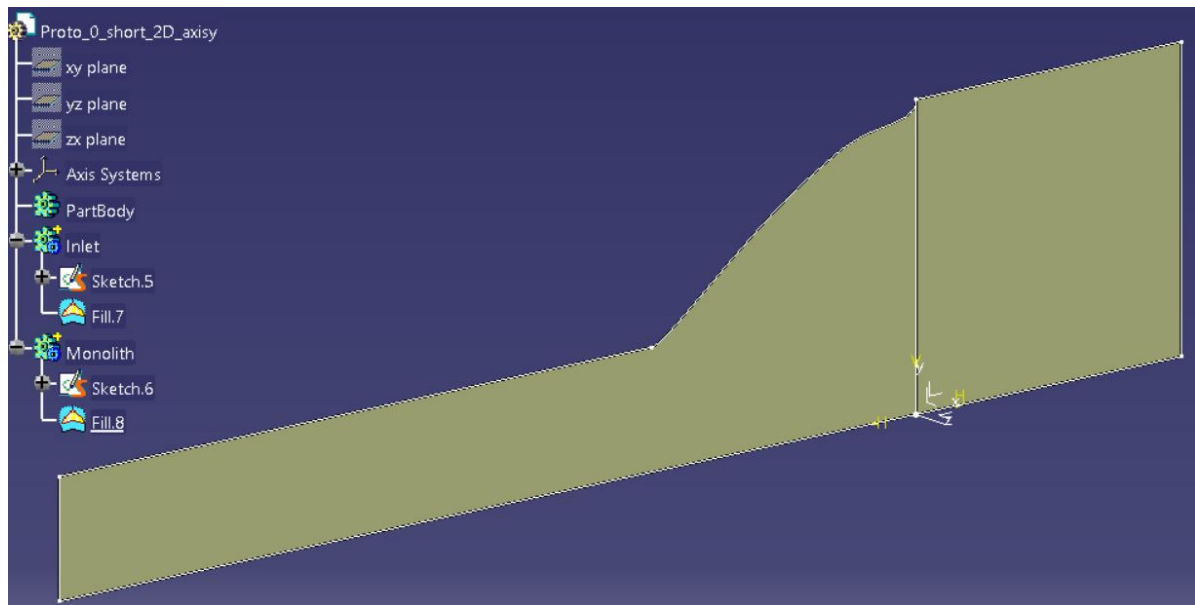


Fig. 74. Prepared 2D axisymmetric model in Catia

The best way to start preparing a simulation is creating components in ANSYS Workbench (Fig. 75), separately for geometry, mesh and solution in Fluent. In order to exchange information, components should be connected by lines in the entire schematic project.

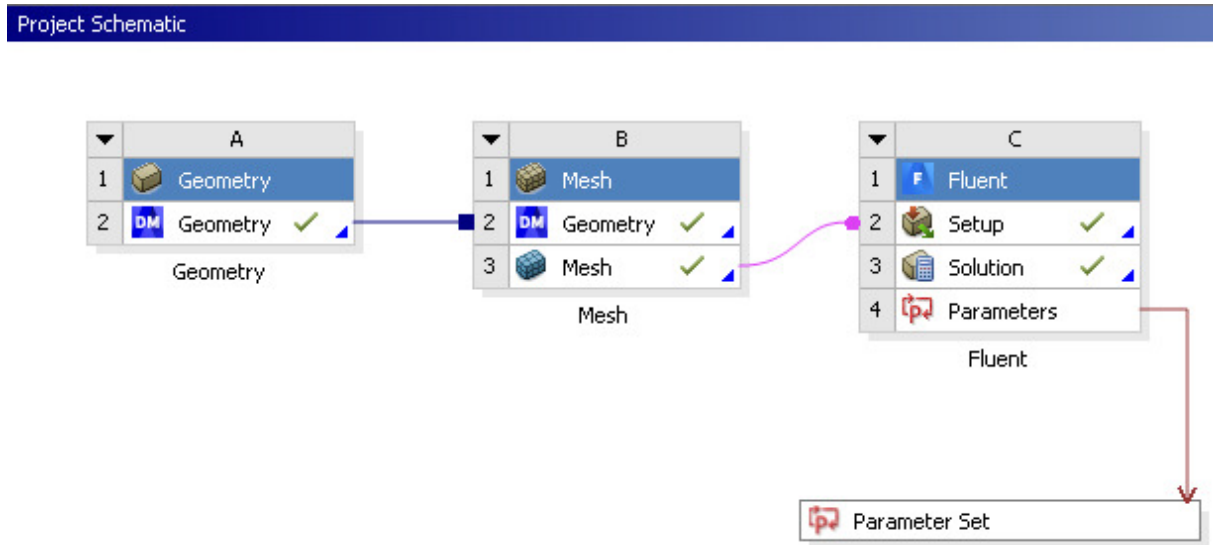


Fig. 75. Prepared components in ANSYS Workbench for simulation

The next step is to create geometry in the implemented ANSYS module (DesignModeler). In the example presented, the geometry has already been done and only requires importing and setting a few options (Fig. 76). First the 2D model has been divided into two separate surfaces (pipe + cone and monolith). From more important things, one part from these two separate surfaces must be created. This ensures the exchange of information by continuity of the mesh. Choosing the Share Topology option also provides connection and continuity of the mesh. Finally it is good to set the names for boundary conditions (inlet, outlet, the surface of the inlet side and the surface of the monolith).

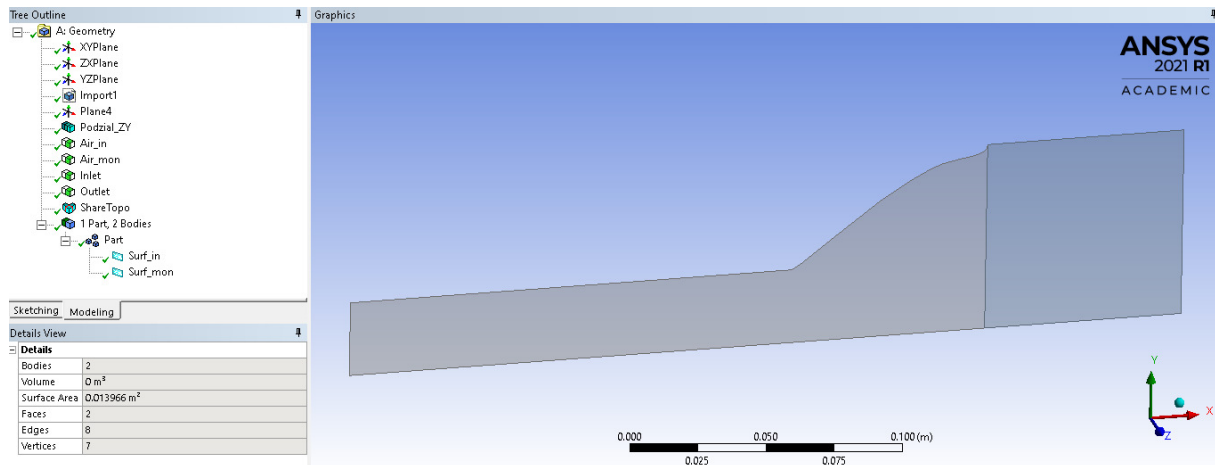


Fig. 76. Imported 2D geometry in ANSYS DesignModeler

The last step towards preparing a 2D model for simulation is the discretization of the model by applying a mesh. In the details of mesh it is required to set physic preference on CFD and solver as Fluent. Then, a global mesh was automatically generated with a standard element size of 3 mm (Fig. 77). The grid mainly consists of Quad4 (4 Node Linear

Quadrilateral (rectangle)) and in non-standard areas as fillets, a small amount of the Tri3 (3 Node Linear Triangle) mesh was adapted. The mesh size and density can be changed and improved in important areas, however, in this case the mesh has the appropriate quality and is sufficient for calculations. Mesh quality is mainly determined by maximum skewness < 0.95 , minimum orthogonal quality > 0.15 and maximum aspect ratio < 10 . In this model, the values were in the ranges and were 0.82 for maximum skewness, 0.25 for minimum orthogonal quality and 8.1 for maximum aspect ratio. A boundary name was also added for the axis of the axially symmetric 2D model. The mesh adapted into the model is ready for selecting the correct simulation settings, boundary conditions and finally simulation calculations.

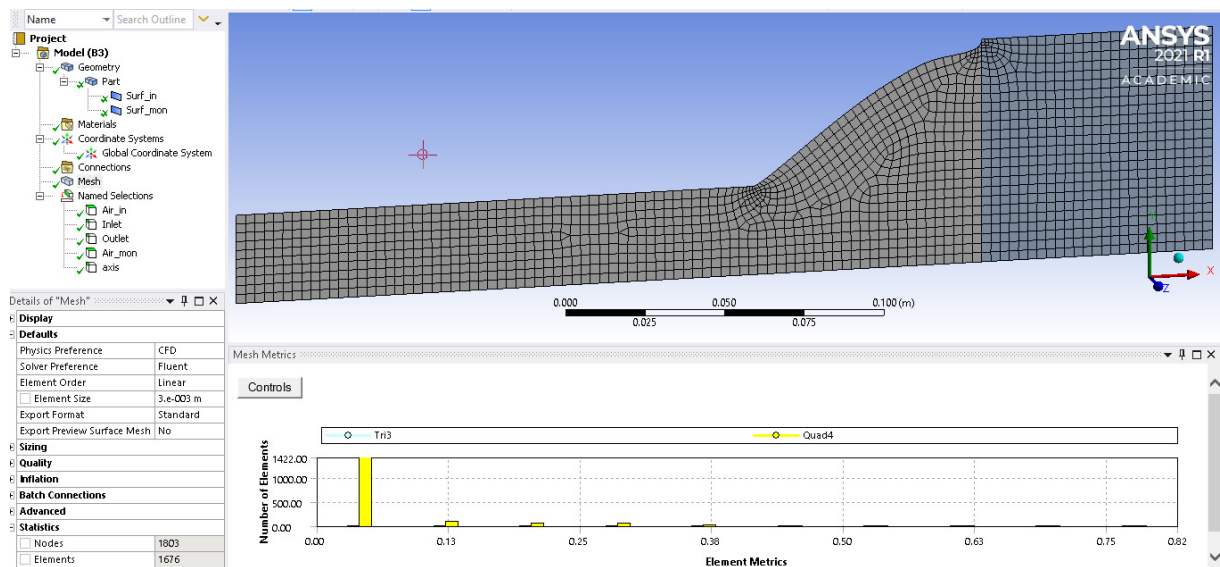


Fig. 77. Mesh completed for 2D geometry in ANSYS Meshing

10.3.2 3D CAD model with mesh for CFD simulation

As in the previous section (10.3.1), the steps needed to prepare a CAD model with a mesh for CFD simulation will be presented. For the purposes of the description of the 3D model, case 6 (complete prototype with mixer C) from Tab. 9 will be presented. The 3D model (Fig. 78) was created in Catia v5 software using the modules of Generative Shape Design (for the surfaces) and Part Design (for solids). The entire model consisted of five separate bodies: inlet side (inlet pipe with injection connection, a cut out geometry of mixer and cone), front catalyst, middle pipe with cones, rear catalyst and outlet pipe with cone. The whole model represents only the inside of the SCR system, where the exhaust gases flow. The coordinate system was centrally located on the front face of the front monolith. The prepared 3D model was exported to the .igs file extension for easy importing into the ANSYS software.

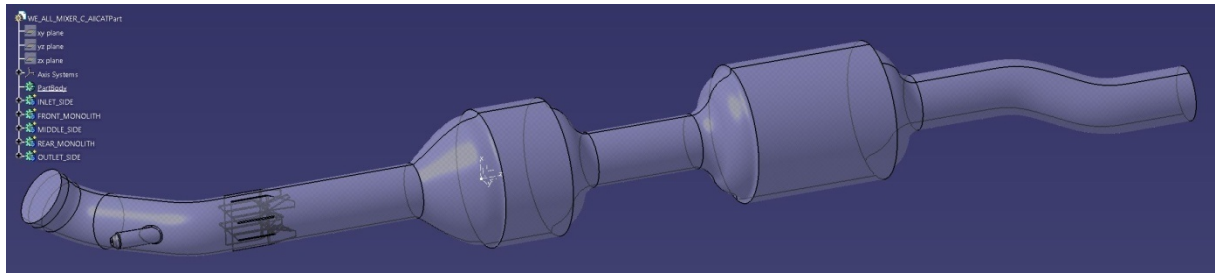


Fig. 78. Prepared 3D model in Catia

As shown previously in the Fig. 75, identical components were created in ANSYS Workbench. The 3D model was imported directly into ANSYS the geometry module (DesignModeler) as shown in the Fig. 79. An additional operation was performed in the model, namely the place where the mixer is located was divided into an additional solid body by creating two planes to split and two slice operations. Thanks to this, it is possible to prepare a thickened mesh in this place. As previously, all boundary conditions and surfaces were named i.e.: inlet and outlet surface of pipes, front and rear body of catalysts, air front body (inlet pipe, mixer and cone), air middle body (cones with middle pipe), air rear body (cone with outlet pipe), as well as the inlet/outlet surfaces of catalysts. These names will help to identify the geometry when setting the boundary conditions and displaying the required simulation results in ANSYS Fluent. Finally, the Share Topology option was used and one part geometry was created consisting of all seven solid bodies.

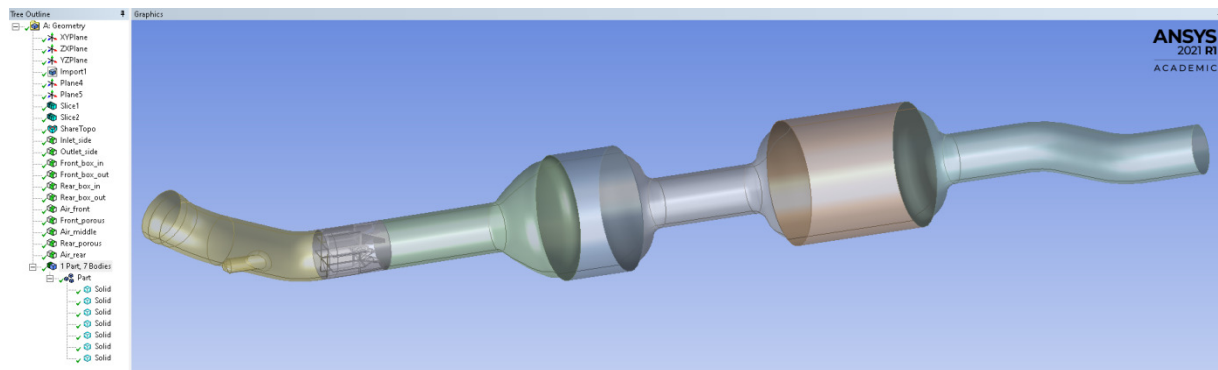


Fig. 79. Imported 3D geometry in ANSYS DesignModeler

The last step in preparing a 3D model for simulation is the discretization of the model by applying a mesh. In the details of mesh it is required to set physic preference on CFD and solver as Fluent. Then, a global mesh was automatically generated with a standard element size of 4 mm (Fig. 80). In addition, the area of the injector connection has been thickened to 1 mm of mesh by the Face Sizing option. In turn, the mixer area was thickened by Tetrahedron method with the Patch Independent algorithm to a maximum element size of 4 mm. The mesh model mainly consisted of Hex8 (8 Node Linear Hexahedron) and Tet4 (4 Node Linear

Tetrahedron). As a result, a satisfactory mesh quality was obtained, the values were in the acceptable ranges and were 0.85 for maximum skewness, 0.15 for minimum orthogonal quality and 10.7 for maximum aspect ratio. The 3D model prepared in this way (as well as the rest of the cases) will be further used for the CFD simulation in Fluent.

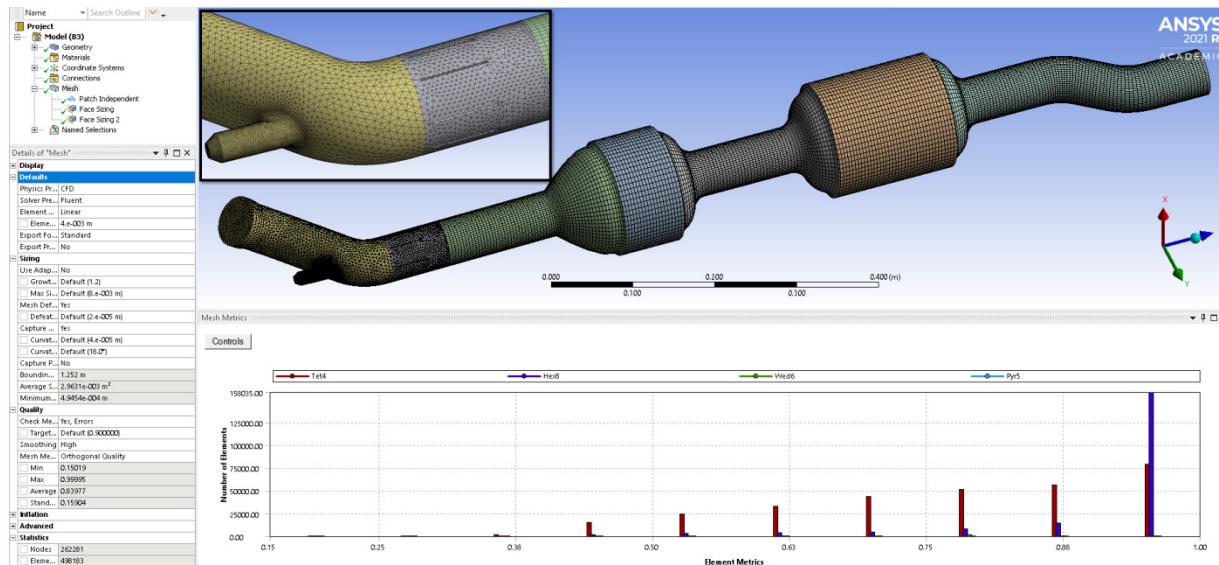


Fig. 80. Mesh completed for 3D geometry in ANSYS Meshing

10.4 2D axisymmetric flow simulation

After starting ANSYS Fluent, the program recognizes that the task is two-dimensional (Fig. 81). It is worth enabling the option “Double Precision”, which represents the accuracy of the calculation to 15 decimal places. There is a possibility of calculating on a larger number of processors (Parallel), depending on the resources of the user equipment, which speeds up the execution of the calculations. In this case the 2D model is simple which will contribute to fast calculations even on one processor.

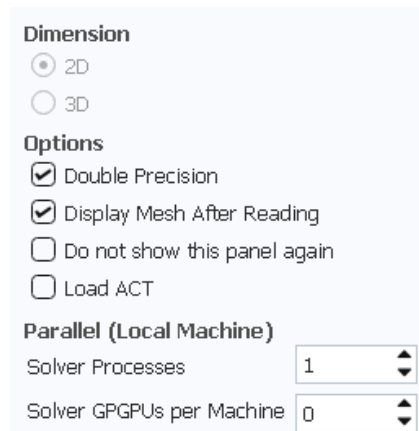


Fig. 81. Fluent launcher for 2D geometry

10.4.1 Main settings with boundary conditions for 2D simulation

The mesh for the whole 2D axisymmetric model has been loaded into the ANSYS Fluent program (Fig. 82). On the left side of the view (in the tree), relevant and required options for the numerical simulation will be turned on one after the other. In the general options, both the steady state flow and the 2D axisymmetric model were selected. By default, the models that are enabled are the mass and momentum continuity (conservation) equations, however, energy model equations must be turned on. In the discussed case, the flow is turbulent, therefore the turbulence model k-epsilon RNG with standard wall functions has been activated. In order to simulate the flow with an exhaust gas mixture, the equation of the mass balance of chemical compounds (species transport model) had to be included. These equations allow for the simulation of volumetric reactions with finite-rate turbulence chemistry interaction as well as including the diffusion of the energy source, full multicomponent diffusion and thermal diffusion. The mixture includes successively such exhaust gas components as H_2O , O_2 , NH_3 , NO , CO_2 and N_2 as balance.

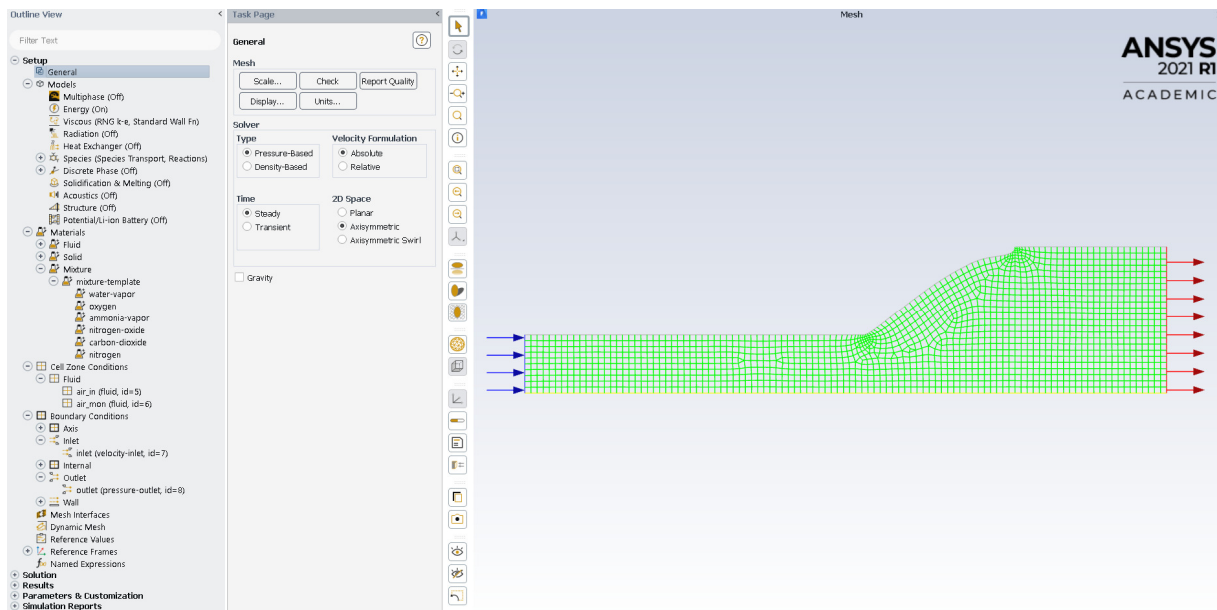


Fig. 82. The 2D model loaded in Fluent

The “standard SCR” reaction for stoichiometry from Eq. (19) and the calculated values of the pre-exponential factor from Eq. (99) and activation energy from Eq. (100) has been implemented into the Fluent code based on reaction kinetics presented by Marangozis [139].

Another important element is setting the conditions (cell zone conditions) for the porous media (catalyst) in which the reaction and the laminar zone are turned on. In the

porous zone, it was necessary to set the coefficients of viscous and inertial resistance for case 1 from Tab. 20. For the X direction the values were as calculated, while for the Y direction the order was three times larger due to the lack of flow in this direction in the catalyst. Finally, the porosity was also defined according to Eq. (42) which is $\varepsilon_b = 0.44$.

The last step was to set the boundary conditions. Marangozis et al. [139] conducted research for stoichiometric NH_3/NO ratio with oxygen 3 vol %. The operational parameter 2 (OP2) from Tab. 13 was validated in 2D axisymmetric model. Thus, the species mole fractions at the inlet were arranged as follows: $\text{H}_2\text{O}=0$, $\text{O}_2=0.03$, $\text{NH}_3=0.000124$, $\text{NO}=0.000124$, $\text{CO}_2=0$, with temperature 668 K (maximum temperature from Tab. 26, which is similar to OP2). At the inlet, the velocity magnitude was set to 3 m/s normal to the boundary with turbulence intensity 5% and viscosity ratio 5. In turn, at the outlet all the species mole fractions were zero with ambient temperature 295 K and gauge pressure 0 PA normal to boundary due to that the global operating pressure is set to 101 325 Pa (1 atm). It should be mentioned that in the discussed case the walls of the model are insulated (they do not exchange heat), hence their thermal conditions are set to heat flux 0 W/m².

To sum up, all the important settings in Fluent for 2D axisymmetric model have been summarized in the Tab. 29 and in this way, the model is ready for the simulation which will be presented in the next subchapter.

Tab. 29. General settings for CFD simulation of the 2D axisymmetric model

Option	Setting
Analysis type	Steady state
Turbulence model	K-Epsilon / RNG / Standard wall
Species transport:	Mixture of gases
- Reactions Volumetric	Finite-Rate, diffusion: energy / multicomponent / thermal
Mixture reactions	According to chapter 10.2.3
Inlet conditions	Species mole fraction and other according to Tab. 13
Outlet conditions	Open to atmosphere & temperature 295 K
Porous zone	Laminar / Viscous & Inertial resistance according to Tab. 20 / Reaction / Porosity $\varepsilon_b = 0.44$

10.4.2 Simulation results for 2D axisymmetric model

The solution methods were selected as default in the Fluent, i.e.: pressure-velocity coupling scheme - simple, spatial discretization for gradient - least squares cell based, for pressure - standard, for turbulent kinetic energy and dissipation rate - first order upwind, for momentum, energy and all chemical compounds - second order upwind. The solution should be initialized to the initial state (initial values should be entered into all cells that the

equations and boundary conditions match). For this purpose, a hybrid initialization was selected in which Fluent automatically sets the initial conditions.

Finally, the number of iterations should be set and the calculation run. In order for the obtained results to be reliable, the residual sizes should be as low as possible, as they are an indicator of imbalance of discredited equations. Residual values are determined in each iteration. As a criterion to complete the calculations were the values of residuals for each equation below 10^{-3} . The residual curves should smoothly show a downward trend until reaching a given level. In the analyzed case, Fluent achieved the solution convergence in iteration 123 as shown in the Fig. 83.

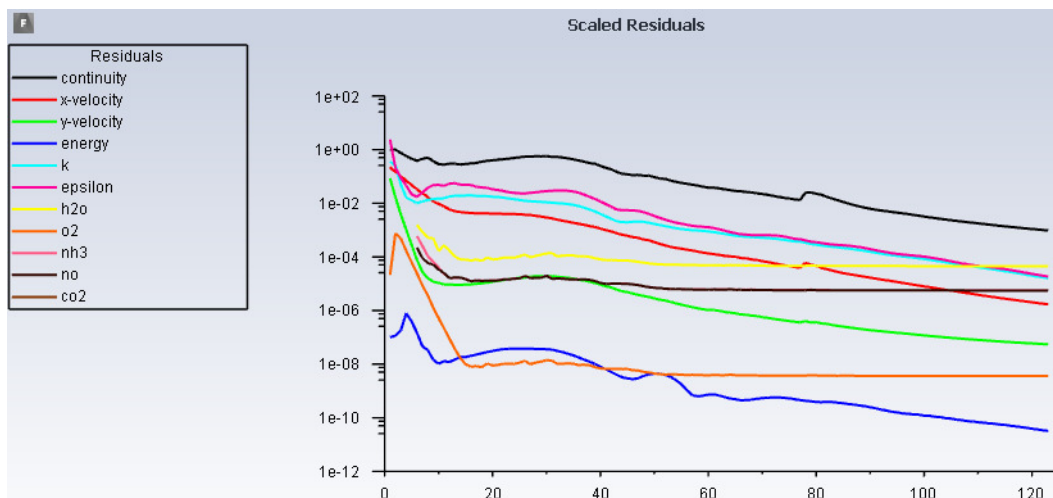


Fig. 83. Residual values in individual iteration for 2D model

Ultimately, the results of the solution were obtained. Fig. 84 shows the NO reduction in the SCR catalyst. The nitric oxide reduction increases with the length of the monolith. This reduction strongly depends on the kinetic parameters of the active layer of SCR catalyst as well as its geometry and boundary conditions such as flow velocity and temperature.

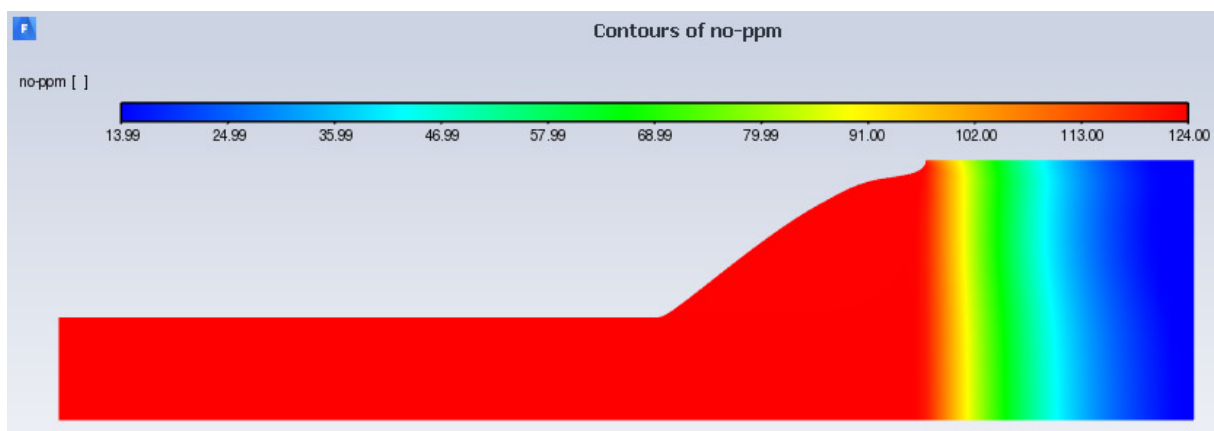


Fig. 84. NO reduction in the 2D model of SCR catalyst

The reduction of nitric oxide on the catalyst will be validated with the analytical model in the next section in such a way that the average NO reduction in 10 equal points of the monolith from the inlet to the outlet will be checked.

The velocity of the flowing gases is shown in Fig. 85. The average velocity in the monolith was 0.47 m/s (this value will be used for analytical calculation), which was caused by the porous body and laminar flow. It is clear that reducing the inlet velocity will result in an even greater conversion, due to a slower flow and more time for NO reduction.

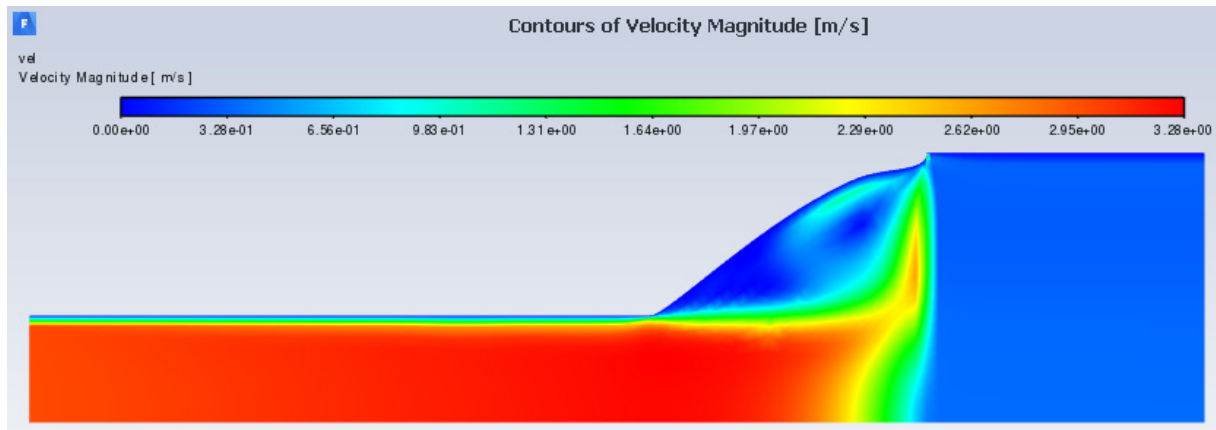


Fig. 85. Velocity contours in the 2D model of SCR catalyst

The pressure drop is also noticeable (Fig. 86) which is caused by the porous body. This pressure depends on the structure of the catalyst described by the viscous and inertial resistance coefficients as well as depending on the velocity and temperature. At the inlet, pressure is about 30 Pa and it decreases to 0 at the outlet of the catalyst.

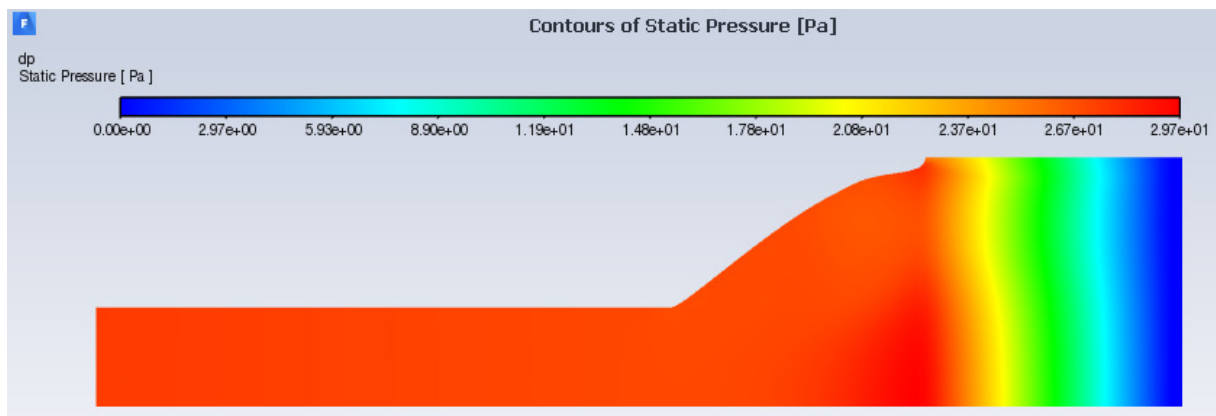


Fig. 86. Static pressure in the 2D model of SCR catalyst

The last Fig. 87 shows the temperature fields in the 2D SCR catalyst. Despite the similar temperature in the whole model, a 1 K higher temperature in the catalyst can be seen due to the chemical reaction taking place. The generated heat indicates the exothermic nature of the SCR standard reaction.

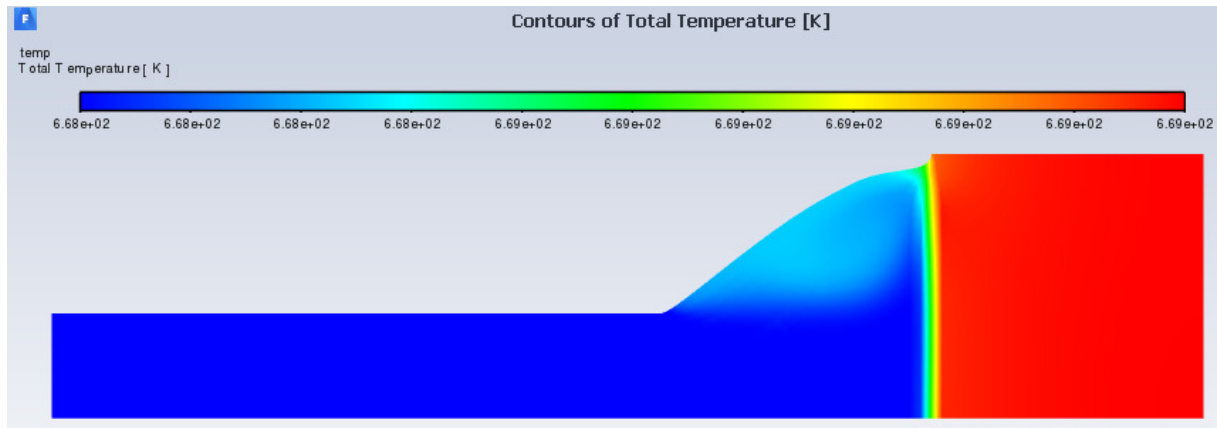


Fig. 87. Temperature contours in the 2D model of SCR catalyst

10.5 3D model flow simulation

All numerical simulations for 3D models were carried out on remote access to the computing cluster of the Silesian University of Technology at the Faculty of Energy and Environmental Engineering in the Department of Thermal Technology. Thanks to the courtesy of the University for remote access, it was possible to perform calculations on a larger number of processors, which significantly accelerated the calculations. The procedure consisted only in booking a place in the queuing system (HPC Job Manager) and reading the already discrete mesh in Fluent Launcher.

10.5.1 Main settings with boundary conditions for 3D simulation

The main settings for the 3D model do not differ much from the settings presented in the 2D axisymmetric model. The 3D mesh model must be loaded into Fluent (Fig. 88). First, the easier setting for a “cold flow” simulation will be presented. Typically, the energy equation and the turbulence model k-epsilon RNG with standard wall functions should be turned on. Air with ideal gas density was used as the working fluid for the cold simulation.

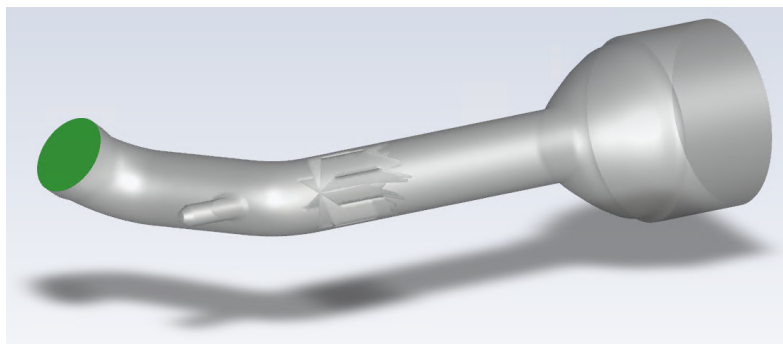


Fig. 88. The 3D model loaded in Fluent

Then the porous zone conditions must be set, where the coefficients of viscous and inertial resistance are defined according to Tab. 20 and fluid porosity.

The next step was to set the boundary conditions at the inlet (Fig. 89) and outlet. The mass flow rate (according to Tab. 12) at the inlet side was set normal to boundary with turbulence intensity 5% and viscosity ratio 5. The inlet and outlet temperature was like in a laboratory (ambient temperature). All the important settings in Fluent for 3D model (cold flow simulation) have been summarized in the Tab. 30.

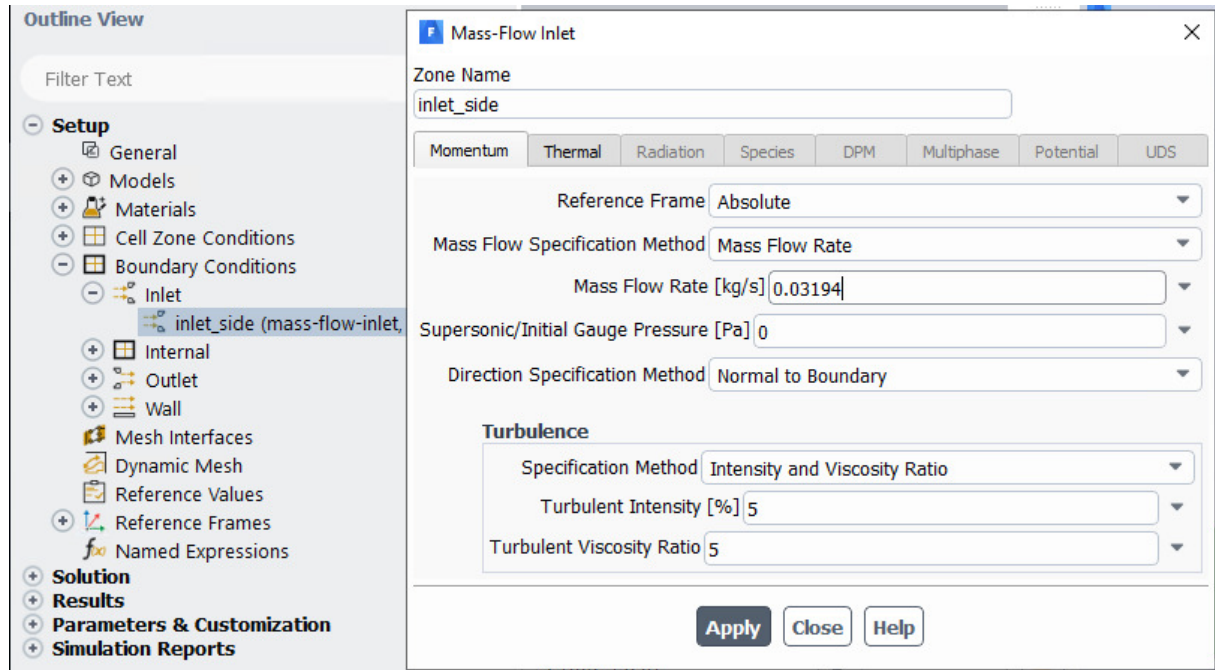


Fig. 89. Inlet conditions for cold flow simulation

Tab. 30. General settings for cold flow CFD simulation of the 3D model

Option	Setting
Analysis type	Steady state with gravity turned on
Energy equation	Turned on
Turbulence model	K-Epsilon / RNG / Standard wall
Fluid material	Air with ideal-gas density
Porous zone	Laminar / Viscous & Inertial resistance according to Tab. 20 / Porosity $\varepsilon_b = 0.44$
Inlet conditions	According to Tab. 12
Outlet conditions	Open to atmosphere & temperature 295.15 K

When it comes to the “hot flow” simulation settings, there are already some extra steps that need to be set that will be briefly described. As in the 2D model simulation, to simulate the flow with exhaust gas mixture, the species transport model must be enabled. These equations allow for simulation of volumetric reactions with finite-rate turbulence chemistry interaction as well as including diffusion of energy source, full multicomponent diffusion and thermal diffusion. The defined mixture in the fluent “urea-water-air” was selected as the material mixture. Nitric oxide was also added manually to this mixture for the later definition

of chemical reactions. Hence, the entire mixture of urea-water-air includes such components as O_2 , H_2O , $CO(NH_2)_2$, $HNCO$, NH_3 , CO_2 , NO and N_2 as balance.

The next important step is to enable the DPM (Discrete Phase Model) model for the injector (three injections simultaneously). In this DPM model, interaction with continuous phase was included with a DPM update every 10 iterations internally. Additionally, the physical model of temperature dependent latent heat included. Moreover, for the DPM model, three separate injections with the same physical properties (Fig. 90) were defined separately. However, each injection has different values of its initial position and injection angle. Injection components were defined as AdBlue, i.e. $CO(NH_2)_2$ and H_2O with mass fraction 0.325 for urea and 0.675 for water.

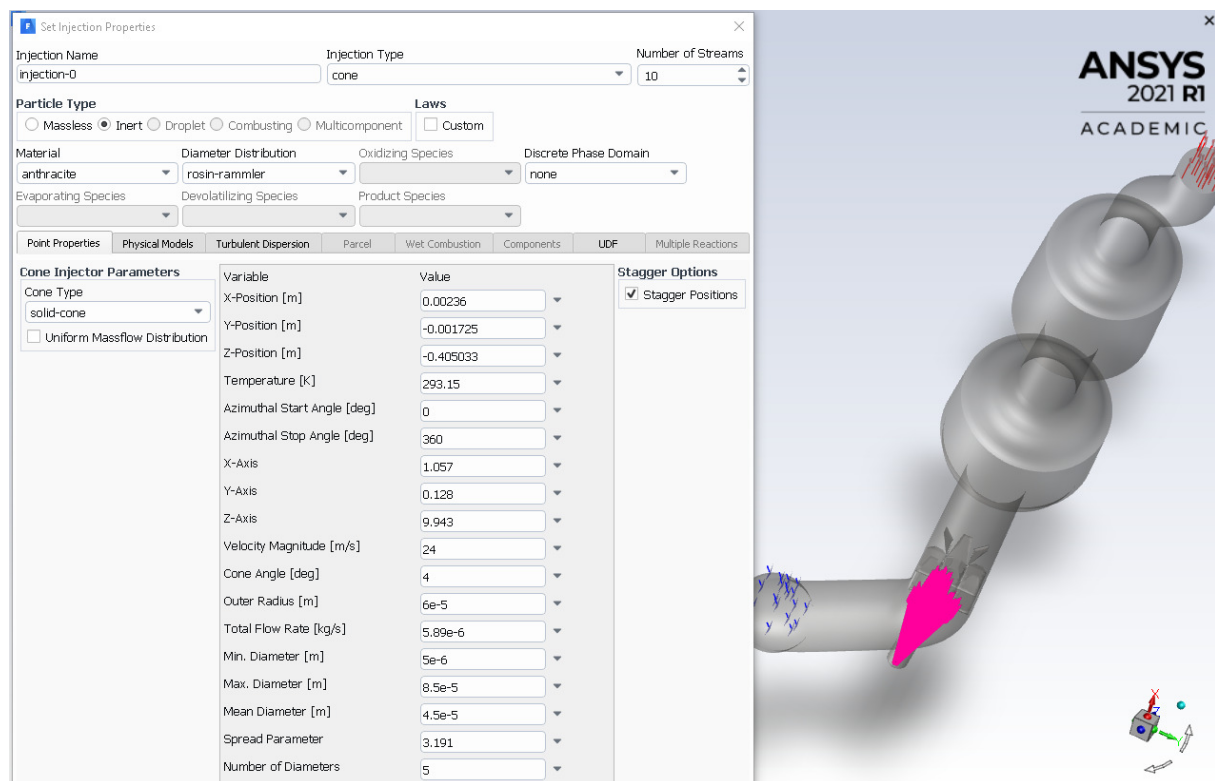


Fig. 90. Defining injection for OP2 in the DPM model

In a mixture (urea-water-air) properties three reactions were formed (Fig. 91). The thermolysis and hydrolysis reaction was already defined as standard in Fluent. The standard SCR reaction (deNO-standard) was implemented according to chapter 10.2.3. From these reactions, two mechanisms were established. The first concerned the decomposition of UWS (for thermolysis and hydrolysis reactions), which will be used at the inlet of the SCR system (inlet pipe with mixer). The second mechanism (for standard SCR reaction) will be used only in catalysts (porous zones). These mechanisms should be selected properly in cell zone conditions for the appropriate geometries of the SCR system together with the calculated

coefficients of viscous and inertial resistance. The last option used in mixture, however, in particle mixture properties for urea-water was to select an option of convection/diffusion-controlled in the vaporization/boiling model.

The figure displays three screenshots of a software interface for defining chemical reactions in a 3D model. Each screenshot shows a different reaction configuration.

Reaction 1: Thermolysis

- Mixture: urea-water-air
- Total Number of Reactions: 3
- Reaction Name: Thermolysis, ID: 1
- Reaction Type: Volumetric
- Number of Reactants: 1, Number of Products: 2
- Reactants:

Species	Stoich. Coefficient	Rate Exponent
co<nh2>2	1	1
- Products:

Species	Stoich. Coefficient	Rate Exponent
nh3	1	0
hnco	1	0
- Arrhenius Rate:
 - Pre-Exponential Factor: 1e+15
 - Activation Energy [J/kgmol]: 100
- Mixing Rate:
 - A: 4, B: 0.5

Reaction 2: Hydrolysis

- Mixture: urea-water-air
- Total Number of Reactions: 3
- Reaction Name: Hydrolysis, ID: 2
- Reaction Type: Volumetric
- Number of Reactants: 2, Number of Products: 2
- Reactants:

Species	Stoich. Coefficient	Rate Exponent
hnco	1	1
h2o	1	-0.001
- Products:

Species	Stoich. Coefficient	Rate Exponent
nh3	1	0
co2	1	0
- Arrhenius Rate:
 - Pre-Exponential Factor: 250000
 - Activation Energy [J/kgmol]: 6.222e+07
- Mixing Rate:
 - A: 4, B: 0.5

Reaction 3: deNO-standard

- Mixture: urea-water-air
- Total Number of Reactions: 3
- Reaction Name: deNO-standard, ID: 3
- Reaction Type: Volumetric
- Number of Reactants: 3, Number of Products: 2
- Reactants:

Species	Stoich. Coefficient	Rate Exponent
no	2	1
nh3	2	0.127
o2	0.5	0.25
- Products:

Species	Stoich. Coefficient	Rate Exponent
n2	2	0
h2o	3	0
- Arrhenius Rate:
 - Pre-Exponential Factor: 1.92e+09
 - Activation Energy [J/kgmol]: 4.97e+07
- Mixing Rate:
 - A: 4, B: 0.5

Fig. 91. Main reactions used in the 3D model

The last element was setting the boundary conditions. At the inlet setting of mass flow rate, temperature and species in mole fractions were according to Tab. 13. Additionally, the DPM type is selected as escape. An additional operation was to set a porous-jump with trap option for DPM for internal inlet face of front catalyst. This option ensures that after hitting non-decomposed AdBlue droplets, they will be vaporized on the front wall of the catalyst. In order to facilitate decomposition and achieve a steady state faster, the walls of the front side of the SCR with the mixer were set with temperature as inlet. All the important settings in Fluent for 3D model (hot flow simulation) have been summarized in the Tab. 31.

Tab. 31. General settings for hot flow CFD simulation of the 3D model

Option	Setting
Analysis type	Steady state with gravity turned on
Energy equation	Turned on
Turbulence model	K-Epsilon / RNG / Standard wall
Species transport:	Mixture of gases: urea-water-air and nitrogen oxide
- Reactions Volumetric	Finite-Rate, diffusion: energy / multicomponent / thermal
Vaporization model	convection/diffusion-controlled of particle mixture (urea-water)
DPM (type reflect)	Continuous phase & Iteration; Temp. Dependent Latent Heat
- Injection x3:	Solid-cone / multicomponent
- Components	urea - water (32.5 % / 67.5 %)
- Size distribution	Rosin-Rammler: 5, 45, 85 μm , 5 diameters with spread 3.191
- Temp. & velocity	293.15 K & 24 m/s
- Outer radius	60 μm (radius of injector hole)
- Cone angle	4° (included half-angle)
- Total flow rate	According to Tab. 13, divided into three injection
Mixture reactions	According to chapter 10.2.3
Porous zone	Laminar / Viscous & Inertial resistance according to Tab. 20 / Reaction / Porosity $\varepsilon_b = 0.44$ / Inlet face of front catalyst as a porous-jump with trap option for DPM
Inlet conditions	Species mole fraction and other according to Tab. 13
Outlet conditions	Open to atmosphere & temperature 295.15 K
Wall	Inlet side with thermal temperature as inlet and DPM type reflect

10.5.2 Cold flow simulation results for 3D model

CFD simulations for the 3D model were first performed for the cold flow as it was in the experimental tests. The solution methods were similar to the 2D model i.e. mostly default settings in Fluent, the pressure-velocity coupling scheme was set to simple with standard pressure. The solution was initialized by hybrid initialization and the calculations were run for 500 iterations. Residual values (below 10^{-1}) for each equation were minimally falling and stabilized. The mass flow rate at the outlet of the SCR system quickly stabilized after just

around 75 iterations (Fig. 92). On the other hand, the uniformity index (UI) of velocity at the outlet oscillated about 0.97, from an iteration of 200 to 500 (Fig. 93).

The results of numerical CFD simulations for cases 1-4 are presented in Tab. 32. These simulations showed the effect of mixer design and positioning on the flow distribution at the outlet side of the monolith as well as pressure drop. The uniformity index of velocity (UI_v), $ETA_{15\%}$ index, eccentricity index and pressure drop of the mixer were compared.

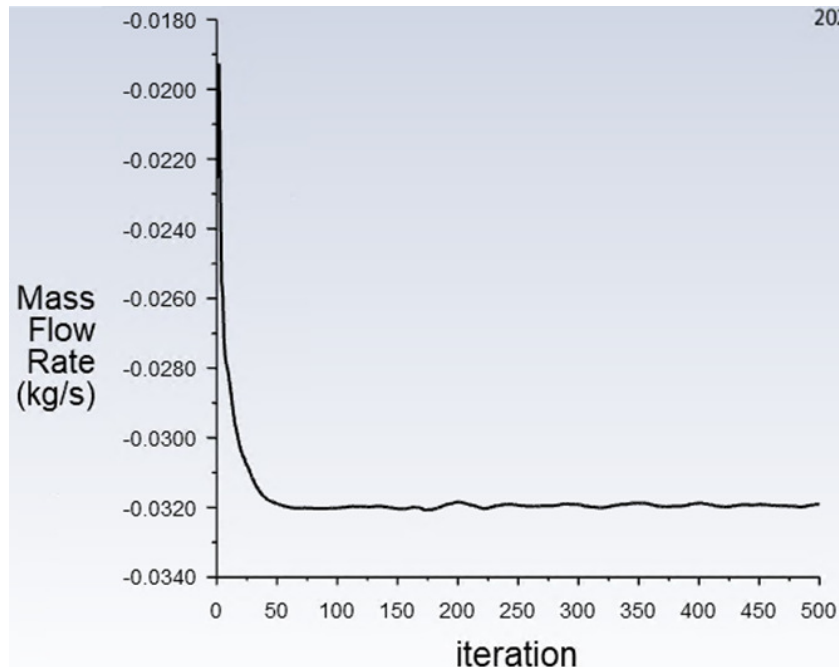


Fig. 92. Mass flow rate at outlet for 3D cold flow simulation

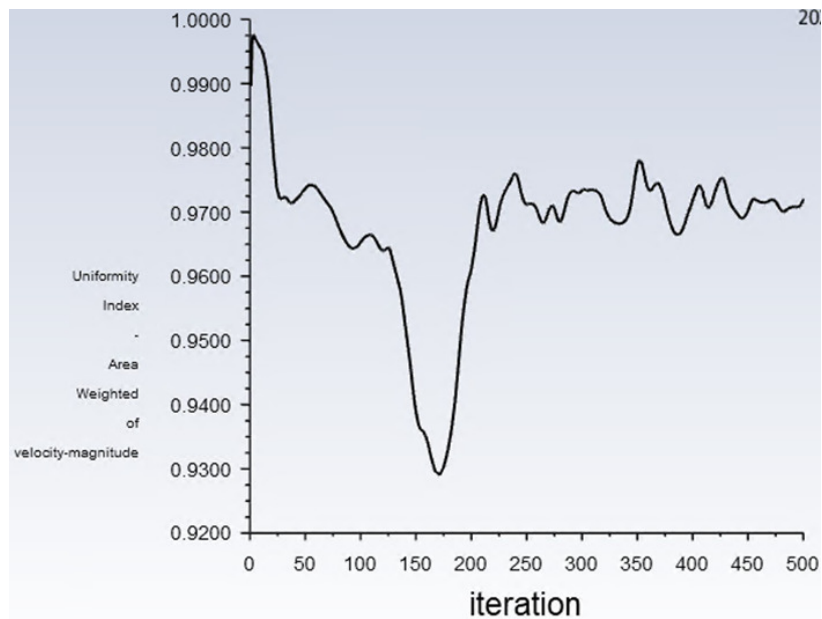


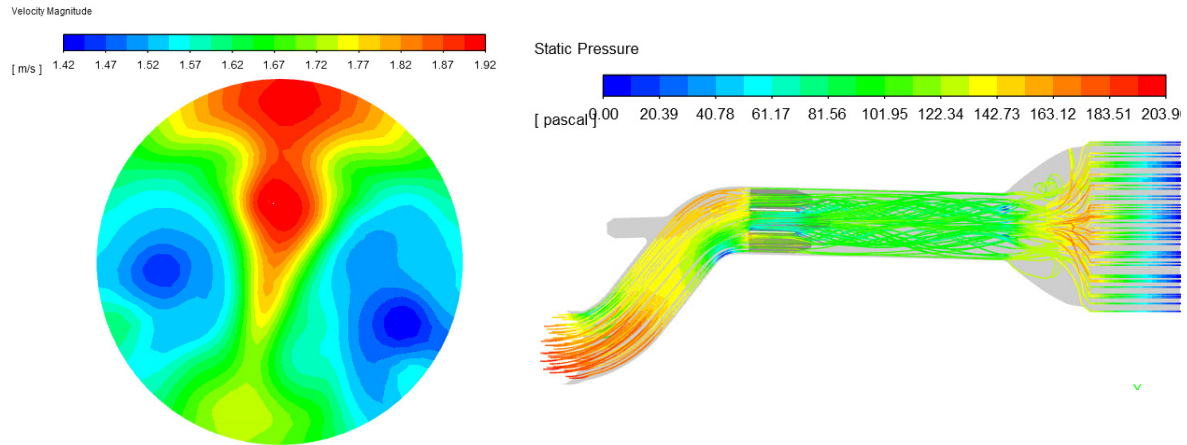
Fig. 93. Velocity UI at outlet for 3D cold flow simulation

For all cases, the average velocity at the outlet was around 1.65 m/s. In the first case, where the mixer A was closer to the injector, the uniformity index was better $UI_v=0.969$, $Eccen.=0.42$ index and $ETA_{15\%}=98.6$ index, however, the pressure drop across the mixer was 44.1 Pa higher than in the case of the mixer A with a distance of 155mm.

Tab. 32. Velocity distribution and pressure drop for cold flow CFD simulation (Case 1-4)

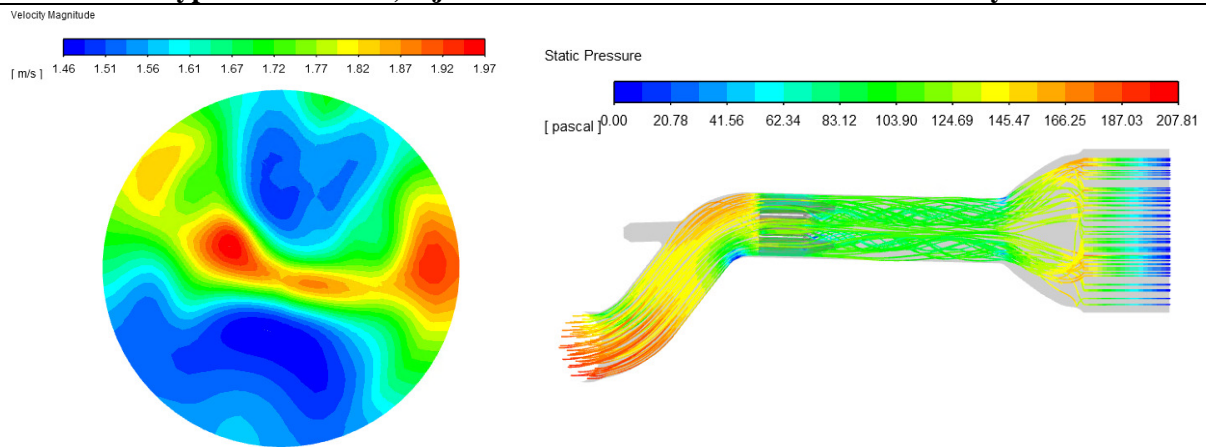
Case 1: Prototype with mixer A; injector-mixer distance L=120mm	
$UI_v=0.969$; $v_{ave}=1.65\text{m/s}$; $ETA_{15\%}=98.6$; $Eccen.=0.42$; $\Delta p_{mix}=44.1\text{Pa}$	
Case 1: Prototype with mixer A; injector-mixer distance L=155mm	
$UI_v=0.967$; $v_{ave}=1.65\text{m/s}$; $ETA_{15\%}=95.6$; $Eccen.=0.80$; $\Delta p_{mix}=28\text{Pa}$	
Case 2: Prototype with mixer B; injector-mixer distance L=120mm	
$UI_v=0.971$; $v_{ave}=1.64\text{m/s}$; $ETA_{15\%}=93.2$; $Eccen.=0.96$; $\Delta p_{mix}=22.7\text{Pa}$	

Case 3: Prototype with mixer C; injector-mixer distance L=120mm



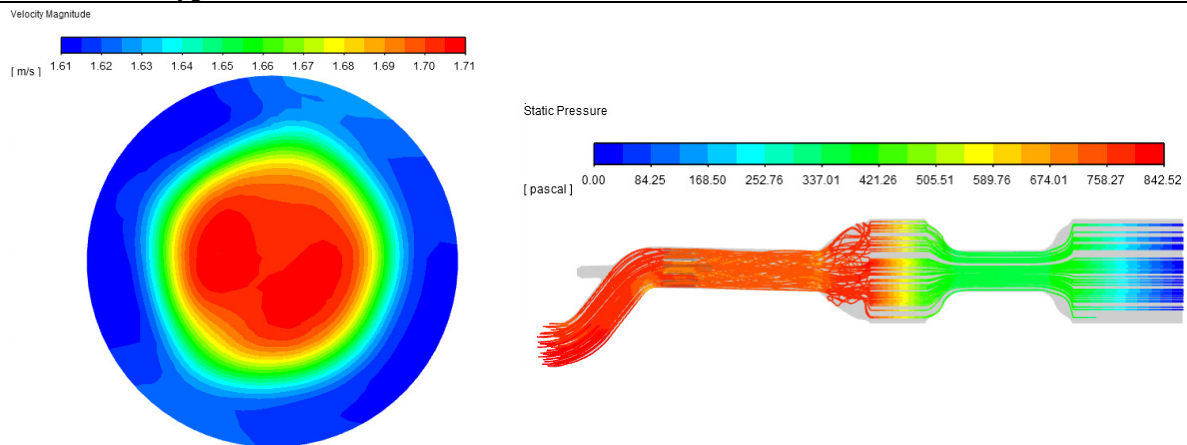
$UI_v=0.967$; $v_{ave}=1.65\text{m/s}$; $ETA_{15\%}=98.5$; $Eccen.=0.34$; $\Delta p_{mix}=31.4\text{Pa}$

Case 3: Prototype with mixer C; injector-mixer distance L=120mm & rotated by 90°



$UI_v=0.966$; $v_{ave}=1.65\text{m/s}$; $ETA_{15\%}=97.3$; $Eccen.=0.30$; $\Delta p_{mix}=34.5\text{Pa}$

Case 4: Prototype with mixer C (1st and 2nd box)



$UI_v=0.989$; $v_{ave}=1.65\text{m/s}$; $ETA_{15\%}=100$; $Eccen.=0.28$; $\Delta p_{mix}=33.9\text{Pa}$

In the second case, mixer B obtained the lowest pressure drop of the mixer (22.7 Pa) due to its low design complexity. Nevertheless, it reached the best uniformity index ($UI_v=0.971$), despite having the highest index of $Eccen.=0.96$, which is not desirable (flow distribution on the edges of the monolith).

The third case obtained rational results. Mixer C obtained a fairly high uniformity index ($UI_v=0.967$) with index of Eccen.=0.34 (strong distribution in the centre of the monolith) and an average pressure drop of the mixer (31.4 Pa). Mixer C rotation by 90° does not significantly affect the results, but only changes the distributions of the stronger flux in a different position.

The last, fourth case, showed an increased pressure drop in the entire system (from 204 Pa to 842 Pa) after the addition of the second catalyst. The middle pipe additionally mixed and stabilized the flow distribution (the strongest flow in the centre of the monolith), increasing all indexes to a plus.

In the Fig. 94 shows a comparison of the tested mixers during experimental tests in cold flow condition. The indexes ($ETA_{15\%}$, eccentricity and UI for velocity) were taken into account. Mixer B had the weakest indexes. Mixer A in configuration $L=150\text{mm}$ from the injector looked better. Finally, mixer C rotated by 90° turned out to be the best one. This mixer had the best area coverage of mean velocity ($ETA_{15\%}=83.9\%$) with the highest flow rate in the centre of the catalyst (Eccen.=0.10) as well as the best flow uniformity at the outlet of the catalyst $UI_v=0.953$.

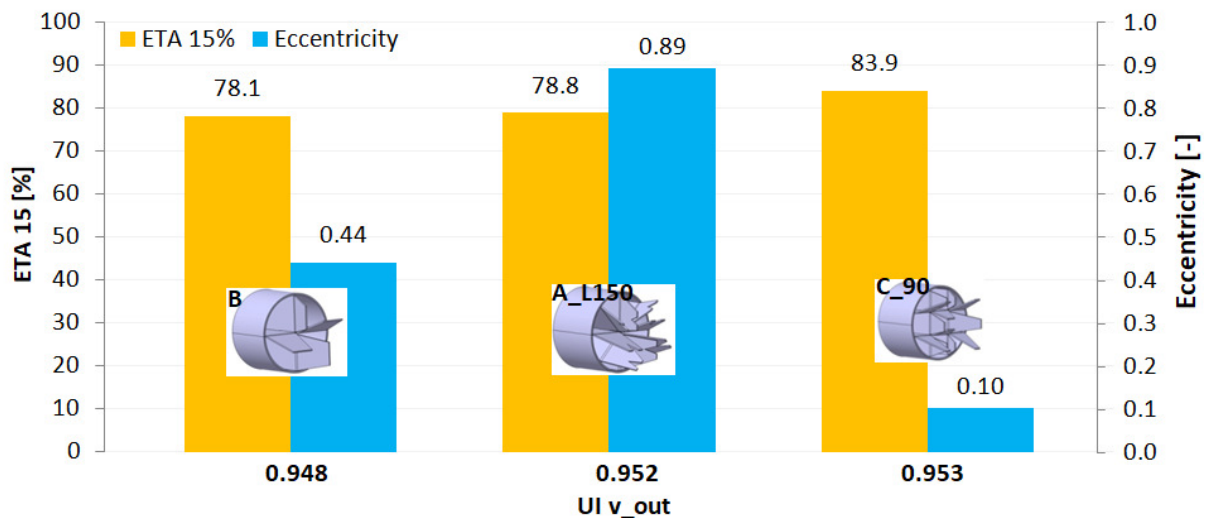


Fig. 94. Comparison of the parameters of mixers for the experimental cold flow

10.5.3 Hot flow simulation results for 3D model

The next more important simulations for the 3D model were in hot flow conditions and were carried out for the same cases as in the experimental tests in order to validate the numerical model. The solution methods in Fluent were the same as in 3D model cold flow conditions. The solution was initialized by hybrid initialization and the calculations were run

for 250 iterations. The Fig. 95 shows residual values, mass flow rate at the outlet of the SCR system, uniformity index at the inlet face of the front SCR catalyst ($UI_{NH_3_in}$) and NO average reduction (NO_{ave_out}) at outlet of SCR system, here an example for Case 6 and OP2. These graphs made it possible to determine the end of the calculations at the moment of their rational stabilization. Residual value for $CO(NH_2)_2$ takes the form of the systematic peaks due to the appearance of urea in the system and then thermally decomposes to ammonia. The remaining residual values for each equation and species were below 10^{-1} with a decreasing trend and stabilization. Mass flow rate itself stabilized very quickly, after 25 iterations. On the other hand, $UI_{NH_3_in}$ and NO_{ave_out} achieved a reasonable stabilization around 250 iterations.

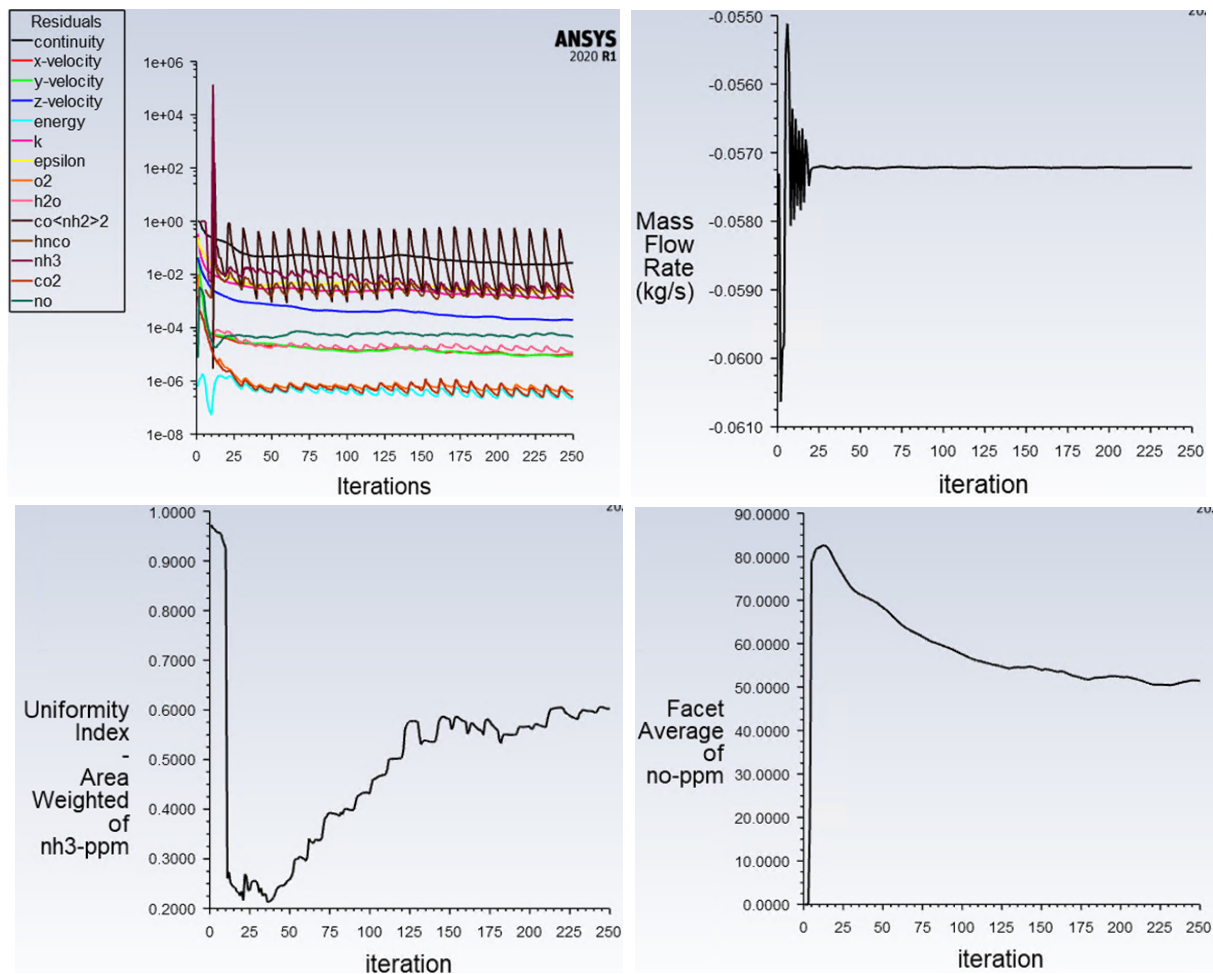
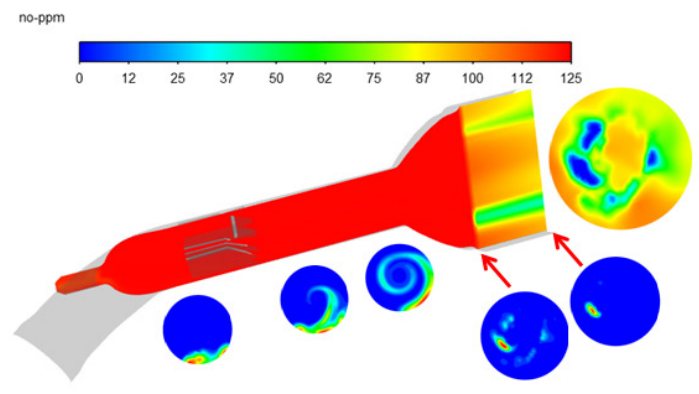
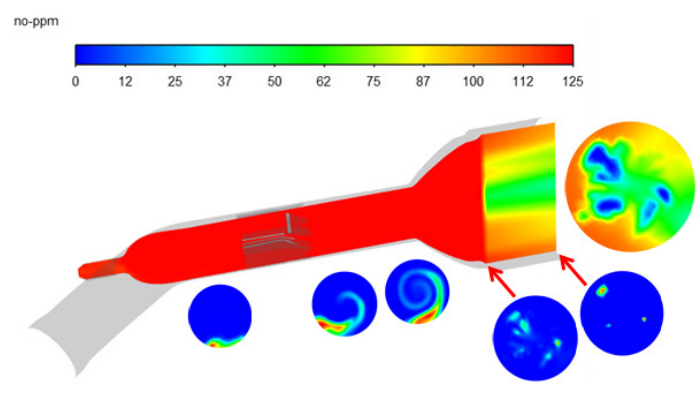


Fig. 95. Residuals, mass flow rate, $UI_{NH_3_in}$ and NO_{ave_out} (Case 6, OP2)

The results of numerical CFD simulations for individual cases will be presented successively in tabular form, which will also include the relevant parameters determining the performance of a given case for the purpose of comparing all cases. The graphic representation of the SCR system mainly shows the reduction of nitric oxide, but also the degree of ammonia mixing in individual sections (cross-sections) of the SCR system.

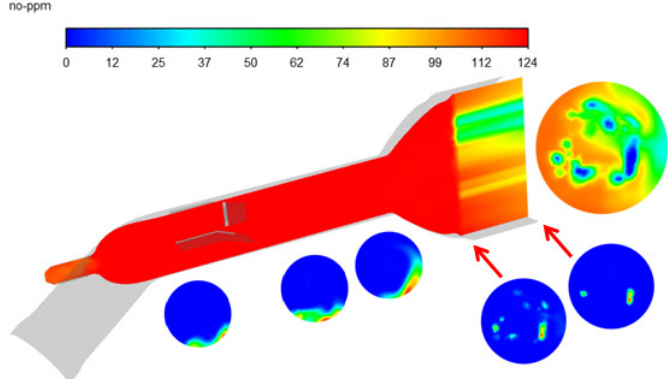
Tab. 33. NO reduction and NH₃ mixing for hot flow CFD simulation (Case 1, OP2)

<p>Case 1: Prototype with mixer A injector-mixer distance L=120mm OP2 (Medium)</p>		<p>$UI_{NO_out}=0.885$ $NO_{ave_out}=77.83ppm$ $X_{NO}=37.23\%$ $UI_{NH3_in}=0.514$ $CoV_{NH3_in}=2.42$ $NH3_{ave_out}=7.12ppm$ $\Delta p_{mix}=201.81Pa$</p>
<p>Case 1: Prototype with mixer A injector-mixer distance L=155mm OP2 (Medium)</p>		<p>$UI_{NO_out}=0.831$ $NO_{ave_out}=71.84ppm$ $X_{NO}=42.06\%$ $UI_{NH3_in}=0.597$ $CoV_{NH3_in}=2.09$ $NH3_{ave_out}=1.56ppm$ $\Delta p_{mix}=248.76Pa$</p>

In the first case (Tab. 33), it is possible to compare the dependence of the mixer distance from the injector. Numerical simulations confirm the experimental results, that mixer A with a distance of $L=155mm$ from the injector resulted in a better conversion in the system from $X_{NO}=37.23\%$ to $X_{NO}=42.06\%$. The longer distance between the mixer and the injector allowed for a better distribution of ammonia to the front face of the SCR catalyst, which is confirmed by $UI_{NH3_in}=0.597$ and $CoV_{NH3_in}=2.09$. What's more, the average ammonia slip is lower at the outlet of the SCR catalyst ($NH3_{ave_out}=1.56ppm$). On the other hand, the uniformity index at the outlet of the catalyst for NO has decreased from $UI_{NO_out}=0.885$ to $UI_{NO_out}=0.831$ and the pressure drop on the mixer has increased about 47 Pa.

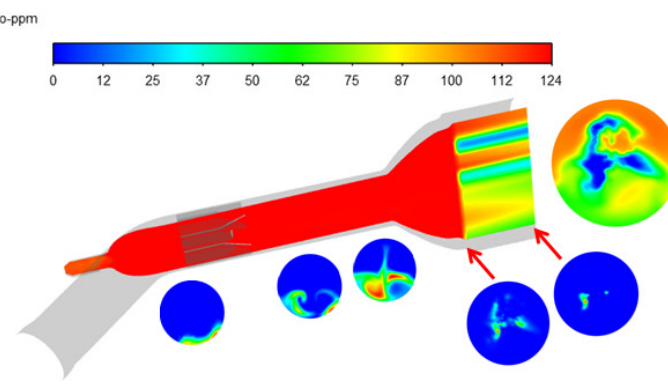
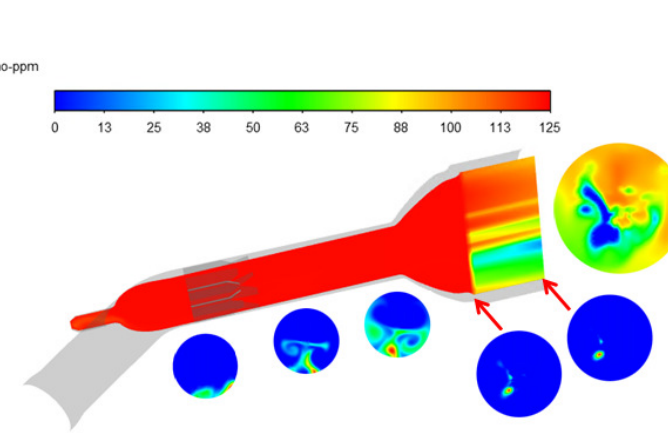
In the second case (Tab. 34), mixer B achieved a weaker NO conversion in the SCR catalyst ($X_{NO}=35.43\%$) compared to mixer A. The uniformity index is not satisfactory for the NH₃ inlet face ($UI_{NH3_in}=0.403$) due to the small complication of the mixer which confirms the lower pressure drop for this mixer (153.48 Pa). The cross-sections show that the ammonia mixing is poor with its large point concentration on the front face of the catalyst. This case causes a large ammonia slip at the outlet of SCR catalyst. Although in these areas there is full NO conversion, in others areas the high concentration of NO is still maintained. Such situations, however, should be avoided.

Tab. 34. NO reduction and NH₃ mixing for hot flow CFD simulation (Case 2, OP2)

<p>Case 2: Prototype with mixer B injector-mixer distance L=120mm OP2 (Medium)</p>		<p> $UI_{NO_out}=0.857$ $NO_{ave_out}=80.07\text{ppm}$ $X_{NO}=35.43\%$ $UI_{NH3_in}=0.403$ $CoV_{NH3_in}=4.04$ $NH3_{ave_out}=7.74\text{ppm}$ $\Delta p_{mix}=153.48\text{Pa}$ </p>
---	--	--

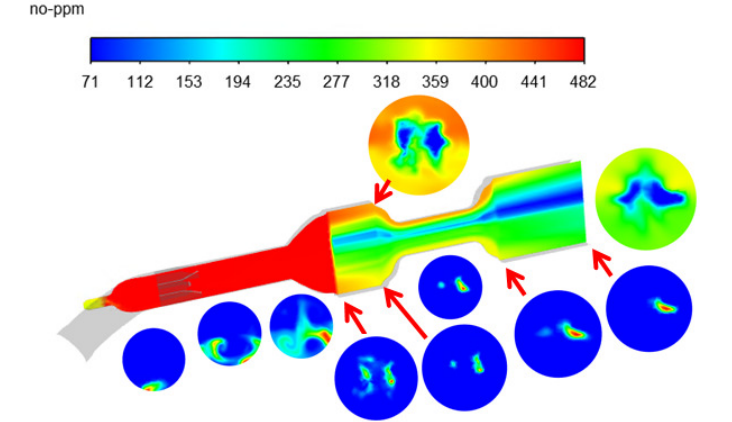
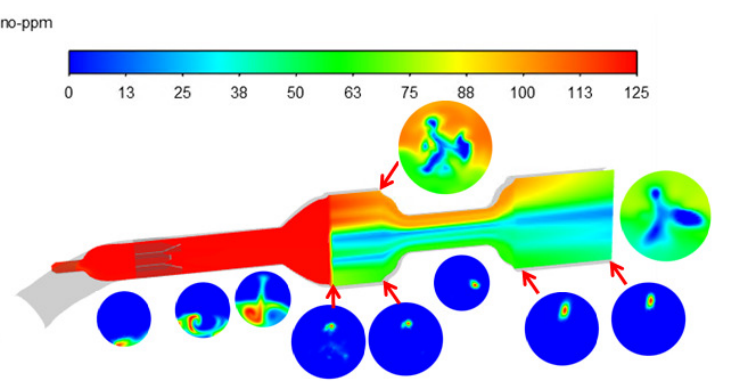
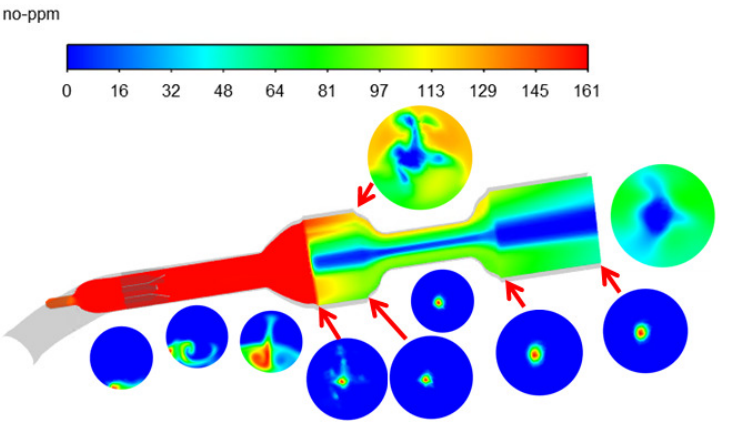
In the third case (Tab. 35), mixer C in both the basic position and rotated by 90° were compared. The rotated mixer turned out to be worse. The better mixing of the ammonia (increasing the concentration from the centre to the top of the catalyst face) resulted in a better conversion of NO from $X_{NO}=37.31\%$ to $X_{NO}=39.63\%$. This is also confirmed by the UI_{NH3_in} and CoV_{NH3_in} . The pressure drop for mixer C is lower than mixer A but higher than mixer B. Mixer C gives relatively good results in comparison to the previous ones.

Tab. 35. NO reduction and NH₃ mixing for hot flow CFD simulation (Case 3, OP2)

<p>Case 3: Prototype with mixer C injector-mixer distance L=120mm OP2 (Medium)</p>		<p> $UI_{NO_out}=0.848$ $NO_{ave_out}=74.86\text{ppm}$ $X_{NO}=39.63\%$ $UI_{NH3_in}=0.542$ $CoV_{NH3_in}=2.71$ $NH3_{ave_out}=3.85\text{ppm}$ $\Delta p_{mix}=183.65\text{Pa}$ </p>
<p>Case 3: Prototype with mixer C injector-mixer distance L=120mm & rotated by 90° OP2 (Medium)</p>		<p> $UI_{NO_out}=0.871$ $NO_{ave_out}=77.73\text{ppm}$ $X_{NO}=37.31\%$ $UI_{NH3_in}=0.497$ $CoV_{NH3_in}=3.80$ $NH3_{ave_out}=11.04\text{ppm}$ $\Delta p_{mix}=190.96\text{Pa}$ </p>

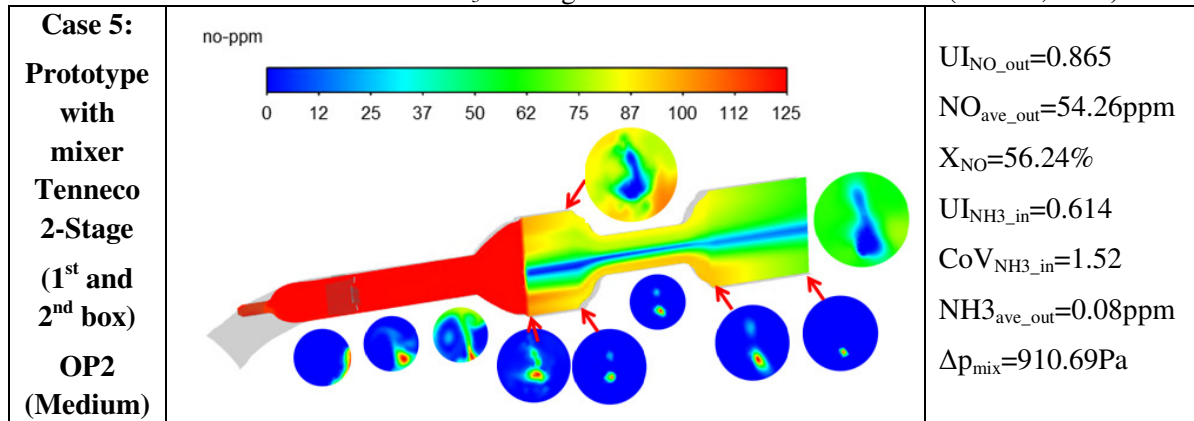
In the fourth case (Tab. 36), three operating parameters were compared after the addition of the second SCR catalyst. For the strongest operating parameter (OP1), the NO conversion was the lowest ($X_{NO}=49.47\%$), and for the weakest operating parameter (OP3) was the highest ($X_{NO}=65.03\%$). The decreasing flow in the system causes the SCR catalysts to have more time for nitrogen oxide conversion. What is also obvious is that the pressure drop across mixer C also decreases as mass flow rate decreases. The OP1 is so large that despite the high ammonia slip in the middle part of the catalyst, the NO conversion was not 100% complete. Nevertheless, mixer C needs to be improved due to the fact that in any case the distribution of the ammonia is focused on the central part of the SCR catalyst.

Tab. 36. NO reduction and NH₃ mixing for hot flow CFD simulation (Case 4, OP1-3)

<p>Case 4: Prototype with mixer C (1st and 2nd box) OP1 (High)</p>		<p>$UI_{NO_out}=0.862$ $NO_{ave_out}=243.55\text{ppm}$ $X_{NO}=49.47\%$ $UI_{NH3_in}=0.508$ $CoV_{NH3_in}=2.63$ $NH3_{ave_out}=11.69\text{ppm}$ $\Delta p_{mix}=1419.36\text{Pa}$</p>
<p>Case 4: Prototype with mixer C (1st and 2nd box) OP2 (Medium)</p>		<p>$UI_{NO_out}=0.835$ $NO_{ave_out}=54.29\text{ppm}$ $X_{NO}=56.22\%$ $UI_{NH3_in}=0.529$ $CoV_{NH3_in}=3.69$ $NH3_{ave_out}=3.74\text{ppm}$ $\Delta p_{mix}=194.71\text{Pa}$</p>
<p>Case 4: Prototype with mixer C (1st and 2nd box) OP3 (Low)</p>		<p>$UI_{NO_out}=0.859$ $NO_{ave_out}=55.95\text{ppm}$ $X_{NO}=65.03\%$ $UI_{NH3_in}=0.509$ $CoV_{NH3_in}=2.38$ $NH3_{ave_out}=5.17\text{ppm}$ $\Delta p_{mix}=37.66\text{Pa}$</p>

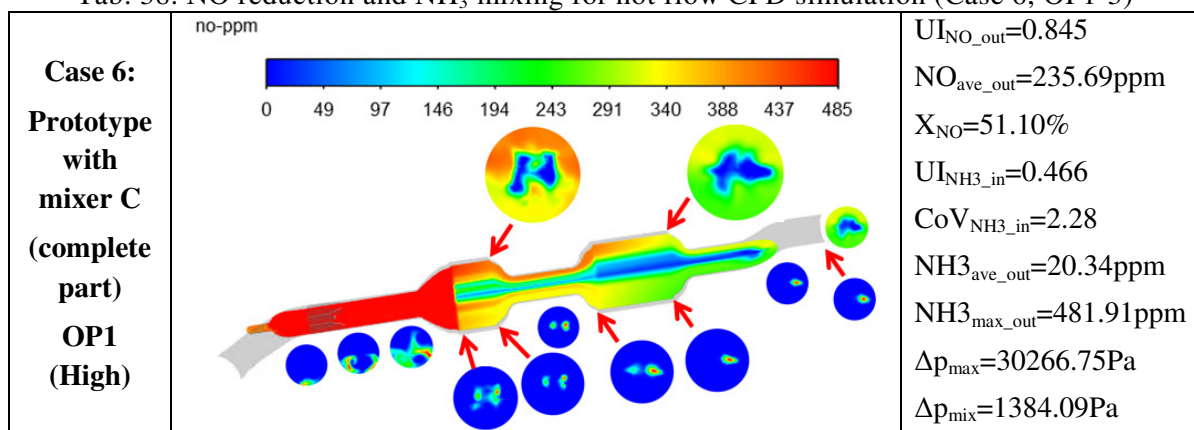
In the fifth case (Tab. 37), Tenneco 2-Stage mixer was checked and compared to mixer C for the parameter OP2. The advanced design of the Tenneco mixer contributes to a better splashing of urea and mixing of ammonia ($UI_{NH_3_in}=0.614$) compared to mixer C ($UI_{NH_3_in}=0.529$). This is also confirmed by the average ammonia slip which was at a very low level ($NH_{3_ave_out}=0.08ppm$). This has other costs as well, such as the greater pressure drop on the Tenneco mixer which is more than four times higher than with mixer C.

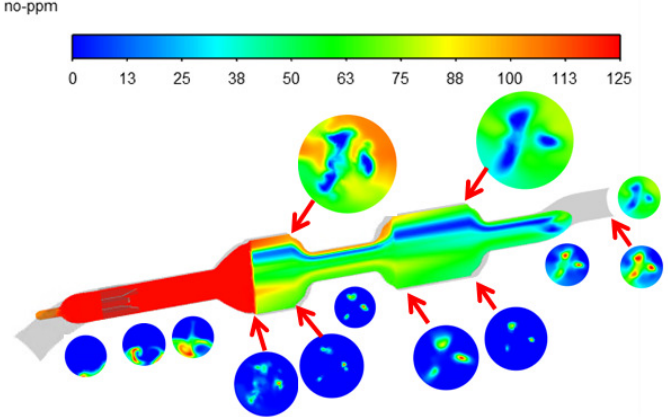
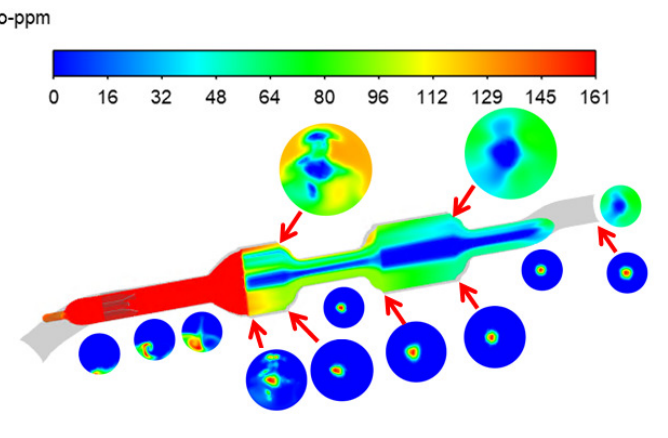
Tab. 37. NO reduction and NH_3 mixing for hot flow CFD simulation (Case 5, OP2)



In the sixth case (Tab. 38), CFD simulations were performed for the complete SCR system with mixer C and all operating parameters. The NO conversion results are comparable to the experiment but slightly lower. This is due to the fact that in the experiment the reduction was tested only in the central part of the outlet pipe, and in the simulation the results were averaged over the entire face of the outlet pipe. In this case, it can be noticed that as the flow decreases (from OP1 to OP3), the coefficient of variation ($CoV_{NH_3_in}$) decreases, which indicates a better degree of ammonia mixing. In the operating condition OP1 at high flow, ammonia concentration was concentrated in the central part of the system, which resulted in a very high ammonia slip. A slightly lower ammonia slip was also observed in case OP3.

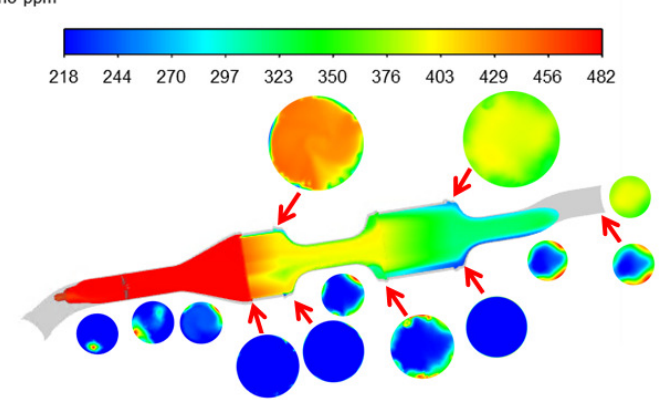
Tab. 38. NO reduction and NH_3 mixing for hot flow CFD simulation (Case 6, OP1-3)

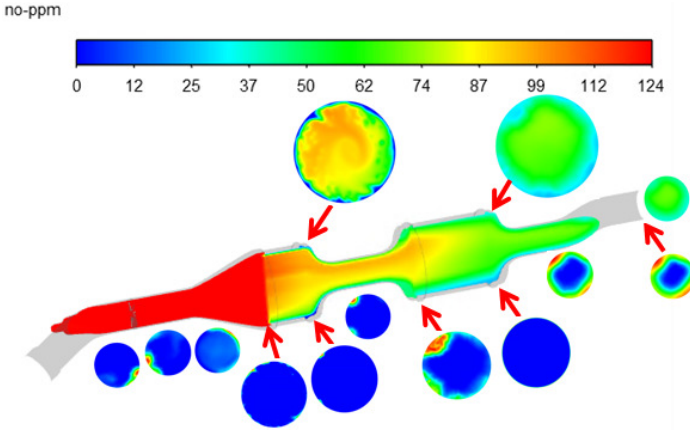
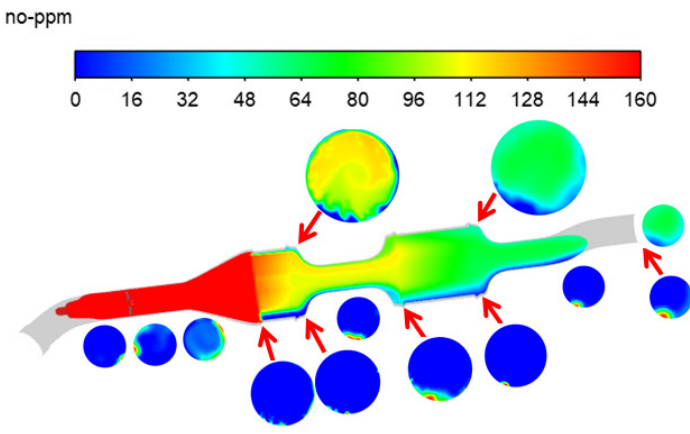


<p>Case 6: Prototype with mixer C (complete part) OP2 (Medium)</p>		<p>$UI_{NO_out}=0.864$ $NO_{ave_out}=52.52ppm$ $X_{NO}=57.65\%$ $UI_{NH3_in}=0.602$ $CoV_{NH3_in}=1.96$ $NH3_{ave_out}=1.67ppm$ $NH3_{max_out}=5.07ppm$ $\Delta p_{max}=5125.35Pa$ $\Delta p_{mix}=188.39Pa$</p>
<p>Case 6: Prototype with mixer C (complete part) OP3 (Low)</p>		<p>$UI_{NO_out}=0.861$ $NO_{ave_out}=55.52ppm$ $X_{NO}=65.30\%$ $UI_{NH3_in}=0.509$ $CoV_{NH3_in}=1.48$ $NH3_{ave_out}=3.99ppm$ $NH3_{max_out}=59.49ppm$ $\Delta p_{max}=1331.99Pa$ $\Delta p_{mix}=36.82Pa$</p>

In the seventh case (Tab. 39), CFD simulations were performed for the original VW SCR system and mixer for all operating parameters. Also in this case, the NO conversion results were lower than in the experimental results. Probably the results differ because, in fact, in the original SCR, the Cu-ZSM-5 catalysts were used, and in the numerical simulation the kinetic mechanism for Vanadium SCR catalysts were applied. Nevertheless, attention can be focused on the effectiveness of the original mixer, which gives very satisfactory results (high uniformity index of NO at outlet for all operating parameters).

Tab. 39. NO reduction and NH₃ mixing for hot flow CFD simulation (Case 7, OP1-3)

<p>Case 7: Original VW part and mixer (complete part) OP1 (High)</p>		<p>$UI_{NO_out}=0.971$ $NO_{ave_out}=308.35ppm$ $X_{NO}=36.03\%$ $UI_{NH3_in}=0.636$ $CoV_{NH3_in}=2.46$ $NH3_{ave_out}=2.84ppm$ $NH3_{max_out}=7.39ppm$ $\Delta p_{max}=38530.17Pa$ $\Delta p_{mix}=9506.41Pa$</p>
---	--	--

<p>Case 7: Original VW part and mixer (complete part) OP2 (Medium)</p>		<p>$UI_{NO_out}=0.923$ $NO_{ave_out}=56.87\text{ppm}$ $X_{NO}=54.14\%$ $UI_{NH3_in}=0.549$ $CoV_{NH3_in}=2.58$ $NH3_{ave_out}=1.81\text{ppm}$ $NH3_{max_out}=3.82\text{ppm}$ $\Delta p_{max}=5840.27\text{Pa}$ $\Delta p_{mix}=1224.95\text{Pa}$</p>
<p>Case 7: Original VW part and mixer (complete part) OP3 (Low)</p>		<p>$UI_{NO_out}=0.916$ $NO_{ave_out}=59.71\text{ppm}$ $X_{NO}=62.68\%$ $UI_{NH3_in}=0.418$ $CoV_{NH3_in}=3.04$ $NH3_{ave_out}=0.69\text{ppm}$ $NH3_{max_out}=5.79\text{ppm}$ $\Delta p_{max}=1290.59\text{Pa}$ $\Delta p_{mix}=216.30\text{Pa}$</p>

Additionally, there is no high ammonia slip in the SCR system. The only disturbing fact is that the greatest concentration of ammonia is at the outer edges of the inlet face of SCR catalyst (an unwanted deposit may accumulate in these areas). The design of the mixer itself is not complicated but requires the construction of an expensive tool to obtain the required bending shape. However, the pressure drop for the original mixer is six times higher than for mixer C.

10.5.4 Simulation results for improved mixer

Due to the fact that mixer prototype C did not fully fulfil its task due to unsatisfactory results, it was decided to create a new design of an improved mixer (Fig. 96). The improved mixer consists of two horizontal and vertical plates with a bent end and cut into squares to which additional three special bent blades are welded for each horizontal and vertical plate. The construction of the mixer becomes a mirror image both horizontally and vertically. During the design of the mixer, the possibility of its easy assembly and universal use was taken into account. What is more, during the flow of urea through the mixer, in most cases it

hits the blades at least three times, causing the droplets to splash to a smaller diameter, thanks to which its decomposition into ammonia is faster and better for mixing with flowing gases.

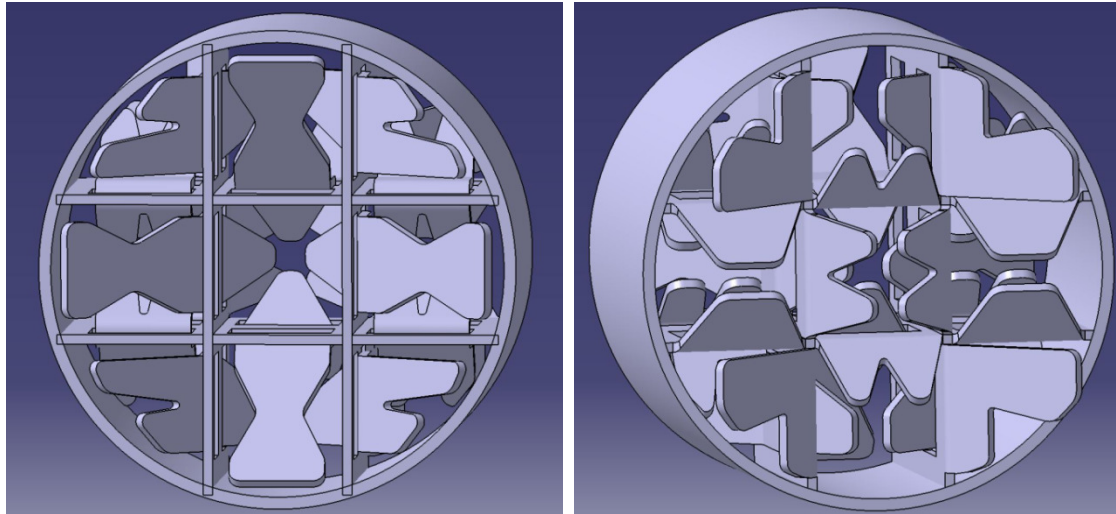


Fig. 96. The design of the improved mixer

For the improved mixer, the same CFD simulations were carried out for the complete SCR system in all operating parameters. At first glance, during the numerical simulation, the uniformity index of NH_3 at the inlet face of SCR catalyst on the Fig. 97 significantly jumped to the value of around 0.7, where for mixer C it was around 0.6.

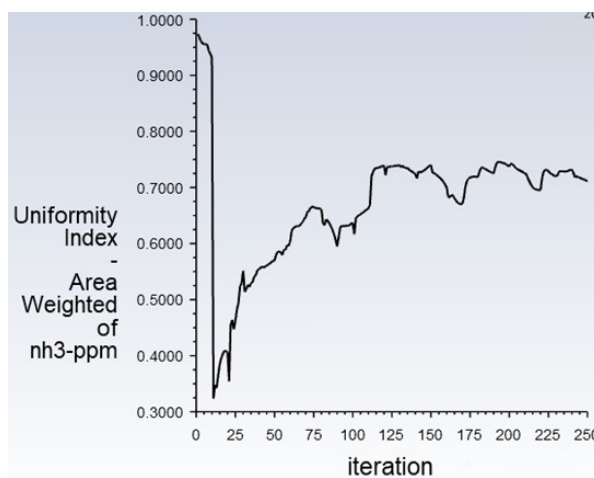
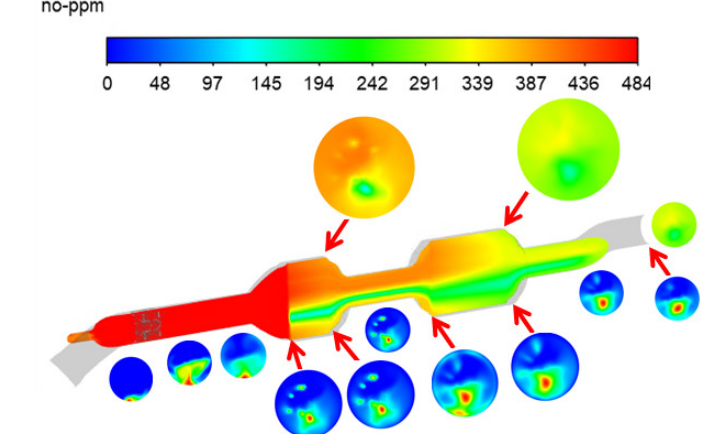
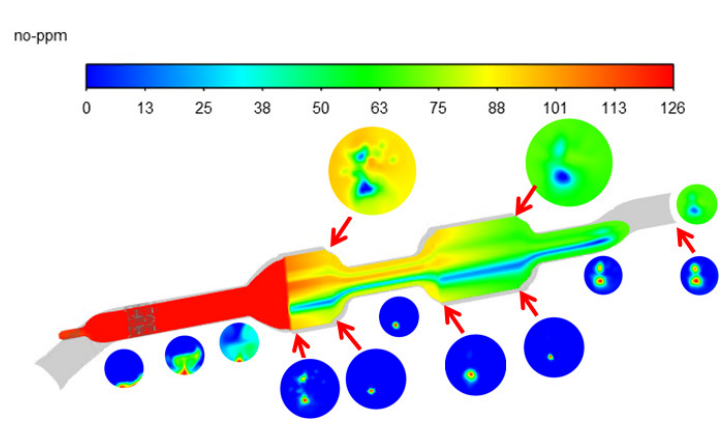
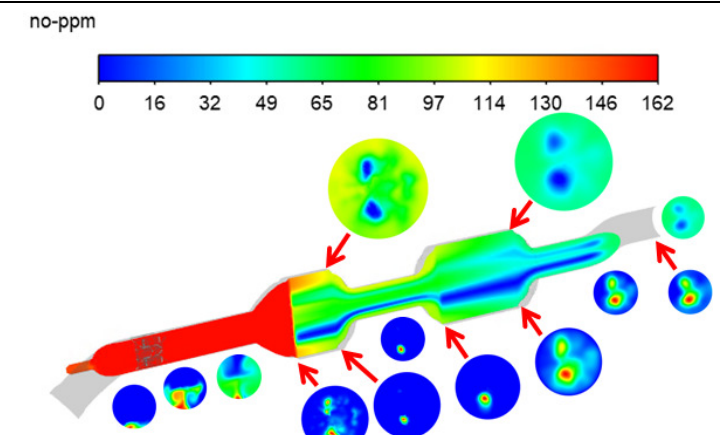


Fig. 97. $UI_{\text{NH}_3_{\text{in}}}$ for SCR system with improved mixer (OP2)

In an additional case where an improved mixer was used (Tab. 40), there was a significant improvement in the uniformity index of NO at the outlet face of SCR tail pipe (above 0.9) where for the system with mixer C this value was above 0.8. The values for $CoV_{\text{NH}_3_{\text{in}}}$ also decreases and $UI_{\text{NH}_3_{\text{in}}}$ as already mentioned increases, which indicates a better mixing of ammonia. Additionally important, the maximum ammonia slip is less than 10 ppm for OP1, which significantly reduces the ammonia slip compared to mixer C. The cost of this, however, is a much higher pressure drop across the improved mixer due to its design

complications compared to the mixer C. What may be surprising is that the reduction of NO for OP1 and OP2 slightly decreases, which indicates a better distribution of ammonia to the SCR catalyst and a better uniform NO conversion.

Tab. 40. NO reduction and NH₃ mixing for hot flow simulation (improved mixer, OP1-3)

<p>Additional Case: Prototype with improved mixer (complete part) OP1 (High)</p>		<p>UI_{NO_out}=0.966 NO_{ave_out}=300.21ppm X_{NO}=37.72% UI_{NH3_in}=0.782 CoV_{NH3_in}=0.66 NH_{3_ave_out}=3.09ppm NH_{3_max_out}=9.06ppm Δp_{max}=53046.45Pa Δp_{mix}=24890.45Pa</p>
<p>Additional Case: Prototype with improved mixer (complete part) OP2 (Medium)</p>		<p>UI_{NO_out}=0.944 NO_{ave_out}=63.59ppm X_{NO}=48.72% UI_{NH3_in}=0.711 CoV_{NH3_in}=1.60 NH_{3_ave_out}=1.05ppm NH_{3_max_out}=3.95ppm Δp_{max}=8127.51Pa Δp_{mix}=3239.05Pa</p>
<p>Additional Case: Prototype with improved mixer (complete part) OP3 (Low)</p>		<p>UI_{NO_out}=0.936 NO_{ave_out}=56.44ppm X_{NO}=64.73% UI_{NH3_in}=0.686 CoV_{NH3_in}=1.35 NH_{3_ave_out}=0.35ppm NH_{3_max_out}=0.91ppm Δp_{max}=1876.09Pa Δp_{mix}=589.26Pa</p>

Looking in more detail at the complete SCR system with improved mixer, first Fig. 98 shows the static pressure fields in the system. The maximum static pressure in the system is about 8 kPa, whereas in the system with mixer C it was about 5 kPa. The greatest pressure drop is on the mixer, then through the first SCR catalyst and the second SCR catalyst.

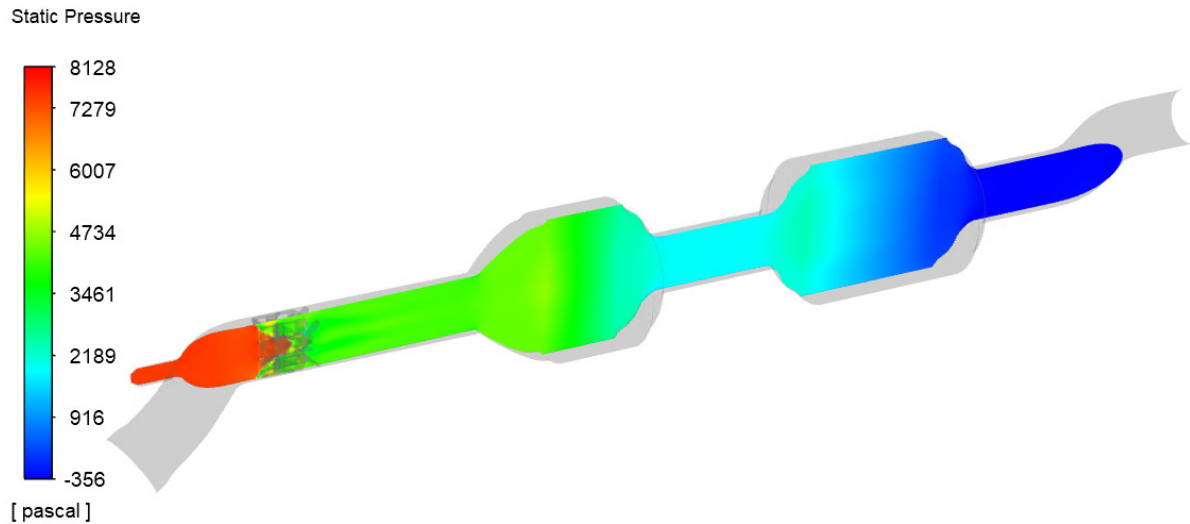


Fig. 98. Static pressure fields in the system for the case with the improved mixer (OP2)

The next Fig. 99 shows the temperature fields in the complete SCR system for OP2. It can be seen that downstream of the mixer and at the front face of first the SCR catalyst, the gases are slightly cooled by dosing AdBlue. Then, in the SCR catalysts themselves, there is slight heating due to exothermic reactions.

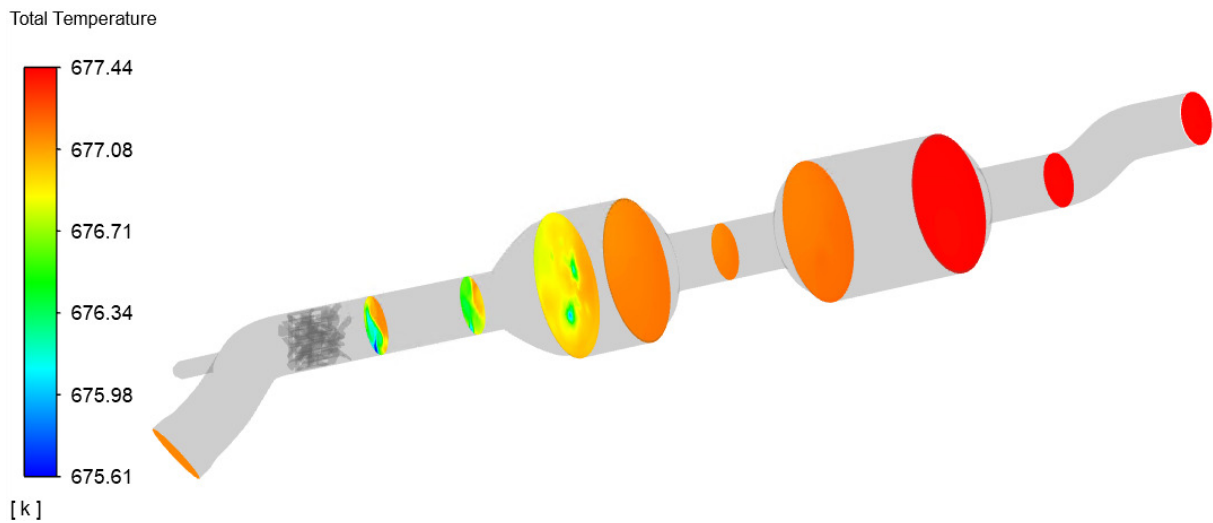


Fig. 99. Temperature fields in the system for the case with the improved mixer (OP2)

Further, in Fig. 100 is shown velocity vector is shown in the complete SCR system for OP2. The highest velocities are created in the mixer itself when the gases are mixed turbulently. The average velocities after the mixer then decrease in the SCR catalysts themselves where the flow is laminar. Fig. 101 shows the method of mixing the improved mixer within it and the velocity trajectories of gases after leaving the mixer. The mixer disturbs the flow very well, mixing the trajectories in the entire pipe in a harmonic uniform way, which is of course desirable to mix ammonia with gases in the best way.

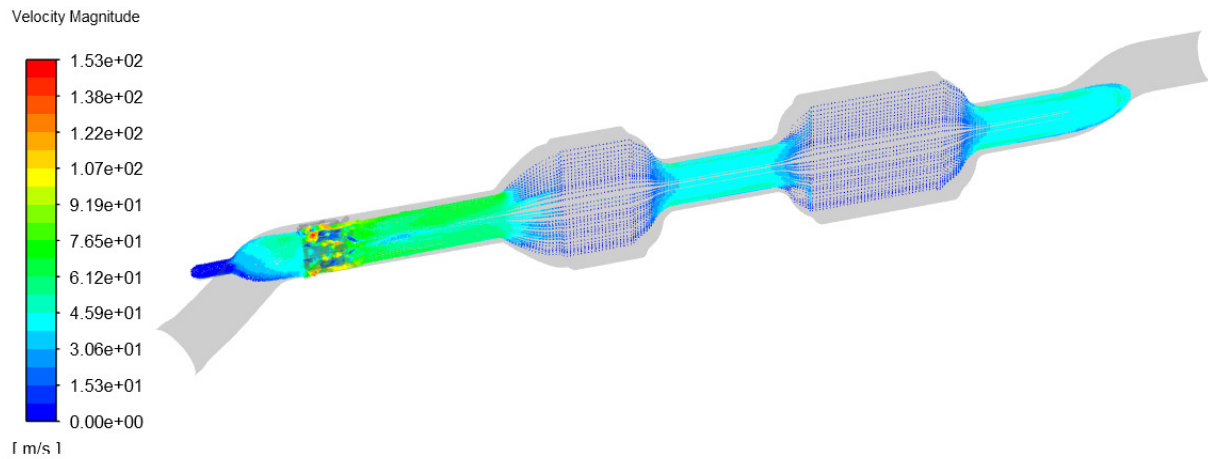


Fig. 100. Velocity vectors in the system for the case with the improved mixer (OP2)

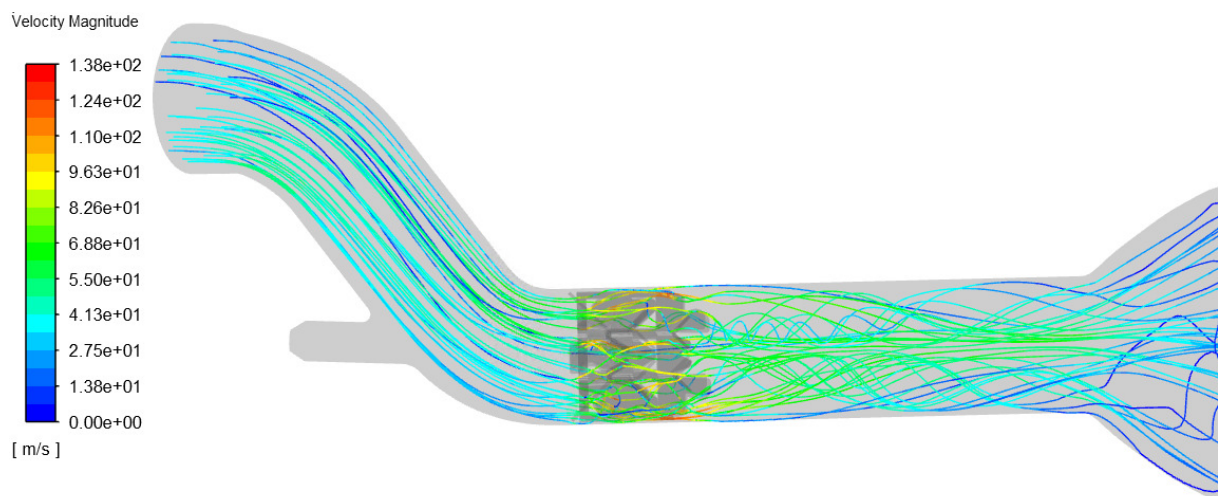


Fig. 101. Gas velocity trajectories for the case with the improved mixer (OP2)

Fig. 102 shows the urea-water solution (UWS) injection into the SCR system and the trajectories of their droplets denoting their diameters. Droplet diameters decrease after crossing the mixer, but unfortunately not all of them (some had to not collide with the mixer).

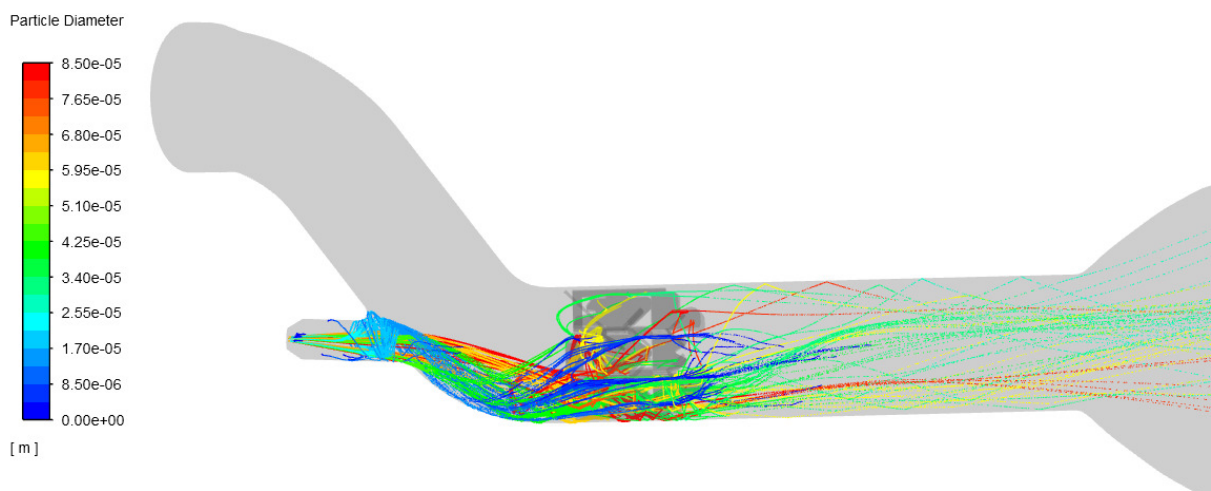


Fig. 102. Trajectories of UWS colored by diameter for the case with the improved mixer

Smaller droplets evaporate faster, releasing ammonia, larger droplets, in turn, hit the inlet face of the SCR catalyst and evaporate there, releasing a greater concentration of NH_3 in this area without having a chance to mix with the gas behind the mixer. The improved mixer, however, distributes the droplets downstream of the mixer well through the entire tube volume.

Finally, one more additional SCR system case in which no mixer was mounted was simulated for OP2. After running the simulation, the UI of NH_3 at the inlet face of the SCR catalyst (Fig. 103) fluctuated around 0.4 which proves the poor level of NH_3 mixing.

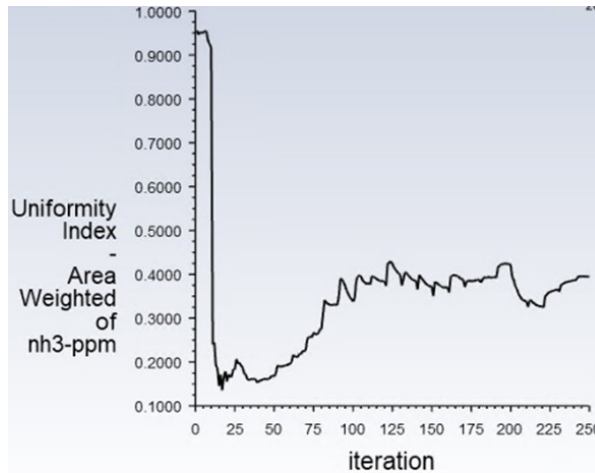


Fig. 103. $UI_{\text{NH}_3_{\text{in}}}$ for SCR system without mixer (OP2)

Although the average NO reduction is at a good level (Tab. 41), it can be seen that it is not uniform in the SCR catalysts. Ammonia was concentrated mainly in the upper left region of the SCR catalyst, which contributes to more NO conversion in these areas and less NO reduction in the lower right areas of the SCR catalysts. High concentration in point areas causes that there was a large maximum ammonia slip at the outlet, which also confirms the high $CoV_{\text{NH}_3_{\text{in}}}=6.12$. Such a solution is not practically used because some areas of the SCR catalyst are not fully covered and used, and areas with high ammonia concentrations may cause deposits there.

Tab. 41. NO reduction and NH_3 mixing for hot flow CFD simulation (no mixer, OP2)

<p>Additional Case: Prototype without mixer (complete part) OP2 (Medium)</p>		<p>$UI_{\text{NO}_{\text{out}}}=0.838$ $\text{NO}_{\text{ave}_{\text{out}}}=58.64\text{ppm}$ $X_{\text{NO}}=52.71\%$ $UI_{\text{NH}_3_{\text{in}}}=0.395$ $CoV_{\text{NH}_3_{\text{in}}}=6.12$ $\text{NH}_3_{\text{ave}_{\text{out}}}=12.96\text{ppm}$ $\text{NH}_3_{\text{max}_{\text{out}}}=356.95\text{ppm}$ $\Delta p_{\text{max}}=4999.85\text{Pa}$</p>
---	--	---

11 Analysis and comparison of test results

This section presents the numerical simulation results and their validation with analytical calculations and experimental results. Various comparisons of the CFD results with the experimental results are also presented. Moreover, several simulations were carried out to check the influence of various parameters of the SCR system on the simulation results.

11.1 Validation of results for a 2D axisymmetric model

As already mentioned in subsection 10.2.3, to validate the conversion of kinetic data and implementation of reaction scheme into a CFD model, a 1D analytical model presented in [139] has been used and compared with CFD simulation by a 2D axisymmetric model. The 1D model given by Eq. (106) was used for analytical calculations. In this equation, the pseudo-first-order apparent reaction rate constant ($k_v \eta C_{O_2}^\beta = 27 \text{ s}^{-1}$) is known from the Tab. 26 for temperature ($T = 668 \text{ K}$) and known average velocity ($v = 0.47 \text{ m/s}$) in the SCR monolith from 2D simulation. Therefore, the reduction of nitric oxide on the catalyst from simulation can be validated with the analytical model in such a way that the average NO reduction in 10 equal points of the monolith (z) from the inlet to the outlet were calculated (Tab. 42).

Tab. 42. Validation results for 2D axisymmetric model

Reactor height	Analytical 1D model conversion, molar fraction		2D model conversion from CFD, molar fraction		Relative difference $RE = \frac{ C_{NO \ 1D} - C_{NO \ CFD} }{C_{NO \ 1D}}$
	$z, \text{ cm}$	$C_{NO}, \text{ ppm}$	$X_{NO}, \%$	$C_{NO}, \text{ ppm}$	
0.00	124.0	0.0	123.6	0.3	0.003
0.82	95.2	23.2	99.0	20.2	0.04
1.65	73.1	41.0	77.6	37.4	0.06
2.47	56.2	54.7	60.1	51.5	0.07
3.30	43.1	65.2	46.6	62.4	0.08
4.12	33.1	73.3	39.3	68.3	0.19
4.94	25.4	79.5	30.5	75.4	0.20
5.77	19.5	84.2	23.6	80.9	0.21
6.59	15.0	87.9	18.3	85.3	0.22
7.42	11.5	90.7	14.9	88.0	0.29
Average relative difference					0.14

The graphical presentation of the Tab. 42 is shown in the Fig. 104. The NO conversion results for the 2D CFD model and 1D analytical model are very similar with an average relative difference of 0.14, which is acceptable for the needs of the CFD simulations. Minor discrepancies could result from the fact that Eq. (106) did not take into account the

temperature increase as a result of the process, which minimally increased the NO conversion efficiency. However, the verification shows that the model has been implemented correctly into the Fluent code.

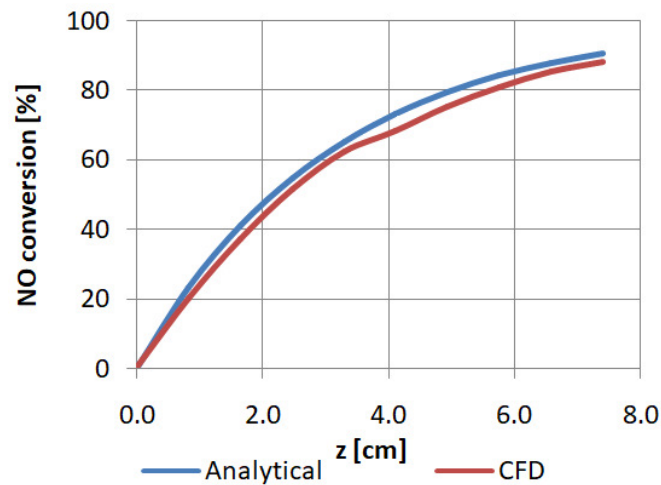


Fig. 104. Verification of reaction kinetics for 2D axisymmetric model

11.2 Validation of results for a 3D model

At the beginning, the results of CFD simulations were compared with the experimental results of pressure drops in the first and second SCR catalyst in a system where no mixer was installed (Fig. 105). The polynomials presented for experimental results on the plots were used to calculate the viscous and inertial resistance for the CFD porous model. The pressure drop on the first SCR catalyst is twice as high as on the second SCR catalyst, because the first catalyst additionally takes into account the pressure exerted by the second catalyst. The average of percentage relative difference (PRD) is the percentage mean relative difference (PMRD) and for the first SCR catalyst it is 2.3% and for the second SCR catalyst 5.8%, which reflects a very good validation of the numerical simulations with experimental results.

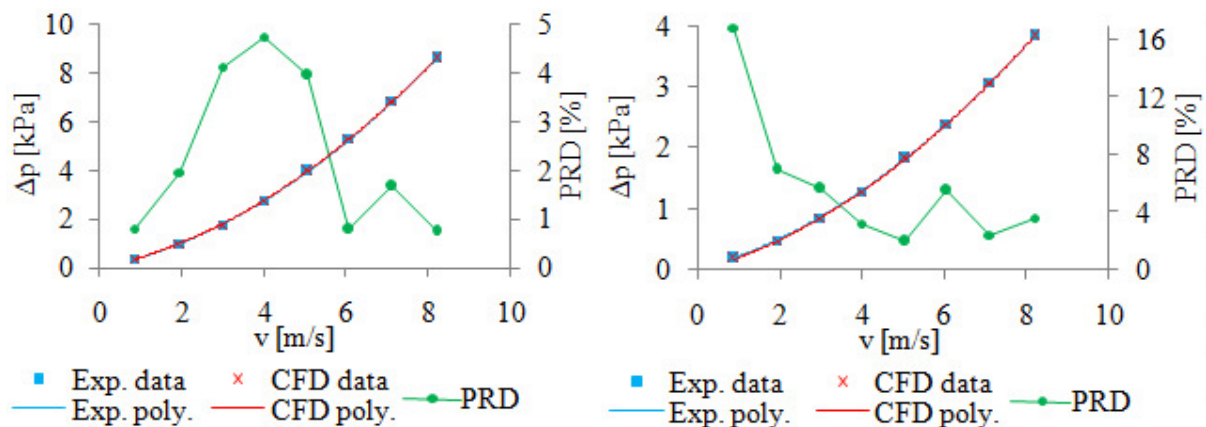


Fig. 105. Pressure drop vs. velocity (exp. vs. CFD): Case 6 w/o mixer for 1st & 2nd catalyst

It is also worth presenting the pressure drop for individual mixers and their degree of ammonia mixing ($UI_{NH_3_in}$) on the front face of the SCR catalyst (Fig. 106). It is obvious that with the degree of complexity of the mixer design, the pressure drop increases as well as the uniformity index for ammonia.

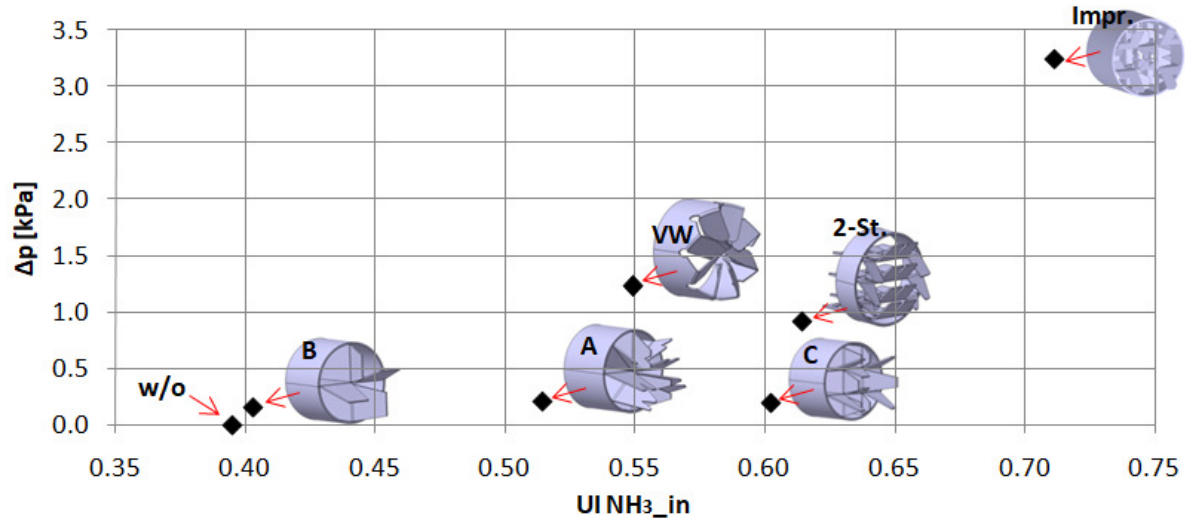


Fig. 106. Calculated pressure drop vs. $UI_{NH_3_in}$ for different mixers (OP2)

It is also worthwhile comparing the experiment results with the numerical ones in terms of visualization. For example, Fig. 107 shows the visualization of the outlet face of SCR catalyst for the cold flow in Case 1. The CFD simulation predicted the area of velocity fields in which there are small and large values.

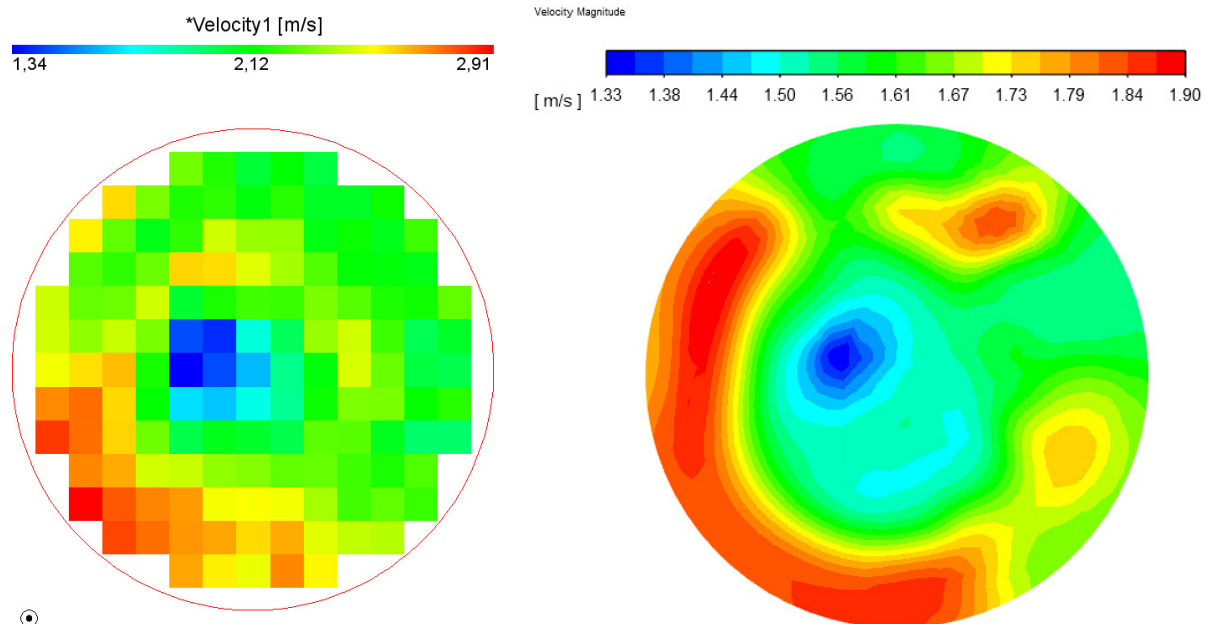


Fig. 107. Comparison of measured and calculated velocity for Case 1 (cold flow)

Similarly for the hot flow, the mole fractions of NO at the outlet face of SCR catalyst for case 4 in OP2 was visually compared (Fig. 108). The numerical simulation well estimated the poor conversion in the upper parts of the SCR catalyst and the highest conversion in its middle.

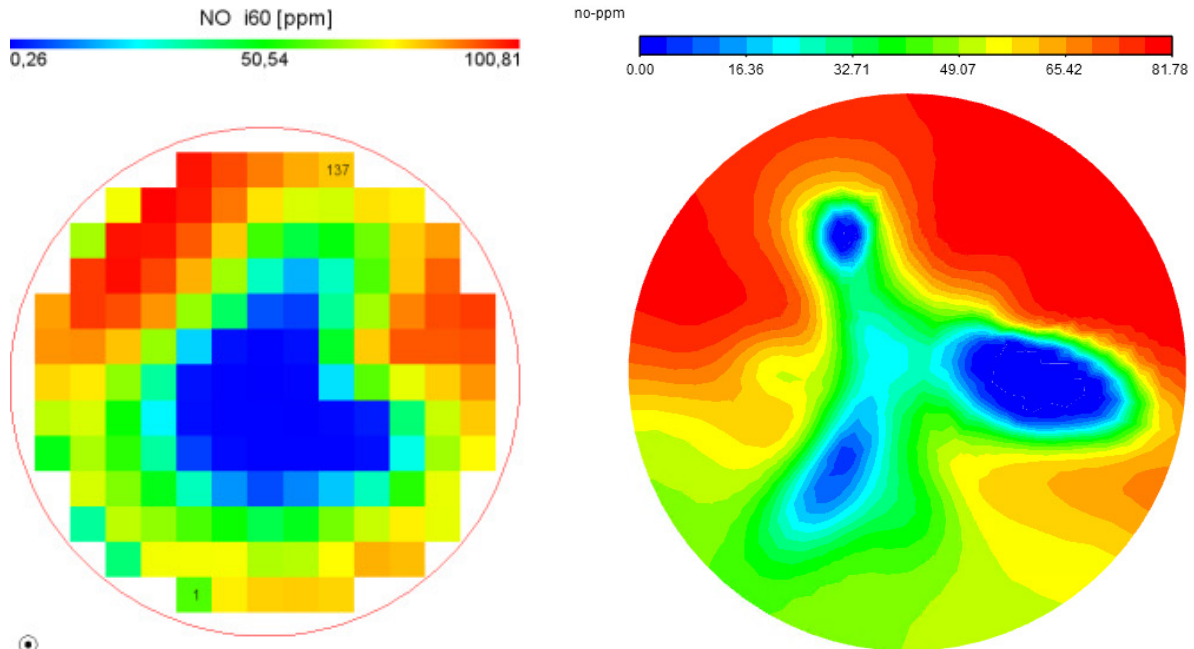


Fig. 108. Comparison of measured and calculated mole fractions of NO for Case 4 (OP2)

The 3D model and its NO conversion were validated for case 4 for all operational parameters (Fig. 109). The comparative results of the experiment with CFD simulation are very similar, where the greatest percentage relative difference (PRD) did not exceed 3%.

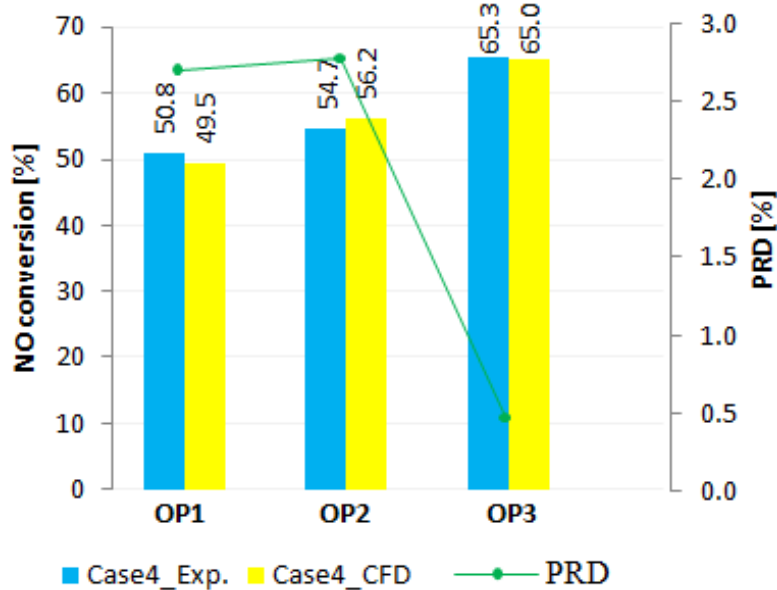


Fig. 109. Comparison of measured and calculated NO conversion for Case 4

Finally, for a complete SCR system, the effects of their mixers on NO reduction and the degree of NO mixing as well as maximum ammonia slip were compared. According to Fig. 110, when the design of the mixer is better and more advanced, the uniformity index of nitrogen oxide (UI_{NO_out}) at the outlet of the SCR system increases. It is surprising that the NO reduction is falling contrary to this trend. This can be explained by the fact that a weaker mixer results in larger point areas of ammonia concentration, which contributed to a complete reduction of nitric oxide in these areas with a slip of ammonia that was in excess. Thus, the average NO conversion was higher for the weaker mixer. This is also somewhat confirmed by Fig. 111, where a less complicated version of the mixer (“empty passages” of urea without any collision with the mixer) causes a higher ammonia slip at the outlet of SCR system, especially for higher mass flow rate e.g. OP1. This situation, however, was resolved in a more advanced mixer design, which made the ammonia more homogeneous and the NO conversion proceeded uniformly through the whole reactor area with minimal ammonia slip.

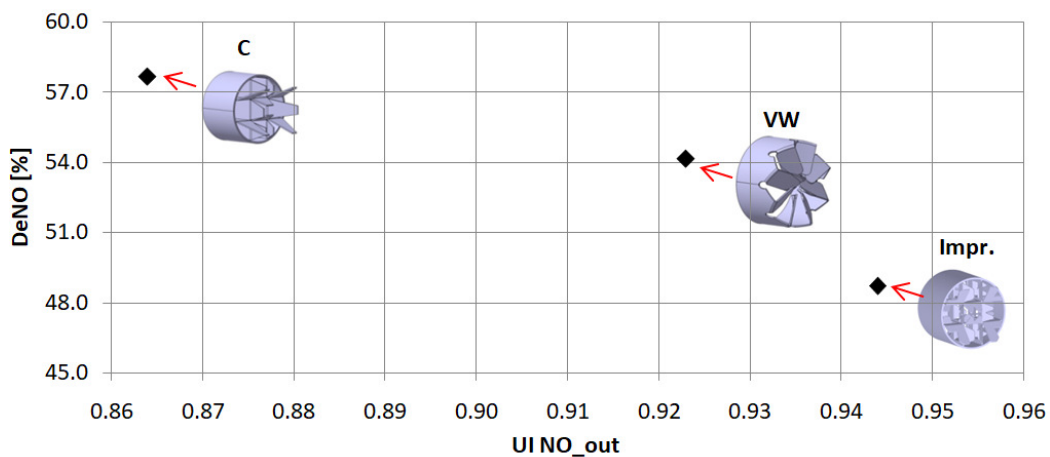


Fig. 110. Calculated NO reduction vs. UI_{NO_out} for different mixers in SCR systems (OP2)

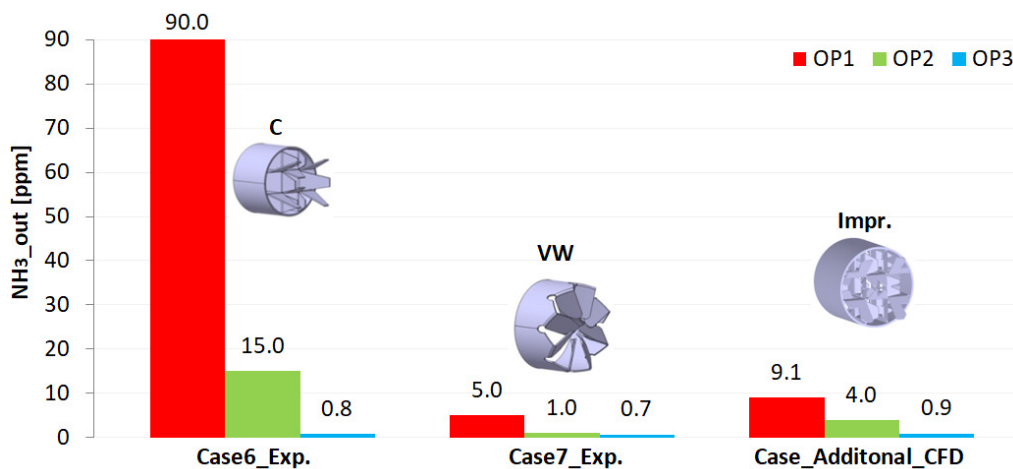


Fig. 111. Maximum ammonia molar fraction for different mixers in SCR systems

11.3 Impact of other parameters on the research results

In this subsection, other parameters that affect the SCR system performance are additionally presented. Additional CFD simulations were performed for the complete SCR system with an improved mixer and for OP2 but with changes for the tested parameter.

First, the influence of oxygen and later water concentration in the inlet gases on the reduction of the SCR system was checked (Fig. 112). Increasing the oxygen mole fraction in the SCR system from 2% to 20% (at the expense of nitrogen) increases the NO reduction by about 10%. This is because oxygen is directly involved in the standard SCR reaction. On the contrary, when the exhaust gases in the SCR system are more humid, the NO conversion then decreases, however, not so much, by about 2%. The decrease is caused by the fact that water is involved in the hydrolysis reaction of UWS where the exponent rate for water is negative.

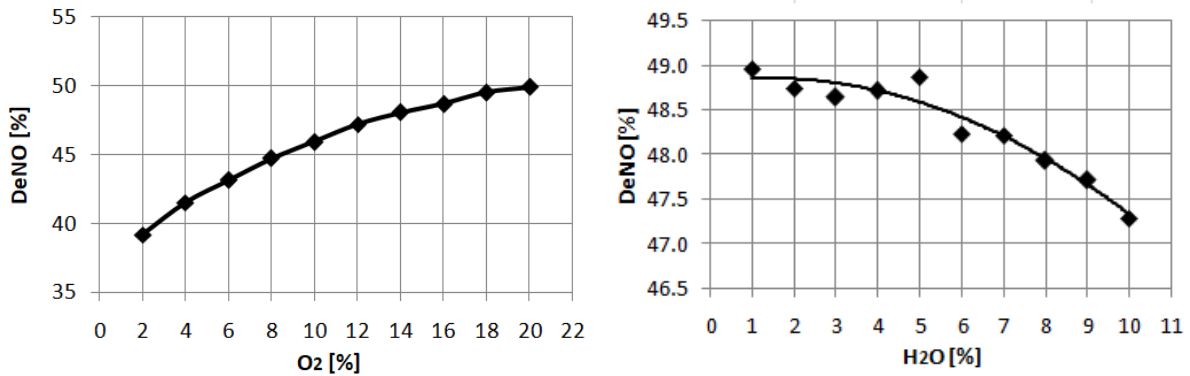


Fig. 112. Influence of the O₂ & H₂O on DeNO in SCR with improved mixer

In the next case (Fig. 113), the influence of the ammonia on the nitrogen oxide ratio (ANR) and the final NO reduction in the SCR system was investigated.

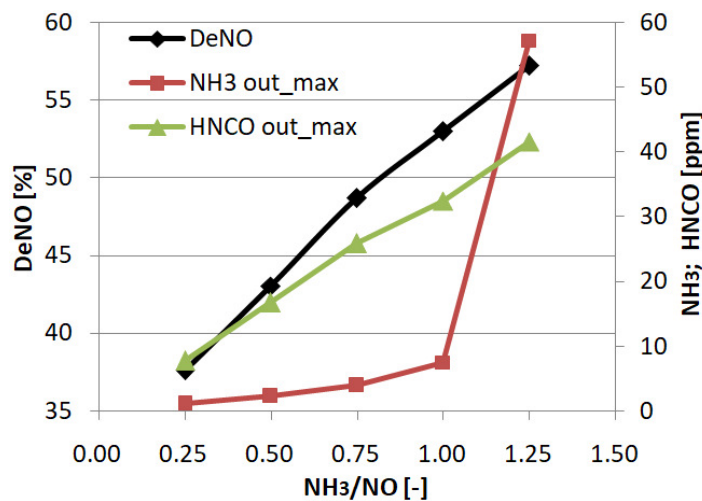


Fig. 113. Influence of the ANR on DeNO in SCR with improved mixer

It can be seen that as the ANR increases, the DeNO in the SCR system increases. The results confirmed the predictions that when $ANR > 1$, there is a significant increase in NH_3 and isocyanic acid at the outlet of the SCR system. The optimal condition seems to be $ANR = 1$, then a large NH_3 slip and the formation of a deposit in the SCR system can be avoided.

Then, the influence of NH_3 rate order (rate exponent in Fluent) on the NO reduction was checked. As already mentioned, many authors use the rate order for NH_3 equal to zero to simplify the model and others in turn presented this value even to 0.29 depending on the temperature. Fig. 114 shows that the rate order of NH_3 close to zero gives the highest NO conversion, however, from the value of 0.09 the NO reduction starts to drop significantly.

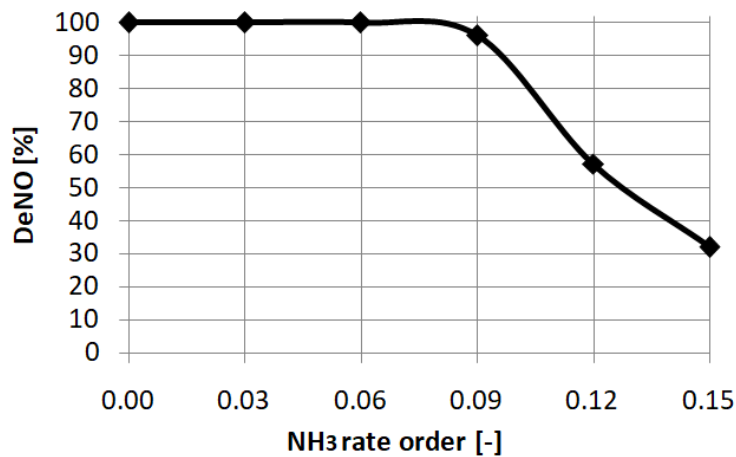


Fig. 114. Influence of the NH_3 rate order on DeNO in SCR with improved mixer

Another parameter that influences NO reduction is the mass flow rate of exhaust gas in the SCR system. As the mass flow rate increases, the DeNO decreases (Fig. 115). This is because faster flow through the catalysts gives less time for the DeNO process inside them.

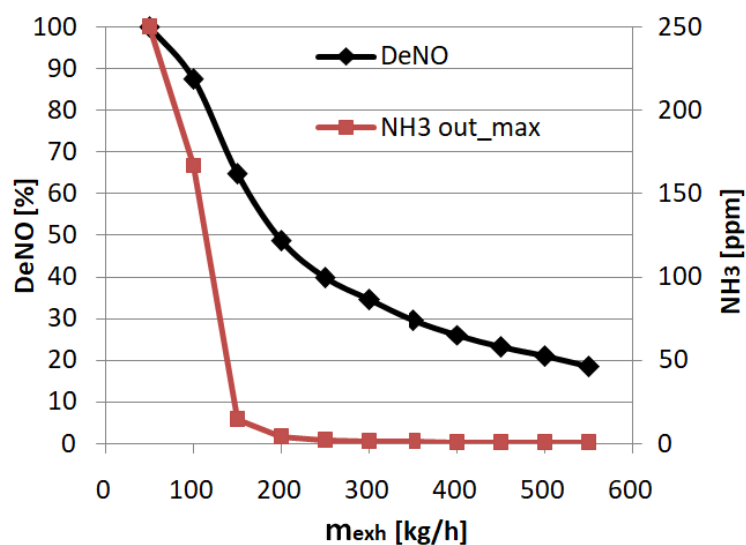


Fig. 115. Influence of the mass flow rate of exhaust gas on DeNO in SCR with improved mixer

It is also interesting that at high ammonia slip occurs with a lower mass flow rate. This means that for the low mass flow rate there is enough time for NO conversion and too much AdBlue dosed. Therefore, the amount of AdBlue injected and regulated by the Engine Control Unit (ECU) depends on the engine load and amount of NO_x in exhaust gas.

Staying with the mass flow rate, it is worth adding that an increase in this parameter causes an increase in pressure in the SCR system. What's more, Fig. 116 also shows how the average velocity of flow gases through the front and rear SCR catalyst increases. In the front SCR catalyst (CAT 1) where the temperature is slightly higher, the average velocity is about 1 m/s higher than in the rear SCR catalyst (CAT 2).

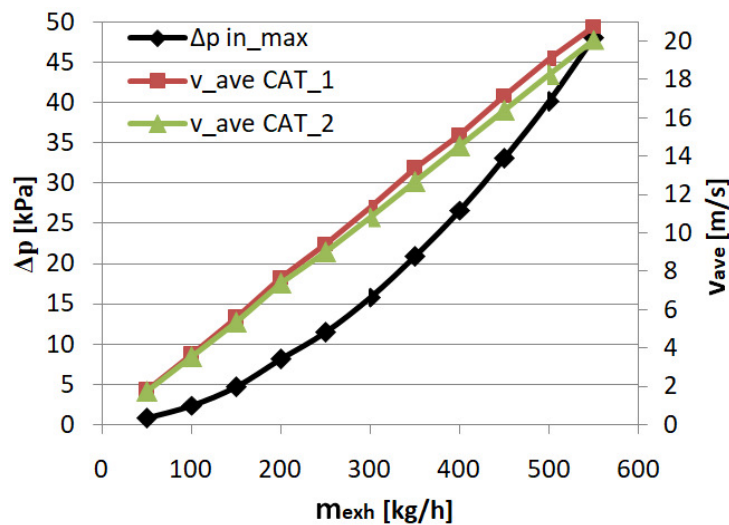


Fig. 116. Influence of the mass flow rate on pressure drops and velocities in catalysts

The last important parameter that has been tested in the CFD numerical simulation and has an impact on the SCR system is temperature (Fig. 117).

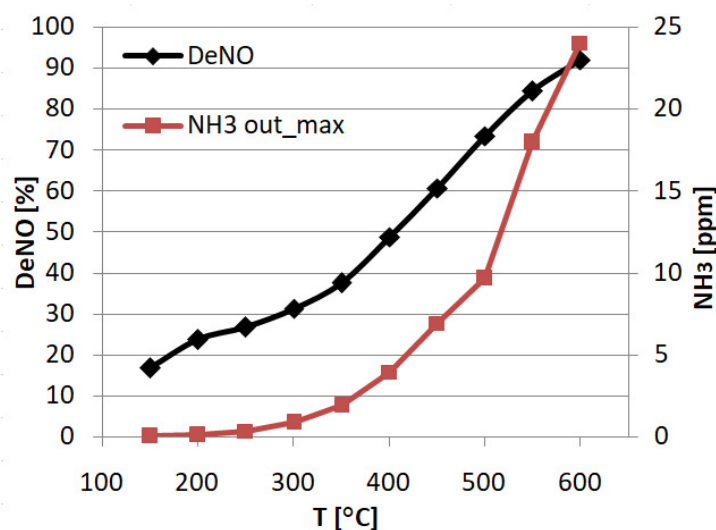


Fig. 117. Influence of the temperature on DeNO and ammonia slip in SCR with the improved mixer

NO conversion increases with the rising temperature, which is obvious due to the favorable conditions for the occurrence of exothermic reactions in the SCR catalyst. This is also seen in a greater amount of ammonia (its excess) in the outlet as the temperature increases, due to a better decomposition of urea in the thermolysis reaction.

An increase in temperature also causes an increase in pressure in the SCR system, which takes the form of a linear function (Fig. 118).

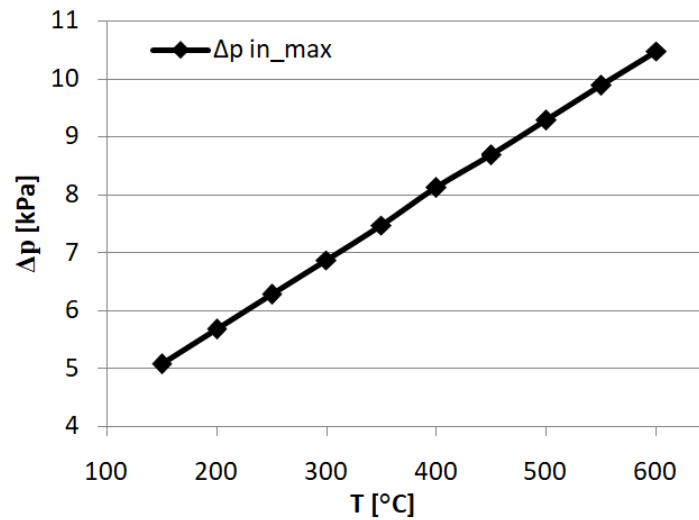


Fig. 118. Influence of the temperature on pressure drops in SCR with the improved mixer

12 Emission tests in the certification laboratory

This chapter presents the results of the emission tests for WALKER aftermarket and original SCR system which were carried out by the certified unit (TÜV SÜD Auto Service GmbH in Germany). To one of their laboratories in Garching, a dedicated car for these SCR systems was delivered (VW Passat 2.0 Blue TDI, 103 kW, 2014 Euro 6b) and properly prepared together with the SCR systems (according to the prepared additional plan for gas sampling for research purposes as shown in the Fig. 119).

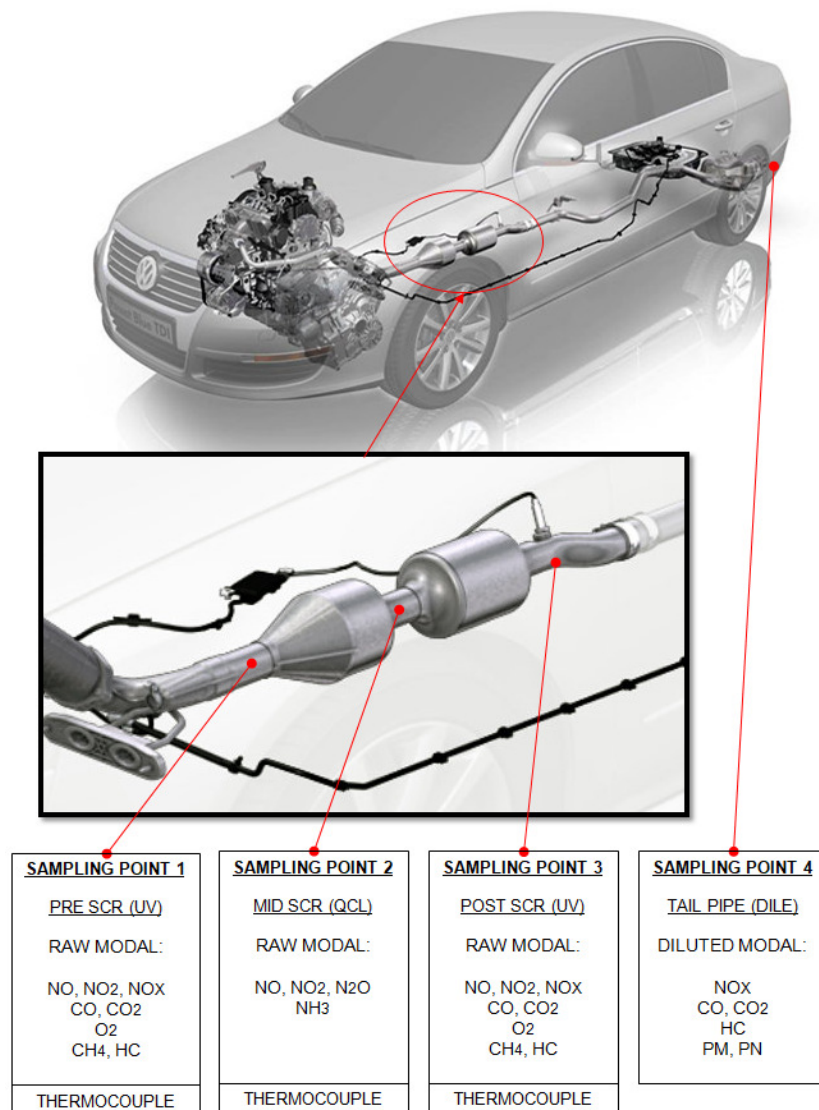


Fig. 119. Measuring points during the emission approval tests

According to ECE Regulation No. 103, to obtain ECE Type approval, the car with the WALKER SCR system also had to be tested and compared with the original SCR system regarding noise and exhaust backpressure. The sound measurement was performed with a

Brüel & Kjaer 2236 device in both driving and stationary conditions. In turn, the measurements of the exhaust backpressure were done upstream in the SCR system through the WIKA CPH6200-S2 device. These measurements were made by the Garching laboratory according to ECE Regulation No. 59. Subsequently, emission tests in the NEDC cycle have been carried out in the Heimsheim laboratory. The laboratory is equipped with a MAHA AIP-ECDM 48L-4x4 brake dynamometer, HORIBA CVS 9330 T sampling system and HORIBA MEXA 7000 pollution analyzer. The tests were carried out according to ECE Regulation No. 103, ECE R83 and Regulation EC No. 715/2007.

WALKER SCR prototypes before shipping them to the laboratory, were wrapped in the front side by thermal insulation from Culimeta company in order to provide better thermal insulation which is supposed to keep the exhaust gas temperature higher, necessary for chemical reactions.

Fig. 120 shows the correct mounting of SCR systems under the cars with sampling points of gases for the ultraviolet (UV) analyzer and quantum cascade lasers (QCL) as well as thermocouples. Further Fig. 121 presents a prepared car on a chassis dynamometer in the laboratory for measurement of exhaust emissions using the CVS method from measuring bags during the NEDC cycle.



Fig. 120. Installed OEM and WALKER SCR systems under the car with sampling points



Fig. 121. Car prepared for emission tests on chassis dynamometer

12.1 Regulations for a replacement exhaust gas aftertreatment system

If an original pollution control device is damaged or its effectiveness deteriorates, it can be replaced by a replacement pollution control device from the aftermarket. In order to introduce a replacement pollution control device to the market, approval tests must be carried out in accordance with UNECE (United Nations Economic Commission for Europe) Regulation 103 or Council Regulation 715/2007 amended for motor vehicles categories, which are tested for emissions by UNECE Regulations 83. These regulations define demands that the devices have to meet and what tests must be fulfilled. According UNECE Regulations 103, the same type of pollution control device may not differ with regard to the following parameters [134]:

- quantity of coated substrates, their structure (cell density) and material;
- type of catalytic activity with material content and ratio;
- monolith volume and ratio of front area;
- dimensions (e.g. diameter and length) and monolith shape;
- thermal protection.

Approval of a replacement of pollution control device means the approval of a pollution control device (e.g. catalytic converter) intended to be mounted as a replacement part for specific types of vehicles with regards to [134], [135]:

- the limitation of pollutant emissions;
- noise level;
- effect on the vehicle performance;
- on-board diagnostic (OBD);
- durability (shall cover 160,000 km from Euro 5).

Except that, UNECE Regulations 103 also defines general requirements [134], [135]:

- the installation of the replacement pollution control device should be in the same position as the original part;
- the position of the exhaust line, the oxygen sensor and other sensors shouldn't be changed;
- if the original part contains thermal protections, the replacement device should also include them;
- the replacement device should be durable regarding the corrosion and oxidation phenomena.

Regarding emissions, the assessment includes a comparison of emission of pollutants from the exhaust system of a vehicle fitted with an original pollution control device and replacement. Three measurements are carried out for each device according to UNECE Regulations 83. The replacement pollution control device fulfils requirements if the results meet the specific limits off each exhaust gas component for the given Euro standard and the following conditions [134]:

$$M \leq 0.85 \cdot S + 0.4 \cdot G \quad (110)$$

$$M \leq G \quad (111)$$

where:

M - mean value of the emissions of one pollutant (CO, THC, NMHC, NO_x, PM, PN) obtained from the three type tests with the replacement pollution control device, S - mean value of the pollutant emissions obtained from the three type tests with the original part, G - limit value of the emission of the pollutant according to the type approval of the vehicle divided by the deterioration factors (e.g. Tab. 43) determined by UNECE Regulations 103.

Tab. 43. Deterioration factors for diesel engine applicable from Euro 5

CO	NO _x	HC+NO _x	PM	PN
1.5	1.1	1.1	1.0	1.0

Regarding the OBD system, during emission tests the replacement pollution control device cannot turn on the Malfunction Indicator Lamp (MIL). What's more, a vehicle equipped with a replacement pollution control device in the exhaust system does not affect the vehicle performance. Due to this, measurements of the exhaust backpressure are performed which should not be greater than the maximum allowed value by the manufacturer of the engine. Alternatively, the measured power of the vehicle equipped with a replacement pollution control device shall not be more than 5% lower from the value of power for a vehicle with the original part [134].

According to regulation 103, the pollution control devices before emission tests should be preconditioned (extra-urban cycle (EUDC) has to be repeated 12 times) in the vehicle. The pollutant emission from the exhaust system is determined according to the test type of UNECE Regulation 83. The tests are carried out for vehicles which are conditioned for at least six hours (and continue until the engine oil and coolant temperatures are at the room temperature) at ambient temperatures of $20\pm 30^{\circ}\text{C}$ and tests of emission upon start-up of a cold engine then engine and control pollution device should be fully warmed up through three exhaust gas tests in a specific cycle (e.g. NEDC) on the exhaust gas roller test bench. For the replacement pollution control device, the weighted mean of emission of pollutants from the exhaust system multiplied by emission deterioration factors (these factors are intended to take account the ageing of device instead durability on test track on the road) should be lower or equal to the emissions limit for every pollutant [134], [135].

12.2 Emission test results

To obtain ECE Type approval, first the car's sound level and exhaust backpressure according to measurement points had to be checked as in Fig. 122 and Fig. 123.

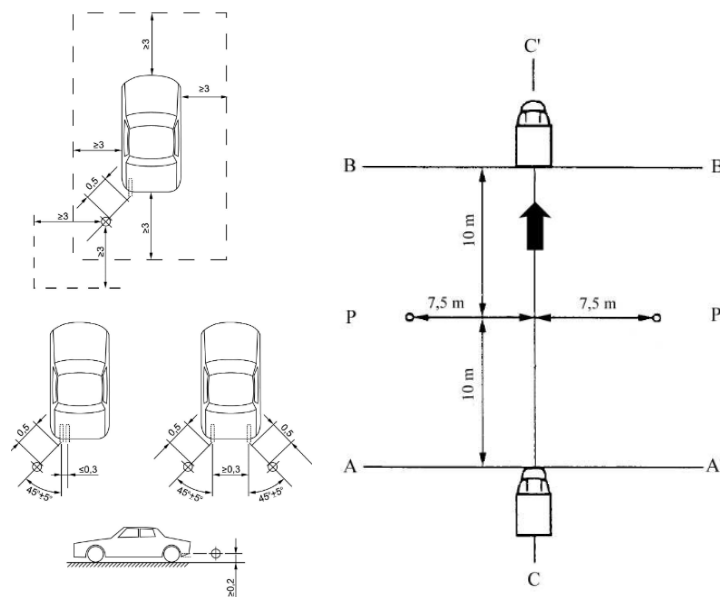


Fig. 122. Measuring points of sound level for stationary and in motion vehicle [137]

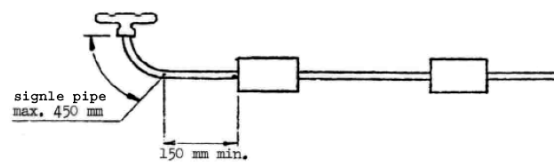


Fig. 123. Example of possible measuring point for backpressure tests [136]

These tests are not the subject of the work, however, they will be briefly presented as tests that have been performed during emission tests. Vehicle noise is measured by two methods, vehicle in motion (50km/h) and stationary (idling with 75% engine speed). At least three measurements are made for each position. The noise level must not exceed by more than 3 dB of the reference value indicated in the approval of the type and the limit applicable to the category of vehicle. Measurement of the backpressure is being performed in the inlet manifold of the exhaust system and the value of backpressure from the replacement part shall not exceed the value of the original part by more than 25% [136], [137]. The noise and backpressure measurements (Tab. 44) were in accordance with the ECE Regulation No. 59.

Tab. 44. Results of the sound and backpressure testing

Driving sound level [dB]			Stationary sound level [dB]		
Original SCR system	Replacement SCR system	Limit of type approval	Original SCR system	Replacement SCR system	Limit of type approval
70,6	70,9	69	69,5	71,7	69
Backpressure [mbar]					
Original SCR system			Replacement SCR system		
130			151 (+ 16.2 %)		

Then, emission tests for the original and replacement SCR systems were performed - for each three NEDC cycles (described in section 6). The replacement SCR system had two prototypes tested (as in Tab. 10 for low and high Vanadium loading).

Tab. 45. Results of emission tests

Part	Test	CO	NO _x	THC+NO _x	PM	PN	CO ₂
		[mg/km]	[mg/km]	[mg/km]	[mg/km]	[/#/km]	[mg/km]
Original	1	180.390	77.620	101.160	0.840	1.89E+10	173.150
	2	184.670	56.700	77.360	0.580	4.00E+08	174.060
	3	185.120	56.080	74.950	0.550	2.30E+09	174.290
S (mean value)		183.393	63.467	84.490	0.657	7.20E+09	173.833
Replacement (low loading)	1	170.980	53.420	75.250	0.380	1.50E+09	172.690
	2	262.210	59.940	96.400	0.250	9.00E+08	177.570
	3	244.760	57.930	91.280	0.280	9.80E+08	176.400
M (mean value)		225.983	57.097	87.643	0.303	1.13E+09	175.553
Replacement (high loading)	1	151.420	50.810	77.250	0.310	2.43E+10	171.630
	2	-	-	-	-	-	-
	3	-	-	-	-	-	-
M (mean value)		151.420	50.810	77.250	0.310	2.43E+10	171.630
Euro limits		500.0	80.0	170.0	4.5	6.00E+11	-
DF (Deterioration factor)		1.5	1.1	1.1	1	1	-
G (Euro limits/DF)		333.3	72.7	154.5	4.5	6.00E+11	-
0.85×S+0.4×G		289.218	83.038	133.635	2.358	2.46E+11	-

The Tab. 45, presents the results of emission tests (diluted emission from the tail pipe). The replacement of SCR system with high loading (RHL) has only been tested in one NEDC cycle duo to the replacement with low loading (RLL) passed the tests (all formulas were compliant according to Eq. (112) and Eq. (113)) and willingness to save the final cost of the tests. To better visualize the required limits and results, tabular values are presented in the Fig. 124.

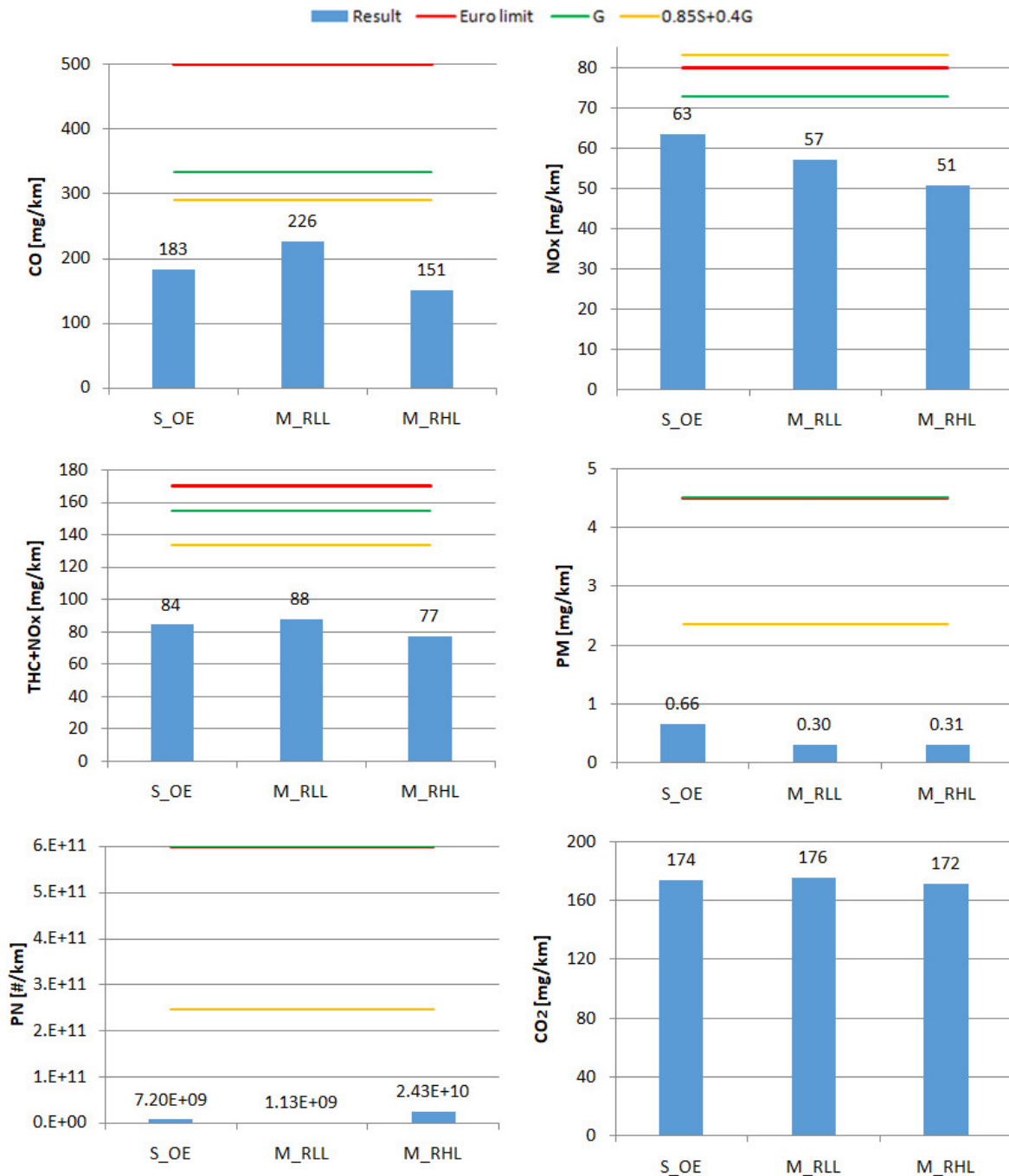
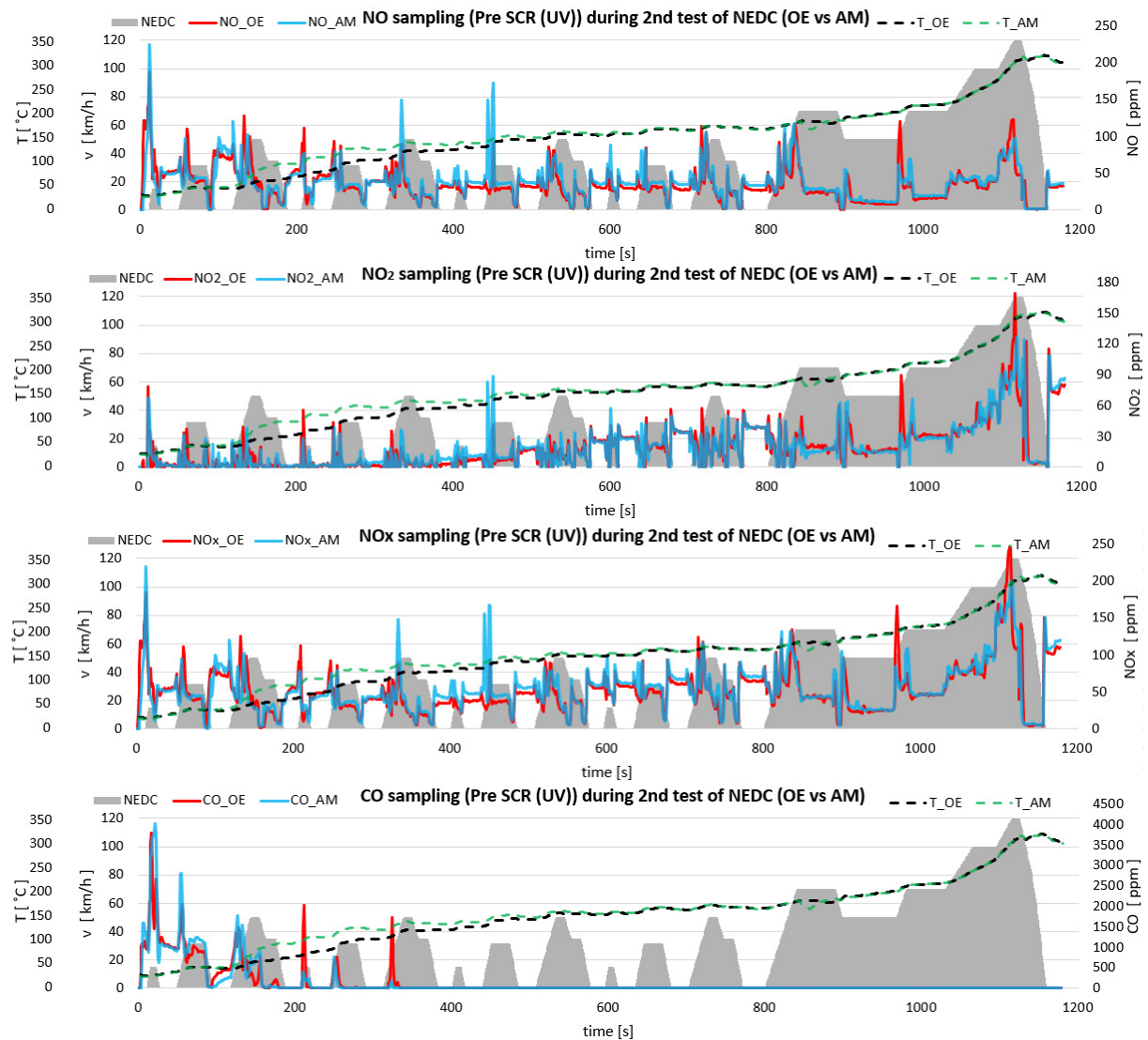


Fig. 124. Emission results with required limits and formulas conditions

It is worth mentioning that the replacement SCR system with low loading had a better conversion NO_x than the original SCR system about 9.5 percentage points (relative increase

in NO_x conversion), furthermore, the replacement with high loading even better 19 percentage points. Almost in all results, the amounts of tested exhaust gas components were lower for the replacement SCR system than the original part and the higher content of the active vanadium layer further improved it. A higher content of the active layer is expensive, therefore, lower content was finally used in the replacement of the SCR system, because it allows for meeting all the requirements in the emission tests. However, such a comparison of the active layers (low and high loading) in prototypes allowed the determination of their impact on the final emission results.

Further presenting the emission results, represents a comparison, by sampling points (in Pre, Mid, Post and Tail pipe points), of exhaust gas components and temperatures for the original SCR system (OE) and the replacement SCR system (AM - the Aftermarket prototype with low loading) during the second NEDC test. All exhaust gas components and temperatures upstream of the SCR system (Pre SCR) are shown in the Fig. 125.



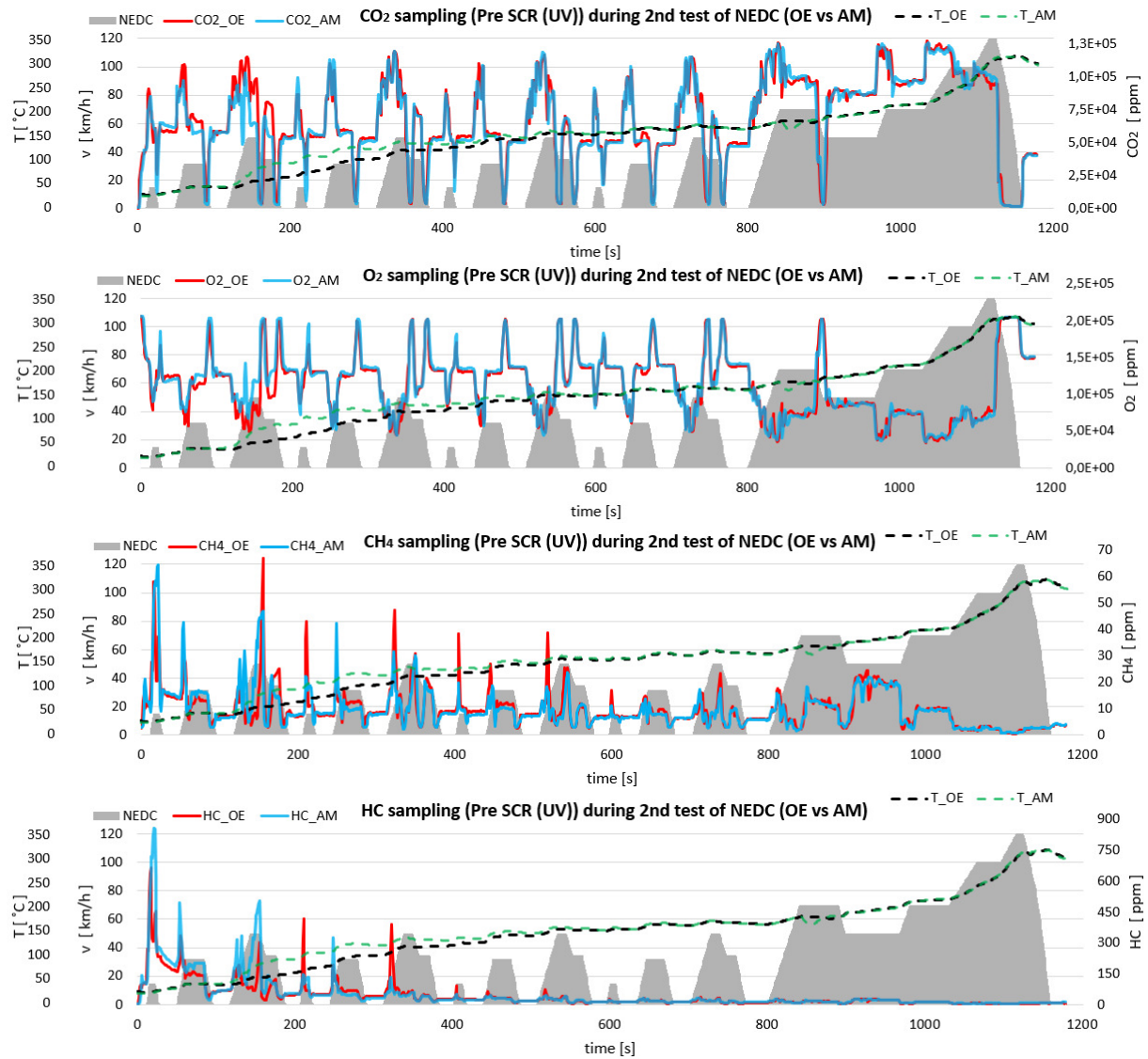


Fig. 125. Exhaust gas components (Pre SCR) for OE and AM parts in the NEDC test

From the start of the NEDC cycle, the temperatures began to rise and the highest value was achieved after the motorway cycle and was around 325°C. With the end of the first cycle, the exhaust gas temperature increased faster for the replacement SCR system, probably due to better thermal insulation of the inlet side. It can be also stated that the aftertreatment system (DOC+DPF) before the SCR system reached the operating temperature (“light-off”) in around 400s due to a noticeable decrease in the values for CO and HC as well as a little for CH₄. The values of CO₂ and O₂ have been presented only for information in order to use them as input values e.g. for CFD simulations. Observing the values for NO and NO₂, may be noticed with the beginning of the test that NO/NO₂ ratio was around 3 (~75% of NO and ~25% of NO₂), however, after reaching the state of light-off by DOC+DPF, the ratio was around 1 as the end of the test was approaching. Values of nitrogen oxides as well as other exhaust gas

components were quite similar during the whole NEDC test for both systems, but larger peaks could be observed in some cases.

Essential exhaust gas components and temperatures between boxes (monoliths) of the SCR system (Mid SCR) are shown in the Fig. 126.

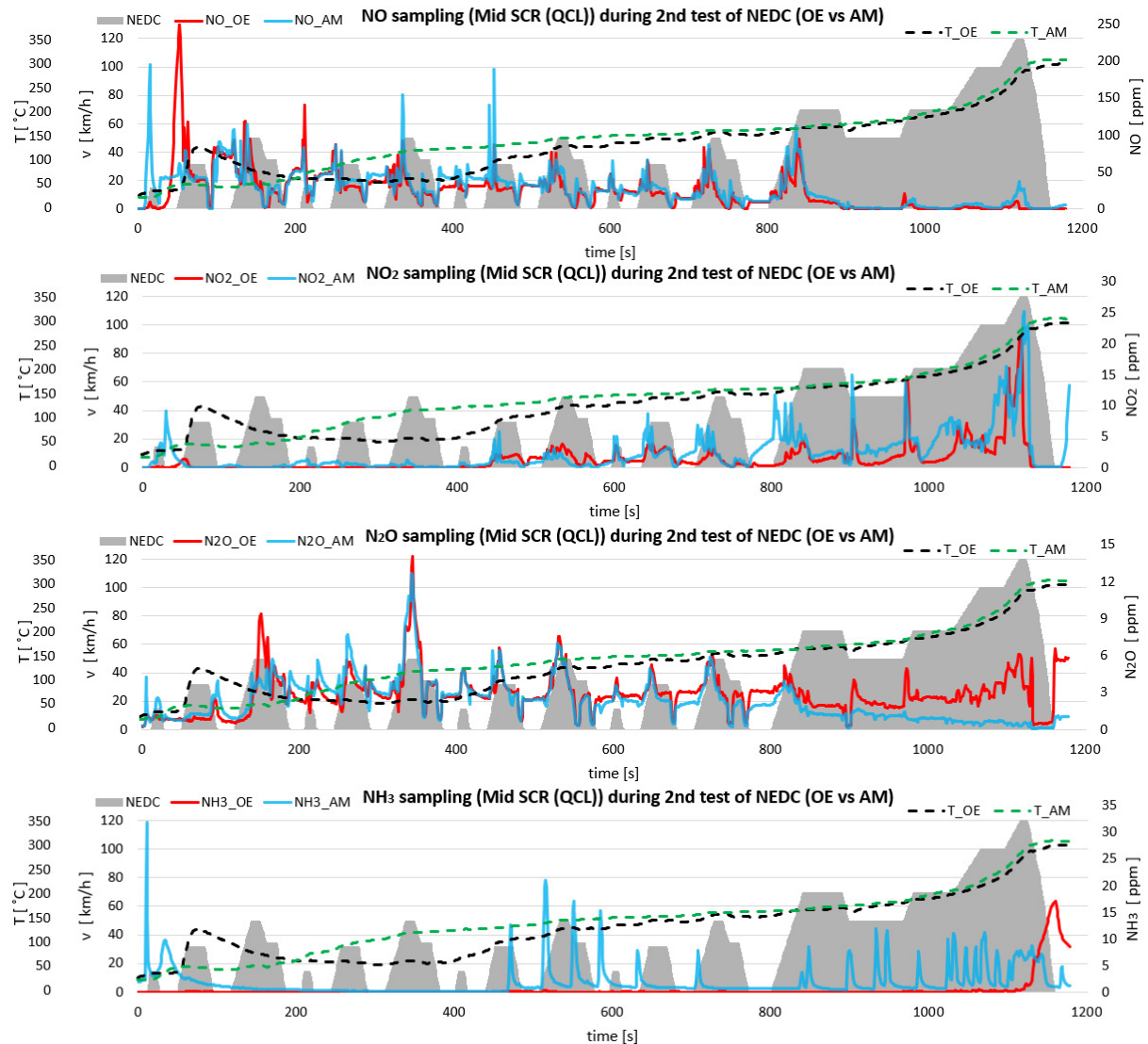


Fig. 126. Exhaust gas components (Mid SCR) for OE and AM parts in the NEDC test

Exhaust gas temperature in the replacement system at the beginning of the test was lower, however, after 200s it was higher than in the original SCR system. The QCL measurement for NO₂ showed a significant reduction of this gas. When it comes to N₂O, it can be said that the replacement SCR system reduced this component better than the original SCR system, although the values were not of a high level. As already confirmed by experimental tests, after crossing the first monolith, ammonia slip for the replacement SCR part is noticeable. The 10 ppm value for NH₃ is acceptable but higher values could be reduced by a second monolith of SCR.

The next sampling results for gas components and temperatures behind the SCR system (Post SCR) are shown in the Fig. 127.

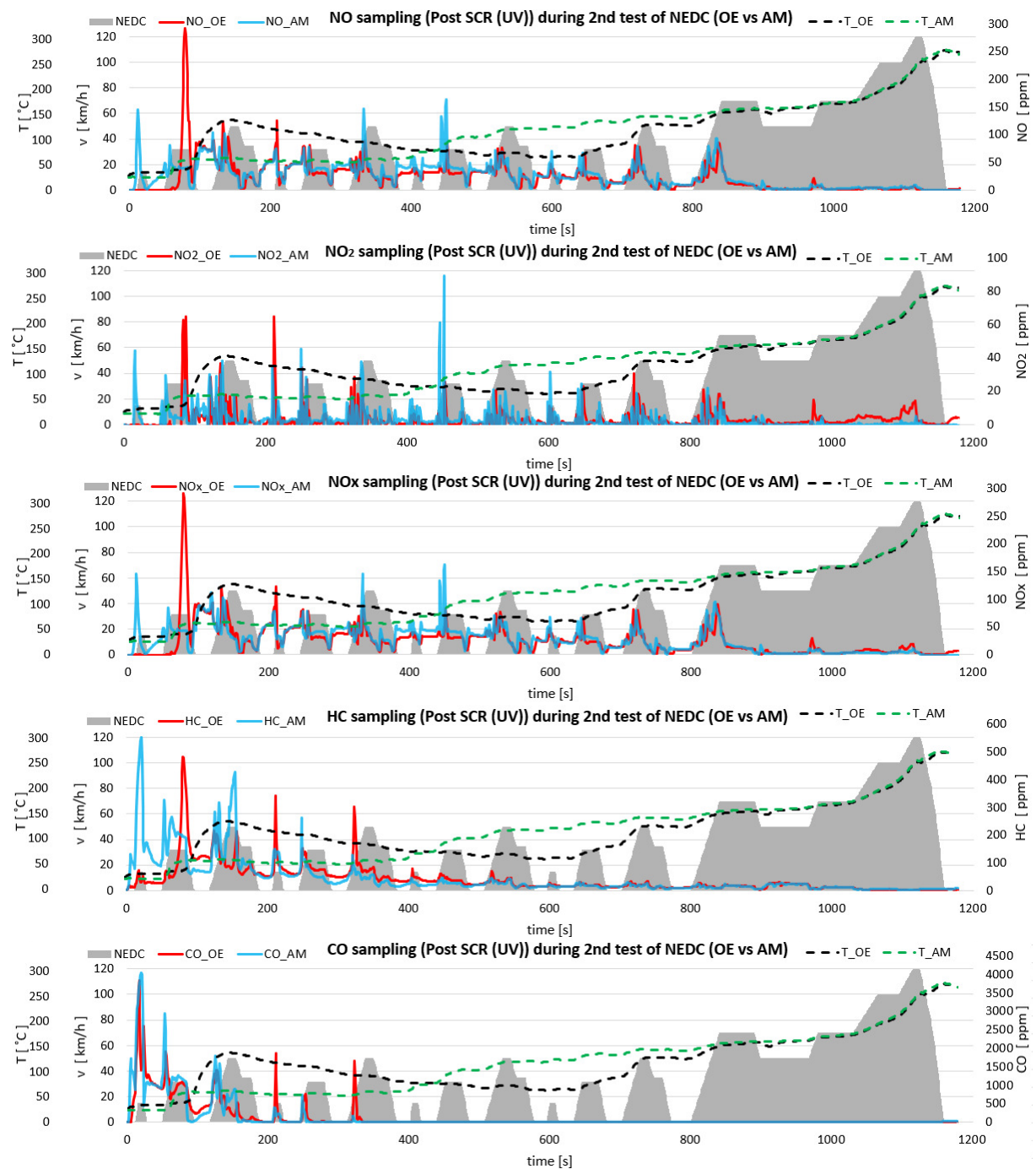


Fig. 127. Exhaust gas components (Post SCR) for OE and AM parts in the NEDC test

Same as before, the exhaust gas temperature in the replacement system at the beginning of the test was lower, probably the original SCR system, which has Cu-zeolites, heats up faster but also releases heat faster or the system has a weaker thermal insulation than in the replacement SCR system. It can be seen that the values of nitric oxide, nitrogen dioxide as well as nitrogen oxides behind SCR systems have been lowered; this is especially evident in the EUDC

(Motorway) cycle due to the higher exhaust gas temperature above 150°C. Carbon monoxide and hydrocarbons, as before, their reduction was significant after reaching “light-off” (prior to this state, the emission on a cold engine was the highest) by aftertreatment system before SCR system i.e. DOC+DPF.

Finally, exhaust gases from the tail pipe were diluted with air, and the emissions of harmful gases and greenhouse gas (CO₂) (tail pipe SCR) are shown in the Fig. 128.

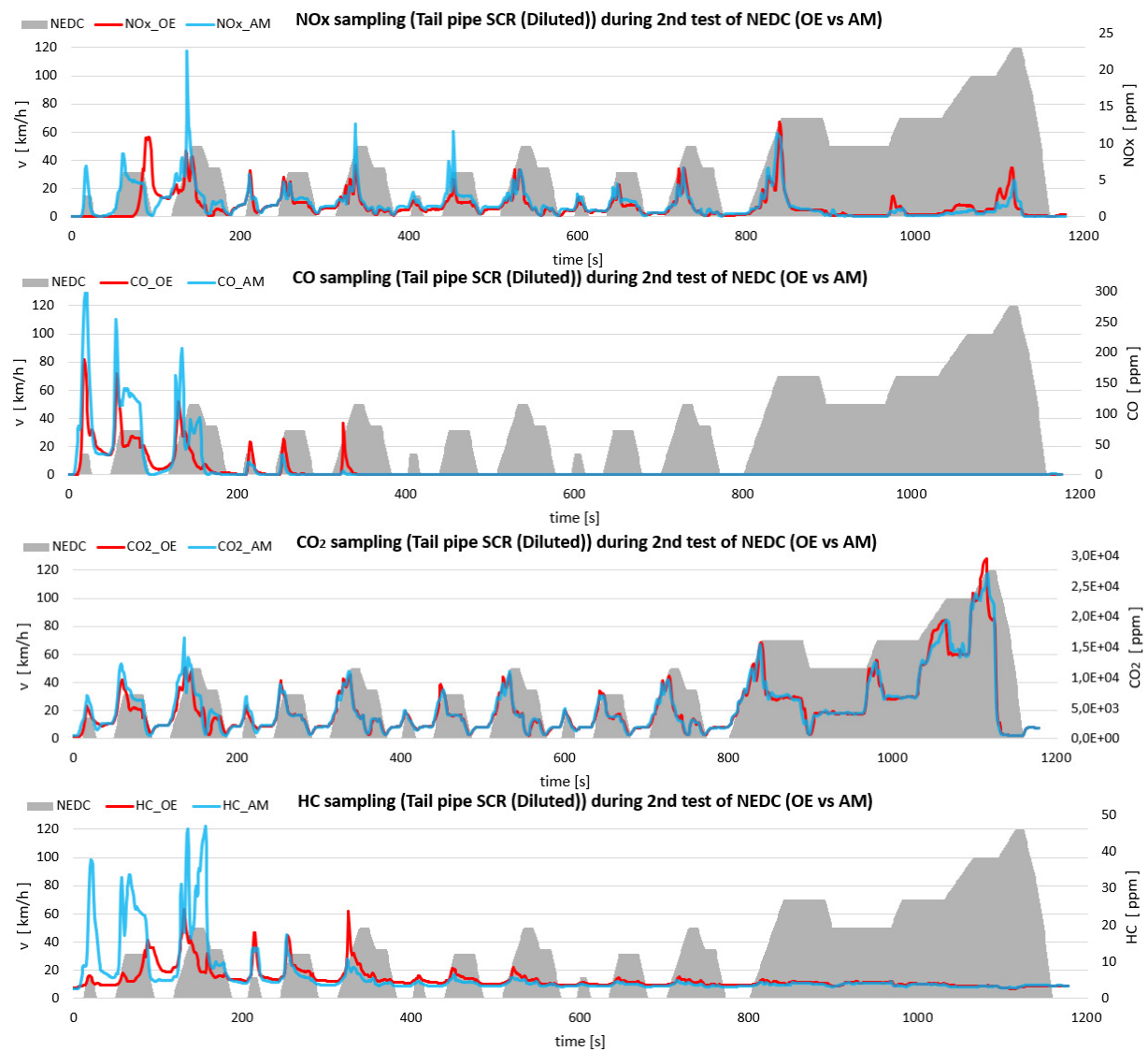


Fig. 128. Exhaust gas components (car tail pipe) for OE and AM parts in the NEDC test

The specified small portion of the resulting mixture was continuously drawn from a tunnel and stored for the duration of the test in tanks - measuring bags. In Tab. 45 for the second NEDC test, all exhaust gas components that appear in Fig. 128 were minimally higher for the replacement SCR system which can be clearly seen in Fig. 128. Nevertheless, all conditions of compliance with the regulation have been met. As already mentioned earlier in chapter 6, the concentration of the individual exhaust components is equal to the average concentration

for the entire duration of the test. The final measurement result was corrected for the measured amount of exhaust gas components, which was received together with the air diluted. Particulate matter was measured by the gravimetric method by measuring the mass of filters on which solid particles were deposited.

Successful passing of all regulatory requirements for a replacement SCR system in the emission laboratory allowed for application for approval. The necessary application documents for homologation have been sent to the National Standards Authority of Ireland (NSAI) at the Transport Department in Dublin. After positive consideration, the replacement SCR system received a certified approval of the ECE type with the number E24*103R00/04*0569*00. The Approval number will be stamped on the SCR system and can now be officially sold to customers under the WALKER brand.

13 Summary and conclusions

In this doctoral dissertation, a wide range of acquired knowledge about exhaust gas aftertreatment systems contributed to an appropriate approach in the field of conducting experimental tests and numerical CFD simulations in this area. Experimental studies for flow tests (pressure drops), flow rig tests (velocity distribution in cold flow and distribution of NH_3 as well as NO_x reduction efficiency in hot flow) were conducted and reverse engineering (obtaining a 3D model from laser scanning) for the various constructions of SCR system and mixers allowed a correct building of a numerical model for CFD simulations. The prepared CFD model was able to correctly predict the performance of the SCR system under various operating conditions. Therefore, the correlation of the experimental and numerical results was at a very good level. Moreover, the designed replacement SCR system with mixer met all requirements in a certified emission laboratory, which allowed for granting the necessary approval for its possible sale on the aftermarket.

In this work, various prototype designs of the mixer and various levels of complexity of the SCR system (with first and second catalyst as well as the complete system) were tested. The designed replacement SCR system was then compared to the original SCR system. The investigated various parameters for the mixers allowed a determination of which mixer is the most optimal in terms of the highest efficiency of the SCR system. The simple design of the mixer, e.g. (prototype B) contributes to a poor degree of urea decomposition and the mixing of gases with ammonia. Despite the low pressure drop, the mixer worked very poorly and was

comparable to the numerical results from the SCR where the mixer was not mounted at all. Additionally, in these SCR catalysts there was a non-uniform conversion of nitric oxide and in some areas there was a very high concentration of ammonia with subsequent ammonia slip. Such an easy solution can contribute to the formation of undesirable deposits in the SCR system. Mixers A and C worked a bit better. They had a relatively low pressure drop and a better level of gas mixing. Unfortunately, at higher flows, the ammonia slip was still at a high level. A slightly higher pressure drop was already noticed in mixers of more advanced design (the original VW mixer and Tenneco 2-Stage mixer). These mixers have already eliminated the ammonia slip phenomenon due to a better level of urea decomposition and mixing of ammonia with gases. Based on the tested mixers, their results and the experience gained, a new prototype of an improved mixer was designed. The improved mixer achieved the best results in the degree of gas mixing. Most importantly, the ammonia slip was at a low, acceptable level under all operating conditions. The only disadvantage, however, was the highest level of pressure drop due to its extensive design. Most likely it will be the subject of further research for this mixer to redesign it to find a balance between pressure drop and good mixing as well as high NO_x conversion and low ammonia slip.

As part of this study, a CFD model for simulation of the SCR systems was developed on the basis of experimental research as well as obtained necessary data from the literature. The model allows the prediction of important flow variables with the relevant species concentrations and phenomena in the SCR system. Particular attention has been focused on the analysis and implementation of the reaction kinetics represented by a global mechanism for vanadium SCR catalyst. Due to lack of accurate kinetic data of the tested SCR catalyst, it was necessary to conduct appropriate research to obtain the desired form of the model and its parameters. The verification of the implemented chemical mechanism and validation of the overall CFD model showed good agreement between the measured and simulated NO conversion. The model was used to study different types and configurations of SCR systems as well as being useful for future tests for other SCR systems and for improving the mixer itself.

Choosing a different, cheaper type of catalyst (vanadium) for a replacement SCR system than in the original part (Cu-Zeolite) did not worsen the NO conversion. The division of the SCR catalyst into two smaller catalysts, that were moved away from each other and connected by a short tube, demonstrated a positive effect on the operation of the system and increased the NO conversion rate. An additional mixing space between them was

accomplished and more uniform ammonia distribution supplied to the rear SCR catalyst was reached. Furthermore, a faster reaching operating temperature (called “light-off”) in the front SCR catalyst was obtained due to its smaller volume and thermal inertia. This was also confirmed by the tests in a certified emission unit. The SCR prototype with the lower vanadium loading already had slightly lower NO_x emissions than the original SCR system. In turn, the prototype of the SCR system with a higher loading of vanadium only proved that it was possible to further reduce NO_x emission, which already met the requirements of the Euro 6b standard. The prototype of the replacement SCR system with the prototype of the mixer C during experimental tests and in a certified emission unit as well as in CFD simulations had a high ammonia slip from the outlet pipe. Although ammonia emission is not controlled during the NEDC type approval tests, it can contribute to the formation of solid deposits, which increase the backpressure and deactivation of the SCR catalyst. Therefore, the mixer was improved in this work, which eliminated the ammonia slip to a level below 10 ppm, which was also confirmed by CFD simulations, however, at the expense of a higher pressure drop on the mixer due to its more complex design. Another possible solution to eliminate the ammonia slip phenomenon is installing an additional ammonia slip catalyst (ASC) as the last element of the system or applying it as a dual-layer (e.g. vanadium together with platinum) for example on the last inch of the SCR catalyst.

The following experimental studies will be considered in order to obtain additional data on the SCR system and its full advanced understanding of the following:

- tests of deposit formation in the SCR system under low temperature conditions;
- visual tests of AdBlue injection for several conditions of its mass flow rate;
- tests to obtain kinetic data of activation energy and pre-exponential factor for all chemical reactions appearing in SCR system and for various types of SCR catalysts (Vanadium catalyst, Cu and Fe zeolites) and their different loading of the active layer;
- checking the level of the active layer loading in the original SCR system by chemical analysis as it was done for one prototype of the vanadium catalyst in this work;
- checking the operation of the SCR system with and additional separate ammonia slip catalyst or the SCR system with and additional layer of ammonia slip catalyst on the last inch of the SCR monolith;
- checking the ageing of the SCR catalyst under extreme operating conditions.

Similarly, for the numerical model, the following studies will be considered in further CFD simulations:

- simulation for transient flow especially for injection and deposit formation through examination of wall-film;
- implementation of the remaining chemical reactions in the SCR system;
- implementation of a more advanced kinetics for surface reactions on the basis of Eley-Rideal and Langmuir-Hinshelwood mechanisms;
- simulations to check the performance of the SCR system after using additional thermal insulation;
- simulations for the complete exhaust aftertreatment system, i.e.: a diesel oxidation catalyst (DOC), with a diesel particulate filter (DPF) and the SCR system;
- coupled simulations, i.e.: CFD simulation in ANSYS Fluent and additional other software such as GT-Suite, where it is possible to connect an engine and check the emission of the exhaust aftertreatment system during a simulated NEDC test.

Bibliography

- [1] Volpato O., Theunissen F., Mazara R.: *Control System for Diesel - Compressed Natural Gas Engines*, SAE International, 2006.
- [2] Ganesan V.: *Internal Combustion Engines*, 2nd ed. Tata McGraw Hill, New Delhi, 2003.
- [3] Merker G. P., Schwarz C., Teichmann R.: *Combustion Engines Development. Mixture Formation, Combustion, Emissions and Simulation*, Springer, 2010.
- [4] Rokosch U.: *Układy oczyszczania spalin i pokładowe systemy diagnostyczne samochodów*, WKŁ, Warszawa, 2007.
- [5] Postrzednik S., Żmudka Z.: *Termodynamiczne oraz ekologiczne uwarunkowania eksploatacji tłokowych silników spalinowych*, WPS, Gliwice 2007.
- [6] Naber J. D., Johnson J. E.: *Internal combustion engine cycles and concepts*, in *Alternative Fuels and Advanced Vehicle Technologies for Improved Environmental Performance*, ed. Falkson R., WP, 2014, pp. 197-224.
- [7] Balogh R. M., Ionel I., Stepan D., Rabl H. P., Pfaffinger A.: *NO_x reduction using selective catalytic reduction system - a variation test*, Termotehnica, 2011, pp. 38-42.
- [8] Degraeuwe B., Pisoni E., Peduzzi E., De Meij A., Monforti-Ferrario F., Bódis K., Mascherpa A., Astorga-Llorens C., Thunis P., Vignati E.: *Urban NO₂ Atlas*, Publications Office of the European Union, Luxembourg, 2019.
- [9] Guarnieri M., Balmes J. R.: *Outdoor air pollution and asthma*, Lancet, 2014, pp. 1581-1592.
- [10] Li J., He H., Hu C., Zhao J.: *The abatement of major pollutants in air and water by environmental catalysis*, FESE, 2013, pp. 302-325.
- [11] European Environment Agency: *Air quality in Europe*, EEA Report No 10/2019.
- [12] Crippa M., Oreggioni G., Guizzardi D., Muntean M., Schaaf E., Lo Vullo E., Solazzo E., Monforti-Ferrario F., Olivier J. and Vignati E.: *Fossil CO₂ and GHG emissions of all world countries*, Joint Research Centre (JRC), Luxembourg, 2019.
- [13] Khajepour A., Fallah M. S., Goodarzi, A.: *Electric and Hybrid Vehicles: Technologies, Modeling and Control - A Mechatronic Approach*, Wiley, 2014.
- [14] Bera P., Hegde M. S.: *Recent advances in auto exhaust catalysis*, Journal of the Indian Institute of Science, 2010, pp. 299-325.
- [15] Valera-Medina A., Xiao H., Owen-Jones M., David W. I. F., Bowen P. J.: *Ammonia for power*, Progress in Energy and Combustion Science, Elsevier Ltd, 2018, pp. 63-102.

- [16] Leman A. M., Feriyanto D., Farhana N., Rahmat R., Bakar B. A., Baba I.: *Oxidation Resistance Analysis Of Metallic (FeCrAl Foil) Catalytic Converter Developed By Ultrasonic Approach*, MATEC Web of Conferences, 2016, pp. 1-10.
- [17] Mohiuddin A. K., Nurhafez M.: *Experimental analysis and comparison of performance characteristics of catalytic converters including simulation*, International Journal of Mechanical and Materials Engineering, 2007, pp. 1-7.
- [18] Jimenez de Aberasturi D., Pinedo R., Ruiz de Larramendi I., Ruiz de Larramendi J. I., Rojo T.: *Recovery by hydrometallurgical extraction of the platinum-group metals from car catalytic converters*, Minerals Engineering, 2011, pp. 505-513.
- [19] Lindhjem C., Khair M.: *Air quality technology development needs: diesel NO_x emission reduction technologies*, Environ International Corporation, 2003.
- [20] Reşitoğlu İ. A., Altinişik K., Keskin, A.: *The pollutant emissions from diesel-engine vehicles and exhaust aftertreatment systems*. Clean Techn Environ Policy, 2015, 15–27.
- [21] Pardiwala J. M., Patel F., Patel S.: *Review paper on Catalytic Converter for Automotive Exhaust Emission*, International conference on current trends in technology, 2011, 1-6.
- [22] Parthasarathi B., Hegde M. S.: *Recent advances in auto exhaust catalysis*, Journal of the Indian Institute of Science, 2010, pp. 299-325.
- [23] Pereda-Ayo B., González-Velasco J. R.: *NO_x Storage and Reduction for Diesel Engine Exhaust Aftertreatment in Diesel Engine - Combustion, Emissions and Condition Monitoring*, Bari S., IntechOpen, 2013, pp. 161-196.
- [24] Glielmo L., Milano M., Santini S.: *A machine learning approach to modeling and identification of automotive three-way catalytic converters*, IEEE/ASME Transactions on Mechatronics, 2000, pp. 132-141.
- [25] Kannepalli S., Gremminger A., Tischer S., Deutschmann O.: *Optimization of axial catalyst loading in transient-operated zone-structured monoliths: Reduction of cumulative emissions in automotive oxidation catalysts*, Chem. Eng. Sci., 2017, 189–202
- [26] Williams J. L.: *Monolith structures, materials, properties and uses*, Catalysis Today, 2001, pp. 3-6.
- [27] Holder R., Bollig M., Anderson D. R., Hochmuth J. K.: *A discussion on transport phenomena and three-way kinetics of monolithic converters*, Chem. Eng. Sci., 2006, pp. 8010–8027.
- [28] Adler J.: *Ceramic diesel particulate filters*, International Journal of Applied Ceramic Technology, 2005, pp. 429–439.

- [29] Hanamura K., Karin P., Cui L., Rubio P., Tsuruta T., Tanaka T., Suzuki T.: *Micro- and macroscopic visualization of particulate matter trapping and regeneration in wall-flow diesel particulate filters*, Int. J. Engine Res., 2009, pp. 305-321.
- [30] Bari S., Marian R.: *Evolution of risk of diesel engine emissions on health during last 4 decades and comparison with other engine cycles - An innovative survey*, ASME International Mechanical Engineering Congress & Exposition (IMECE), 2015, pp. 1-10.
- [31] Kittelson D., Kraft M.: *Particle formation and models in internal combustion engines*, Cambridge Centre for Computational Chemical Engineering, 2014.
- [32] Boger T.: *Integration of SCR functionality into diesel particulate filters*, in Urea-SCR technology for deNO_x after treatment of diesel exhausts, ed. Nova I., Tronconi E., Springer, 2014, pp. 623-655.
- [33] Spiess S., Wong K. F., Richter J. M., Klingmann R.: *Investigations of Emission Control Systems for Gasoline Direct Injection Engines with a Focus on Removal of Particulate Emissions*, Top Catal, 2013, pp. 434–439.
- [34] Jang J., Lee J., Choi Y., Park S.: *Reduction of particle emissions from gasoline vehicles with direct fuel injection systems using a gasoline particulate filter*, Science of the Total Environment, 2018, pp. 1418–1428.
- [35] Lambert C., Chanko T., Dobson D., Liu X., Pakko J.: *Gasoline Particle Filter Development*, Emiss. Control Sci. Technol, 2017, pp. 105–111.
- [36] Guan B., Zhan R., Lin H., Huang Z.: *Review of the state-of-the-art of exhaust particulate filter technology in internal combustion engines*, Journal of Environmental Management, 2015, pp. 225-258.
- [37] Joshi A., Johnson T. V.: *Gasoline Particulate Filters - a Review*, Emission Control Science and Technology, 2018, pp. 1-21.
- [38] Wang J., Yan F., Fang N., Yan D., Zhang G., Wang Y., Yang W.: *An Experimental Investigation of the Impact of Washcoat Composition on Gasoline Particulate Filter (GPF) Performance*, Energies, 2020, pp. 1-9.
- [39] Van Essen V. M.: *Fundamental limits of NO formation in fuel-rich premixed methane-air flames*, University of Groningen, 2007.
- [40] Kumaran P., Mohanamurugan S., Shankar P, Narayanan R.: *Investigation of urea decomposition and uniform concentration of urea water solution in SCR system for diesel engine exhaust using CFD*, Rasayan J. Chem., 2017, pp. 621-629.
- [41] Kaczmarczyk K.: *Koncepcja system redukcji tlenków azotu z ognioszczelnego napędu*

- spalinowego*, *Maszyny Górnicze*, 2015, pp. 23-28.
- [42] Yang L., Franco V., Campestrini A., German J., Mock P.: *NOx control technologies for Euro 6 diesel passenger cars*, The International Council on Clean Transportation, 2015.
- [43] Kamela W., Kruczyński S.W.: *Badania symulacyjne procesu magazynowania NOx w reaktorze LNT*, *Zeszyty Naukowe Instytutu Pojazdów, PW*, 2013, pp. 21-29.
- [44] Johnson T.: *Vehicular Emissions in Review*, *SAE Int. J. Engines*, 2013, pp. 699-715.
- [45] Kröcher O.: *Chapter 9 Aspects of catalyst development for mobile urea - SCR systems - From Vanadia-Titania catalysts to metal-exchanged zeolites*, *Studies in Surface Science and Catalysis*, 2007, pp. 261-289.
- [46] Johnson T. V.: *Review of Selective Catalytic Reduction (SCR) and Related Technologies for Mobile Applications*, in *Urea-SCR technology for deNOx after treatment of diesel exhausts*, ed. Nova I., Tronconi E., Springer, 2014, pp. 3-31.
- [47] Latha H. S., K. V. Prakash, M. Veerangouda, Devanand Maski, Ramappa K. T.: *A Review on SCR System for NOx Reduction in Diesel Engine*, *Int. J. Curr. Microbiol. App. Sci.*, 2019, pp. 1553-1559.
- [48] Yuan X., Liu H., Gao Y.: *Diesel Engine SCR Control: Current Development and Future Challenges*, *Emiss. Control Sci. Technol.*, 2015, pp. 121–133.
- [49] Brandenberger S., Kröcher O., Tissler A., Althoff R.: *The State of the Art in Selective Catalytic Reduction of NOx by Ammonia Using Metal-Exchanged Zeolite Catalysts*, *Catalysis Reviews*, 2008, pp. 492-531.
- [50] Jansson J.: *Vanadia-Based Catalysts for Mobile SCR*, in *Urea-SCR technology for deNOx after treatment of diesel exhausts*, ed. Nova I., Tronconi E., Springer, 2014, pp. 65-96.
- [51] Scheuer A., Drochner A., Gieshoff J., Vogel H., Votsmeier M.: *Runtime efficient simulation of monolith catalysts with a dual-layer washcoat*, *Catalysis Today*, 2012, pp. 70-79.
- [52] Dhillon P. S., Harold M. P., Wang D., Joshi S., Kumar A.: *Enhanced transport in ammonia slip catalyst (ASC) washcoat by using sacrificial agents*, *ISCRE25: Bridging Science and Technology*, 2018, pp. 1-2.
- [53] Rogóż R., Kapusta Ł. J., Bachenek J., Vankan J., Teodorczyk A.: *Improved urea-water solution spray model for simulations of selective catalytic reduction systems*, *Renewable and Sustainable Energy Reviews*, 2020, pp. 1-10.
- [54] Watling T. C., Ravenscroft M. R., Avery G.: *Development, validation and application of*

- a model for an SCR catalyst coated diesel particulate filter*, Catalyst Today, 2012, pp. 32-41.
- [55] Neusser H. J., Kahrstedt J., Dorenkamp R., Jelden H.: *The euro 6 engines in the modular diesel engine system of Volkswagen*, MTZ, 2013, pp. 4-10.
- [56] Braun T., Lückert P., Duvinage F., Mackense A.: *Mercedes-Benz diesel technology OM654 near-engine-mounted SCR system for WLTP and RDE*, 16. Internationales Stuttgarter Symposium, 2016, pp. 239-255.
- [57] Döring A., Rothe D.: *Downsizing of the EuroVI exhaust aftertreatment components to fit into the EuroIII silencer*, 33. International Vienna Motor Symposium, 2012, pp. 1-17.
- [58] Karamitros D., Koltsakis G.: *SCR Reactor Models for Flow-Through and Wall-Flow Converters*, in Urea-SCR technology for deNOx after treatment of diesel exhausts, ed. Nova I., Tronconi E., Springer, 2014, pp. 385-424.
- [59] DieselNet, 17 Nov. 2020: <https://dieselnet.com/search>.
- [60] Tenneco EMEA, Technical Advanced Digital Information System (TADIS), 17 June 2022: <https://ta.garagegurus-eu.info/tadis/tadis-html-en/>.
- [61] Ricardo: *Expectations for Actual Euro 6 Vehicle Emissions*, 22 Nov. 2020: https://www.concawe.eu/wp-content/uploads/2018/04/RD18-000697-2-CONCAWE_Expectations_for_Actual_Euro_6_Vehicle_Emissions.pdf
- [62] Continental: *Worldwide Emission Standards and Related Regulations*, 22 Nov. 2020: https://www.continental-automotive.com/getattachment/8f2dedad-b510-4672-a005-3156f77d1f85/EMISSIONBOOKLET_2019.pdf
- [63] Giakoumis E. G.: *Driving and Engine Cycles*, Springer, 2017.
- [64] Hooftman N., Messagie M., Van Mierlo J., Coosemans T.: *A review of the European passenger car regulations – Real driving emissions vs local air quality*, Renewable and Sustainable Energy Reviews, 2018, pp. 1-21.
- [65] Suarez-Bertoa R., Mendoza-Villafuerte P., Riccobono F., Vojtisek M., Pechout M., Perujo A., Astorga C.: *On-road measurement of NH3 emissions from gasoline and diesel passenger cars during real world driving conditions*, Atmospheric Environment, 2017, pp. 488-497.
- [66] Fernández-Yáñez P., Armas O., Martínez-Martínez S.: *Impact of relative position vehicle-wind blower in a roller test bench under climatic chamber*, Applied Thermal Engineering, 2016, pp. 266-274.
- [67] Merkisz J., Pielecha J.: *Selected remarks about RDE test*, Combustion Engines, 2016,

pp. 54-61.

- [68] Czerwinski J., Zimmerli Y., Hüsey A.: *Testing and evaluating real driving emissions with PEMS*, Combustion Engines, 2018, pp. 17-25.
- [69] Merkisz J., Pielecha J.: *Comparison of Real Driving Emissions tests*, IOP Conf. Ser.: Mater. Sci. Eng., 2018, pp. 1-10.
- [70] Engeljehring K.: *Passenger car emission regulations*, 25 Nov. 2020: <https://www.avl.com/documents/10138/1027860/AVL-Italy+TechDay+-+Light-Duty+Emission+-+2014-10-21b.pdf/da9591d9-3e75-42c2-9157-d7cc9a680b1f>
- [71] Gierczycki A. T., Kubica R.: *Basic course on technical and fluid mechanics*, Wydawnictwo Politechniki Śląskiej, Gliwice, 2012.
- [72] Versteeg H. K., Malalasekera W.: *An Introduction to Computational Fluid Dynamics, The Finite Volume Method*, Person, 2nd edition, 2007.
- [73] ANSYS, Inc.: *ANSYS Fluent Theory Guide*, Release 17.0, 2016.
- [74] ANSYS, Inc.: *ANSYS Fluent User's Guide*, Release 15.0, 2013.
- [75] ANSYS, Inc.: *ANSYS Fluent UDF Manual*, Release 15.0, 2013.
- [76] Nowak R.: *Estimation of viscous and inertial resistance coefficients for various heat sink configurations*, Procedia Engineering, 2016, pp. 122-130.
- [77] Kurzydym D., Klimanek A., Żmudka Z.: *Experimental and numerical analysis of flow through catalytic converters for original part and WALKER's replacement using reverse engineering and CFD*, IOP Conf. Ser.: Mater. Sci. Eng., 2018, pp. 1-10.
- [78] Kurzydym D., Klimanek A., Żmudka Z.: *Experimental research and CFD analysis of flow parameters in a SCR system for the original part and WALKER's replacement*, Combustion Engines, 2019, pp. 12-19.
- [79] Kurzydym D., Klimanek A., Żmudka Z.: *Experimental research and CFD analysis of selective catalytic reduction of nitric oxides in the original SCR system and WALKER's replacement*, CPOTE 2020, pp. 891-898
- [80] Mehdi G., Zhou S., Zhu Y., Shah A. H., Chand K.: *Numerical Investigation of SCR Mixer Design Optimization for Improved Performance*, Processes, 2019, pp. 1-22.
- [81] Ibrahim H. A., Abdou S., Ahmed W. H.: *Understanding Flow through Catalytic Converters*, 4th Int. Conf. of Fluid Flow, Heat and Mass Transfer, 2017, pp. 1-7.
- [82] Ma Q., Zhang D., Gan X.: *Simulation of the flow field and the chemical reaction coupling of selective catalytic reduction (SCR) system using an orthogonal experiment*, PLoS ONE, 2019, pp. 1-18.

- [83] Hayes R. E., Fadic A., Mmbaga J., Najafi A.: *CFD modelling of the automotive catalytic converter*, Catalysis Today, 2012, pp. 94-105.
- [84] Stec M., Synowiec P. M.: *Study of Fluid Dynamic Conditions in the Selected Static Mixers Part III - Research of Mixture Homogeneity*, The Canadian Journal of Chemical Engineering, 2018, pp. 1-13.
- [85] Prabhu S. S., Nayak N. S., Kapilan N., Hindasageri V.: *An experimental and numerical study on effects of exhaust gas temperature and flow rate on deposit formation in Urea-Selective Catalytic Reduction (SCR) system of modern automobiles*, Applied Thermal Engineering, 2017, pp. 1211-1231.
- [86] Shahariar G. M. H., Lim O. T.: *Investigation of urea aqueous solution injection, droplet breakup and urea decomposition of selective catalytic reduction systems*, Journal of Mechanical Science and Technology, 2018, pp. 3473-3481.
- [87] Mutyal J., Shrivastava S., Faltsi R., Braun M.: *Development and Validation of a Simulation Model for Urea-Water-Solution Decomposition for Automotive SCR Systems*, SAE Technical Paper, 2015, pp. 1-9.
- [88] Gao X., Zhu Y.P., Luo Z. H.: *CFD modeling of gas flow in porous medium and catalytic coupling reaction from carbon monoxide to diethyl oxalate in fixed-bed reactors*, Chemical Engineering Science, 2011, pp. 6028-6038.
- [89] Zheng G., Wang F., Zhang S., Zhang J., Tao J., Zhiguo Z., Fan J.: *Development of Compact SCR Systems with Closely Coupled Injector Configurations*, SAE Technical Paper, 2014, pp. 1-13.
- [90] Anetor L., Osakue E., Odetunde C.: *Reduced Mechanism Approach of Modeling Premixed Propane-Air Mixture Using ANSYS Fluent*, Eng. Journal, 2012, pp. 67-86.
- [91] Jafari Nasr M. R., Balaei A.: *Analysis of Fouling in HVAC Heat Exchangers by CFD*, Iran. J. Chem. Chem. Eng., 2015, pp. 51-60.
- [92] Baleta J., Martinjak M., Vujanović M., Pachler K., Wang J., Duić N.: *Numerical analysis of ammonia homogenization for selective catalytic reduction application*, Journal of Environmental Management, 2017, pp. 1047-1061.
- [93] Hajimirzaee S., Doyle A., M.: *3D printed catalytic converters with enhanced activity for low-temperature methane oxidation in dual-fuel engines*, Fuel, 2020, pp. 1-11.
- [94] Jha N., K., Sapali S. N.: *CFD Analysis of Perforated Water Filter*, International Journal of Engineering and Management Research, 2015, pp. 35-39.
- [95] Baharudin L., Watson M., J.: *Monolithic substrate support catalyst design*

- considerations for steam methane reforming operation, *Reviews in Chemical Engineering*, 2017, pp. 1-21.
- [96] Govender S., Friedrich H., B.: *Monoliths: A Review of the Basics, Preparation Methods and Their Relevance to Oxidation*, *Catalysts*, 2017, pp. 1-29.
- [97] Heck R., M., Gulati S., Farrauto R., J.: *The application of monoliths for gas phase catalytic reactions*, *Chemical Engineering Journal*, 2001, pp. 149-156.
- [98] Akhtar F., Andersson L., Ogunwumi S., Hedin N., Bergström L.: *Structuring adsorbents and catalysts by processing of porous powders*, *ScienceDirect*, 2014, pp. 1643-1666.
- [99] Sala R., Krasowski J., Dzida J., Woodburn J.: *Experiment of selective catalytic reduction retrofit for euro 6 NO_x emission level compliance for euro 5 light duty vehicle*, *IOP Conf. Series: Materials Science and Engineering*, 2018, pp. 1-7.
- [100] Zheng G., Palmer G., Salanta G., Kotrba A.: *Mixer development for urea SCR applications*, *SAE*, 2009, pp. 1-10.
- [101] Murkute A. D., Vanderwiell D.: *Active Sites Evaluation of Vanadia Based Powdered and Extruded SCR Catalysts Prepared on Commercial Titania*, *Catalysis Letters*, 2015, pp. 1224-1236.
- [102] Tan L., Feng P., Yang S., Guo Y., Liu S., Li Z.: *CFD studies on effects of SCR mixers on the performance of urea conversion and mixing of the reducing agent*, *Chem. Eng. & Process: Process Intensification*, 2018, pp. 82-88.
- [103] Tian X., Xiao Y., Zhou P., Zhang W., Chu Z., Zheng W.: *Study on the mixing performance of static mixers in selective catalytic reduction (SCR) systems*, *Journal of Marine Engineering & Technology*, 2015, pp. 1-5.
- [104] Liu X., Wu X., Xu T., Weng D., Si Z., Ran R.: *Effects of silica additive on the NH₃-SCR activity and thermal stability of a V₂O₅/WO₃-TiO₂ catalyst*, *Chinese Journal of Catalysis*, 2016, pp. 1340-1346.
- [105] Kobayashi M., Kuma R., Masaki S., Sugishima N.: *TiO₂-SiO₂ and V₂O₅/TiO₂-SiO₂ catalyst: Physico-chemical characteristics and catalytic behavior in selective catalytic reduction of NO by NH₃*, *Applied Catalysis B: Environmental*, 2005, pp.173-179.
- [106] Qi G., Wang L., Yang R. T.: *Low-Temperature Selective Catalytic Reduction (SCR) of NO_x with NH₃ Over Zeolites and Metal Oxide-Based Catalysts and Recent Developments of H₂-SCR*, in *Urea-SCR technology for deNO_x after treatment of diesel exhausts*, ed. Nova I., Tronconi E., Springer, 2014, pp. 149-177.
- [107] Eijima W., Shibata G., Kobashi Y., Koiwai R., Ogawa H., Shimizu K., Kusaka J.:

- Kinetic Modeling of Ammonia-SCR and Experimental Studies over Monolithic Cu-ZSM-5 Catalyst*, SAE, 2019, pp. 1-9.
- [108] Han L., Cai S., Gao M., Hasegawa J., Wang P., Zhang J., Shi L., Zhang D.: *Selective Catalytic Reduction of NO_x with NH₃ by Using Novel Catalysts: State of the Art and Future Prospects*, Chemical Reviews, 2019, pp. 1-61.
- [109] Devadas M., Kröcher O., Wokaun A.: *Catalytic investigation of Fe-ZSM5 in the Selective Catalytic Reduction of NO_x with NH₃*, Reaction Kinetics and Catalysis Letters, 2005, pp. 347-354.
- [110] Grossale A., Nova I., Tronconi E.: *Study of a Fe-zeolite-based system as NH₃-SCR catalyst for diesel exhaust aftertreatment*, Catalysis Today, 2008, pp. 18-27.
- [111] Xi Y., Ottinger N. A., Liu Z. G.: *Effect of hydrothermal aging on the catalytic performance and morphology of a vanadia SCR catalyst*, SAE, 2013, pp. 1-10.
- [112] Marberger A., Elsener M., Ferri D., Kröcher O.: *VO_x surface coverage optimization of V₂O₅/WO₃-TiO₂ SCR catalysts by variation of the v loading and by aging*, Catalysts, 2015, pp. 1704-1720.
- [113] Zhang L., Wang D., Liu Y., Kamasamudram K., Li J., Epling W.: *SO₂ poisoning impact on the NH₃-SCR reaction over a commercial Cu-SAPO-34 SCR catalyst*, Applied Catalysis B: Environmental, 2014, pp. 371-377.
- [114] Ma Z., Wu X., Feng Y., Si Z., Weng D., Shi L.: *Low-temperature SCR activity and SO₂ deactivation mechanism of Ce-modified V₂O₅-WO₃/TiO₂ catalyst*, Progress in Natural Science: Materials International, 2015, pp. 342-352.
- [115] Brzeżański M., Sala R.: *In-service problems of selective catalytic reduction systems for reduction of nitrogen oxides*, Combustion Engines, 2013, pp. 969-976.
- [116] Sugimoto K.: *Prediction for SCR systems performance using 3D CFD simulation: aiming at SCR development for various layouts*, YANMAR Technical Review, 2017.
- [117] Shahariar G. M. H., Lim O. T.: *A study on urea-water solution spray-wall impingement process and solid deposit formation in urea-SCR de-NO_x system*, Energies, 2018, pp. 1-18.
- [118] Lauer T.: *Preparation of ammonia from liquid AdBlue – modeling approaches and future challenges*, Chem. Ing. Tech., 2018, pp. 783-794.
- [119] Zheng G., Fila A., Kotrba A., Floyd R.: *Investigation of urea deposits in urea SCR systems for medium and heavy duty trucks*, SAE, 2010, pp. 1-10.
- [120] Smith H., Lauer T., Mayer M., Pierson S.: *Optical and numerical investigations on the*

- mechanisms of deposit formation in SCR systems*, SAE, 2014, pp. 525-542.
- [121] Praveena V., Jesu M. L.: *Design optimization of urea injectors and mixers in a compact SCR system*, SAE, 2018, pp. 1-7.
- [122] Abidin Z., Das K., Roberts C.: *3D-semi 1D coupling for a complete simulation of an SCR system*, SAE, 2013, pp. 1-9.
- [123] Choe M., Choi D.: *Study of the optimization of the SCR catalyst position in by exhaust system of using mixer*, Indian Journal of Science and Technology, 2016, pp. 1-5.
- [124] Rajadurai S., Sukumaran S.: *NO_x aftertreatment using urea SCR for Tier 4 final application*, International Journal of Innovative Science, Engineering & Technology, 2017, pp. 306-312.
- [125] Habchi C., Nicolle A., Gillet N.: *Numerical study of deposits formation in SCR systems using urea-water solution injection*, Journal of Materials Science & Nanotechnology, 2018, pp. 1-9.
- [126] Brzeżański M.: *Diesel engines with respect to Euro 6 and Bin5/Lev II emission limits*, Journal of KONES Powertrain and Transport, 2011, pp. 33-40.
- [127] Floyd R., Michael L., Shaikh Z.: *DEF systems and aftertreatment architecture considerations*, in Urea-SCR technology for deNO_x after treatment of diesel exhausts, ed. Nova I., Tronconi E., Springer, 2014, pp. 455-484.
- [128] Kittelson D. B.: *Engines and nanoparticles: a review*, Journal of Aerosol Science, 1998, pp. 575-588.
- [129] Fischer S.: *Simulation of the urea-water-solution preparation and ammonia-homogenization with a validated CFD-model for the optimization of automotive SCR-systems* (PhD thesis, Institut für Fahrzeugantriebe und Automobiltechnik, Wien), 2012. Retrieved from <https://repositum.tuwien.at/handle/20.500.12708/10933>.
- [130] Motor1, 19 June 2021: <https://de.motor1.com/reviews/164926/vw-passat-variant-bluetdi-im-test-euro-6-per-scr-schon-heute/>
- [131] Mudroch E., Azcue J., M., Mudroch P.: *Manual of physic-chemical analysis of aquatic sediments*, CRC Press, 1996.
- [132] Sneddon J., Vincent M., D.: *ICP-OES and ICP-MS for the determination of metals: application to oysters*, Analytical Letters, 2008, pp. 1291-1303.
- [133] Nölte J.: *ICP Emission Spectrometry: A Practical Guide*, 2nd ed., WILEY-VCH, 2021.
- [134] Gis W., Grzelak P., Taubert S., Żółkowski A.: *Evolution of the effectiveness of*

- replacement catalytic converters*, PTNSS, 2013, pp. 569-574.
- [135] Schmidt H., Johannsen R.: *Examination of pollutants emitted by vehicles in operation and of emission relevant components - Replacement catalytic converters*, BAST - Bundesanstalt für Straßenwesen (Federal Highway Research Institute), 2014, pp. 1-24.
- [136] Euro-Lex: *Regulation No 59 of the Economic Commission for Europe of the United Nations (UN/ECE) — Uniform provisions concerning the approval of replacement silencing systems*, Official Journal of the European Union, 2006.
- [137] Euro-Lex: *Regulation (EU) No 540/2014 of the European Parliament and of the Council of 16 April 2014 on the sound level of motor vehicles and of replacement silencing systems, and amending Directive 2007/46/EC and repealing Directive 70/157/EEC*, Official Journal of the European Union, 2014.
- [138] Kurzydym D., Żmudka Z., Perrone D., Klimanek A.: *Experimental and numerical investigation of nitrogen oxides reduction in diesel engine selective catalytic reduction system*, Fuel, 2021.
- [139] Marangozis J.: *Comparison and analysis of intrinsic kinetics and effectiveness factors for the catalytic reduction of NO with ammonia in the presence of oxygen*, Ind. Eng. Chem. Res., 1992, pp. 987-994.
- [140] Iwasaki M.: *Mechanistic aspect of NO-NH₃-O₂ reacting system*, in Urea-SCR technology for deNO_x after treatment of diesel exhausts, ed. Nova I., Tronconi E., Springer, 2014, pp. 221-246.
- [141] Jarosiński J.: *Techniki czystego spalania*, WNT, Warszawa, 1996.
- [142] Odenbrand C.U.I., Ludin S.T., Andersson L.A.H.: *Catalytic reduction of nitrogen oxides 1. The reduction of NO*, Applied Catalyst, 1985, pp. 335-352.
- [143] Lintz H.G., Turek T.: *Intrinsic kinetics of nitric oxide reduction by ammonia on a vanadia-titania catalyst*, Applied Catalyst A, 1992, pp. 13-25.
- [144] Fogler H.S.: *Elements of chemical reaction engineering*, fifth ed., Prince Hall, 2016, Chapter 15.
- [145] Odebrand C.U.I.: *The kinetics of the oxidation of ammonia on a V₂O₅/TiO₂ SCR catalyst deactivated in an engine rig. Part I. Determination of kinetic parameters by simulation*, Environmental Research & Technology, 2019, pp. 211-221.
- [146] Modlinski N.: *Numerical simulation of SNCR (selective non-catalytic reduction) process in coal fired grate boiler*, Energy, 2015, pp. 1-10.

List of figures

Fig. 1. The average composition of exhaust gases from a petrol vehicle [4].....	17
Fig. 2. The average composition of exhaust gases from a diesel vehicle [4].....	17
Fig. 3. Share of different sectors in NO _x emissions for 30 European cities [8].....	18
Fig. 4. Concentrations of PM ₁₀ , 2017- daily limit value [11]	19
Fig. 5. Total global annual emissions of fossil CO ₂ by sector [12].....	19
Fig. 6. Annual emissions of fossil CO ₂ for the EU28 and large emitting countries [12].....	20
Fig. 7. Schematic representation of exhaust gas recirculation. Adapted from [41]	24
Fig. 8. Schematic representation of storage and reduction NO _x by LNT catalyst [23]	25
Fig. 9. Sketch showing the physical and chemical processes in SCR system.....	26
Fig. 10. Conversion performance over various types of SCR catalysts [45]	27
Fig. 11. DeNO _x performance of SCR catalyst during different NO ₂ /NO _x ratio [46].....	29
Fig. 12. Main chemical reactions in SCR system [48].....	29
Fig. 13. Layout of the dual-layer catalyst [51]	31
Fig. 14. NO _x conversion and NH ₃ slip as a function of Ammonia NO _x Ratio (ANR) [50]....	32
Fig. 15. SCR coated on a DPF [57].....	32
Fig. 16. Compact design of exhaust gas aftertreatment [55].....	33
Fig. 17. Different design layouts for combination of DPF and SCR [58].....	34
Fig. 18. Example of an exhaust system for Euro 1 (Category M ₁ , Diesel) [60]	35
Fig. 19. Example of an exhaust system for Euro 2 (Category M ₁ , Diesel) [60]	35
Fig. 20. Example of an exhaust system for Euro 3 (Category M ₁ , Diesel) [60]	36
Fig. 21. Example of an exhaust system for Euro 4 (Category M ₁ , Diesel) [60]	37
Fig. 22. Example of an exhaust system for Euro 5 (Category M ₁ , Diesel) [60]	37
Fig. 23. Example of an exhaust system for Euro 6 (Category M ₁ , Diesel) [60]	38
Fig. 24. Timing and stages of the Euro 6 emission standard (Category M ₁) [61], [62].....	40
Fig. 25. Global emission standards [62].....	40
Fig. 26. Driving cycles (NEDC): urban (ECE) + extra urban (EUDC) cycle [63]	41
Fig. 27. Front (left) and back (right) of the roller test bench under climatic chamber [66]....	42
Fig. 28. WLTC cycle for Class 3b vehicles [59].....	44
Fig. 29. Portable Measurement Systems (PEMS) on a vehicle [70]	45
Fig. 30. Example of RDE test cycle recorded during road testing [62]	46
Fig. 31. SCR catalyst with catalytic material coated on a monolith substrate [50]	48
Fig. 32. Schematic diagram of the extrusion process [98]	51
Fig. 33. Schematic representation of coating process [59]	51
Fig. 34. Mechanistic cycle of the SCR reaction over the vanadium-based catalyst [10].....	54
Fig. 35. SCR activity over the hydrothermally pretreated different copper zeolites [106].....	55
Fig. 36. Mechanism of the simplified copper redox cycle [107]	55
Fig. 37. Ammonia storage capacity of Fe-zeolite and vanadia-based catalyst [110].....	56
Fig. 38. Mechanism of the standard SCR reaction on Fe-zeolite [10].....	57
Fig. 39. NO _x reduction activity in the fresh (a) and aged state (b) [112]	57
Fig. 40. SEM images along and perpendicular flow direction after ageing [111]	58
Fig. 41. SCR reaction activity with and without absence of SO ₂ [113].....	59
Fig. 42. The SO ₂ deactivation mechanism over V ₂ O ₅ -WO ₃ /TiO ₂ SCR catalysts [114]	60
Fig. 43. Deactivation processes and the strategies for control them [108]	60
Fig. 44. Overall process from spray to deposit creation [117].....	61
Fig. 45. UWS decomposition scheme including undesired deposit formation [129]	63
Fig. 46. Deposit formation on the pipe, catalyst, injector and mixer [116], [120].....	63
Fig. 47. SCR development process flow [127]	65

Fig. 48. Mixer development process flow [100]	66
Fig. 49. Car with the tested SCR system [130]	68
Fig. 50. Scheme of the exhaust gas aftertreatment system for a dedicated car [130]	69
Fig. 51. Engine and aftertreatment system unveiled at the motor show	69
Fig. 52. Fixture in the phase of construction of a prototype of the SCR.....	73
Fig. 53. Exhaust system backpressure [60]	74
Fig. 54. Measurement of pressure drops: original part (left), prototypes (right)	74
Fig. 55. Results of pressure drops for Case 1-3	75
Fig. 56. Endoscopic photo of the original mixer.....	75
Fig. 57. Results of pressure drops for Case 6-7	76
Fig. 58. Results of pressure drops for individual boxes	76
Fig. 59. Flow rig	77
Fig. 60. Cases during flow rig tests	78
Fig. 61. Conventional simultaneous ICP atomic emission spectrometer [131]	101
Fig. 62. Scanning a part with the ROMER Absolute Arm and obtaining a point cloud.....	102
Fig. 63. Process of reverse engineering for the prototype of SCR system.....	103
Fig. 64. Process of reverse engineering for the original SCR system.....	104
Fig. 65. Wall film model [73]	111
Fig. 66. Splashing regime map according to Kuhnke [85].....	112
Fig. 67. Cone injector geometry [74]	116
Fig. 68. Applied AdBlue injector in the SCR system	116
Fig. 69. Spray of injector with its main angles.....	117
Fig. 70. UWS droplet distribution at 5 bar injection [86]	118
Fig. 71. Cumulative size distribution of particles	119
Fig. 72. Arrhenius plot of apparent reaction rate constant [139]	123
Fig. 73. Arrhenius plot of apparent reaction rate [140].....	126
Fig. 74. Prepared 2D axisymmetric model in Catia	128
Fig. 75. Prepared components in ANSYS Workbench for simulation.....	129
Fig. 76. Imported 2D geometry in ANSYS DesignModeler.....	129
Fig. 77. Mesh completed for 2D geometry in ANSYS Meshing	130
Fig. 78. Prepared 3D model in Catia.....	131
Fig. 79. Imported 3D geometry in ANSYS DesignModeler.....	131
Fig. 80. Mesh completed for 3D geometry in ANSYS Meshing	132
Fig. 81. Fluent launcher for 2D geometry	132
Fig. 82. The 2D model loaded in Fluent	133
Fig. 83. Residual values in individual iteration for 2D model	135
Fig. 84. NO reduction in the 2D model of SCR catalyst.....	135
Fig. 85. Velocity contours in the 2D model of SCR catalyst.....	136
Fig. 86. Static pressure in the 2D model of SCR catalyst	136
Fig. 87. Temperature contours in the 2D model of SCR catalyst	137
Fig. 88. The 3D model loaded in Fluent	137
Fig. 89. Inlet conditions for cold flow simulation.....	138
Fig. 90. Defining injection for OP2 in the DPM model.....	139
Fig. 91. Main reactions used in the 3D model	140
Fig. 92. Mass flow rate at outlet for 3D cold flow simulation	142
Fig. 93. Velocity UI at outlet for 3D cold flow simulation	142
Fig. 94. Comparison of the parameters of mixers for the experimental cold flow	145
Fig. 95. Residuals, mass flow rate, $UI_{NH_3_in}$ and NO_{ave_out} (Case 6, OP2).....	146
Fig. 96. The design of the improved mixer	153

Fig. 97. $UI_{NH_3_in}$ for SCR system with improved mixer (OP2)	153
Fig. 98. Static pressure fields in the system for the case with the improved mixer (OP2)	155
Fig. 99. Temperature fields in the system for the case with the improved mixer (OP2)	155
Fig. 100. Velocity vectors in the system for the case with the improved mixer (OP2)	156
Fig. 101. Gas velocity trajectories for the case with the improved mixer (OP2).....	156
Fig. 102. Trajectories of UWS colored by diameter for the case with the improved mixer ..	156
Fig. 103. $UI_{NH_3_in}$ for SCR system without mixer (OP2)	157
Fig. 104. Verification of reaction kinetics for 2D axisymmetric model	159
Fig. 105. Pressure drop vs. velocity (exp. vs. CFD): Case 6 w/o mixer for 1 st & 2 nd catalyst	159
Fig. 106. Calculated pressure drop vs. $UI_{NH_3_in}$ for different mixers (OP2)	160
Fig. 107. Comparison of measured and calculated velocity for Case 1 (cold flow)	160
Fig. 108. Comparison of measured and calculated mole fractions of NO for Case 4 (OP2).	161
Fig. 109. Comparison of measured and calculated NO conversion for Case 4.....	161
Fig. 110. Calculated NO reduction vs. UI_{NO_out} for different mixers in SCR systems (OP2)	162
Fig. 111. Maximum ammonia molar fraction for different mixers in SCR systems.....	162
Fig. 112. Influence of the O ₂ & H ₂ O on DeNO in SCR with improved mixer.....	163
Fig. 113. Influence of the ANR on DeNO in SCR with improved mixer.....	163
Fig. 114. Influence of the NH ₃ rate order on DeNO in SCR with improved mixer.....	164
Fig. 115. Influence of the mass flow rate of exhaust gas on DeNO in SCR with improved mixer.....	164
Fig. 116. Influence of the mass flow rate on pressure drops and velocities in catalysts.....	165
Fig. 117. Influence of the temperature on DeNO and ammonia slip in SCR with the improved mixer.....	165
Fig. 118. Influence of the temperature on pressure drops in SCR with the improved mixer.	166
Fig. 119. Measuring points during the emission approval tests	167
Fig. 120. Installed OEM and WALKER SCR systems under the car with sampling points .	168
Fig. 121. Car prepared for emission tests on chassis dynamometer	169
Fig. 122. Measuring points of sound level for stationary and in motion vehicle [137]	171
Fig. 123. Example of possible measuring point for backpressure tests [136].....	171
Fig. 124. Emission results with required limits and formulas conditions	173
Fig. 125. Exhaust gas components (Pre SCR) for OE and AM parts in the NEDC test	175
Fig. 126. Exhaust gas components (Mid SCR) for OE and AM parts in the NEDC test.....	176
Fig. 127. Exhaust gas components (Post SCR) for OE and AM parts in the NEDC test	177
Fig. 128. Exhaust gas components (car tail pipe) for OE and AM parts in the NEDC test ...	178
Fig. 129. Cross-section of a Compression-Ignition (CI) Engine [1]	199
Fig. 130. Four-stroke cycle of operation in a CI engine [2].....	200
Fig. 131. p-V diagram of Diesel cycle for a four-stroke CI engine [2].....	201
Fig. 132. The excess air ratio (λ) influence regarding pollutants amount from SI engine [3]	202
Fig. 133. The excess air ratio (λ) influence on pollutants amount from CI engine [5].....	203
Fig. 134. Particulate matter size [9]	205
Fig. 135. Ceramic and metallic substrates [16], [17]	208
Fig. 136. Electron microscope images of the honeycomb structure [18].....	209
Fig. 137. Diesel oxidation catalyst (DOC) [20]	210
Fig. 138. Schematic of catalytic converter	212
Fig. 139. Air-to-fuel ratio (A/F) for gasoline engines with narrow window for TWC [23].	213
Fig. 140. Fabrication of monolithic honeycomb substrates [26].....	214
Fig. 141. Sketch of a monolith channel including physical and chemical phenomena [27]..	215
Fig. 142. Typical engine exhaust particle size distribution [31], [128]	216
Fig. 143. Filters: segmented SiC (on the left) and monolith cordierite (on the right) [60]....	217

Fig. 144. Electron microscope images of SiC (on the left) and cordierite (on the right) [29]	217
Fig. 145. Diesel Particulate Filter operation [30]	218
Fig. 146. Electron microscope images of PM trapped inside DPF wall pores [29]	219
Fig. 147. The construction of the GPF filter [35]	224
Fig. 148. Two different (single and twin-sided) catalyst coating of GPF [38]	224
Fig. 149. Experimental setup and samples evaluated in NEDC tests [33]	224
Fig. 150. NO _x and PN emission during NEDC tests [33]	225
Fig. 151. Mesh components [75]	228
Fig. 152. Some examples of meshes from ANSYS Fluent [74]	229
Fig. 153. FVM computational domain [71]	231

List of tables

Tab. 1. Emission standards for gasoline and diesel passenger car [59]	39
Tab. 2. Test bed layout for EU certification of light duty vehicles according to AVL [70]	43
Tab. 3. WLTC test cycles [59]	44
Tab. 4. Comparison of parameters from key emission cycles	46
Tab. 5. Deposit composition and conditions for creation [116]	62
Tab. 6. Contributing factors to urea deposit formation [119]	64
Tab. 7. Examples of static mixers	67
Tab. 8. Tested static mixers	70
Tab. 9. Investigated cases	71
Tab. 10. Geometrical and chemical properties of SCR monoliths	72
Tab. 11. The scope of research for individual cases	72
Tab. 12. Operating inlet conditions for cold flow without UWS	81
Tab. 13. Operating inlet conditions for hot flow with UWS	81
Tab. 14. Tested operational parameters for individual cases	82
Tab. 15. Velocity distribution for cold flow rig tests at outlet (Case 1-4)	83
Tab. 16. NO _x reduction efficiency for hot flow rig tests at outlet (Case 1-3, OP2)	90
Tab. 17. NO _x reduction efficiency for hot flow rig tests at outlet (Case 4-5, OP1-3)	95
Tab. 18. NO _x reduction efficiency for hot flow rig tests at tailpipe (Case 6-7, OP1-3)	99
Tab. 19. The results of the chemical composition analysis of the SCR catalyst	102
Tab. 20. Viscous and inertial resistance for porous model	115
Tab. 21. The main parameters describing the injector	117
Tab. 22. Particle size distribution	118
Tab. 23. The values of Yd and n , determined from the given data in Tab. 24	119
Tab. 25. Reaction orders for the Selective Catalytic Reduction of NO [139]	122
Tab. 26. Summary of catalyst reaction rate parameters [139]	123
Tab. 27. Kinetic data for V ₂ O ₅ -W/TiO ₂ catalyst [140]	126
Tab. 28. Kinetic data for 3D CFD simulations	127
Tab. 29. General settings for CFD simulation of the 2D axisymmetric model	134
Tab. 30. General settings for cold flow CFD simulation of the 3D model	138
Tab. 31. General settings for hot flow CFD simulation of the 3D model	141
Tab. 32. Velocity distribution and pressure drop for cold flow CFD simulation (Case 1-4)	143
Tab. 33. NO reduction and NH ₃ mixing for hot flow CFD simulation (Case 1, OP2)	147
Tab. 34. NO reduction and NH ₃ mixing for hot flow CFD simulation (Case 2, OP2)	148
Tab. 35. NO reduction and NH ₃ mixing for hot flow CFD simulation (Case 3, OP2)	148
Tab. 36. NO reduction and NH ₃ mixing for hot flow CFD simulation (Case 4, OP1-3)	149
Tab. 37. NO reduction and NH ₃ mixing for hot flow CFD simulation (Case 5, OP2)	150

Tab. 38. NO reduction and NH ₃ mixing for hot flow CFD simulation (Case 6, OP1-3).....	150
Tab. 39. NO reduction and NH ₃ mixing for hot flow CFD simulation (Case 7, OP1-3).....	151
Tab. 40. NO reduction and NH ₃ mixing for hot flow simulation (improved mixer, OP1-3).	154
Tab. 41. NO reduction and NH ₃ mixing for hot flow CFD simulation (no mixer, OP2).....	157
Tab. 42. Validation results for 2D axisymmetric model.....	158
Tab. 43. Deterioration factors for diesel engine applicable from Euro 5.....	170
Tab. 44. Results of the sound and backpressure testing.....	172
Tab. 45. Results of emission tests	172
Tab. 46. Comparison of reactors with ceramic and metal substrates [4], [5].....	210
Tab. 47. Physical properties of common particulate filter materials [28], [32]	218
Tab. 48. Operating properties of liquid catalytic fuel additive EOLYS [4], [5]	221

Appendices

I. Introduction to emissions of internal combustion engines

Internal combustion engines (ICE) are the primary transportation mover in today's society. These engines convert the chemical energy available in fuel through combustion to thermal energy, and, through expansion of the working fluid, convert the thermal energy to mechanical work (the crank-slider mechanism converting linear force to rotational torque to the output shaft) [6]. The most mature and refined in terms of construction and the possibility of using, are reciprocating engines, also often known as a piston engine using spark ignition (SI) in Otto engines (gasoline fuel) or compression ignition (CI) in Diesel engines, which is shown in Fig. 129.

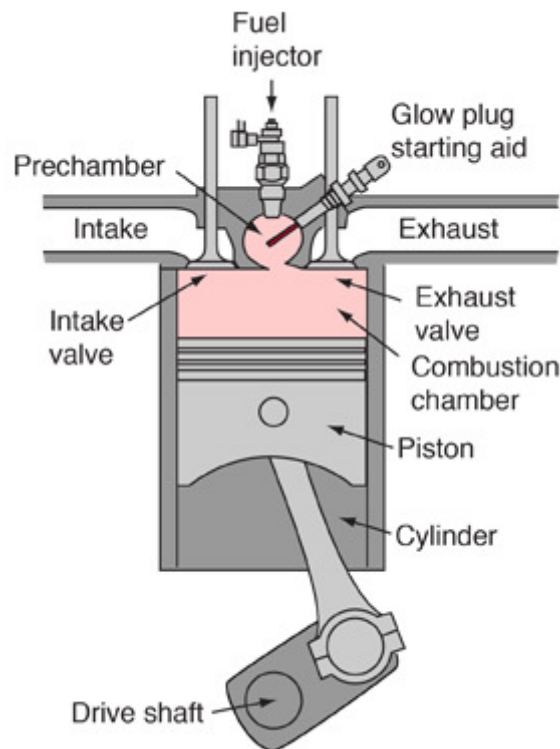


Fig. 129. Cross-section of a Compression-Ignition (CI) Engine [1]

Republished with permission of SAE International, from *Control System for Diesel - Compressed Natural Gas Engines*, Volpato O., Theunissen F., Mazara R., 2006-01-2849, 2006; permission conveyed through Copyright Clearance Center, Inc.

The main element of the piston engine is the cylinder-piston system and the associated piston-crank system by means of which the reciprocating movement of the piston is changed into the rotational movement of the crankshaft [5]. The CI engine Diesel cycle differs from the gasoline engine Otto cycle, among others, by using a higher compression ratio (from 16 to

22) for fuel self-ignition rather than using a spark plug as for SI engine. The sequence of operations for the four-stroke compression-ignition engine is as follows [2]:

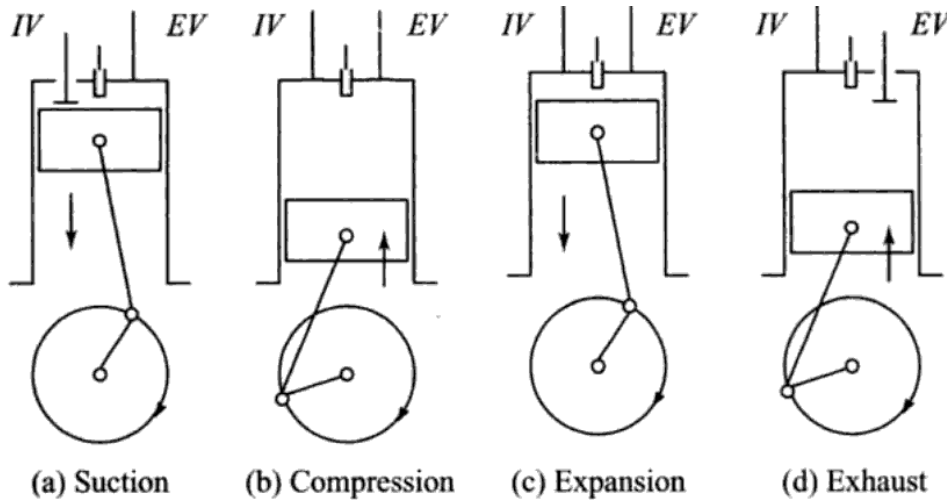


Fig. 130. Four-stroke cycle of operation in a CI engine [2]

Reproduced from *Internal Combustion Engines*, Ganesan V., ISBN 0-07-049457-6; Copyright 2003 Tata McGraw-Hill

Suction Stroke in Fig. 130 (a): the air itself is supplied to the cylinder during the suction stroke. During this stroke the intake valve (*IV*) is open and the exhaust valve (*EV*) is closed.

Compression Stroke in Fig. 130 (b): air supplied during the suction stroke is compressed into the combustion chamber volume. Both the valves (*IV* and *EV*) remain closed during this stroke.

Expansion Stroke in Fig. 130 (c): fuel injection starts nearly at the end of the compression stroke. The rate of injection is such that combustion maintains the pressure almost constant in spite of the piston movement on its expansion stroke increasing the volume. Heat is assumed to have been added at a constant pressure. After the injection of fuel is completed, the products of combustion expand. Both the valves (*IV* and *EV*) remain closed during this stroke.

Exhaust Stroke in Fig. 130 (d): the piston travelling from BDC (Bottom Dead Centre) to TDC (Top Dead Centre) pushes out the products of combustion. The exhaust valve (*EV*) is open and the intake valve (*IV*) is closed during this stroke.

In four-stroke engines, there is one power stroke for every two revolutions of the crankshaft. There are two non-productive strokes of exhaust and suction which are necessary for flushing the products of combustion from the cylinder and filling it with the fresh charge [2]. The Diesel cycle is shown in Fig. 131 and is modelled as a reversible adiabatic compression (there is no heat exchange, all energy is supplied or received as work: process 1-2) followed by a constant pressure combustion (isobaric heat supply 2-3), then isentropic

expansion (process 3-4) and an isochoric heat removal (process 4-5). Charge exchange is represented by the 5-0-1 processes.

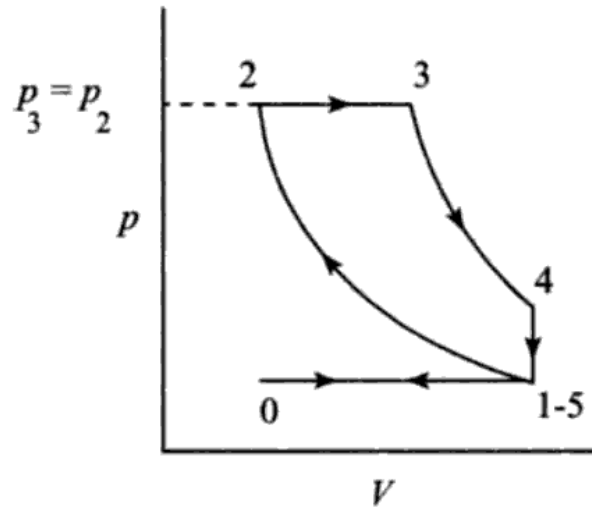


Fig. 131. p-V diagram of Diesel cycle for a four-stroke CI engine [2]

Reproduced from *Internal Combustion Engines*, Ganesan V., ISBN 0-07-049457-6; Copyright 2003 Tata McGraw-Hill

In the SI engine the amount of air sucked into the cylinder (L_{real}) is always slightly smaller or larger than the stoichiometric amount ($L_{stoichio.}$) that would be desired for the combustion reaction of the injected fuel dose. The actual composition of the air-fuel mixture reflects the so-called excess air ratio (λ), which is defined as follows [4]:

$$\lambda = \frac{L_{real}}{L_{stoichio.}} \quad (112)$$

Monitoring the value of this ratio is the basic task of the OBD (On-Board Diagnostics) system. The interpretation of the excess air ratio (λ), is as follows:

- $\lambda = 1$: stoichiometric composition of the mixture;
- $\lambda > 1$: excess air, i.e. fuel shortage (lean mixture);
- $\lambda < 1$: air shortage, i.e. excess fuel (rich mixture).

The graph (Fig. 132) presents dependence of the emissions on the composition of the combustible mixture, on the example of the most important toxic compounds contained in the exhaust gas for a spark ignition engine. The unfavorable situation is that the monotonicity of the molar fractions of incomplete combustion products and nitrogen oxides are formed in the opposite way, i.e. when the fractions of [CO] and [HC] decrease in the function λ , then the fraction of [NO_x] increases and vice versa [4], [5].

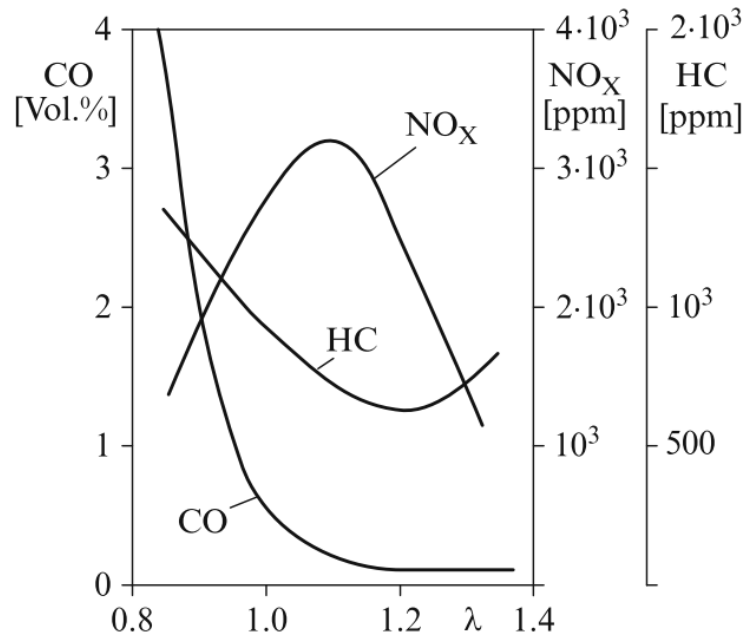


Fig. 132. The excess air ratio (λ) influence regarding pollutants amount from SI engine [3]
 Republished with permission of Springer, from *Combustion Engines Development*, Merker G. P., Schwarz C., Teichmann R., ISBN 978-3-642-02951-6, 2010; permission conveyed through Copyright Clearance Center, Inc.

Preparation of the mixture and the combustion process in a compression ignition engine differ essentially from the combustion process in a spark ignition engine. The most important differences result from the fuel injection, which in the diesel engine occurs at the end of the compression stroke. Liquid fuel must evaporate and mix with air shortly after injection into the combustion chamber, covering, as far as possible, the entire combustion chamber. Another significant difference in relation to the spark ignition engine, concerns the division of the combustion process into a phase of combustion at constant volume and constant pressure. Too short a delay time of self-ignition leads to an increase of particulate emissions, but ensures a more silent operation of the engine. Too long a delay time of self-ignition results in increased noise, high loads on engine components and increased emissions of nitrogen oxides, however, it reduces particulate emissions. The figure (Fig. 133) shows the relationship between the concentration of toxic components in the exhaust gas and the excess air ratio λ for diesel engines. The range of rich mixtures is not analyzed, because due to the presence of smoke limit, combustion in compression ignition engines always occurs in conditions of excess air [4].

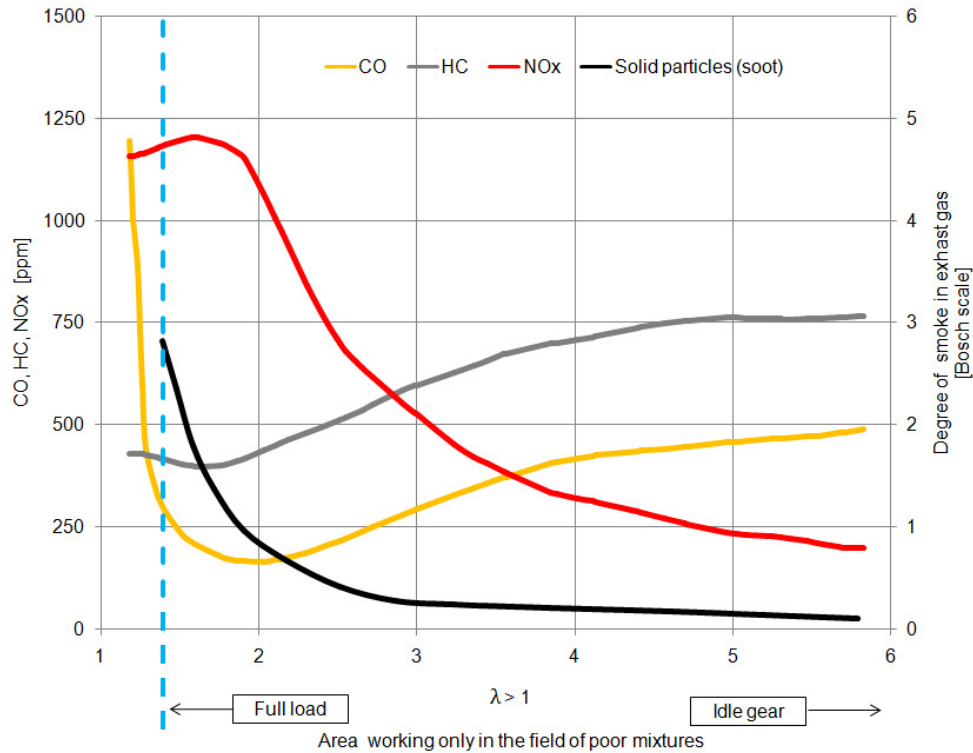


Fig. 133. The excess air ratio (λ) influence on pollutants amount from CI engine [5]

Adapted from *Termodynamiczne oraz ekologiczne uwarunkowania eksploatacji tłokowych silników spalinowych*, Postrzednik S., Żmudka Z., ISBN 978-83-7335-421-0; Copyright 2007 Wydawnictwo Politechniki Śląskiej.

Carbon monoxide (CO) is a colorless and odorless gas. It enters to the human body through breathing, the first sign of poisoning is disruption of the proper functioning of the central nervous system and the circulatory system. Carbon monoxide combines with haemoglobin, displacing oxygen from this combination, thereby blocking the ability to transport oxygen from the lungs to the tissues and leads to suffocation. Breathing air with a carbon monoxide volume concentration of 0.3% leads to death by suffocation in a short time. Carbon monoxide emissions are not a serious problem for diesel engines. Combustion of a rich mixture in spark ignition engines is an incomplete process and it leads inevitably to the formation of large amounts of CO [4].

Hydrocarbons (HC) contained in the exhaust gas in the largest quantities are from incomplete combustion (when the oxygen supplied is less than the amount required for stoichiometric combustion of carbon to CO_2) of a rich fuel mixture. The hydrocarbons contained in the exhaust gas affect humans by irritating the mucous membranes and respiratory tract. Hydrocarbons are very numerous groups of chemical compounds (paraffin hydrocarbons, olefins, aromatic hydrocarbons and aldehydes). Hydrocarbons are adsorbed onto the surface of a soot that forms solid particles and due to their small size they get into the

alveoli along with the inhaled air. They are carcinogenic and the most dangerous of them are benzol (C_6H_6), toluol and xylol (dimetylobenzol). Long term breathing air, which contains small amounts of benzol, leads to changes in the blood picture and cancer (leukaemia) [4].

Nitrogen oxides (NO_x) are formed in the combustion chamber at high temperatures (at high engine load) for poor mixtures. Combustion in compression ignition engines generally takes place in conditions of excess air, which is why nitrogen oxides emissions are a more difficult problem than for spark ignition engines. They are one of the main causes of smog, acid rain, resulting in the extinction of forests and contributing to ozone formation. Nitrogen oxides inhaled by humans get into the bloodstream and poison the body; they are also attributed to carcinogenic effects. The term nitrogen oxides (NO_x) are understood as different combinations of nitrogen and oxygen: NO (nitric oxide), NO_2 (nitrogen dioxide), NO_3 (nitrate radical), N_2O (nitrous oxide), N_2O_5 (dinitrogen pentoxide). Nitrogen dioxide is a gas with an irritating odour and red-brown colour. After reaching the respiratory track it irritates them and combines with haemoglobin contained in blood. NO_x plays a major role in the photochemistry of troposphere (~15 km altitude) and stratosphere (~50 km altitude), where it catalyses the formation of ground level ozone and ozone (O_3) depletion, respectively. Ground level ozone or tropospheric ozone is a greenhouse gas, a pollutant, a health hazard and harmful to plants and materials and therefore, increase in ozone in the troposphere is a cause for concern. On the other hand, stratospheric ozone is very much necessary for life on earth, because here it filters out photons with shorter wavelengths of ultraviolet (UV) rays from the sun that would be harmful to most forms of life in large doses. In the troposphere or lower atmosphere, when NO_x and the volatile organic compounds (VOCs) react in the presence of sunlight, they form photochemical smog, a significant form of air pollution, especially in the summer [14]. It is considered the most harmful of all existing compounds with oxygen and therefore the total amount of NO_x has been drastically reduced in newer emission limits [4].

Sulphur oxides (SO_x) are formed due to the sulphur content in the fuel. During the combustion process, sulphur atoms combine with oxygen and water vapour, and the products of these reactions may be sulphur oxides or sulphuric acid (H_2SO_4 or H_2SO_3). Sulphuric acid is the main cause of acid rain and, as a consequence, the extinction of forests. Sulphur oxide is a gas that dissolves in water, it works by irritating the eye mucosa and upper respiratory tract and increasing the amount of secretions, it can also lead to redness and swelling. Sulphur oxides adsorbed on the surface of soot forming solid particles and they get, with these

particles, into the lower respiratory tract. Asthmatics and young children are particularly exposed to the sulphur compounds contained in the air. Modern systems of catalysts are sensitive to sulphur in the fuel, because their high content may lead to irreversible damage.

Particulate matters (PM) and soot are clusters of carbon atoms that are a byproduct of the incomplete combustion of hydrocarbons. The reason for the incomplete combustion is the local oxygen deficiency in the combustion chamber and rapid cooling of the gases contained in the flame zone, which results in an interruption to the combustion process. The solid particles contained in the engine exhaust gas are not only clusters of carbon atoms, but also unburned hydrocarbons from fuel and lubricating oil, condensed water vapour, metal friction wear products, sulphur compounds and ash. Particulates differ in both shape and size (Fig. 134). Therefore, several groups of solid particles can be distinguished [4], [9]:

- Total Suspended Particulates (TSP) $< 15 \mu\text{m}$;
- Coarse PM (large solid particles) $2.5\text{-}10 \mu\text{m}$, deposits mainly in the head and large conducting airways;
- $\text{PM}_{10} < 10 \mu\text{m}$, they get into the bronchi;
- $\text{PM}_{2.5} < 2.5 \mu\text{m}$, fine particles deposits throughout the respiratory tract, particularly in small airways and alveoli;
- $\text{PM}_1 < 1 \mu\text{m}$, solid and liquid aerosols;
- Ultrafine Particles (UFP) $< 0.1 \mu\text{m}$, deposits in the alveoli.

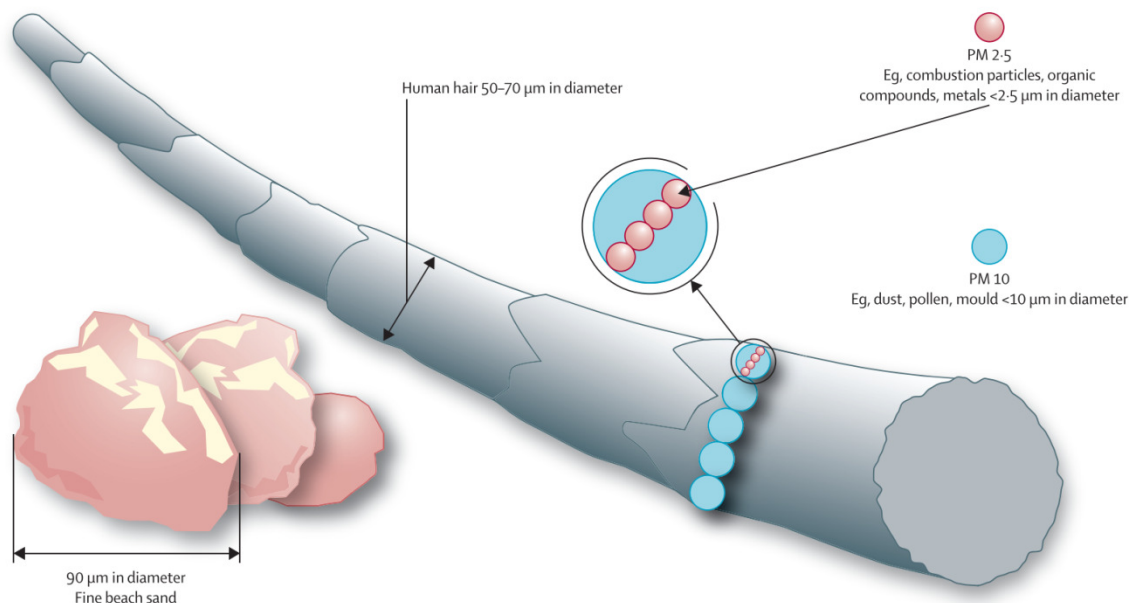


Fig. 134. Particulate matter size [9]

Reprinted from *The Lancet*, Vol. 383, Guarneri M., Balmes J. R., *Outdoor air pollution and asthma*, 1581-1592, Copyright 2014, with permission from Elsevier.

The mass, size and quantity of solid particles are significantly affected by the processes of joining individual particles into larger clusters. An important role is also played by the phenomenon of adsorption of compounds contained in exhaust gases, occurring on the surface of clusters of carbon atoms (soot) constituting the nuclei of solid particles. The adsorbed part of the substance can have a mass up to three times greater than the primary mass of carbon atoms, which is the core of the solid particles. The group of the smallest solid particles emitted by the engine is fine particle dust, which consists primarily of solid particles, polycyclic hydrocarbons, heavy metals, sulphur compounds and lubricating oil called the volatile organic compounds (VOCs) or the soluble organic fraction (SOF) [4], [10], [14].

Carbon dioxide (CO_2) is a non-flammable gas, colourless and has a slightly acidic flavour. Carbon dioxide is not a toxic gas, moreover, it is a component of exhaled air, where it occurs in a concentration of about 3% to 4%. High concentrations of carbon dioxide in inhaled air, exceeding its normal level in exhaled air, lead to headaches, tinnitus and palpitations. Concentrations between 8% and 10% are dangerous to life, which cause shortness of breath, loss of consciousness and respiratory arrest. The same concentration of carbon dioxide leads to the extinguishing of a wax candle. A concentration of 12% leads to rapid death. The mechanism of the impact of carbon dioxide on the human body consists in disrupting the natural regulatory processes of breathing, which leads to hypoxia. Carbon dioxide is not considered a toxic gas because it occurs naturally in nature and regulates many life processes in the world of plants and animals. Carbon dioxide is also a target of complete combustion occurring within the cylinder and is a product of the oxidation of toxic compounds in the catalytic converter.

Burning fossil fuels (coal, natural gas and oil) leads to a gradual increase in the concentration of carbon dioxide in the atmosphere, which in turn contributes to the greenhouse effect. Gases such as methane (CH_4), nitrous oxide (N_2O) and chlorofluorocarbons (CFCs) are also responsible for the greenhouse effect. Carbon dioxide, water vapor and other greenhouse gases affect the balance of heat radiation on the earth's surface. The layer of these gases in the atmosphere means that the visible part of solar radiation reaches the earth's surface without obstacles, but thermal radiation - infrared (IR), emitted by a heated earth's crust is absorbed. If the effect of absorbing infrared radiation by the atmosphere were excluded, the temperature on the earth's surface would drop to around -15°C . The described phenomenon is called the greenhouse effect. Greenhouse gas emissions associated with the burning of fossil fuels (anthropological emission caused by human

activities) increases the concentration of these gases in the upper atmosphere, which in turn increases the greenhouse effect. It is estimated that emissions of fuel combustion products will lead to such an increase in greenhouse gas concentrations by 2050 that the average surface temperature will increase by 4°C. Such a rise in temperature can lead to the melting of glaciers, raising the water level in the ocean by about 30 cm, desertification and gully erosion. Winds, natural movements of air masses and sea currents will change. The economic disaster may consist of flooding large areas of land [4], [13].

Ammonia (NH₃) is easily detected by its smell and is lighter than air. The National Fire Protection Association (NFPA), USA, has classified ammonia as a toxic substance, thus making it a chemical of high risk for health. Ammonia vapour in the air is flammable and may explode when ignited. Acute inhalation may result in irritation of eyes and nose with a sore throat, cough, chest tightness, headache and confusion. Ingestion of ammonia solutions may result in burns to the mouth and throat. After contact with skin it may cause deep burns and after contact with the eyes may cause inflammation, tearing and photophobia. Ammonia is also corrosive when mixed with water. The corrosiveness of ammonia will mix with body fluids like sweat and respiratory tract moisture to cause irritation. The environmental threat increases when NH₃ goes into a live body of water. NH₃ is corrosive to copper, brass and zinc alloys, forming a greenish/blue colour corrosion.

The original applications of ammonia were in the chemical and agriculture industries and it still finds its greatest application as a fertilizer for intensive crop farming. Ammonia is formed under certain conditions in selective catalytic reduction and its effect is desirable to reduce NO_x [4], [15].

II. Systems limiting the emission of CO, HC and NO_x

In order to reduce toxic gases contained in the exhaust gas (CO, HC and NO_x), which cannot be eliminated inside the combustion chamber of the engine, catalytic reactors are used, which create such conditions that the toxic gases are oxidized or reduced and the products are non-toxic gases such as carbon dioxide (CO₂), water (H₂O) and molecular nitrogen (N₂). Catalytic reactors began to be used in the USA in 1975 and on European roads the first cars equipped with this type of devices appeared in 1985. In 1993 the European Union introduced new emission standards (EURO 1), which effectively forced the use of catalytic reactors. Over the past 30 years there has been an extraordinary development in catalytic reactor

technology, thanks to which the latest achievements and advanced techniques in automotive aftertreatment systems allow it to adhere to the required emission limits of current and future standards [4], [5].

The catalytic reactor is a metal can in which the carrier (metal or ceramic monolith as in the Fig. 135, compared in Tab. 46) is located with a channel network and their large wall surfaces located in the exhaust gas path. The surface of the substrate is covered by an intermediate layer (washcoat), it is an oxide layer whose task is to increase the porosity of the channel walls. Thanks to the porosity the surface of contact with flue gas increases. Finally, the intermediate layer is coated with an appropriate coating, which is a catalytic layer. This layer contains precious metals (PGM – platinum group metals), most often they are: platinum (Pt), palladium (Pd) which support oxidation reactions and rhodium (Rh) supporting reduction reactions. These metals are the catalyst in a chemical sense [4], [5].

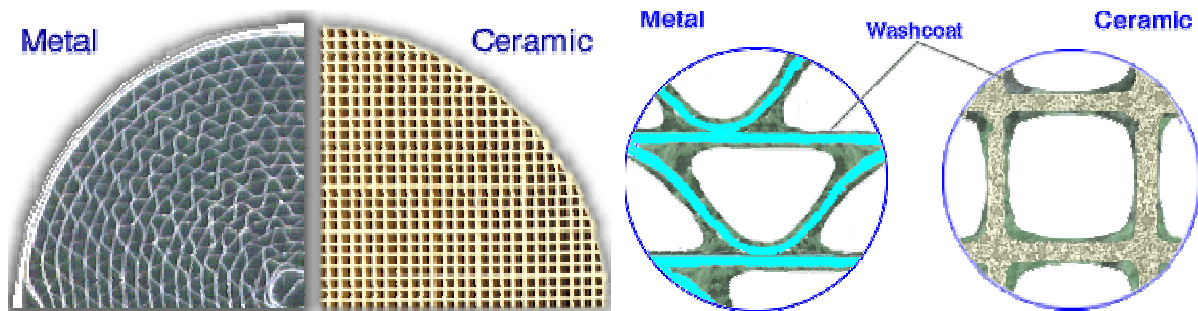


Fig. 135. Ceramic and metallic substrates [16], [17]

Reprinted from MATEC Web Conf., Vol. 78, Oxidation Resistance Analysis Of Metallic (FeCrAl Foil) Catalytic Converter Developed By Ultrasonic Approach, Leman A. M., Feriyanto D., Farhana N., Rahmat R., Bakar B. A., Baba I.; The Authors copyright 2016 (CC BY 4.0).

Reprinted from IJMME, Vol. 2, Experimental analysis and comparison of performance characteristics of catalytic converters including simulation, Mohiuddin A. K. M., Nurhafez M.; The Authors copyright 2007 (OA).

The housing of the reactor is made of high quality steel which is resistant to corrosion. The reactor housing is particularly exposed to corrosion, because one of the products of the conversion of exhaust gases taking place in the reactor is water and forming acids [4], [5].

To support the monolith in the housing, a mat of wire braid or more often fibreglass is used. This mat must be able to compensate for the difference in thermal expansion of the monolith and housing. In addition, it should have the ability to damp vibrations, strokes and transfer inertia forces acting on the substrate [4], [5].

Ceramic monolith is obtained in the process of extrusion of aluminium oxide (Al_2O_3) or cordierite i.e. magnesium aluminosilicate ($2\text{MgO}\cdot 2\text{Al}_2\text{O}_3\cdot 5\text{SiO}_2 - 14\%\text{MgO}, 35\% \text{Al}_2\text{O}_3$ and $51\% \text{SiO}_2$) [16]. The monolith consists of a thousand parallel channels, which in cross-section are arranged in a honeycomb structure. The number of channels per unit of cross-

sectional area is determined by rate of cpsi (cell per square inch). For example, a value of 400 cpsi means that there are 400 channels on one square inch of surface i.e. 62 channels per cm^2 . The wall thicknesses between the channels in older solutions are 0.15 mm and in the current even 0.05 mm. The monolith is covered with an intermediate layer - washcoat (Fig. 136) i.e. $\gamma\text{-Al}_2\text{O}_3$, TiO_2 , CeO_2 or ZrO_2 increasing porosity and containing PGM additives that increase the activity of the catalyst. The washcoat constitutes about 5 to 15 % of the weight of the monolith. Its thickness typically varies in the range 10-30 μm on the walls and 60-150 μm on the corners of the square cells [4], [5], [14], [21].

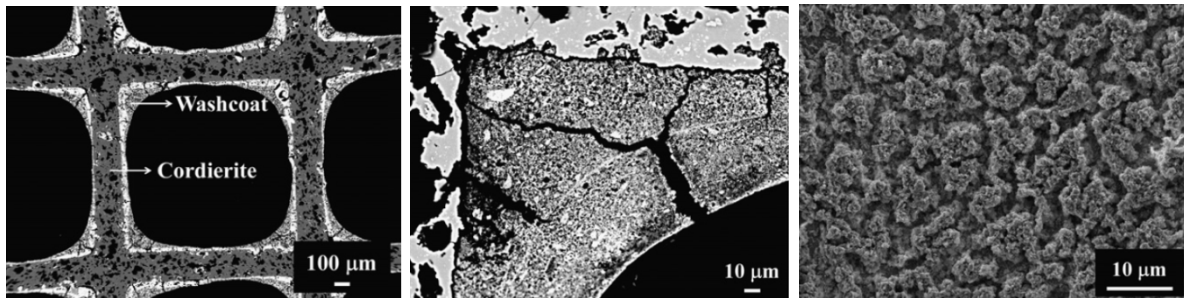


Fig. 136. Electron microscope images of the honeycomb structure [18]

Reprinted from *Minerals Engineering*, Vol. 24, Jimenez de Aberasturi D., Pinedo R., Ruiz de Larramendi I., Ruiz de Larramendi J. I., Rojo T., *Recovery by hydrometallurgical extraction of the platinum-group metals from car catalytic converters*, 505-513, Copyright 2011, with permission from Elsevier.

The metal substrate is formed by spirally winding corrugated and flat metal sheets (stainless steel or metal alloys e.g. FeCrAl) with a thickness of 0.05 mm to even 0.02 mm. The next layers of metal form channels. The entire cylindrical or oval substrate is pressed into the metal tube that forms its outer housing. The sheets are soldered on the surfaces of mutual contact and on the surface of contact with the outer housing. Coating of the sheet with an intermediate layer (washcoat) and a proper active catalytic layer (PGM) is also used [4], [5].

The cost of producing a catalytic reactor is primarily due to the price of PGM. The price of one gram of Pt on the world market is \$37, Pd is \$91 and Rh is \$739, where the price of gold is \$60 (prices from June 2021). There are very few precious metals in the earth's crust, mining is difficult and expensive, and reserves are slowly running out. That is why it is extremely important to recycle used reactors to close the scarcity of raw material. The durability of reactors is around 150.000 km, but it depends on how the car is operated [4], [5].

Tab. 46. Comparison of reactors with ceramic and metal substrates [4], [5]

Ceramic substrate reactor	Metal substrate reactor
Wall thickness: 0.05 ÷ 0.15 mm	Wall thickness: 0.02 ÷ 0.05 mm
cpsi: 200, 400, 600, 900	cpsi: 400, 600, 800, 1000, 1600
Geometric surface area density of the substrate: 2,4 m ² /dm ³ (400 cpsi)	Geometric surface area density of the substrate: 3,2 m ² /dm ³ (400 cpsi)
Thermal conductivity coefficient: 1 ÷ 1,08 W/(m K)	Thermal conductivity coefficient: 14 ÷ 22 W/(m K)
Specific heat capacity: 1,05 kJ/(kg K)	Specific heat capacity: 0,5 kJ/(kg K)
Density of solid material: 2,2 ÷ 2,7 g/cm ³	Density of solid material: 7,4 g/cm ³
Coefficient of linear expansion: 1 ΔL/L 10 ⁻⁶ K	Coefficient of linear expansion: 15 ΔL/L 10 ⁻⁶ K
Lower production cost	Increased production cost
Little resistance to mechanical damage and vibration	Relatively resistant to mechanical damage and vibration
Little resistant to high temperature, from 1200°C the catalytic layer is destroyed and the substrate melts at 1400°C	Higher temperatures are permissible, however, above 1600°C there are ageing processes
Longer warm-up time to working temperature (light-off)	A short warm-up time
Increased flow resistance (thicker walls)	Negligible flow resistance (thinner walls)
Increased fuel consumption	Does not increase fuel consumption
Standard used in most cars	In high power, high performance engines or as a starter reactor

A. Diesel Oxidation Catalyst (DOC)

The diesel oxidation catalyst (DOC) or two-way catalyst is used in aftertreatment systems as an additional reactor during the heating phase, especially is applied for engines operated under overall lean conditions. Operation of the oxidation reactor is limited to the oxidation of carbon monoxide, unburned hydrocarbons as well as the SOF portion of PM.

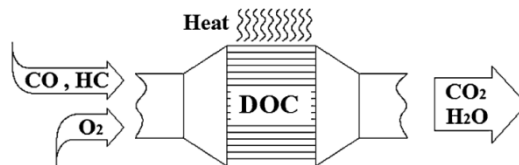


Fig. 137. Diesel oxidation catalyst (DOC) [20]

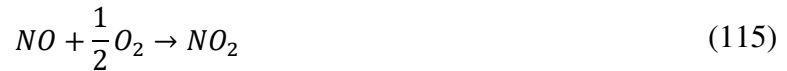
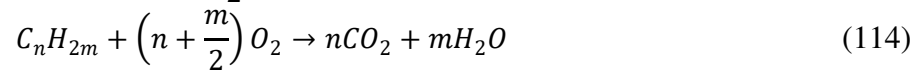
Reproduced with permission from *Clean Technologies and Environmental Policy*, Vol. 17, *The pollutant emissions from diesel-engine vehicles and exhaust aftertreatment systems*, Reşitoğlu İ. A., Altinişik K., Keskin, A.; The Authors copyright 2014 (OA).

Oxidation reactors also reduce the mass of particulate matter to some extent (about 30%). Although the solid particle nucleus formed by the cluster of soot is not transformed in the reactor, however, hydrocarbons and carbon monoxide particles settling on the nucleus of the

solid particle are eliminated. Additional benefits of the DOC include oxidation of several non-regulated, HC-derived emissions, such as aldehydes or PAHs (polycyclic aromatic hydrocarbons), as well as a reduction or elimination of the odour of diesel exhaust. Some of the oxidation reactions can produce undesirable products and, in effect, be counterproductive to the catalyst purpose [3], [4], [19], [20].

The oxidizing pre-reactor or starter reactor is made of a metal substrate or ceramics and located close to the engine so that it reaches its starting temperature (about 160°C) as soon as possible after start-up. Besides this carrier structure, it consists of an oxide mixture (washcoat) composed of aluminium oxide ($\gamma\text{-Al}_2\text{O}_3$), cerium oxide (CeO_2 - enhances precious metal activity, stabilizes the washcoat layer, improves the thermal activity and oxygen storage capacity (OSC)), zirconium oxide (ZrO_2), and active catalytic noble metals such as platinum and sometimes palladium. The quantity of noble metals used for the coating, which is often referred to as the loading, is approximately 50–90 g/ft³. Decrease of emissions from DOC use are estimated to be around 60–90 % for HCs and CO [3], [4], [14], [19], [20], [27].

There are four main global reactions which occur in DOCs [3]:



The reaction mechanism in diesel oxidation catalysts is explained by the presence of active catalytic sites that are deposited on the surface of the catalyst carrier and have the ability to adsorb oxygen. The catalytic reaction has three stages: (1) O_2 is bonded to a catalytic site, (2) reactants, such as CO and HC, diffuse to the surface and react with the bonded O_2 , (3) reaction products, such as CO_2 and H_2O , desorb from the catalytic site and diffuse to the bulk of the exhaust gas [19].

DOCs may also be used in conjunction with SCR catalysts to oxidize NO into NO_2 and increase the $\text{NO}_2:\text{NO}_x$ ratio. In the untreated engine exhaust gas, the NO_2 component in the NO_x is only about 10 % at most operating points. A high NO_2 concentration in the NO_x generates to increase efficiency of DPF and SCR which are placed after DOC [20], [25].

B. Three-Way Catalytic Converter (TWC)

The three-way catalytic converter (Fig. 129) has the advantage of performing the oxidation of carbon monoxide, unburned hydrocarbons and the reduction of nitrogen oxides simultaneously. Noble metals like Pt, Pd are for oxidation reactions and Rh is promoting the reduction reactions in the active phase of TWC. Also, water gas shifts and steam reforming reactions occur [21].

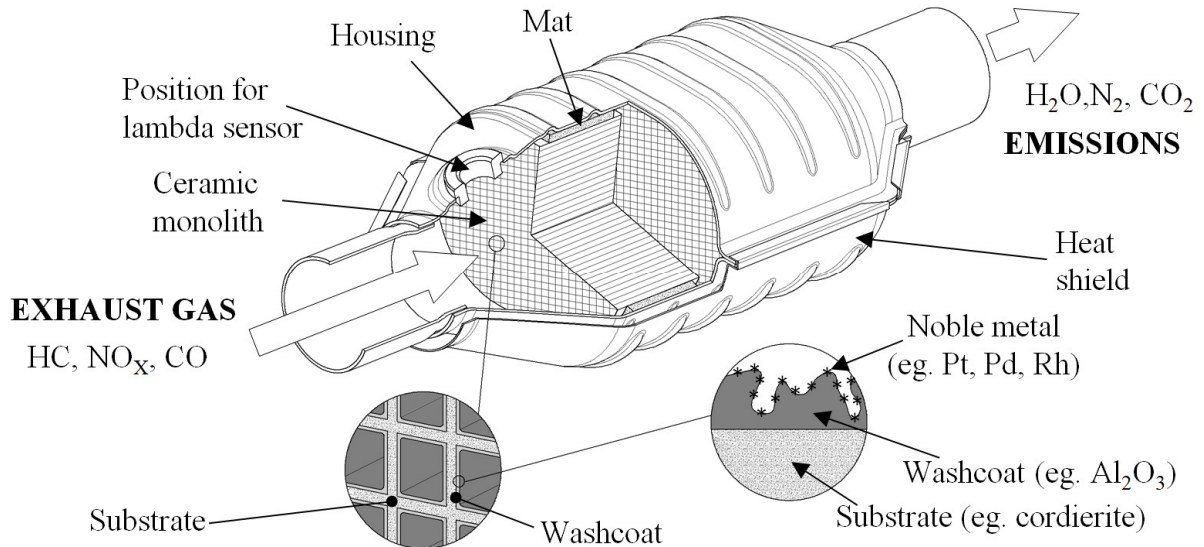
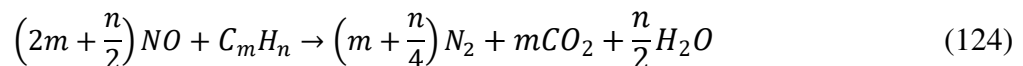
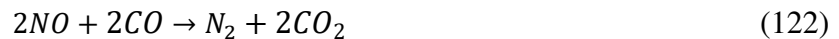
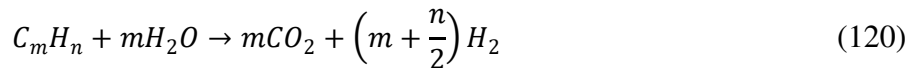
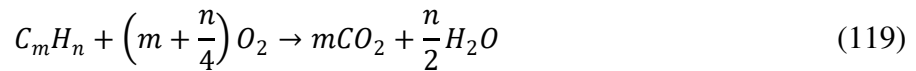


Fig. 138. Schematic of catalytic converter

The major reactions are oxidation of CO and HC and the reduction of NO_x. Harmful flue gases are converted into non-toxic gases by the following chemical reactions [5], [22]:



Currently, in the three-way catalytic converter it is standard to control the mixture composition in a feedback loop by using an oxygen sensor, which ensures precise dosing of

fuel, and the mixture has a composition similar to the stoichiometric composition ($A/F \sim 14,7$ and $\lambda \sim 1$) in the conventional gasoline engines. This configuration constitutes the basis of the so-called engine on-board diagnostics (OBD). Around the stoichiometric point ($\lambda = 1 \pm 0.005$), all the pollutants are almost totally removed (Fig. 139). However, when the environment is rich in oxygen (lean combustion) as in diesel engines (A/F ratios from 20:1 to 65:1), although this environment enhances the oxidation reactions, the reduction of NO becomes practically inefficient, then this pollutant cannot be appropriate removed with TWC [21], [23].

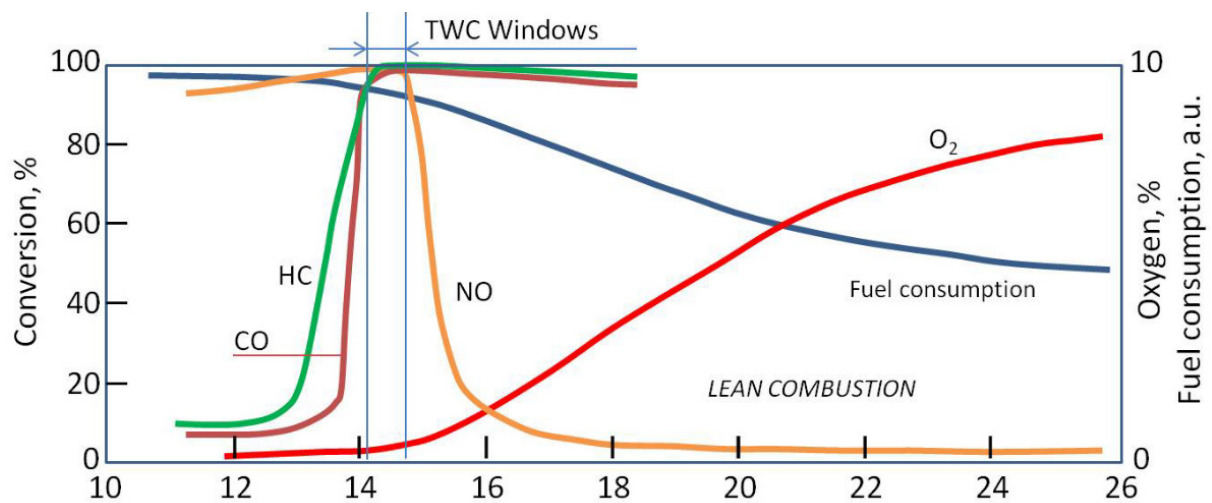


Fig. 139. Air-to-fuel ratio (A/F) for gasoline engines with narrow window for TWC [23]

Reproduced with permission from *NOx Storage and Reduction for Diesel Engine Exhaust Aftertreatment*, Pereda-Ayo B., González-Velasco J. R.; The Authors copyright 2013, Licensee Intech (CC BY 3.0).

During the emission test, the largest part of harmful substances is formed within the first three minutes of the test (cold-start). At that time, the catalytic converter usually does not reach its start-up temperature. The TWC is said to light-off (operating temperature) when conversion efficiency reaches 50% and this is usually achieved at $\sim 300^\circ\text{C}$ [24]. This problem can be partially overcome by preheating the catalytic converter electrically or bringing the catalytic converter closer to the engine (Close-Coupled Catalyst). The reactor is then often integrated with the exhaust manifold. Two-reactor systems are also used, consisting of a preliminary reactor at the outlet manifold (for removal HCs) and a main reactor under the car's chassis (for removing the remaining CO and NO_x). In more recent solutions, it is expected that the reactor will begin to operate properly within 15 seconds after a cold start. For this purpose, various methods of thermal insulation of the pipes supplying the exhaust gas into the reactor are used [4]. Another solution may be a zone-structured catalyst by dividing the channel's length into 2 zones, thanks to which the increased noble metal surface area in

the first section of the monolith significantly minimizes the cold start pollutant emissions [14], [25].

Ceramic monoliths are formed by extrusion (Fig. 140). The extrusion of cordierite starts from a good mixing of raw materials. It is necessary to ensure a complete reaction and interaction of raw materials. Plasticizing with solvent, usually water, is required to bring the batch materials to a condition suitable for forming by extrusion. Extrusion is done with a series of unique dies developed for this process. Uniform drying of monoliths is necessary to insure that enough moisture is driven off without cracking the monolith body. In the final step, the dry monolith part is calcined at 1400°C [26].

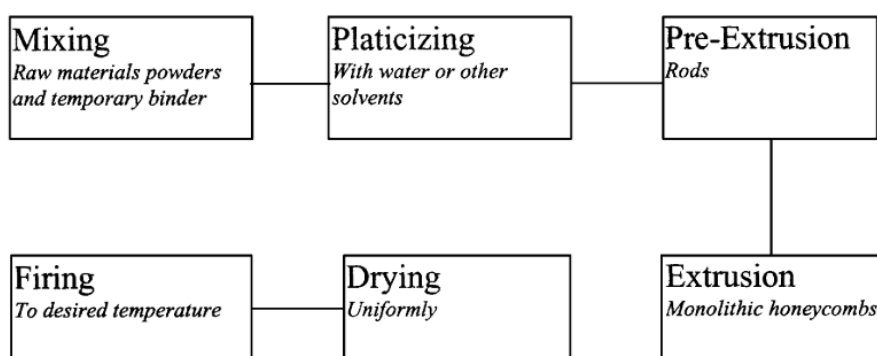


Fig. 140. Fabrication of monolithic honeycomb substrates [26]

Reprinted from *Catalyst Today*, Vol. 69, Williams J. L., *Monolith structures, materials, properties and uses*, 3-9, Copyright 2001, with permission from Elsevier.

To prepare the active monolith, a layer of washcoat is first deposited on the substrate and the catalysts are then deposited on the washcoat or dipping the monolith into a slurry containing washcoat components and platinum group metals. The excess of the deposited material (washcoat) is removed using high-pressure air or by applying a vacuum. Then the monolith is calcined to obtain the finished catalyst [21].

The catalyst (active layer) sometimes (due to limited resources and prices) also includes oxides of base metals e.g. copper (Cu), chromium (Cr), nickel (Ni), cobalt (Co), zinc (Zn), aluminium (Al), magnesium (Mg), ruthenium (Ru), iridium (Ir), molybdenum (Mo), manganese (Mn), iron (Fe), however, the most common with higher performance are noble metals platinum (Pt), palladium (Pd) and rhodium (Rh). The PGM loading typically varies from about 1.0 to 1.8 g/dm³ (30 to 50 g/ft³) with different ratio of Pt/Pd/Rh, which gives between 0.1 and 0.15 % by the weight of monolith and these PGMs are highly dispersed [17], [21].

The diffusion of reactants through the gas phase and the porous washcoat is followed by catalytic reactions, occurring on precious metal surface sites at the gas–solid interface

inside the porous washcoat. The physical and chemical processes in a monolithic reactor are sketched in Fig. 141. Inside the gas phase convective and diffusive transport of mass, momentum, and energy ($[X]$, u , T) occur in axial and radial directions. In the shown cross-section of the monolith, laminar profiles of velocity, temperature and species concentration mainly occur. Inside the porous washcoat convective transport can be neglected. The diffusive mass transport may have a significant influence on the conversion behavior of the catalyst. The energy balance of the solid is affected by diffusive transport (conduction) as well as radiation and chemical reactions (reaction enthalpy) [27].

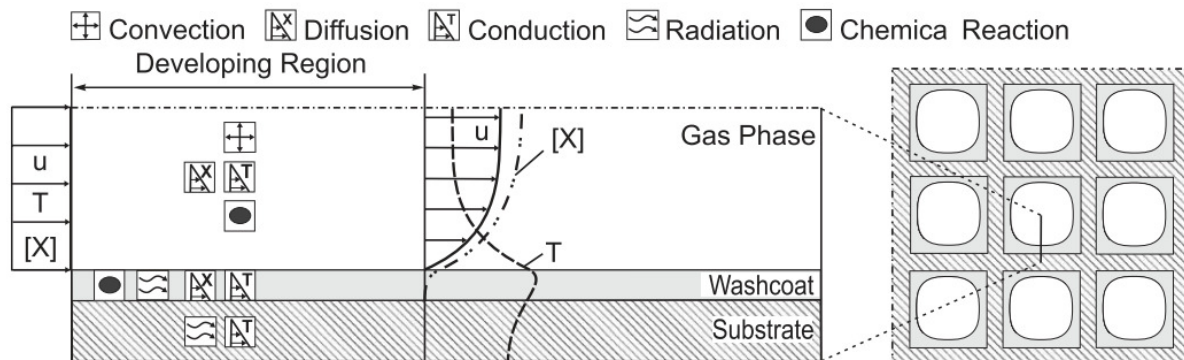


Fig. 141. Sketch of a monolith channel including physical and chemical phenomena [27]
 Reprinted from *Chemical Engineering Science*, Vol. 61, Holder R., Bollig M., Anderson D. R., Hochmuth J. K., *A discussion on transport phenomena and three-way kinetics of monolithic converters*, 8010-8027, Copyright 2006, with permission from Elsevier.

Catalyst ageing occurs by different chemical and physical processes. Increased local solid temperatures, so-called “hot spots”, might induce a change to a lower surface area phase. Moreover, the agglomeration of precious metals at high temperatures effectively reduces the active site concentration and hence the surface site density. Chemical poisoning, which is the irreversible process of deactivating surface sites, also reduces the catalyst activity [27].

III. Systems limiting the emission of PM

In order to remove solid products of incomplete combustion from the exhaust gas, i.e. particulate matters, the solid particles filters are used such as diesel particulate filter (DPF) and gasoline particulate filter (GPF). These filters remove about 95% of the mass of the solid and can reduce 99.9% of solid particles, including ultrafine particles. The size of the solid particles is one of the basic problems related to the development of filter structures. The problem is that the filtration process is a physical process and the porous filter baffle only retains particles larger than the pore size and in the diesel exhaust gas up to 98% of the mass of the solid particles can be in the range $0.01 \mu\text{m}$ to $0.5 \mu\text{m}$ (Fig. 142). With such small pores

in the filter partition, the design of the filter must provide a very large surface area to obtain the lowest possible exhaust gas pressure drop on the filter, i.e. the lowest possible exhaust gas flow resistance [5].

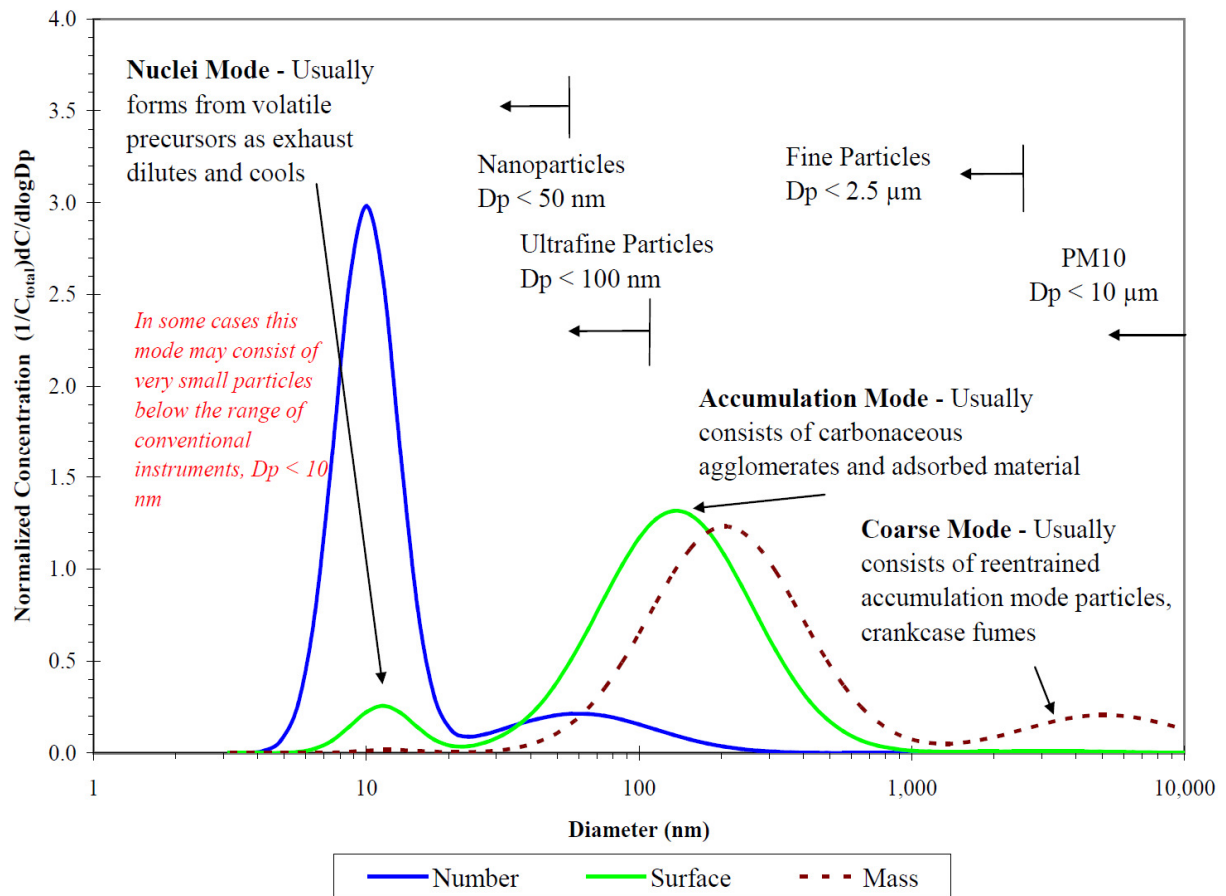


Fig. 142. Typical engine exhaust particle size distribution [31], [128]

Reprinted with permission from Cambridge Centre for Computational Chemical Engineering, ISSN 1473 – 4273, Kittelson D., Kraft M., *Particle formation and models in internal combustion engines*, Copyright 2014. However, adapted from *Journal of Aerosol Science*, Vol. 97, Kittelson D. B., *Engines and nanoparticles: a review*, 575-588, Copyright 1998, with permission from Elsevier.

The most important requirements, for operational reasons, that must be met by the particulate filtration systems are as follows [5]:

- high filtration efficiency (over 99%) with fast and efficient regeneration;
- no secondary emission (which may be the result of the filter regeneration process);
- high durability and resistant to high temperature;
- low maintenance costs and no increase in fuel consumption;
- low flow resistance (pressure drop).

The material of the ceramic filter is silicon carbide (SiC) and cordierite ($2\text{MgO}\cdot 2\text{Al}_2\text{O}_3\cdot 5\text{SiO}_2$) with the honeycomb structure monolith (compared in Tab. 47) with the channels blocked (with cement) at alternate ends (Fig. 143 and Fig. 144). The channels

plugged at ends force the particulate matter through the porous substrate walls, which act as a mechanical filter. As soot particles pass through the walls, they are transported into the pore walls by diffusion where they adhere [20]. Usually a square cell channel shape in 200 or 300 cpsi monoliths is used with a wall thickness of about 350–400 μm . Filter substrates with washcoat coating show up to 65% porosity and 20 μm mean pore size. The overall size of the filter for typical standard passenger cars is 5.66 in. diameter and 6 in. length [28]. Filters made in the technology of sintering of metal powders are also rarely used (they have a lower pressure drop but the filtration efficiency is much lower than ceramic). The material of the metallic filters is aluminium titanium alloy (Al_2TiO_5) [4], [28], [29], [30].



Fig. 143. Filters: segmented SiC (on the left) and monolith cordierite (on the right) [60]
Reproduced from Tenneco EMEA, Technical Advanced Digital Information System (TADIS): Emission control (<https://ta.garagegurus-eu.info/tadis/tadis-html-en/>), Copyright 2022, Tenneco Inc.

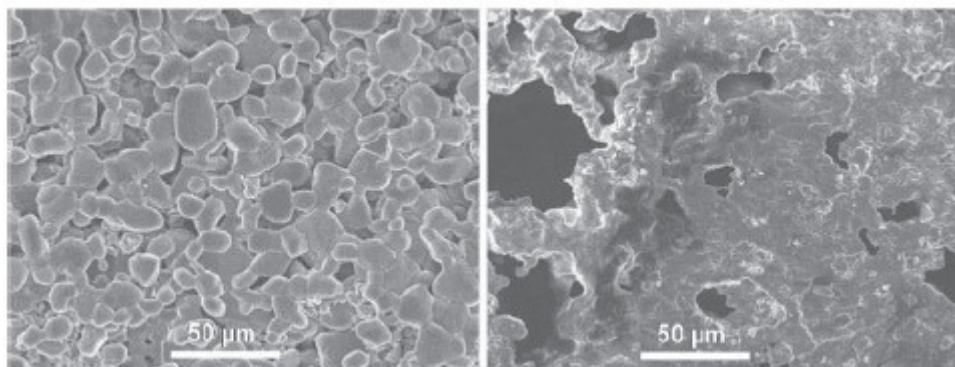


Fig. 144. Electron microscope images of SiC (on the left) and cordierite (on the right) [29]
Reprinted from International Journal of Engine Research, Vol. 10, Hanamura K., Karin P., Cui L, Rubio P., Tsuruta T., Tanaka T., Suzuki T., Micro- and macroscopic visualization of particulate matter trapping and regeneration in wall-flow diesel particulate filters, 305-321, Copyright 2009, with permission from SAGE.

Tab. 47. Physical properties of common particulate filter materials [28], [32]

Material:	Cordierite	SiC
Density of solid material [g/cm ³]	2,51	3,24
Thermal conductivity coefficient [W/(m K)]	~ 1	~ 12
Specific heat capacity [J/(g K)]	1,11	1,12
Volumetric heat capacity [J/(cm ³ K)]	2,79	3,63
Coefficient of thermal expansion [10 ⁻⁶ 1/K]	0,9-2,5	4,7-5,2
Young's modulus [GPa]	130	410
Thermal limit for application [°C]	1350	1500
Price	cheaper	expensive

A. Diesel Particulate Filter (DPF)

Diesel particulate filter (DPF) is designed to control particulate matter in diesel engines. DPFs have been applied in the production of vehicles since 2000 in heavy-duty vehicles and later as a standard for light-duty cars [32]. Fig. 145 shows an example of DPF.

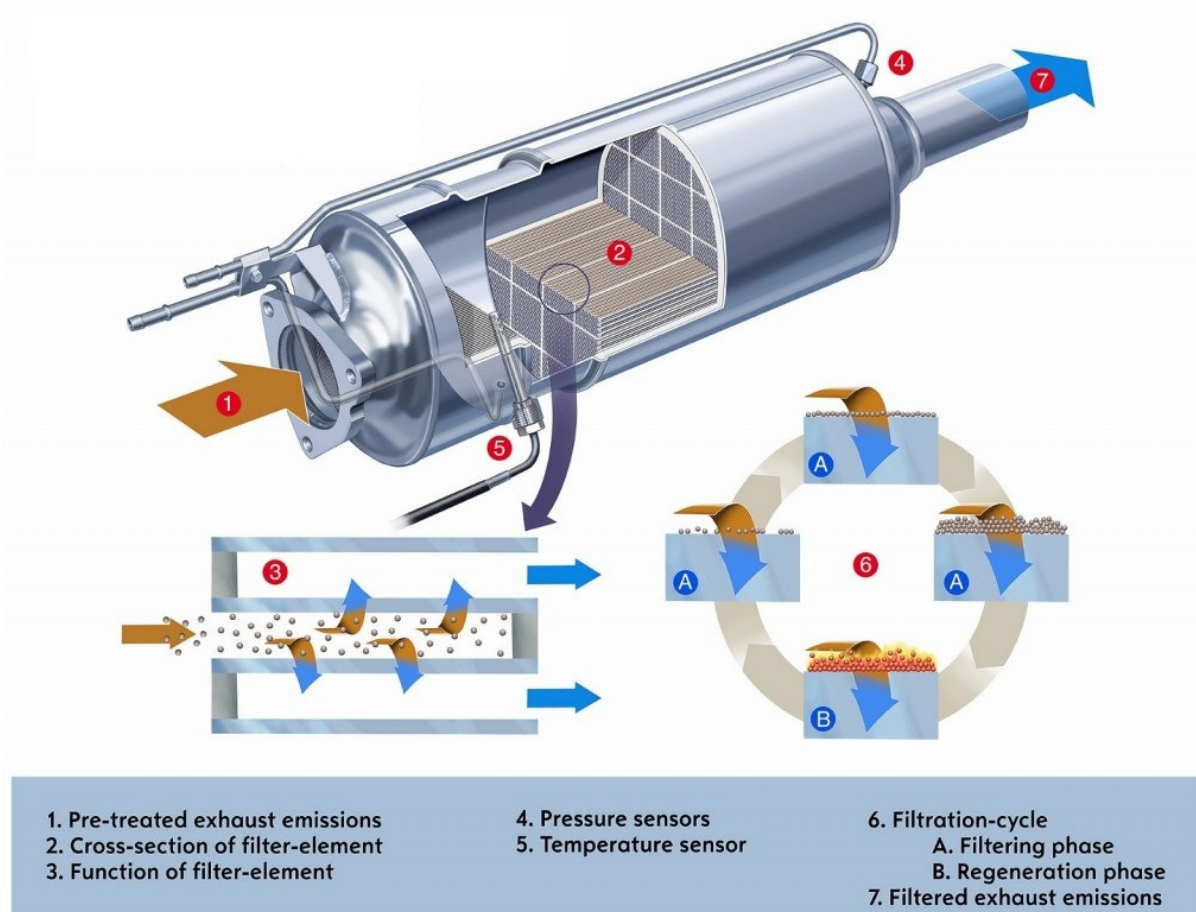


Fig. 145. Diesel Particulate Filter operation [30]

Republished with permission of ASME, from *Evolution of risk of diesel engine emissions on health during last 4 decades and comparison with other engine cycles - an innovative survey*, Bari S., Marian R.: Copyright 2015, ASME.

In jargon, a particulate filter is sometimes called a soot filter, which is an ambiguous and incorrect term. Soot is clusters of carbon atoms - it only creates the nucleus on which

various compounds are deposited, inter alia hydrocarbons, thus forming solid particles. During thermal regeneration, quite a long time and high temperature (over 550°C) are needed to burn the solid phase (soot and hydrocarbons). These conditions should be ensured in the particle filter, in which, after the accumulation of solid particles (Fig. 146), the process of burning them off is carried out - cleaning the filter (regeneration phase).

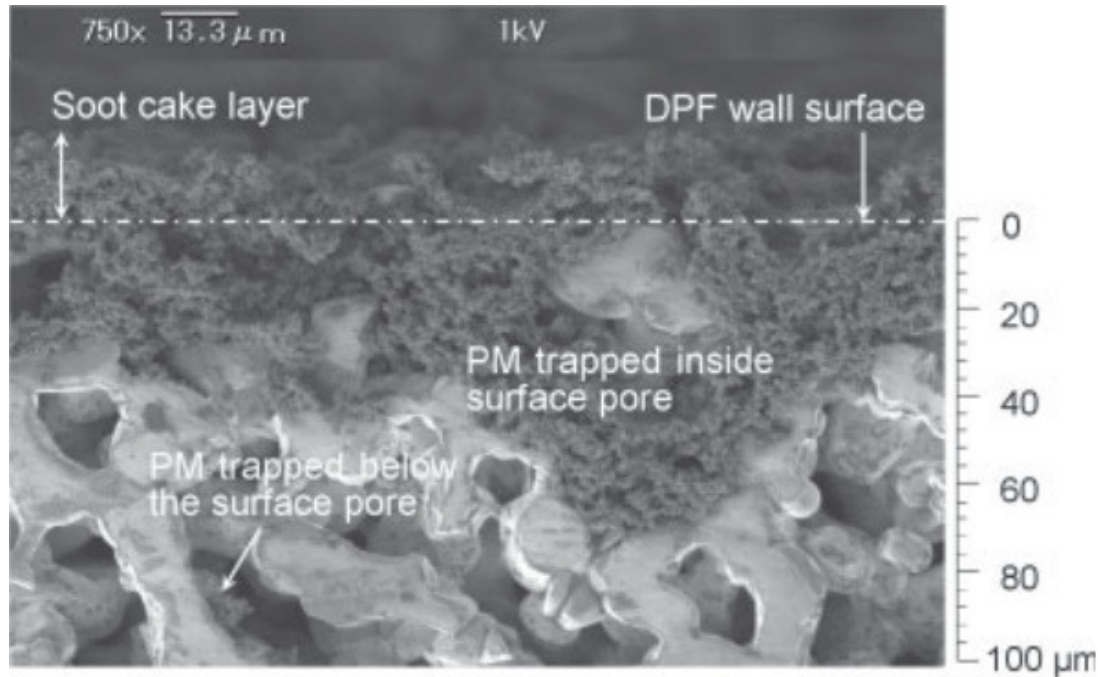


Fig. 146. Electron microscope images of PM trapped inside DPF wall pores [29]

Reprinted from *International Journal of Engine Research*, Vol. 10, Hanamura K., Karin P., Cui L, Rubio P., Tsuruta T., Tanaka T., Suzuki T., *Micro- and macroscopic visualization of particulate matter trapping and regeneration in wall-flow diesel particulate filters*, 305-321, Copyright 2009, with permission from SAGE.

This is a very important process, because an overfilled filter reduces the engine power and can even damage it due to excessive exhaust gas pressure in the exhaust manifold between the engine and the filter. This process takes place effectively at temperatures greater than 600°C. Unfortunately, in most operating conditions, exhaust gases from a compression-ignition engine have a much lower temperature. Such a high temperature of the exhaust gas flowing into the filter is achieved only during the long operation of the engine at high rotational speed and at almost maximum load. In exploitation practice, it is necessary to use other solutions that allow the regeneration of the filter without the need to run the engine at maximum power. In practice, two solutions are possible, either periodically raising the temperature of the exhaust gas or lowering the ignition temperature of the solid particles, which requires the use of a catalyst (in a chemical sense). In this respect, the filter regeneration methods can be divided as follows [4], [5], [30]:

- thermal afterburning (executed periodically),
- catalytic oxidation:
 - executed periodically,
 - executed continuously:
 - catalytic substance as a fuel additive,
 - a catalytically active layer of platinum applied to the walls of the filter.

Taking into account the method of achieving the afterburning temperature of the solid phase accumulated in the filter, regeneration can be distinguished [5], [28], [30]:

- passive regeneration - exhaust gas temperature is sufficiently high (above 550°C and between 300 - 400°C with a catalytic substance) to perform a regeneration process,
- active regeneration - requires feeding additional energy (the exhaust gas temperature is too low and ~600°C is needed) to the filter in order to carry out the regeneration process.

In passenger cars with diesel engines and common rail fuel systems, an active system is used to properly regenerate the filter, which is a combination of both methods - thermal and catalytic. This regeneration system includes two approaches [5], [28]:

- increasing the exhaust gas temperature to 300°C by additional fuel injection at the end of the working stroke i.e. post-injection (ignition of an additional dose of fuel contributes to an increase in the exhaust gas temperature, additionally, the exhaust gas temperature is also increased in the oxidizing reactor before the filter as a result of the oxidation of hydrocarbons and carbon dioxide),
- the use of fluid catalytic additive (EOLOYS - Tab. 48) to the fuel which reduces the temperature of the combustion of the soot well below 500°C: the system is called Fuel Borne Catalyst (FBC).

Tab. 48. Operating properties of liquid catalytic fuel additive EOLYS [4], [5]

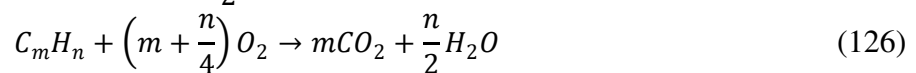
Generation:	1st generation DPX 9	2nd generation DPX 10	3rd generation DPX 13
Active substance	cerium oxide (CeO ₂)	cerium and iron oxides (CeO ₂ -Fe ₂ O ₃)	iron oxide (Fe ₂ O ₃)
Mass fraction of the substance in a liquid	4,2%	6,5%	10%
Dosage - concentration of active substance in fuel	25 ppm	10-12 ppm	7 ppm
Activation temperature (filter regeneration)	460°C	410°C	400°C
Filter regeneration time with an average engine load	1600 s	210 s	175 s
Maximum temperature during filter regeneration	700°C	750°C	750°C
The amount of fluid needed to overcome the distance 160 000 km	7 dm ³	3 dm ³	1,1 dm ³
Periodic inspection	every 80 000 km	every 120 000 - 150 000 km	every 250 000 km
The amount of ash formed after the mileage of 250 000 km	644 g	270 g	210 g

One of the most important problems currently associated with the use of particulate filters in engine exhaust systems is ash which is a product of burning off the accumulated solid particles; this ash is not removable. Each regeneration therefore leads to a reduction of the filter capacity, because part of the space in which the solid particles could be collected is covered by ash. Thus, the durability and service life of the filter is largely determined by the effect of ash accumulation (sometimes non-uniformity deposition of soot). Therefore, the filters require periodic cleaning (e.g. alternating cleaning with water) as part of the servicing process. Currently in-use filters require the cleaning of accumulated ash after a car mileage of 120,000 to 150,000 km. An important exploitation parameter characterizing the degree of filter filling is the difference in exhaust gas pressure before and after the filter, delivering through exhaust gas pressure sensors to OBD. The pressure drop on the filter as a function of rotational speed and engine load is only one of the criteria for deciding to start filter regeneration. It is advantageous to carry out the regeneration while driving on a highway (in urban traffic exhaust gas temperature may not be enough), with a relatively high engine load and exhaust gas temperature. The time necessary for a full regeneration of the currently used filters is up to 15 minutes (at an engine speed of approximately 2000 rpm and driving smoothly in top gear). Regeneration takes place every 800 km, depending on the exploitation conditions. There is an additional indicator lamp (MIL - Malfunction Indicator Lamp or DPF clogged lamp) in the instrument panel of cars equipped with a particulate filter, which shines

yellow if the filter cannot be regenerated due to the inadequate exploitation of the car. All manufacturers prohibit the tuning of engines with a particulate filter. Increasing the engine power increases exhaust emissions and noise, which contributes to the expiry of the car's approval for driving with all legal consequences [4], [5], [30], [32].

Today there are also different combinations such as Continuous Regeneration Trap (CRT) which consists of a diesel oxidation catalyst (DOC) and a particulate filter enclosed in one housing. The oxidation reactor oxidizes the nitric oxide NO to the nitrogen dioxide NO₂. This is important because nitric oxide does not burn off the solid particulates. The reaction products of nitrogen dioxide with solid particles are mainly non-toxic gases: molecular nitrogen N₂, carbon dioxide CO₂ and water vapor H₂O. The PSA concern (Peugeot Citroën) labels this system as FAP (Filtre à Particules). There is also a system marked CCRT (Catalyzed Continuously Regeneration Trap) or CSF (Catalyzed Soot Filter) and it is a system similar to the CRT, however in this system a catalytic coating is applied to the ceramic monolith of the filter, which supports the oxidation reactions. The use of platinum on the front of the filter is advisable in order to reach regeneration temperature faster. During the regeneration of the filter, the highest temperature is in the rear part of the filter, where ash accumulates, and the catalytic layer could be damaged. Such a system allows for the regeneration of filters at a temperature of 280°C [4], [5], [32].

In the case of a self-regenerating filter with a catalytic coating, the reaction chain takes place as follows [4], [5], [32]:



B. Gasoline Particulate Filter (GPF)

Gasoline direct injection (GDI) engines are continuously gaining market share globally, especially in the European market due to superior fuel economy and drivability. The European Union requires passenger car manufactures to decrease CO₂ emissions, therefore this trend will be intensified. However, boosted (turbocharged) and downsized GDI engines have a higher emission of particles (broadly in the 10–100 nm size range) compared to port fuel injection (PFI) engines under certain operating conditions such as cold start (more at low ambient temperatures) and high-load operating conditions [33], [35], [37], [38]. It was found that the vehicles equipped with GDI engines emitted approximately two orders of magnitude of the ultrafine particles than the diesel vehicles (with DPF) and the PFI gasoline engines [36]. On the other hand, GDI engines have a lower particulate mass (1–3 mg/km compared to 10 mg/km for diesel) and lower particulate numbers ($1-10 \times 10^{12}$ #/km compared to $1-10 \times 10^{13}$ #/km for diesel) [37]. In the PFI engine, fuel is injected just before the intake valve so that fuel and air flow simultaneously into the combustion chamber during the intake process, thus the fuel mixture is homogeneous. On the contrary, in the GDI engine, since air is injected into the cylinder and the fuel is injected during engine compression, the fuel mixture is not mixed smoothly. This results in a richer combustion near the spark plug than in the PFI engine, however, it raises particle emission as a result of wall wetting and pool fires above the piston. Especially with cold starts, when the engine is not fully warmed up, fuel injected into the combustion chamber forms a film on the inner wall of the combustion chamber or piston [34].

With the introduction of emission standard Euro 6d-temp (September 2017) a solid particle number (PN) limit has been established to level 6×10^{11} #/km, as well as for particulate matter mass (PM) to level of 4.5 mg/km in new test WLTP (Worldwide harmonized Light vehicles Test Procedure) [34], [35], [37]. In order to achieve such low limits, it was decided to implement a gasoline particulate filter (GPF) into the exhaust aftertreatment system. The construction of the GPF filter (Fig. 147) is very similar to the DPF filter. Sometimes additional coating (Pd, Rh) is applied to the walls of the filter (Fig. 148), thus receiving a three-way catalyst with a filter called catalyzed gasoline particulate filter (cGPF) or four-way conversion catalyst (FWC). The closer location of the filter to the engine, where it is warmer, may lead to lower soot loadings due to modern gasoline vehicles operating at stoichiometric or even rich A/F ratios and the supplied oxygen ensures passive soot burn [35]. The coated GPF has more advantages, such as reducing the cost of substrates,

packaging improvements, and an increase in soot regeneration performance under cold running conditions [38].

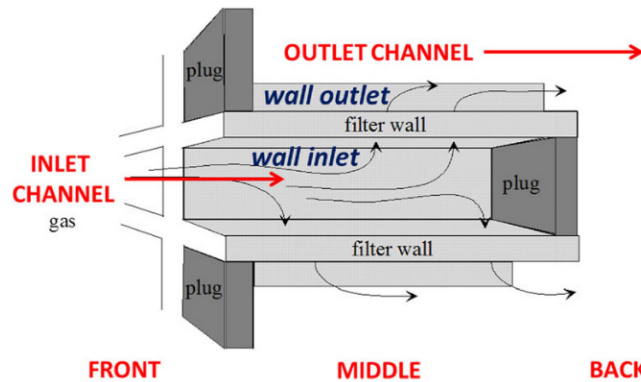


Fig. 147. The construction of the GPF filter [35]

Republished with permission of Springer Nature, from *Gasoline Particle Filter Development*, Lambert C., Chanko T., Dobson D., Liu X., Pakko J., 2017; permission conveyed through Copyright Clearance Center, Inc.

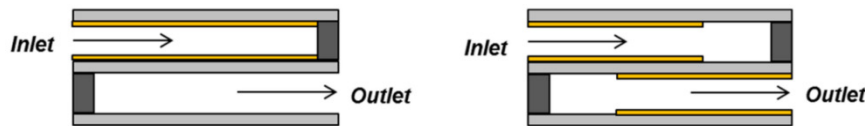


Fig. 148. Two different (single and twin-sided) catalyst coating of GPF [38]

Reprinted from *Energies*, Vol. 13, Wang J., Yan F., Fang N., Yan D., Zhang G., Wang Y., Yang W., *An Experimental Investigation of the Impact of Washcoat Composition on Gasoline Particulate Filter (GPF) Performance*; The Authors copyright 2020, Licensee MDPI (CC BY 4.0).

Spiess et al. [33] conducted research on close-couple TWC and under-floor filter (uncatalyzed GPF (bare filter) and catalyzed filter (GPF)) during NEDC (New European Driving Cycle) tests as shown in Fig. 149. Cordierite was used as a substrate for all filters with 65% porosity (porosity >60% leads to the lowest backpressure [35]), 300 cpsi of cell density and 12 mil wall thickness. The filter dimensions were 118.4 mm in diameter by 152 mm in length. The advantage of the catalyzed GPF systems (examples 2 and 3) are shown in Fig. 150.

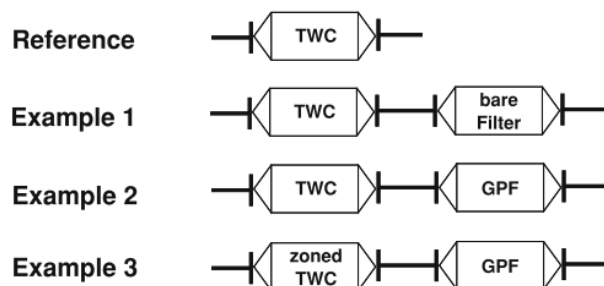


Fig. 149. Experimental setup and samples evaluated in NEDC tests [33]

Republished with permission of Springer Nature, from *Topics in Catalysis, Investigations of Emission Control Systems for Gasoline Direct Injection Engines with a Focus on Removal of Particulate Emissions*, Spiess S., Wong K. F., Richter J. M., Klingmann R., Vol. 56, 434-439, 2013; permission conveyed through Copyright Clearance Center, Inc.

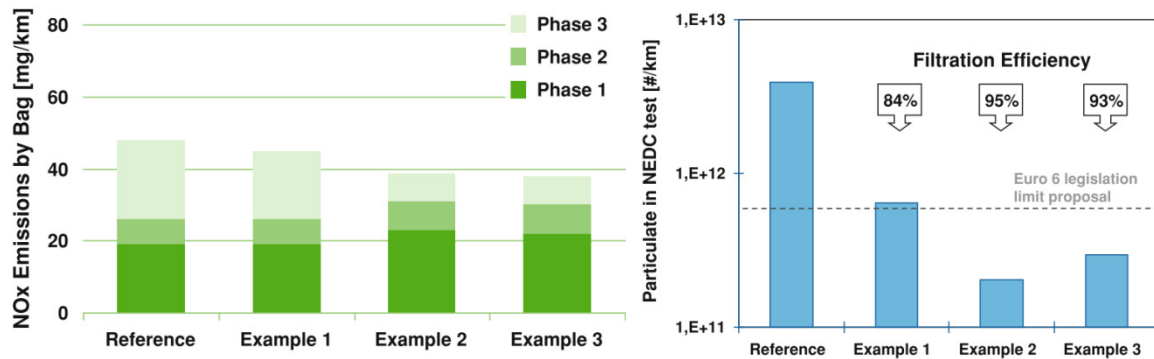


Fig. 150. NO_x and PN emission during NEDC tests [33]

Republished with permission of Springer Nature, from *Topics in Catalysis, Investigations of Emission Control Systems for Gasoline Direct Injection Engines with a Focus on Removal of Particulate Emissions*, Spiess S., Wong K. F., Richter J. M., Klingmann R., Vol. 56, 434-439, 2013; permission conveyed through Copyright Clearance Center, Inc.

Despite a small NO_x increase during the engine cold start, a significant reduction of NO_x achieved during phase 3 of the NEDC test, especially using zone coated TWC. More importantly, applying a washcoat to the filter allowed for a significant reduction in the particle emissions of the engine and met the Euro 6 limit. The lower temperature in the under-floor position leads to lower inlet flow velocity and thus an approximately 15% higher filtration efficiency. Spiess et al. [33] also noticed a significant reduction in particulate emission when there is an increase the distance (layout) between the TWC and the GPF filter from 10 cm to 150 cm, minimizing the pressure drop. Moreover, as the number of tests increases, the improvement in particulate emission reduction has been noticed (filtration efficiency increases with mileage by 60-80% after 3000 km [37]). The accumulation of a small amount of soot (later ash) layer and lower gas temperature in under-floor position contributes to a lower number of regeneration which supports the filtration efficiency (>90%). Jang et al. [34] also noticed higher PN filtering efficiency in the under-floor position. However, the soot layer formed by accumulated particles on the filter surface increases the pressure drop. On the other hand, the high exhaust gas temperatures also accelerate the exhaust gas velocity and the small particles can pass through the filter wall which leads to lower filtration efficiency [34]. Lambert et al. [35] found out that GPF filter has become clogged of non-combustible material (60 g) after over 150 000 miles (~241 000 km) what was full useful life of vehicle.

Particulate matters emitted from the engine is filtered and collected on the porous walls through a particle filter and then the filter must be regenerated to remove the collected PM. In a gasoline engine, the exhaust gas temperature is higher (up to 900°C compared to < 400°C for diesel engine) than the oxidation temperature of the soot. The regeneration of the

GPF occurs through natural (passive) regeneration when the fuel cut generated in the deceleration phase results in excess oxygen (~ 18%) that then oxidizes the collected PM. Regeneration of GPF occurs instantaneously and it is determined that the emission of small size particles (nanoparticles smaller than 20 nm) increases with the regeneration number [34], [37]. It should also be emphasized that employing GPF as a solution to reduce particulate emission also results in an increase of the pressure drop of the entire exhaust aftertreatment system. Therefore, the pressure drop increases the backpressure of the exhaust manifold, and thus imposes an unfavorable effect on the engine power output, fuel economy, and CO₂ emissions. Different kinds of coatings (Wang et al. [38] used high bulk density of aluminium and cerium zirconium oxides) as shown in the Fig. 148, together with integrated pores characteristic of the filter walls were proved to have an evident effect on the minimization of the pressure drop and increase particulate filtration efficiency with minimal impact on fuel economy [37], [38]. Guan et al. [36] also mentions that the GPF backpressure is 25% lower when it was placed downstream of the TWC.

It should also be mentioned that GDI engines operate under rapid heating and cooling conditions, so good thermal shock performance is a key requirement for GPFs. Cordierite monolith (200 cpsi for uncoated GPF and 300 cpsi for coated GPF with 8-12 mil wall thickness) is well fitted for this application, given its low coefficient of thermal expansion and excellent thermal shock performance. The low thermal mass of cordierite filter also enables quick heat-up and early catalyst light-off and higher regeneration efficiency under passive soot oxidation. It is established that cordierite can withstand ash interactions at the temperatures expected for gasoline applications. The channel friction depends on the geometry (cell density, GPF diameter and length). The porosity (45-55% for uncoated GPF and 60-65% for coated GPF) and mean pore size (13-15 μm for uncoated GPF and 15-20 μm for coated GPF) of the filter walls are optimized to provide a good balance between high filtration efficiency and low pressure drop [37].

IV. Introduction to applied computational fluid dynamics (CFD)

Computational fluid dynamic (CFD) is a technique for the prediction of fluid flow, heat and mass transfer, chemical reactions as well as associated phenomena by numerical solution of the mathematical equations, which govern these processes. The use of CFD software permits the user to perform development and analysis of a virtual prototype of a future product, allowing for the prediction of key processes and design parameters. CFD has

been part of the broad industrial community since the 1990s and the most commercially available codes are ANSYS Fluent/CFX, Fidap, Polyflow, Phoenix, Star CD, Flow 3d and many others [71], [72].

CFD analysis gives significant unique advantages when used in any process instead of experiment-based approaches:

- improved product quality;
- decreased number of physical prototypes (traditional routine of design-build-test);
- reduction of lead times and costs of new designs, experiments or person hour costs;
- the possibility of systems analysis where experiments are difficult (large systems, hazardous conditions);
- fast market introduction;
- unlimited level of detail of the results;
- reduced field failures and avoided product claims [71], [72].

In figuring out fluid flow problems the physics is complicated and the results achieved by a CFD program are at best as good as the physics and chemistry installed in it and at worst as good as its user (who must have skills in a number of areas). There is a need to consider the physical and chemical phenomena in the stage of identification and formulation of the flow problem. At the end of a simulation the operator must judge whether the results are sufficiently good e.g. by comparing them with experimental test work [72].

A. Modelling procedure

CFD software is composed around numerical algorithms that can deal with fluid problems. The procedure involved in the typical basic CFD process, includes three main elements: pre-processor, a solver and a post-processor.

Pre-processing is composed of the input of a flow problem to a CFD software by an user-friendly interface and the following transformation of this input into a convenient scheme for use by the solver. The procedure includes the following activities:

- geometry definition (the computational domain) - volumes, faces, edges and points;
- volume mesh generation (discretization) - collection of cells called the grid (mesh);
- definition of appropriate boundaries and conditions at cells;
- choice of correct the physical and chemical phenomena;
- settings of fluid properties based on empirically derived values;

- definition of numerical control settings (iteration, convergence).

Inside each cell (at nodes) as in Fig. 151, the solution to a flow problem is represented. The efficiency of a CFD solution is conducted by the number of cells in the grid. The solution has better accuracy when the number of cells are larger. However, it costs more in terms of required computer hardware and calculation time. Optimal meshes are usually non-uniform: finer in areas where large variations occurs from point to point and rough in fields with rarely change. The definition of the domain geometry and grid generation takes about 50% of the time in a CFD project [71], [72].

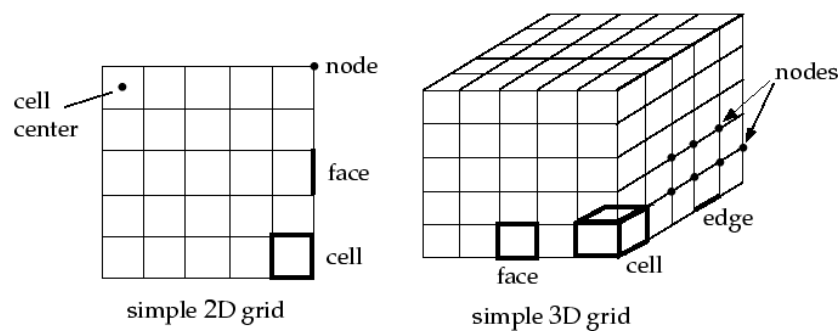


Fig. 151. Mesh components [75].
Copyright 2013, Images used courtesy of ANSYS, Inc.

The cells of the mesh are grouped into boundary zones where boundary conditions are applied and the grid has a significant impact on rate of convergence, solution accuracy and CPU time required. Mesh quality is very important when a reliable solution is the goal. The following main parameters influence overall quality of the grid in ANSYS Fluent:

- density of the mesh;
- orthogonal quality (worst 0 - 1 perfect) is acceptable greater than 0.15 and means how close the angles between adjacent element faces (or edges) are to some optimal angle;
- skewness (perfect 0 - 1 worst) is acceptable less than 0.95 and means how close to ideal (e.g. equilateral or equiangular) a face or cell is;
- aspect ratio (perfect 1 - ∞ worst) is acceptable less than $10 \div 100$ and is defined as length to height ratio in 2D or the radius of circumscribed to the inscribed circles in 3D [71], [74].

Many different meshes (Fig. 152) are available and the choice depends on the problem and the solver's capabilities. Mainly the following classification of grids are: Tri mesh (triangular elements), Quad mesh (quadrilateral elements), Hex mesh (hexahedral elements), Tet mesh (tetrahedral elements) and Hybrid mesh (combinations mentioned) [71].

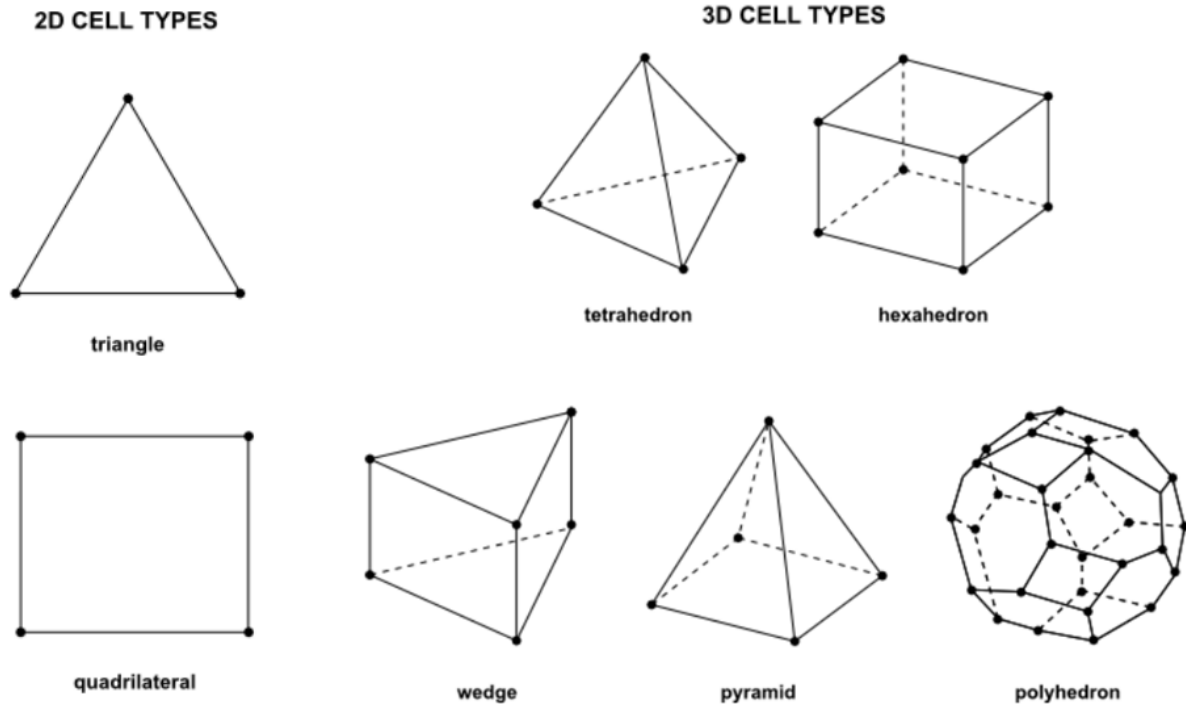


Fig. 152. Some examples of meshes from ANSYS Fluent [74]
Copyright 2013, Images used courtesy of ANSYS, Inc.

Boundary conditions are assigned to zones, which are the flux inlets and outlets, they are also direct motion of flow (walls). A wide range of boundary conditions permit the flow to enter and exit the solution domain: pressure inlet/outlet, velocity or mass flow inlet and outflow. Moreover, several types of thermal boundary conditions are available: material, thickness and roughness can be defined. For each zone, material needs to be specified in ways such as density (incompressible flow - ideal gas or compressible flow), viscosity, heat capacity, molecular weight, thermal conductivity and diffusion coefficients. For mixtures, properties may have to be specified as a function of the mixture composition [71].

The purpose of the turbulence modelling is to develop equations that will predict the time averaged velocity, pressure, and temperature fields without calculating the complete turbulent flow pattern as a function of time. A turbulence model is a computational way to close the system of mean flow equations. A convenient turbulence model must have wide applicability, a high accuracy and be simple and efficient to run. Based on Reynolds Averaged Navier-Stokes (RANS) equations, there are several common turbulence models: mixing length model, Spalart-Allmaras, $k-\epsilon$ or $k-\omega$ model and Reynolds stress model [71].

The Discrete Phase Model (DPM) can be analyzed numerically for transportation and interactions between solid particles dispersed (e.g. aerosol) in a fluid. Discrete phase particles are spherical and can represent solid particulates or droplets, dispersed in a continuous phase.

The DPM can enhance or reduce the gas turbulence when introduced into a turbulent flow. There are two methods of solving DPM: one-way or two-way coupling phases. In the first, the particulates have no influence on the gas phase but fluid acts on the particles by drag and turbulence. In the second, the transfer of particle momentum to the carrier-phase is negligible. The DPM simulation is applicable only for flows in which particle streams are injected into the continuous phase flow with well defined inlet and outlet conditions. The particle trajectory can be changed, when it reaches a boundary layer and can therefore be: reflected via collision, escape by the boundary, trapped on the wall, pass through e.g. porous zone or slide along the wall [71].

Solver is based on solving conservation of mass, momentum (the sum of forces on a fluid particle - Newton's second law) and conservation of energy (the sum of rate of heat addition to and work done on fluid particles) equations which must be satisfied throughout the region of interest. The solution is possible with the finite volume method, a special finite difference formulation that is used by commercial and free CFD codes. The numerical algorithm consists of the following steps:

- integration of the governing equations of fluid flow over the finite control volumes;
- discretisation through conversion integral equations into algebraic equations;
- solution by simultaneous equations (algebraic) by an iterative method to solution.

Discretisation techniques are convenient for the treatment of the crucial transport phenomena, convection and diffusion as well as for source term and the rate of change with respect to time. Physical phenomena are complicated and non-linear so an iterative solution approach is mandatory [71], [72].

The finite volume method (FVM) is the most common numerical technique to solve the set of crucial equations. In a finite volume method, a balance of basic volume i.e. control volume (Fig. 153) does not limit cell shape or grid type (structured or unstructured). The grid defines the boundaries of the control volumes while the computational node lines at the centre of the control volume. The FVM divides the domain into control volume and integrates the differential equation over the control volume and applies the divergence theorem. The results are solved iteratively or simultaneously and set to linear algebraic equations. Furthermore, the solution domain is subdivided into a finite number of small control volumes (cells) by a grid. The variable values at the faces of the control volume are determined by interpolation. The integral conservation equation of the FVM is exactly satisfied and the method is not limited to grid type [71].

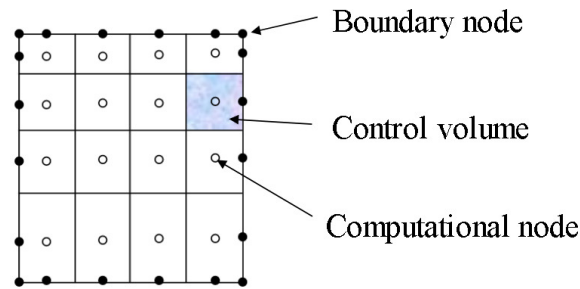


Fig. 153. FVM computational domain [71]

Reproduced with permission from *Termodynamiczne Basic course on technical and fluid mechanics*, Gierczycki A. T., Kubica R., ISBN 978-83-7335-979-6; Copyright 2012 Wydawnictwo Politechniki Śląskiej.

The solution can be considered converged until the change in the variable form (the flow field or scalar fields) from one iteration to the next becomes so small during the iterative process. All conservation equations comply with a specific tolerance and there are no longer changes with additional iterations. Moreover, the monitoring of residuals defines imbalance or error in conservation equations. The face values of calculated variables and their changes are found by making assumptions about variations of the variable between cell centres. There are several different solution schemes starting calculations with a first-order upwind scheme and after 100 iterations, is recommended, then switching to a second-order scheme which provides a good combination of stability and accuracy [71].

Post-processing is the last step when a converged solution is achieved and then there is an opportunity to carry out an analysis of the results. The CFD packages are now equipped with data visualizations tools such as: domain geometry and grid display, vector plots, line plots, 2D and 3D surface plots, particle tracking, view manipulation, animations and other. Moreover, it is possible to export data (alphanumeric) for further manipulation [71], [72].

V. User Defined Functions (UDFs)

A. ETA index

```

/*****
UDF to print ETA15% - It's area range with velocity +/-15% of mean velocity.
*****/
#include "udf.h"

DEFINE_ON_DEMAND(eta_calc)
{
    Domain *d;          /* structure that stores information about the calculated domain */
    Thread *t;         /* structure that stores information about threads */

```

```
cell_t c; /* index of cell within a specific thread */
real z_check; /* current coordinate of z velocity vector */
real w; /* current velocity of cell vector */
real sum_w = 0.; /* sum of all cell velocities */
real wavg = 0.; /* velocity average */
real wavg_min = 0.; /* velocity -15% of mean velocity */
real wavg_max = 0.; /* velocity +15% of mean velocity */
real vol_cell; /* cell volume */
real v_tot; /* total volume */
real v_cal; /* volume where the velocity is +/-15% of mean velocity */
real eta15; /* area range with velocity +/-15% of mean velocity */
real zmin = 0.0722; /* zmin for outlet face of monolith */
real zmax = 0.0762; /* zmax for outlet face of monolith */
real pos[ND_ND]; /* vector of coordinate cell */
int n=0; /* counter for all cells */

d = Get_Domain(1); /* Get the domain using ANSYS Fluent utility */

/* Loop over all cell threads in the domain */

thread_loop_c(t,d)
{
    /* Loop over all cells */

    begin_c_loop(c,t)
    {
        C_CENTROID(pos,c,t);
        /* returns the coordinate vector of the cell centre */

        z_check = pos[2];

        if ((z_check >= zmin) && (z_check <= zmax))
        {
            w = C_W(c,t); /* returns the Z component of the velocity vector */
            sum_w = sum_w + w;
            n += 1;
        }
    }
    end_c_loop(c,t)

    wavg = sum_w / n; /* returns average velocity */
    wavg_min = (wavg - (wavg*0.15)); /* returns velocity -15% of mean velocity */
    wavg_max = (wavg + (wavg*0.15)); /* returns velocity +15% of mean velocity */

    begin_c_loop(c, t)
    {
        C_CENTROID(pos, c, t);
        /* returns the coordinate vector of the cell center */
    }
}
```

```

z_check = pos[2];

if ((z_check >= zmin) && (z_check <= zmax))
{
    w = C_W(c, t); /* returns the Z component of the velocity vector */

    vol_cell = C_VOLUME(c, t);    /* get cell volume */
    v_tot += vol_cell;

    if ((w >= wavg_min) && (w <= wavg_max))
    {
        v_cal += vol_cell;
    }
}
end_c_loop(c, t)

eta15 = v_cal / v_tot;          /* returns ETA15% */
}
Message0("\n All cells = %d \n", n);
Message0("\n Velocity average = %8.4f \n", wavg);
Message0("\n Velocity -15 percent of mean velocity = %8.4f \n", wavg_min);
Message0("\n Velocity +15 percent of mean velocity = %8.4f \n", wavg_max);
Message0("\n Volume where the velocity is +/-15 percent of mean velocity = %g \n",
v_cal);
Message0("\n Volume total = %g \n", v_tot);
Message0("\n ETA15% = %8.4f \n", eta15);
}

```

B. Eccentricity index

```

/*****
UDF to print max velocity on the surface and provide its coordinates with Eccentricity.
*****/
#include "udf.h"

DEFINE_ON_DEMAND(wmax_calc)
{
    Domain *d;          /* structure that stores information about the calculated domain */
    Thread *t;         /* structure that stores information about threads */
    cell_t c;          /* index of cell within a specific thread */
    real x, y, z;      /* coordinates of vector velocity */
    real z_check;     /* current coordinate of z velocity vector */
    real w;           /* current velocity of cell vector */
    real wmax = 0.;   /* wmax max velocity on face */
    real zmin = 0.0722; /* zmin for outlet face of monolith */
    real zmax = 0.0762; /* zmax for outlet face of monolith */
    real R_mon = 0.0719; /* Monolith radius */
}

```

```
real r_cmax = 0.;          /* radius to max velocity vector */
real Eccen = 0.;          /* Eccentricity = r_cmax/R_mon */
real pos[ND_ND];          /* vector of coordinate cell */

d = Get_Domain(1);        /* Get the domain using ANSYS Fluent utility */

/* Loop over all cell threads in the domain */

thread_loop_c(t,d)
{
    /* Loop over all cells */

    begin_c_loop(c,t)
    {
        C_CENTROID(pos,c,t);
        /* returns the coordinate vector of the cell centre */

        z_check = pos[2];

        if ((z_check >= zmin) && (z_check <= zmax))
        {
            w = C_W(c,t); /* returns the Z component of the velocity vector */
            if (w > wmax)
            {
                wmax = w;
                x = pos[0];
                y = pos[1];
                z = pos[2];
                r_cmax = sqrt((x*x) + (y*y));
                Eccen = r_cmax / R_mon;
            }
        }
    }
    end_c_loop(c,t)
}
Message0("\n x = %8.4f y = %8.4f z = %8.4f wmax = %8.4f\n",x,y,z,wmax);
Message0("\n Eccentricity = %8.4f \n", Eccen);
}
```

VI. Research publications

The following publications have been written during this doctorate:

1. Kuta K., Żmudka Z., Kurzydym D., Przybyła G.: *Experimental and numerical investigation of dual-fuel CI ammonia engine emissions and after-treatment with V₂O₅/SiO₂-TiO₂ SCR*, Fuel, 2022 (publication in the Fuel review process).
2. Kurzydym D., Żmudka Z., Perrone D., Klimanek A.: *Experimental and numerical investigation of nitrogen oxides reduction in diesel engine selective catalytic reduction system*, Fuel, 2022. IF: 6.609, MNI_{SW} scoring: 140.
3. Kurzydym D., Klimanek A., Żmudka Z.: *Experimental research and CFD analysis of selective catalytic reduction of nitric oxides in the original SCR system and WALKER's replacement*, CPOTE 2020, pp. 891-898. MNI_{SW} scoring: 20.
4. Kurzydym D., Klimanek A., Żmudka Z.: *Experimental research and CFD analysis of flow parameters in a SCR system for the original part and WALKER's replacement*, Combustion Engines, 2019, pp. 12-19. MNI_{SW} scoring: 70.
5. Kurzydym D., Klimanek A., Żmudka Z.: *Experimental and numerical analysis of flow through catalytic converters for original part and WALKER's replacement using reverse engineering and CFD*, KONMOT, IOP Conf. Ser.: Mater. Sci. Eng., 2018, pp. 1-10. MNI_{SW} scoring: 20.

Abstract

The aim of the dissertation was to conduct experimental and numerical research for a selective catalytic reduction (SCR) system of a passenger cars with a diesel engine. The research consists of comparing the results for two different SCR systems, existing and new developed. The developed SCR system is aimed at introducing it to the secondary market (Aftermarket), which is also associated with the development of its own mixer design.

Due to increasingly stringent emission standards in particular nitrogen oxides (NO_x), the SCR systems have recently been invented and installed in diesel cars around the world. These systems must be validated during emission tests on the reduction of NO_x to the appropriate limit, in order to authorise a car do drive. To achieve this goal a coupled approach needs to be applied incorporating both extensive experimental research and advanced numerical methods based on computational fluid dynamics (CFD).

Therefore, in the research work various design variants of the SCR system and mixers at different operational parameters were studied. Several solutions were investigated under conditions that reflected the real operating conditions of the diesel engine operation. Among other things, pressure drops on monoliths, gas distribution and conversion of nitrogen oxides were tested and analyzed on prototypes in Tenneco laboratories. Furthermore, for the purpose of numerical model development, laser scanning was used to extract 3D models of the real geometries of the system elements by using a reverse engineering approach.

A commercial code ANSYS Fluent was used to perform the multiphase computational fluid dynamics studies. A careful analysis has been done for the subsequent processes occurring in the system, i.e. the evaporation and mixing of the reactants prior to the catalyst, proper distribution of flow through the catalyst and selection of appropriate thermal conditions for the process. Attention was given to the implementation of the SCR reaction kinetics. The CFD model was then validated against the experimental data showing good agreement between the measured and simulated parameters.

The final design of the replacement SCR part was compared with an original system delivered by the original equipment manufacturer. It was found that application of the new mixer in the replacement SCR system led to slightly lower NO_x emission, which was confirmed in the certification unit through emission tests in a car on the chassis dynamometer.

Streszczenie

Celem tej dysertacji było przeprowadzenie badań eksperymentalnych i numerycznych dla układu selektywnej redukcji katalitycznej (SCR) samochodu osobowego z silnikiem diesla. Badania polegały na porównaniu wyników dla dwóch różnych układów SCR, istniejącego i nowo opracowanego. Zaprojektowany układ SCR jest dedykowany do wdrożenia na rynek wtórny (Aftermarket), co również wiąże się z opracowaniem własnej konstrukcji jego miksera.

Ze względu na rosnące ostrzejsze normy emisji, w szczególności tlenków azotu (NO_x), układy SCR zostały niedawno opracowane i instalowane w samochodach z silnikiem diesla na całym świecie. Systemy te muszą być walidowane podczas badań emisyjnych pod kątem redukcji NO_x do odpowiedniego limitu, w celu dopuszczenia samochodu do ruchu drogowego. Aby osiągnąć ten cel, należy stosować podejście w którym są stosowane zarówno szerokie badania eksperymentalne, jak i zaawansowane metody numeryczne oparte na obliczeniowej mechanice płynów (CFD).

W związku z tym w pracy badawczej zbadano różne warianty konstrukcyjne układu SCR i mikserów w różnych parametrach operacyjnych. Przebadano kilka rozwiązań w różnych warunkach, które odzwierciedlają rzeczywiste warunki pracy silnika diesla. W laboratoriach Tenneco przetestowano i analizowano między innymi spadki ciśnienia na monolitach, dystrybucję gazu i konwersję tlenków azotu. Ponadto w celu opracowania modelu numerycznego, wykorzystano skanowanie laserowe do odtworzenia modeli 3D z rzeczywistych geometrii układu przy użyciu inżynierii odwrotnej.

Do przeprowadzenia wielofazowych badań obliczeniowej mechaniki płynów wykorzystano oprogramowanie ANSYS Fluent. Dokonano analizy kolejnych procesów zachodzących w układzie, tj. odparowania i mieszania reagentów przed katalizatorem, właściwej dystrybucji przepływu przez katalizator i doboru odpowiednich warunków termicznych procesu. Uwagę skupiono również na poprawnej implementacji kinetyki reakcji w układzie SCR. Model CFD został zweryfikowany w oparciu o dane eksperymentalne, które pokazały dobrą korelację między mierzonymi i symulowanymi parametrami.

Ostateczna konstrukcja zamiennego układu SCR została porównana z oryginalnym układem dostarczonym przez producenta oryginalnego wyposażenia. Stwierdzono, że zastosowanie nowego miksera w układzie zamiennym SCR prowadzi do nieco niższej emisji NO_x , co zostało potwierdzone w jednostce certyfikującej poprzez badanie emisji w samochodzie na hamowni podwoziowej.